Incompressible Boundary Layer Instability and Transition

Hjort, Søren; Sørensen, Jens Nørkær; Michelsen, Jess

Publication date:
2004

Document Version
Publisher's PDF, also known as Version of record

MEK-FM-PHD 2004-01

Incompressible Boundary Layer Instability and Transition

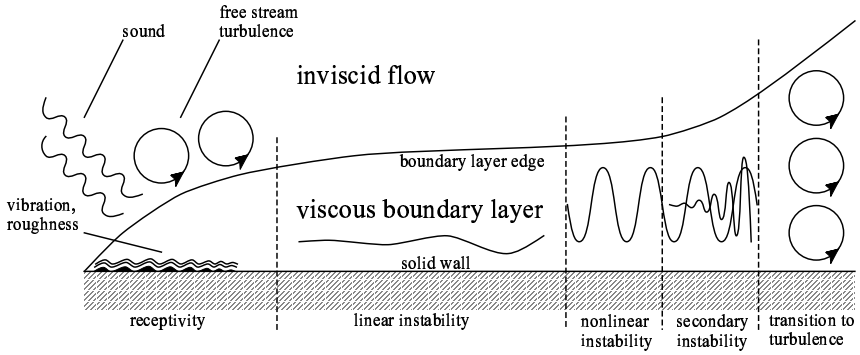

by

Søren Hjort

Dissertation submitted to the Technical University of Denmark in partial fulfillment of the requirements for the degree of Doctor of Philosophy in Mechanical Engineering

Fluid Mechanics
Department of Mechanical Engineering
Technical University of Denmark
March, 2004

Fluid Mechanics
Department of Mechanical Engineering
Nils Koppels Allé, Building 403
Technical University of Denmark
DK-2800 Lyngby, Denmark

Printed in Denmark by DTU-Tryk, Lyngby

MEK-FM-PHD 2004-01 / ISBN 87-7475-xxx-x

This thesis has been typeset using LaTeX2e.

Preface

This thesis is submitted in partial fulfillment of the requirements for the Ph.D. degree from the Technical University of Denmark (DTU). The research work was conducted during the period from July 1999 to June 2003 at the Department of Mechanical Engineering (MEK), Fluid Mechanics Section. I wish to express sincere thanks to my supervisor Professor Jens Nørkær Sørensen for his ever encouraging support.

Another gratitude goes to Associated Professor Jess A. Michelsen for many useful conversations.

Very useful input has been provided by Professor George Karniadakis for opening my eyes to the world of spectral and higher order numerics. Of equally great impact has been the correspondence with Professor Thorwald Herbert concerning three-dimensional PSE, and the Linear Stability code, linearX, that he provided me for free usage.

Also a profound support has been the increasingly meaningful and valuable comments from my children Maya and René. Finally the patience of my dear wife Fanny, who had to endure all the late nights working, should not be underestimated.

Sincerely thanks to all of you!

Lyngby, December, 2003

Søren Hjort

Abstract

The present thesis is an attempt to use classical hydrodynamic stability theory based on a Fourier decomposition of a perturbation around a steady flow solution denoted as the baseflow, and investigate its implications for laminar-turbulent transition modelling. We aim at further bridging the gap that has existed in fluid dynamics for many decades between stability theory and the development of Navier-Stokes solvers. A gap which has been narrowed during the last decade due to advances in nonlinear stability analysis on one side and direct numerical solutions on the other. In particular the nonlinear Parabolized Stability Equations (PSE) will be applied to capture secondary instability waves, the last distinct feature of many unsteady boundary layer flows prior to transition to turbulence.

The historical singularity of parabolic boundary layer solvers that is encountered at a boundary separation point, will affect the PSE in a likewise manner leading to failure of the solution procedure. We try to remedy this shortcoming and shed light into the mechanism that governs the transition in a boundary layer recirculation bubble, introducing for that purpose the Elliptic Stability Equations (ESE).

As a prerequisite to the work outlined above powerful discretization tools must be available. For this purpose a suite of novel 6’th order accurate coupled compact finite difference and finite volume based solvers have been developed in one and two dimensions.

Dansk resumé

Nærværende thesis forsøger at udvide anvendelsesområdet for klassisk hydrodynamisk stabilitetsteori baseret på en Fourier dekomposition af en perturbation omkring en jævn strømning, kaldet basis-strømningen, samt at undersøge de nye muligheder for laminar-turbulent omslagsmodellering. Som et mål bidrages til at indsnævre den kløft der indenfor fluid dynamik har eksisteret i mange årtier mellem stabilitetsteori og udviklingen af strømningsløsere. En kløft der allerede er blevet mindre gennem det sidste årti som følge af fremskridt indenfor ulineær stabilitetsteori på een side, og direkte numeriske løsere (DNS) på den anden. Specielt vil de ulineære Paraboliserede StabilitetsLigninger (PSE) blive anvendt til at beregne sekundære ustabilitetsbølger, som i mange omslagsscenarier optræder som et distinkt karakteristikum umiddelbart før det egentlige omslag til turbulens.

Den historiske singularitet som optræder i parabolske grænselagsløsere ved et separationspunkt, vil påvirke PSE på en lignende måde og føre til et stop i løsningsproceduren. Vi prøver at overkomme denne begrænsning og kaste lys over de mekanismer der er bestemmende for omslagsscenariet i en grænselags recirkulations-bobbel, og introducerer til dette formål de Elliptiske StabilitetsLigninger (ESE).

Som en forudsætning for det ovenfor skitserede arbejde, må der findes effektive diskretiseringsværktøjer. Til dette brug har vi udviklet et sæt af nye 6. ordens nøjagtige koblede kompakte finite difference og finite volume baserede løsere i en og to dimensioner.

Contents

List of Symbols

Roman letters

A	Hermite polynomial coefficient	
a	Hermite polynomial coefficient	
b	Bandwidth	
c_g	Group velocity	$[m/s]$
c_p	Pressure coefficient	$[-]$
cfl	Courant-Friedrichs-Lewy number	$[-]$
$\boldsymbol{D^x}$	x'th order differentiation matrix	
E	Error, discrepancy	
F	Self-similarity function	
f	Function, dependent variable	
G	Self-similarity function	
h	Channel height. Grid spacing	$[m]$
k	Grid spacing	$[m]$
L	Characteristic length	$[m]$
N	Number of Discretization points or DOFs	
P	Point position. Baseflow pressure	$[Pa]$
p'	Pressure perturbation	$[Pa]$
Q	Free stream velocity magnitude	$[m/s]$
$\boldsymbol{r}$	Spatial vector of arbitrary dimension	$[m]^x$
$\boldsymbol{r'}$	Spatial vector increment of arbitrary dimension	$[m]^x$
Re	Reynolds number	$[-]$
T	Chebyshev polynomial	
t	time	$[s]$
U	Baseflow x-velocity	$[m/s]$
u'	x-velocity perturbation	$[m/s]$
V	Baseflow y-velocity	$[m/s]$
v'	y-velocity perturbation	$[m/s]$
W	Baseflow z-velocity	$[m/s]$
w'	z-velocity perturbation	$[m/s]$
x	Distance, position	$[m]$
y	Distance, position	$[m]$
z	Distance, position	$[m]$

Greek letters

α	Streamwise/chordwise wavenumber	$[rad/m]$
β	Spanwise wavenumber	$[rad/m]$
δ	Displacement thickness	$[m]$
Δ	Temporal/spatial interval indicator	
η	Curvilinear direction (2nd axis)	
θ	Wave phase	$[rad]$
λ	Eigenvalue	
ν	Kinematic viscosity	$[m^2/s]$
ξ	Curvilinear direction (1st axis)	
ψ	Stream function	$[m^2/s]$
ω	Temporal wavenumber	$[rad/s]$

Subscripts

$_0$	Initial point
$_e$	Outer inviscid flow
$_i$	Discretization index. Imaginary unit
$_j$	Discretization index.
$_l$	Streamwise/chordwise wavenumber multiplier
$_m$	Temporal wavenumber multiplier
$_n$	Trial function index. Discretization index. Spanwise wavenumber multiplier
$_R$	Reverse flow

Superscripts

$^m/^n$	Order of differentiation in x-/y-direction
$^x/^y/^z$	Partial derivative in x-/y-/z-direction

Acronyms

2D/3D	Two-/Three-Dimensional
CCD	Coupled Compact finite Difference
CCV	Coupled Compact finite Volume
CD	Compact finite Difference
CFD	Computational Fluid Dynamics
CPU	Central Processing Unit
CV	Compact finite Volume
DOF	Degrees Of Freedom
DNS	Direct Numerical Simulation
ESE	Elliptic Stability Equations
FAS	Full Approximation Scheme
FD	Finite Difference
FFT	Fast Fourier Transform
FV	Finite Volume
H.O.T	Higher Order Terms
LHS	Left-Hand-Side
LST	Linear Stability Theory
MFC	Mean Flow Correction
MFD	Mean Flow Deflection
NS	Navier-Stokes
ODE	Ordinary Differential Equation
OS	Orr-Sommerfeld
PDE	Partial Differential Equation
PSE	Parabolized Stability Equations
RHS	Right-Hand-Side
TS	Tollmien-Schlichting

Chapter 1

Introduction

1.1 Motivation

Ever since the discovery of turbulence by O. Reynolds in 1883, the intricacy of the to the observer often chaotic behavior of an unsteady flow has continued to challenge the scientific world, and at present it can still be viewed as the main unsolved problem in classic mechanical physics. Turbulent flows as opposed to laminar flows are the rule rather than the exception, which can be evidenced by many daily life observations: Gusts of wind playing with the dead leaves at fall, stirring the cream in the coffee with a spoon, the trail of hot smoke particles emanating from a lit cigarette just to mention a few. The latter example actually gives the passionate smoke observer a glimpse of enlightening into the chain of events preceding and proceeding transition: From the cigarette tip a smooth laminar buoyancy driven flow is revealed. At some point further up the flow becomes clearly oscillating and soon thereafter breaks down into turbulent eddies, which will cascade into yet smaller eddies, until the size of them become so small that the strain of the fluid will be damped by viscous forces. The British meteorologist Lewis F. Richardson, backed up by experimental evidence, described this process in verse:

Big whorls have little whorls,
Which feed on their velocity,
And little whorls have lesser whorls,
And so on to viscosity.

Knowledge on the occurrence of transition is crucial in aerodynamic applications. In a boundary layer turbulence is characterized by increased skin friction, increased transport of heat and momentum and thus a change of transition location will greatly affect the performance of e.g. an airfoil or a turbine blade. From a commercial point of view, boundary layer turbulence can act co- and counter-productively as well. The boundary layer flow over the wings of a passenger aircraft at free flight is to remain laminar to the extent possible as to minimize skin friction and form drag, thus reducing fuel consumption. Laminar Flow Control is an active field of research. A counter-example of suppressing turbulence is found in the industry of wind turbines. A higher torque on the turbine axis can be generated if turbulence is triggered at an early stage of the boundary layer flow over the turbine blades. Due to increased mixing of momentum, a turbulent boundary layer is more resistant to separation than a laminar one, and stall will then occur at a larger angle of attack.

Whether transition should be suppressed or promoted is not the key issue. The key issue is that transition can be used to enhance the aerodynamic performance in general with respect to one or more parameters. In other words there exists a need to know the mechanisms leading to transition, and to compute the point of transition by adequate computational means. One could rightly argue that the task is conceptually easy since the Navier-Stokes equations that govern the motion of newtonian fluids have been derived more than a century ago. However, integration in time of the fully resolved Navier-Stokes equations (DNS) is an overwhelmingly cpu-intensive challenge. Of course the advent of ever more potent computers following Moore's law on exponential increase in processor power and memory resources allows for optimism, but even so DNS for high Reynolds number flows is not expected to take over before the end of the twenty-first century, according to a recent survey article by Spalart (2000). As of today DNS is a research tool, but not of engineering interest. Other tools have been and still need to be designed in the ongoing endeavor initiated by Osborne Reynolds. This thesis is a modest attempt to remove yet another pebble from the stony road towards fully resolved unsteady convectively dominated boundary layer flows of engineering interest.

1.2 Flow Description

From this early point on we would like to decompose the unsteady boundary layer solution into Fourier modes, at least conceptually. Think of the flow as the sum of Fourier modes each of which has a discrete constant temporal frequency in time and slightly varying spatial frequencies, or wavenumbers, in the wall-parallel directions. These modes will either amplify or decay exponentially in space, but given homogenous boundary conditions at the wall and in the free stream they will evolve with a fixed relative amplitude distribution in the wall normal direction. Also bear in mind that the boundary layer equations are parabolic in nature, which causes the boundary layer to propagate in the downstream direction only. Analogously, the disturbances in the flow are parabolic also, or rather parabolizable as will be shown: They propagate only in the direction of convection and are named convective disturbances. This is in contrast to absolute disturbances which propagate in both up- and downstream direction. In what follows we adopt the term disturbance for any flow-variation superposed to the laminar baseflow solution, and modal disturbance for a Fourier mode or a set of Fourier modes. A non-modal disturbance is typically induced in the boundary layer by inhomogeneties either at the wall or in the free stream. The chain of events that comprises the change of a boundary layer from being laminar to being turbulent is often categorized using 5 stages:

- 1st stage: Receptivity.
  This initial stage deals with how disturbances are introduced into the boundary layer. There are various types of noise: Wall roughness, wall vibration and free stream turbulence are the most common mechanisms, but also sound and body forcing e.g. by magnetism will generate a disturbance. In the ideal and rather unrealistic case of total absence of noise, modal disturbances will grow in an unstable boundary layer from a very small but finite level of disturbance, which is always present in the flow. If the initial disturbance level is low, the non-modal noise will become modal as it grows evolving into the 2nd stage.

- 2nd stage: Linear Instability.
  The modal disturbances evolve according to linear stability theory (LST) with an exponentially growing or decaying amplitude and very slow streamwise variation of the wall-normal amplitude distribution. Due to small amplitudes (less than one percent of free stream velocity) the interaction between different modes is negligible.

- 3rd stage: Nonlinear Instability.
  The amplitudes are now large, more than one percent of free stream velocity, and the different modes interact, eventually saturate at high amplitudes up to 25 percent free stream velocity, and cause a change, the Mean Flow Correction (MFC), in the mean flow, which was up to this stage the laminar solution only.

- 4th stage: Secondary Instability.
  The often highly distorted corrected mean flow is prone to a new array of unstable frequencies, often with very high growth rates and wavenumbers. Experiments have shown that these secondary instabilities precede the final stage.

- 5th stage: Transition to Turbulence.
  The predominantly streamwise wavy nature of the dominating instabilities break down into a broad band of frequencies in time and space which characterizes the onset of turbulence.

An important exception to the above so-called natural transition scenario is by-pass transition. As the name indicates one or various stages are in this case simply by-passed and transition occurs directly from the linear stage or even the receptivity stage. By-pass transition can be observed as a consequence of an absolute instability in the boundary layer, which can lead to self-induction. A separation bubble or a blocking object in the boundary layer could be such examples. Another by-pass mechanism can result from early appearances of turbulent spots probably induced by large-scale receptivity, either at the wall or in the free stream. The present thesis deals with the stages 1-4 for a series of testcases featuring different transition scenarios.

1.3 Literature Survey

Local Methods

The first attempt to explain hydrodynamic instability in the framework of the incompressible Navier-Stokes equations was done by Orr (1907) and Sommerfeld (1908) who derived the famous Orr-Sommerfeld (OS) equation, which constitutes a one-dimensional eigenvalue problem for parallel boundary layer flows. The parallel assumption is generally very good, and the OS equation is heavily used today for LST calculations and transitional modelling based on the e^N method. The first solutions to the OS-equation were presented by Tollmien (1929) followed by Schlichting (1933) who discovered plane convective 2D instabilities, later to be termed Tollmien-Schlichting (TS) waves. Experimental validation of the linear stability results was not reported until Liepmann (1943) and Schubauer & Skramstad (1947) conducted an experiment with vibrating ribbon induced disturbances detected by hotwire anemometry. A summary of local LST is given by Mack (1984), and on its use for transition prediction by

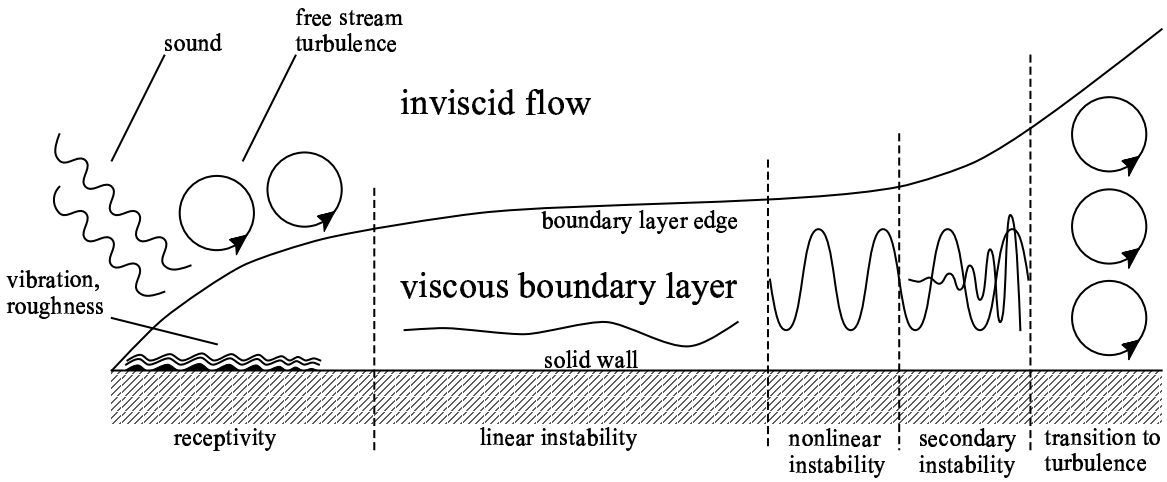

Figure 1.1: Stages of a transitional boundary layer flow.

Arnal (1994).

Over time the shortcomings of the OS-equation became increasingly apparent as the inappropriateness and empiricism of especially the e^N method for transition point location was evidenced by experiments, showing dependence on the factors not taken into account by the OS-equations: 1) The normal velocity of the mean flow profile; 2) The upstream conditions. The problem is mainly parabolic, but is solved locally; 3) Wall and free stream disturbances; 4) Nonlinear mode interaction for large amplitude disturbances and mean flow distortion. The parallel assumption can be replaced by weakly nonparallel approaches using the method of multiple scales within the perturbation theory for the modal disturbance. Bouthier (1972, 1973), Saric & NayFeh (1975) investigated the improvement of nonparallelism on the Blasius boundary. They found critical stability curves (neutral curves) in better agreement with Shubauer & Skramstadt, and later the experiment conducted by Kachanow, Kozlow & Levchenko (1977) further consolidated the relative importance of nonparallelism. Herbert (1974) and Itoh (1974) applied perturbation methods to include modest nonlinear mode interaction assuming once again a strictly parallel boundary layer. Smith (1979) and Goldstein & Durbin (1986) used asymptotic theories valid for very large Reynolds numbers to include nonlinearity and nonparallelism simultaneously.

Nonlocal parabolized Methods

The first nonlocal treatment of a discrete Fourier mode was done by Hall (1983) who considered the spatial evolution of steady spanwise periodic disturbances (Görtler vortices) by solving a set of parabolic equations. Herbert (1994) and Bertolotti (1991) later presented the Parabolized Stability Equations (PSE) of which Hall's Gortler vortex simulation is a special case. In short the PSE circumvent the limitations of LST and compare very well with DNS calculations, though at a fractional computational cost. It exploits fully the close to parabolic nature of the spatially evolving Fourier modes, and linear PSE can be extended to incorporate nonlinearity including the Mean Flow Correction (MFC) in a consistent manner. Independently of Herbert

& Bertolotti, Simen (1992) developed a nonlocal instability theory based on the method of multiple scales. This theory leads to equations identical to the PSE.

Since their appearance the PSE have been used in various contexts by many researchers. Chang et al. (1991) extended PSE into the compressible domain, Wang (1994) applied PSE to the rotating disc flow using cylindrical coordinates, Malik & Li (1994) examined the swept wing crossflow instability, Airiau & Casalis (1994) compared succesfully nonlinear PSE with DNS, Schrauf et al. (1996) used nonlinear PSE for transition prediction comparison with a real flight test boundary layer, Yen & Messersmith (1998) investigated a jet using PSE, Day et al. (1999) applied linear and nonlinear PSE to compute compressible mixing layers and posterior validation with DNS showing excellent agreement, and we have just picked a few. The review by Herbert (1997) summarizes PSE and its applications.

The only drawback of PSE is fundamental: Due to parabolicity in space only convective instabilities can be treated. On the other hand a large group of technologically important flows such as non-separated boundary layers and jets are unidirectional and therefore fully applicable for PSE.

Nonlocal Elliptic Methods

Within the framework of Fourier mode decomposition a spatially elliptic approach is still to be discovered. If we wish to simulate pressure and velocity instability in physical space as opposed to Fourier space the method is spatial DNS. Despite the huge computational resources already mentioned, Fourier modes in physical space, their nonlinear interaction, and transition have been successfully simulated for two- and three-dimensional boundary layers. DNS of two-dimensional Fourier modes in the Blasius boundary layer was performed by Spalart and compared with nonlinear PSE results in Bertolotti et al. (1992). Fundamental K-type transition in a decelerated Falkner-Skan boundary layer was simulated by Kloker (1998) . Brandt & Henningson (2002) were the first to simulate convective by-pass transition using optimal initial disturbances for transient energy amplification. Spalart & Strelets (2000) studied a separation bubble triggering another example of by-pass transition.

Chapter 2

Numerical Methods

Wave phenomena can be modelled using standard lower order discretization techniques. However, high resolution must be used to keep the error below a certain threshold. In contrast, higher order discretization schemes might increase the computational work per meshpoint considerably, but most often the higher order method allows for a much lower resolution, i.e. fewer meshpoints, so that even one-dimensional problems are solved more effectively. In multi-dimensional problems the benefit of lower resolution requirements multiplies.

2.1 Pseudo-Spectral ODE Solver

Also known as the spectral collocation method. In contrast to differentiation schemes involving local interpolants such as finite differences, the unknown solution to the differential equation is expanded as a global interpolant. As a consequence the accuracy of the spectral method is superior: For problems with smooth solutions exponential convergence rates of $O(e^{-cN})$ are common. In comparison, the second order finite difference scheme converges of the order $O(N^{-2})$. The price to pay for exponential convergence is the increased bandwidth of the resulting linear system. Full matrices replace sparse matrices, which means that the computational work for solving the ODE(s) scales like $O(N^3)$ as opposed to $O(N)$ for the local interpolant method. In general the pseudo-spectral method is the method of choice for small to moderate sized one-dimensional boundary value and eigenvalue problems with smooth solutions up to N of the order 100. Much larger values of N, on the other hand, will prove the method catastrophically uneconomical, at least for boundary value problems, due to the $O(N^3)$ scaling of the dense linear system.
For the set of trial functions we choose a basis of Chebyshev polynomials and a set of collocation points spanning the domain

$$T_n(y) = \cos\left(n \arccos(y)\right) \qquad n \in \{0; N-1\} \tag{2.1}$$

$$y_j = \cos\left(\frac{j\pi}{N-1}\right) \qquad j \in \{0; N-1\}, \tag{2.2}$$

over which the Chebychev polynomial basis satisfies a discrete orthogonality relation. The dependent variables are expressed globally as

$$f(y) = \sum_{n=0}^{N-1} a_n T_n(y) \tag{2.3}$$

The derivatives of the dependent variables must also be expressed in terms of Chebyshev polynomials. The following recursive formula, from Schmid & Henningson (2001), can be used in conjunction with (2.1). Polynomial subscript and superscript denote the order of polynomial and differentiation respectively.

$$
\begin{aligned}
T_0^{(k)}(y_j) &= 0 \\
T_1^{(k)}(y_j) &= T_0^{(k-1)}(y_j) \\
T_2^{(k)}(y_j) &= 4T_1^{(k-1)}(y_j) \\
T_n^{(k)}(y_j) &= 2nT_{n-1}^{(k-1)}(y_j) + \frac{n}{n-1}T_{n-1}^{(k)}(y_j) \qquad n \in \{3; N-1\}
\end{aligned} \tag{2.4}
$$

Dirichlet boundary conditions are applied in a straightforward way. For all but the channel poiseuille flow, the domain must be mapped into a semi-infinite domain $[0; \infty]$ suitable for boundary layer calculations. Infinity is set to the non-disturbed farfield, typically 20-50 boundary layer thicknesses away from the wall.

2.2 Coupled Compact Schemes

The drawback of spectral methods is their global dependence, which leads to a dense matrix, amenable to direct Gauss-elimination. This solution method for a linear system is costly as it scales O(N^3) with size, where N is the number of DOFs. Traditional finite difference schemes, in contrast, have compact support, and the resulting matrix to be solved will be banded with a bandwidth, b. Direct Gauss-elimination of this type of matrix scales O(Nb^2) in terms of cpu or floating point operations (flops). For 1D problems b is independent of N. For multi-dimensional problems this is not the case, and even the comparative ease of dealing with a banded matrix instead of a dense matrix might not be reduction enough. For sparse (non-dense) matrices the option of using iterative non-direct solvers is very important. The applicability of iterative solvers depends mostly on the strength of the matrix diagonal, the degree of diagonal dominance. If $2|a(i,i)| \geq \sum_{j=1}^{N} |a(i,j)|$ for all rows, i, the matrix is strictly diagonally dominant and can be solved by iterative solution methods. Less degrees of diagonal dominance will affect the convergence rate until, at some lower limit of diagonal dominance, the iterative solution process diverges. The advantage of iterative versus direct solvers is generally a better scalability for multidimensional problems. Using multigrid many iterative methods can be accelerated to achieve optimal scalability, O(N), for uni- and multi-dimensional problems.
Thus, the motivation to employ difference schemes with small stencils (i.e. compact support) is well justified. The drawback of these schemes is their lower accuracy and limited resolution power. The concept of resolution power addresses the scheme ability to capture wavy solutions with the least number of mesh points, and will be treated in Chapter 3. However, traditional difference schemes can be improved by adding unknowns, while maintaining the small stencil, typically 3-point. These improved difference schemes are referred to as compact difference schemes, due to their compactness despite higher order of accuracy. A multitude of schemes have been proposed over the last 3-4 decades: Ordinary difference schemes, Mitchell & Griffiths (1980), compact difference schemes, Lele (1992), coupled compact difference schemes, Mahesh (1998), compact volumes schemes, Kobayashi (1999), and coupled compact volume schemes, Chapter 3. The above sequence of scheme types is ordered by increasing complexity,

the less complex being special cases of the more complex. Throughout the present thesis higher order schemes are employed. Therefore this chapter will focus on the development of these, and present the specific schemes to be used in subsequent chapters. A small software package to derive all these one- or two-dimensional schemes symbolically will be explained.
The basis for scheme development is the Taylor series expansion around a known point in space of any dimensionality.

$$f(\mathbf{r}+\mathbf{r}^{'}) = \sum_{n=0}^{\infty} \frac{(\mathbf{r}^{'}\cdot\nabla)^n}{n!} f(\mathbf{r}) \tag{2.5}$$

For one- and two-dimensional cases (2.5) reduces to

$$\begin{aligned} &\mathbf{r} = x_0, \qquad \mathbf{r}^{'} = \Delta x \\ f(x) &= \frac{1}{0!}f^{(0)}(x_0)\Delta x^0 + \frac{1}{1!}f^{(1)}(x_0)\Delta x^1 + \frac{1}{2!}f^{(2)}(x_0)\Delta x^2 + \ldots(H.O.T) \end{aligned} \tag{2.6}$$

$$\begin{aligned} &\mathbf{r} = (x_0, y_0), \qquad \mathbf{r}^{'} = (\Delta x, \Delta y) \\ f(x,y) &= \frac{1}{0!}f^{(0,0)}(x_0,y_0)\Delta x^0\Delta y^0 \\ &+ \frac{1}{1!}f^{(1,0)}(x_0,y_0)\Delta x^1\Delta y^0 + \frac{1}{1!}f^{(0,1)}(x_0,y_0)\Delta x^0\Delta y^1 \\ &+ \frac{1}{2!}f^{(2,0)}(x_0,y_0)\Delta x^2\Delta y^0 + \frac{2}{2!}f^{(1,1)}(x_0,y_0)\Delta x^1\Delta y^1 + \frac{1}{2!}f^{(0,2)}(x_0,y_0)\Delta x^0\Delta y^2 \\ &+ \ldots(H.O.T) \end{aligned} \tag{2.7}$$

(2.5-2.7) refer to point values. In a finite volume framework average edge values and average volume values will become the dependent variables to trace, e.g. in a Navier-Stokes simulation. The averaging is done by integrating over the local domain, either an edge or a volume, and division by the domain size. The path of integration is indicated by the index points P_1 and P_2. In a structured mesh, cartesian or curvilinear, averaging over an x- (or ξ-) aligned edge will result when P_1 and P_2 share the same y- (or η-) coordinate, $P_1 = P_{i,j}$ and $P_2 = P_{i+1,j}$. Vice versa for averaging over a y- (or η-) aligned edge. Volume integration will result when P_1 and P_2 do not share neither x- (ξ-) coordinate nor y- (η-) coordinate, $P_1 = P_{i,j}$ and $P_2 = P_{i+1,j+1}$. In the case of edge- and volume-averaging respectively Taylor series expansion will lead to the following. Point indications refer to Fig.2.1 and barred quantities indicate averaging along the specified direction, x, y or both.

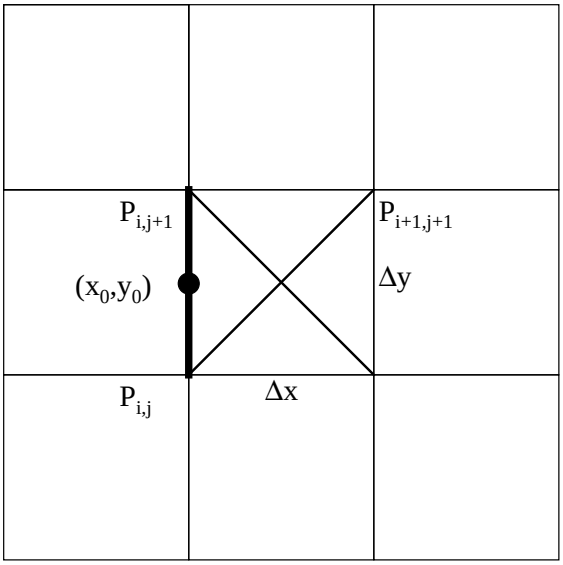

Figure 2.1: Grid schematic of edge- and volume based variables. Cell volume averages are crossed, cell edge averages are marked with a bold line.

$$
\begin{aligned}
\mathbf{r} = y_0, \qquad \mathbf{r}^{'} &= \Delta y \\
\overline{f(y)}^{y} &= f_{P_{i,j}\rightarrow P_{i,j+1}}(y) \\
&= \frac{1}{\Delta y}\int_{-\Delta y/2}^{\Delta y/2} f(y_0+\eta)d\eta \\
&= f^{(0,0)}(y_0) \\
&+ \frac{1}{24}f^{(0,2)}(y_0)\Delta y^2 \\
&+ \frac{1}{1920}f^{(0,4)}(y_0)\Delta y^4 \\
&+ \ldots(H.O.T) \qquad (2.8)\\
\mathbf{r} = (x_0,y_0), \qquad \mathbf{r}^{'} &= (\Delta x, \Delta y) \\
\overline{f(x,y)}^{xy} &= f_{P_{i,j}\rightarrow P_{i+1,j+1}}(x,y) \\
&= \frac{1}{\Delta x \Delta y}\int_{0}^{\Delta x}\int_{-\Delta y/2}^{\Delta y/2} f(x_0+\xi, y_0+\eta)d\xi d\eta \\
&= f^{(0,0)}(x_0,y_0) \\
&+ \frac{1}{2}f^{(1,0)}(x_0,y_0)\Delta x \\
&+ \frac{1}{6}f^{(2,0)}(x_0,y_0)\Delta x^2 + \frac{1}{24}f^{(0,2)}(x_0,y_0)\Delta y^2 \\
&+ \frac{1}{24}f^{(3,0)}(x_0,y_0)\Delta x^3 + \frac{1}{48}f^{(1,2)}(x_0,y_0)\Delta x \Delta y^2 \\
&+ \frac{1}{120}f^{(4,0)}(x_0,y_0)\Delta x^4 + \frac{1}{144}f^{(2,2)}(x_0,y_0)\Delta x^2\Delta y^2 + \frac{1}{1920}f^{(0,4)}(x_0,y_0)\Delta y^4 \\
&+ \frac{1}{}f^{(5,0)}(x_0,y_0)\Delta x^5 + \frac{1}{}f^{(3,2)}(x_0,y_0)\Delta x^3\Delta y^2 + \frac{1}{}f^{(1,4)}(x_0,y_0)\Delta x \Delta y^4
\end{aligned}
$$

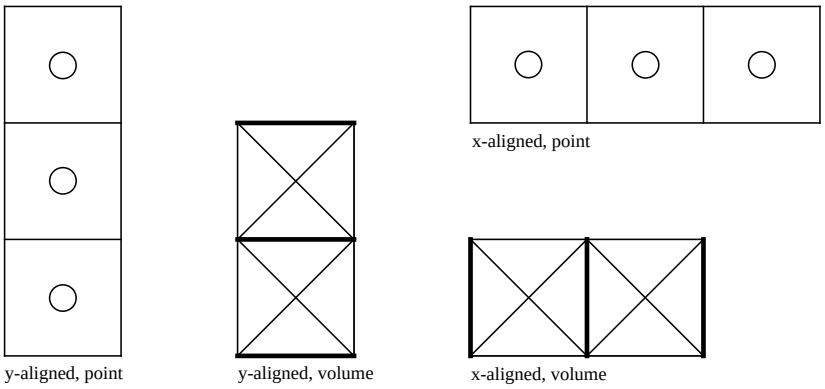

Figure 2.2: Point- and volume-based stencils.

In the lower domain size limit where $P_1 = P_2$, point based expansions are recovered.
Now, equipped with the equations (2.8-2.9) of which we consider point based schemes special cases, we define our scheme generically as either point-based or edge/volume-based. Making distinction between x- and y-aligned schemes leads to four cases as sketched in Fig.2.2. X-aligned point-based 3-point schemes with up to m_{max}-order x-derivative terms are now found from the relation below. Note here that $P_1 = P_2$ simply implies the degenerate case, where the volume-based stencil based on edge- and/or volume-averages has collapsed into points.

$$\sum_{m=0}^{m_{max}} \sum_{n=0}^{0} (A^{(m,n)}_{P_{i-1,j}\rightarrow P_{i-1,j}} f(x,y)^{(m,n)}_{P_{i-1,j}\rightarrow P_{i-1,j}} + A^{(m,n)}_{P_{i,j}\rightarrow P_{i,j}} f(x,y)^{(m,n)}_{P_{i,j}\rightarrow P_{i,j}} + A^{(m,n)}_{P_{i+1,j}\rightarrow P_{i+1,j}} f(x,y)^{(m,n)}_{P_{i+1,j}\rightarrow P_{i+1,j}}) = 0 \tag{2.10}$$

, where m_{max} is normally set to the highest order derivative in the governing equations, i.e. two for the Navier-Stokes equations. Analogously for the x-aligned volume-based 3-cell schemes.

$$\begin{aligned}\sum_{m=0}^{m_{max}} \sum_{n=0}^{0} (&A^{(m,n)}_{P_{i-1,j-1/2}\rightarrow P_{i-1,j+1/2}} f(x,y)^{(m,n)}_{P_{i-1,j-1/2}\rightarrow P_{i-1,j+1/2}} \\ &+A^{(m,n)}_{P_{i,j-1/2}\rightarrow P_{i,j+1/2}} f(x,y)^{(m,n)}_{P_{i,j-1/2}\rightarrow P_{i,j+1/2}} \\ &+A^{(m,n)}_{P_{i+1,j-1/2}\rightarrow P_{i+1,j+1/2}} f(x,y)^{(m,n)}_{P_{i+1,j-1/2}\rightarrow P_{i+1,j+1/2}}) \\ &+A^{(0,0)}_{P_{i-1,j-1/2}\rightarrow P_{i,j+1/2}} f(x,y)^{(0,0)}_{P_{i-1,j-1/2}\rightarrow P_{i,j+1/2}} \\ &+A^{(0,0)}_{P_{i,j-1/2}\rightarrow P_{i+1,j+1/2}} f(x,y)^{(0,0)}_{P_{i,j-1/2}\rightarrow P_{i+1,j+1/2}} = 0\end{aligned} \tag{2.11}$$

Here m_{max} will usually be set to 1 if the governing equations are the Navier-Stokes equations on integral form. The heavily indexed notation of (2.10-2.11) is used to encompass many different types of schemes and to stress their generic nature. Without further ado (2.10-2.11) are trivially satisfied to any degree of accuracy by means of the zero-solution for the set of coefficients, A. Schemes are constructed by imposing at least one coefficient, and solving for the

Table 2.1: Scheme coefficients

Scheme	$A_{-1}^{(0,0)}$	$A_{-1}^{(1,0)}$	$A_{-1}^{(2,0)}$	$A_{0}^{(0,0)}$	$A_{0}^{(1,0)}$	$A_{0}^{(2,0)}$	$A_{1}^{(0,0)}$	$A_{1}^{(1,0)}$	$A_{1}^{(2,0)}$	$A_{-1\to 0}^{(0,0)}$	$A_{0\to 1}^{(0,0)}$	Error
FD2	$\frac{-1}{2}$	0	0	0	$\mathbf{-1}$	0	$\frac{1}{2}$	0	0	-	-	$\frac{\Delta x^2}{6} f^{(3,0)}$
	1	0	0	-2	0	$\mathbf{-1}$	1	0	0	-	-	$\frac{\Delta x^2}{12} f^{(4,0)}$
FV2	0	0	-	$\mathbf{-1}$	0	-	0	0	-	$\frac{1}{2}$	$\frac{1}{2}$	$\frac{\Delta x^2}{6} f^{(2,0)}$
	0	0	-	0	$\mathbf{-1}$	-	0	0	-	-1	1	$\frac{\Delta x^2}{12} f^{(3,0)}$
CD4	$\frac{-3}{4}$	$\frac{-1}{4}$	0	0	$\mathbf{-1}$	0	$\frac{3}{4}$	$\frac{-1}{4}$	0	-	-	$\frac{\Delta x^4}{120} f^{(5,0)}$
	$\frac{6}{5}$	0	$\frac{-1}{10}$	$\frac{-12}{5}$	0	$\mathbf{-1}$	$\frac{6}{5}$	0	$\frac{-1}{10}$	-	-	$\frac{\Delta x^4}{200} f^{(6,0)}$
CV4	$\frac{-1}{4}$	0	-	$\mathbf{-1}$	0	-	$\frac{-1}{4}$	0	-	$\frac{3}{4}$	$\frac{3}{4}$	$\frac{\Delta x^4}{120} f^{(4,0)}$
	0	$\frac{-1}{10}$	-	0	$\mathbf{-1}$	-	0	$\frac{-1}{10}$	-	$\frac{-6}{5}$	$\frac{6}{5}$	$\frac{\Delta x^4}{200} f^{(5,0)}$
CCD6	$\frac{-15}{16}$	$\frac{-7}{16}$	$\frac{-1}{16}$	0	$\mathbf{-1}$	0	$\frac{15}{16}$	$\frac{-7}{16}$	$\frac{1}{16}$	-	-	$\frac{\Delta x^6}{5040} f^{(7,0)}$
	3	$\frac{9}{8}$	$\frac{1}{8}$	-6	0	$\mathbf{-1}$	3	$\frac{-9}{8}$	$\frac{1}{8}$	-	-	$\frac{\Delta x^6}{20160} f^{(8,0)}$
CCV6	$\frac{-7}{16}$	$\frac{-1}{16}$	-	$\mathbf{-1}$	0	-	$\frac{-7}{16}$	$\frac{1}{16}$	-	$\frac{15}{16}$	$\frac{15}{16}$	$\frac{\Delta x^6}{5040} f^{(6,0)}$
	$\frac{9}{8}$	$\frac{1}{8}$	-	0	$\mathbf{-1}$	-	$\frac{-9}{8}$	$\frac{1}{8}$	-	-3	3	$\frac{\Delta x^6}{20160} f^{(7,0)}$

remaining coefficients to obtain the highest possible formal degree of accuracy. In table 2.1 the coefficients of ordinary explicit, compact and coupled compact finite difference and finite volume schemes are listed. All the boldly typed coefficient values are the imposed ones. The truncation error for each scheme indicates the order of accuracy. The resolution capabilities of a scheme generally improves as the truncation error decreases, and this also holds for the presented schemes. However, a rigid scheme resolution analysis is not performed here, in order not to overlap the analysis given in Chapter 3. For each scheme two derivative evaluations are given for the advection and diffusion operator respectively. In a finite difference framework this corresponds to the first and second derivatives. In a finite volume framework it corresponds to the zeroth and first derivatives. The schemes are:

- FD2: Explicit (ordinary) 2nd order accurate finite difference schemes
- FV2: Explicit (ordinary) 2nd order accurate finite volume schemes
- CD4 : Implicit 4th order accurate compact difference schemes, a.k.a. Padé schemes, e.g. Lele (1992).
- CV4: Implicit 4th order accurate compact volume schemes as presented by Kobayashi (1999).
- CCD6: Implicit 6th order accurate coupled compact difference schemes as presented by Mahesh (1998). Chu & Fan (1997) analyzed the same schemes using the term 'combined' instead of coupled. Chu & Fan also published a non-uniform version of the scheme, (1999), which is pretty much the scheme used for the stability calculations in the present thesis. The only difference is for the upwinded boundary schemes adjacent to the wall, where Chu & Fan proposed a 5th order polynomial. In the present work the 6th order accuracy has been maintained.
- CCV6: Implicit 6th order accurate coupled compact volume schemes. These combine the coupled derivative evaluation from the CCD6 schemes with Kobayashis use of sliding

Table 2.2: Example of 1D Taylor series expansions for the CCD6 schemes

Deriv.	LHS							RHS1	RHS2
coeffs.	$A_{-1}^{(0,0)}$	$A_{0}^{(0,0)}$	$A_{1}^{(0,0)}$	$A_{-1}^{(1,0)}$	$A_{1}^{(1,0)}$	$A_{-1}^{(2,0)}$	$A_{1}^{(2,0)}$	$A_{0}^{(1,0)}$	$A_{0}^{(2,0)}$
$f(x_0)^{(0)}$	1	1	1	0	0	0	0	0	0
$f(x_0)^{(1)}$	$-\Delta x$	0	Δx	1	1	0	0	1	0
$f(x_0)^{(2)}$	$\frac{\Delta x^2}{2!}$	0	$\frac{\Delta x^2}{2!}$	$-\Delta x$	Δx	1	1	0	1
$f(x_0)^{(3)}$	$-\frac{\Delta x^3}{3!}$	0	$\frac{\Delta x^3}{3!}$	$\frac{\Delta x^2}{2!}$	$\frac{\Delta x^2}{2!}$	$-\Delta x$	Δx	0	0
$f(x_0)^{(4)}$	$\frac{\Delta x^4}{4!}$	0	$\frac{\Delta x^4}{4!}$	$-\frac{\Delta x^3}{3!}$	$\frac{\Delta x^3}{3!}$	$\frac{\Delta x^2}{2!}$	$\frac{\Delta x^2}{2!}$	0	0
$f(x_0)^{(5)}$	$-\frac{\Delta x^5}{5!}$	0	$\frac{\Delta x^5}{5!}$	$\frac{\Delta x^4}{4!}$	$\frac{\Delta x^4}{4!}$	$-\frac{\Delta x^3}{3!}$	$\frac{\Delta x^3}{3!}$	0	0
$f(x_0)^{(6)}$	$\frac{\Delta x^6}{6!}$	0	$\frac{\Delta x^6}{6!}$	$-\frac{\Delta x^5}{5!}$	$\frac{\Delta x^5}{5!}$	$\frac{\Delta x^4}{4!}$	$\frac{\Delta x^4}{4!}$	0	0
$f(x_0)^{(7)}$	$-\frac{\Delta x^7}{7!}$	0	$\frac{\Delta x^7}{7!}$	$\frac{\Delta x^6}{6!}$	$\frac{\Delta x^6}{6!}$	$-\frac{\Delta x^5}{5!}$	$\frac{\Delta x^5}{5!}$	0	0
$f(x_0)^{(8)}$	$\frac{\Delta x^8}{8!}$	0	$\frac{\Delta x^8}{8!}$	$-\frac{\Delta x^7}{7!}$	$\frac{\Delta x^7}{7!}$	$\frac{\Delta x^6}{6!}$	$\frac{\Delta x^6}{6!}$	0	0

average variables in a finite volume setting. As to the extent of our knowledge these schemes have not been presented earlier in literature. A variant of the CCV6 schemes are used for the multigrid accelerated 2D Navier-Stokes solver to be presented in Chapter 3.

The non-uniform 3-point CCD6 scheme is used in all subsequent stability calculations along the wall-normal direction unless otherwise stated. The scheme coefficients for first and second order derivative evaluations are given below. $\Delta x_1 = x_i - x_{i-1}$ and $\Delta x_2 = x_{i+1} - x_i$.

$$
\begin{aligned}
A_{-1}^{(2,0)} &= -1/2\frac{\Delta x_1 {\Delta x_2}^3}{(\Delta x_1 + \Delta x_2)^3} \\
A_{0}^{(2,0)} &= 0 \\
A_{1}^{(2,0)} &= 1/2\frac{{\Delta x_1}^3 \Delta x_2}{(\Delta x_1 + \Delta x_2)^3} \\
A_{-1}^{(1,0)} &= -\frac{{\Delta x_2}^3(5\Delta x_1 + 2\Delta x_2)}{(\Delta x_1 + \Delta x_2)^4} \\
A_{0}^{(1,0)} &= -1 \\
A_{1}^{(1,0)} &= -\frac{{\Delta x_1}^3(2\Delta x_1 + 5\Delta x_2)}{(\Delta x_1 + \Delta x_2)^4} \\
A_{-1}^{(0,0)} &= -3\frac{{\Delta x_2}^3(5{\Delta x_1}^2 + 4\Delta x_1 \Delta x_2 + {\Delta x_2}^2)}{\Delta x_1(\Delta x_1 + \Delta x_2)^5} \\
A_{0}^{(0,0)} &= 3\frac{\Delta x_2 - \Delta x_1}{\Delta x_1 \Delta x_2} \\
A_{1}^{(0,0)} &= 3\frac{{\Delta x_1}^3({\Delta x_1}^2 + 4\Delta x_1 \Delta x_2 + 5{\Delta x_2}^2)}{\Delta x_2(\Delta x_1 + \Delta x_2)^5}
\end{aligned}
\tag{2.12}
$$

$$
\begin{aligned}
A_{-1}^{(2,0)} &= \frac{{\Delta x_2}^2(3\Delta x_1 - 2\Delta x_2)}{(\Delta x_1 + \Delta x_2)^3} \\
A_{0}^{(2,0)} &= -1 \\
A_{1}^{(2,0)} &= \frac{{\Delta x_1}^2(-2\Delta x_1 + 3\Delta x_2)}{(\Delta x_1 + \Delta x_2)^3} \\
A_{-1}^{(1,0)} &= 6\frac{{\Delta x_2}^2(5{\Delta x_1}^2 - \Delta x_1\Delta x_2 - {\Delta x_2}^2)}{\Delta x_1(\Delta x_1 + \Delta x_2)^4} \\
A_{0}^{(1,0)} &= 0 \\
A_{1}^{(1,0)} &= -6\frac{{\Delta x_1}^2(-{\Delta x_1}^2 - \Delta x_1\Delta x_2 + 5{\Delta x_2}^2)}{\Delta x_2(\Delta x_1 + \Delta x_2)^4} \\
A_{-1}^{(0,0)} &= 6\frac{{\Delta x_2}^2(15{\Delta x_1}^3 + 4{\Delta x_1}^2\Delta x_2 - 2\Delta x_1{\Delta x_2}^2 - {\Delta x_2}^3)}{{\Delta x_1}^2(\Delta x_1 + \Delta x_2)^5} \\
A_{0}^{(0,0)} &= 6\frac{{\Delta x_1}^2 - 3\Delta x_1\Delta x_2 + {\Delta x_2}^2}{{\Delta x_1}^2{\Delta x_2}^2} \\
A_{1}^{(0,0)} &= 6\frac{{\Delta x_1}^2(-{\Delta x_1}^3 - 2{\Delta x_1}^2\Delta x_2 + 4\Delta x_1{\Delta x_2}^2 + 15{\Delta x_2}^3)}{{\Delta x_2}^2(\Delta x_1 + \Delta x_2)^5}
\end{aligned}
\tag{2.13}
$$

At the wall a 4-point non-uniform upwinded scheme is used, which is very lengthy and not reducible to anything nice. Hence, it is not presented. These lengthy boundary schemes, counting in the order of 100 flops to calculate the coefficients given the grid spacing, are only computationally economic if the same set of coefficients can be used many times. For the cpu-intensive (nonlinear) stability calculations to be presented this is fortunately the case.

For local stability analysis the Orr-Sommerfeld equation is to be solved yielding derivative orders of up to four. Extending the ideas from coupled compact difference schemes and Chu & Fan's non-uniform CCD6 scheme, we propose a three-point non-uniform CCD8 scheme with 10'th order accuracy for the first and second order derivative evaluations and 8'th order accuracy for the third and fourth order derivatives. The CCD6 schemes emerged from setting $m_{max} = 2$ in (2.10). Setting $m_{max} = 4$ will lead to the CCD8 schemes. Coefficients are for the first, second, third and fourth order derivatives are given in (2.14-2.17).

Again a 4-point upwinded scheme is used at the boundaries for Dirichlet conditions or in the absence of boundary conditions. Enlarging the stencil size enables the order of accuracy to be maintained. In general these boundary schemes are not only algebraically lengthy, they also suffer from a reduced orthogonality of the coefficient matrix, leading to a large condition number. In practice this means that the remaining residual after solving a differential equation will be larger than if the boundary scheme were orthogonal to the same degree as the central

CCD schemes used for the interior domain discretization.

$$
\begin{aligned}
A_{-1}^{(4,0)} =& -\Delta x_1{}^3\Delta x_2{}^5/(24(\Delta x_1+\Delta x_2)^5)\\
A_{1}^{(4,0)} =& \Delta x_1{}^5\Delta x_2{}^3/(24(\Delta x_1+\Delta x_2)^5)\\
A_{-1}^{(3,0)} =& -\Delta x_1{}^2\Delta x_2{}^5(7\Delta x_1+2\Delta x_2)/(6(\Delta x_1+\Delta x_2)^6)\\
A_{1}^{(3,0)} =& -\Delta x_1{}^5\Delta x_2{}^2(2\Delta x_1+7\Delta x_2)/(6(\Delta x_1+\Delta x_2)^6)\\
A_{-1}^{(2,0)} =& -\Delta x_1\Delta x_2{}^5(28\Delta x_1{}^2+16\Delta x_1\Delta x_2+3\Delta x_2{}^2)/(2(\Delta x_1+\Delta x_2)^7)\\
A_{1}^{(2,0)} =& \Delta x_1{}^5\Delta x_2(3\Delta x_1{}^2+16\Delta x_1\Delta x_2+28\Delta x_2{}^2)/(2(\Delta x_1+\Delta x_2)^7)\\
A_{-1}^{(1,0)} =& -\Delta x_2{}^5(84\Delta x_1{}^3+72\Delta x_1{}^2\Delta x_2+27\Delta x_1\Delta x_2{}^2+4\Delta x_2{}^3)/((\Delta x_1+\Delta x_2)^8)\\
A_{1}^{(1,0)} =& -\Delta x_1{}^5(4\Delta x_1{}^3+27\Delta x_1{}^2\Delta x_2+72\Delta x_1\Delta x_2{}^2+84\Delta x_2{}^3)/((\Delta x_1+\Delta x_2)^8)\\
A_{-1}^{(0,0)} =& -5\Delta x_2{}^5(42\Delta x_1{}^4+48\Delta x_1{}^3\Delta x_2+27\Delta x_1{}^2\Delta x_2{}^2+8\Delta x_1\Delta x_2{}^3+\Delta x_2{}^4)/\\
& (\Delta x_1(\Delta x_1+\Delta x_2)^9)\\
A_{0}^{(0,0)} =& 5(\Delta x_2-\Delta x_1)/(\Delta x_1\Delta x_2)\\
A_{1}^{(0,0)} =& 5\Delta x_1{}^5(\Delta x_1{}^4+8\Delta x_1{}^3\Delta x_2+27\Delta x_1{}^2\Delta x_2{}^2+48\Delta x_1\Delta x_2{}^3+42\Delta x_2{}^4)/\\
& (\Delta x_2(\Delta x_1+\Delta x_2)^9)\\
A_{0}^{(4,0)} =& A_0^{(3,0)}=A_0^{(2,0)}=0, \qquad A_0^{(1,0)}=-1
\end{aligned}
\tag{2.14}
$$

$$
\begin{aligned}
A_{-1}^{(4,0)} =& \Delta x_1{}^2\Delta x_2{}^4(5\Delta x_1-4\Delta x_2)/(12(\Delta x_1+\Delta x_2)^5)\\
A_{1}^{(4,0)} =& \Delta x_1{}^4\Delta x_2{}^2(-4\Delta x_1+5\Delta x_2)/(12(\Delta x_1+\Delta x_2)^5)\\
A_{-1}^{(3,0)} =& \Delta x_1\Delta x_2{}^4(35\Delta x_1{}^2-17\Delta x_1\Delta x_2-7\Delta x_2{}^2)/(3(\Delta x_1+\Delta x_2)^6)\\
A_{1}^{(3,0)} =& -\Delta x_1{}^4\Delta x_2(-7\Delta x_1{}^2-17\Delta x_1\Delta x_2+35\Delta x_2{}^2)/(3(\Delta x_1+\Delta x_2)^6)\\
A_{-1}^{(2,0)} =& \Delta x_2{}^4(140\Delta x_1{}^3-24\Delta x_1{}^2\Delta x_2-38\Delta x_1\Delta x_2{}^2-9\Delta x_2{}^3)/((\Delta x_1+\Delta x_2)^7)\\
A_{1}^{(2,0)} =& \Delta x_1{}^4(-9\Delta x_1{}^3-38\Delta x_1{}^2\Delta x_2-24\Delta x_1\Delta x_2{}^2+140\Delta x_2{}^3)/((\Delta x_1+\Delta x_2)^7)\\
A_{-1}^{(1,0)} =& 10\Delta x_2{}^4(84\Delta x_1{}^4+12\Delta x_1{}^3\Delta x_2-18\Delta x_1{}^2\Delta x_2{}^2-11\Delta x_1\Delta x_2{}^3-2\Delta x_2{}^4)/\\
& (\Delta x_1(\Delta x_1+\Delta x_2)^8)\\
A_{1}^{(1,0)} =& -10\Delta x_1{}^4(-2\Delta x_1{}^4-11\Delta x_1{}^3\Delta x_2-18\Delta x_1{}^2\Delta x_2{}^2+12\Delta x_1\Delta x_2{}^3+84\Delta x_2{}^4)/\\
& (\Delta x_2(\Delta x_1+\Delta x_2)^8)\\
A_{-1}^{(0,0)} =& 10\Delta x_2{}^4(210\Delta x_1{}^5+96\Delta x_1{}^4\Delta x_2-6\Delta x_1{}^3\Delta x_2{}^2-29\Delta x_1{}^2\Delta x_2{}^3-\\
& 13\Delta x_1\Delta x_2{}^4-2\Delta x_2{}^5)/(\Delta x_1{}^2(\Delta x_1+\Delta x_2)^9)\\
A_{0}^{(0,0)} =& 10(2\Delta x_1{}^2-5\Delta x_1\Delta x_2+2\Delta x_2{}^2)/(\Delta x_1{}^2\Delta x_2{}^2)\\
A_{1}^{(0,0)} =& 10\Delta x_1{}^4(-2\Delta x_1{}^5-13\Delta x_1{}^4\Delta x_2-29\Delta x_1{}^3\Delta x_2{}^2-6\Delta x_1{}^2\Delta x_2{}^3+\\
& 96\Delta x_1\Delta x_2{}^4+210\Delta x_2{}^5)/(\Delta x_2{}^2(\Delta x_1+\Delta x_2)^9)\\
A_{0}^{(4,0)} =& A_0^{(3,0)}=A_0^{(1,0)}=0, \qquad A_0^{(2,0)}=-1
\end{aligned}
\tag{2.15}
$$

$$
\begin{aligned}
A_{-1}^{(4,0)} =& -\Delta x_1 {\Delta x_2}^3(5{\Delta x_1}^2 - 10\Delta x_1\Delta x_2 + 3{\Delta x_2}^2)/(2(\Delta x_1 + \Delta x_2)^5)\\
A_{1}^{(4,0)} =& {\Delta x_1}^3\Delta x_2(3{\Delta x_1}^2 - 10\Delta x_1\Delta x_2 + 5{\Delta x_2}^2)/(2(\Delta x_1 + \Delta x_2)^5)\\
A_{-1}^{(3,0)} =& -{\Delta x_2}^3(70{\Delta x_1}^3 - 115{\Delta x_1}^2\Delta x_2 + 4\Delta x_1{\Delta x_2}^2 + 9{\Delta x_2}^3)/((\Delta x_1 + \Delta x_2)^6)\\
A_{1}^{(3,0)} =& -{\Delta x_1}^3(9{\Delta x_1}^3 + 4{\Delta x_1}^2\Delta x_2 - 115\Delta x_1{\Delta x_2}^2 + 70{\Delta x_2}^3)/((\Delta x_1 + \Delta x_2)^6)\\
A_{-1}^{(2,0)} =& -30{\Delta x_2}^3(28{\Delta x_1}^4 - 36{\Delta x_1}^3\Delta x_2 - 9{\Delta x_1}^2{\Delta x_2}^2 + 2\Delta x_1{\Delta x_2}^3 + {\Delta x_2}^4)/\\
& (\Delta x_1(\Delta x_1 + \Delta x_2)^7)\\
A_{1}^{(2,0)} =& 30{\Delta x_1}^3({\Delta x_1}^4 + 2{\Delta x_1}^3\Delta x_2 - 9{\Delta x_1}^2{\Delta x_2}^2 - 36\Delta x_1{\Delta x_2}^3 + 28{\Delta x_2}^4)/\\
& (\Delta x_2(\Delta x_1 + \Delta x_2)^7)\\
A_{-1}^{(1,0)} =& -60{\Delta x_2}^3(84{\Delta x_1}^5 - 78{\Delta x_1}^4\Delta x_2 - 45{\Delta x_1}^3{\Delta x_2}^2 - 7{\Delta x_1}^2{\Delta x_2}^3 + 3\Delta x_1{\Delta x_2}^4 +\\
& {\Delta x_2}^5)/({\Delta x_1}^2(\Delta x_1 + \Delta x_2)^8)\\
A_{1}^{(1,0)} =& -60{\Delta x_1}^3({\Delta x_1}^5 + 3{\Delta x_1}^4\Delta x_2 - 7{\Delta x_1}^3{\Delta x_2}^2 - 45{\Delta x_1}^2{\Delta x_2}^3 - 78\Delta x_1{\Delta x_2}^4 +\\
& 84{\Delta x_2}^5)/({\Delta x_2}^2(\Delta x_1 + \Delta x_2)^8)\\
A_{-1}^{(0,0)} =& -60{\Delta x_2}^3(210{\Delta x_1}^6 - 120{\Delta x_1}^5\Delta x_2 - 123{\Delta x_1}^4{\Delta x_2}^2 - 52{\Delta x_1}^3{\Delta x_2}^3 -\\
& 4{\Delta x_1}^2{\Delta x_2}^4 + 4\Delta x_1{\Delta x_2}^5 + 1{\Delta x_2}^6)/({\Delta x_1}^3(\Delta x_1 + \Delta x_2)^9)\\
A_{0}^{(0,0)} =& -60(\Delta x_1^3 - 5{\Delta x_1}^2\Delta x_2 + 5\Delta x_1{\Delta x_2}^2 - {\Delta x_2}^3)/({\Delta x_1}^3{\Delta x_2}^3)\\
A_{1}^{(0,0)} =& 60{\Delta x_1}^3({\Delta x_1}^6 + 4{\Delta x_1}^5\Delta x_2 - 4{\Delta x_1}^4{\Delta x_2}^2 - 52{\Delta x_1}^3{\Delta x_2}^3 -\\
& 123{\Delta x_1}^2{\Delta x_2}^4 - 120\Delta x_1{\Delta x_2}^5 + 210{\Delta x_2}^6)/({\Delta x_2}^3(\Delta x_1 + \Delta x_2)^9)\\
A_{0}^{(4,0)} =& A_0^{(2,0)} = A_0^{(1,0)} = 0, \qquad A_0^{(3,0)} = -1
\end{aligned}
\tag{2.16}
$$

The CCD8 scheme can be used to discretize a linear system. For 1D scalar problems this leads to a 5x5 block tri-diagonal system, which can be solved directly and efficiently. For 1D scalar eigenvalue problems such as the Orr-Sommerfeld equation, we can use standard global eigenvalue solvers in conjunction with dense differentiation matrices as known from the pseudo-spectral method. To do so, we discretize the 1D domain using the CCD8 scheme. This leads to 4 equations, one for each derivative order, and 5 unknowns at each mesh point. This system is then solved with respect to $f^{(1)}$, $f^{(2)}$, $f^{(3)}$ and $f^{(4)}$. $f^{(0)}$, whose equation is the governing Orr-Sommerfeld equation, goes on the RHS such that after inversion each derivative operator is expressed as a dense matrix for the dependent variable, $f = f^{(0)}$, exactly as for the pseudo-spectral method. The advantage of using the CCD8 scheme to obtain differentiation matrices instead of the spectral method is that the mesh can be defined arbitrarily and hence not by a fixed set of collocation points. A comparison of pseudo-spectral and CCD8 discretization for solving the O-S eigenvalue problem is presented in a proceeding chapter for linear stability calculations.

Symbolic derivation of the schemes is done using the Matlab 5.2 Symbolic Toolbox as follows. Scheme terms of e.g (2.10), (2.11) or any other imposed stencil in 2D are expanded in Taylor series using (2.7). The unknown discretization spacings and A-coefficients are treated symbolically. Derivative terms are collected according to the derivative order. For each order LHS and RHS must cancel out up to the obtainable order of accuracy, where the residual,

$$
\begin{aligned}
A_{-1}^{(4,0)} =& 2\Delta x_2{}^2(5\Delta x_1{}^3 - 20\Delta x_1{}^2\Delta x_2 + 15\Delta x_1\Delta x_2{}^2 - 2\Delta x_2{}^3)/((\Delta x_1 + \Delta x_2)^5) \\
A_{1}^{(4,0)} =& 2\Delta x_1{}^2(-2\Delta x_1{}^3 + 15\Delta x_1{}^2\Delta x_2 - 20\Delta x_1\Delta x_2{}^2 + 5\Delta x_2{}^3)/((\Delta x_1 + \Delta x_2)^5) \\
A_{-1}^{(3,0)} =& 20\Delta x_2{}^2(14\Delta x_1{}^4 - 50\Delta x_1{}^3\Delta x_2 + 25\Delta x_1{}^2\Delta x_2{}^2 + 4\Delta x_1\Delta x_2{}^3 - \Delta x_2{}^4)/ \\
& (\Delta x_1(\Delta x_1 + \Delta x_2)^6) \\
A_{1}^{(3,0)} =& -20\Delta x_1{}^2(-\Delta x_1{}^4 + 4\Delta x_1{}^3\Delta x_2 + 25\Delta x_1{}^2\Delta x_2{}^2 - 50\Delta x_1\Delta x_2{}^3 + 14\Delta x_2{}^4)/ \\
& (\Delta x_2(\Delta x_1 + \Delta x_2)^6) \\
A_{-1}^{(2,0)} =& 60\Delta x_2{}^2(56\Delta x_1{}^5 - 176\Delta x_1{}^4\Delta x_2 + 45\Delta x_1{}^3\Delta x_2{}^2 + 29\Delta x_1{}^2\Delta x_2{}^3 + 3\Delta x_1\Delta x_2{}^4 - \\
& \Delta x_2{}^5)/(\Delta x_1{}^2(\Delta x_1 + \Delta x_2)^7) \\
A_{1}^{(2,0)} =& 60\Delta x_1{}^2(-\Delta x_1{}^5 + 3\Delta x_1{}^4\Delta x_2 + 29\Delta x_1{}^3\Delta x_2{}^2 + 45\Delta x_1{}^2\Delta x_2{}^3 - 176\Delta x_1\Delta x_2{}^4 + \\
& 56\Delta x_2{}^5)/(\Delta x_2{}^2(\Delta x_1 + \Delta x_2)^7) \\
A_{-1}^{(1,0)} =& 120\Delta x_2{}^2(168\Delta x_1{}^6 - 456\Delta x_1{}^5\Delta x_2 + 9\Delta x_1{}^4\Delta x_2{}^2 + 74\Delta x_1{}^3\Delta x_2{}^3 + \\
& 32\Delta x_1{}^2\Delta x_2{}^4 + 2\Delta x_1\Delta x_2{}^5 - \Delta x_2{}^6)/(\Delta x_1{}^3(\Delta x_1 + \Delta x_2)^8) \\
A_{1}^{(1,0)} =& -120\Delta x_1{}^2(-\Delta x_1{}^6 + 2\Delta x_1{}^5\Delta x_2 + 32\Delta x_1{}^4\Delta x_2{}^2 + 74\Delta x_1{}^3\Delta x_2{}^3 + \\
& 9\Delta x_1{}^2\Delta x_2{}^4 - 456\Delta x_1\Delta x_2{}^5 + 168\Delta x_2{}^6)/(\Delta x_2{}^3(\Delta x_1 + \Delta x_2)^8) \\
A_{-1}^{(0,0)} =& 120\Delta x_2{}^2(420\Delta x_1{}^7 - 960\Delta x_1{}^6\Delta x_2 - 195\Delta x_1{}^5\Delta x_2{}^2 + 83\Delta x_1{}^4\Delta x_2{}^3 + \\
& 106\Delta x_1{}^3\Delta x_2{}^4 + 34\Delta x_1{}^2\Delta x_2{}^5 + \Delta x_1\Delta x_2{}^6 - \Delta x_2{}^7)/(\Delta x_1{}^4(\Delta x_1 + \Delta x_2)^9) \\
A_{0}^{(0,0)} =& 120(\Delta x_1{}^4 - 10\Delta x_1{}^3\Delta x_2 + 20\Delta x_1{}^2\Delta x_2{}^2 - 10\Delta x_1\Delta x_2{}^3 + \Delta x_2{}^4)/(\Delta x_1{}^4\Delta x_2{}^4) \\
A_{1}^{(0,0)} =& 120\Delta x_1{}^2(-\Delta x_1{}^7 + \Delta x_1{}^6\Delta x_2 + 34\Delta x_1{}^5\Delta x_2{}^2 + 106\Delta x_1{}^4\Delta x_2{}^3 + \\
& 83\Delta x_1{}^3\Delta x_2{}^4 - 195\Delta x_1{}^2\Delta x_2{}^5 - 960\Delta x_1\Delta x_2{}^6 + 420\Delta x_2{}^7)/(\Delta x_2{}^4(\Delta x_1 + \Delta x_2)^9) \\
A_{0}^{(3,0)} =& A_0^{(2,0)} = A_0^{(1,0)} = 0, \qquad A_0^{(4,0)} = -1
\end{aligned}
\tag{2.17}
$$

$LHS - RHS$, equals the leading truncation error. A 1D example is shown in Table 2.2 for the sixth order accurate CCD6 schemes. $RHS1$ and $RHS2$ lead to the implicit expressions for the first and second derivative respectively, given in Table 2.1. The number of columns on the LHS matrix is given by the number of non-imposed coefficients in the stencil. Prior to symbolic inversion of the matrix, the rank has been checked successively from the first row of the LHS-matrix. Whenever the next row does not increment the rank this row is discarded, since it is a linear combination of the earlier rank-contributing rows, and so on. Matrix inversion proceeds when full rank has been attained, and the unknown scheme coefficients are thereby computed. The leading truncation error is found as the non-zero residual, $LHS - RHS$, of the least order derivative of the rows below the inverted system. The rank checking is not necessary for most 1D expansions. In Table 2.2 The first 7 rows contribute to the rank and thus form the matrix to be inverted. For $RHS1$ the leading truncation error is encountered in row 8 (7th derivative terms), whereas for $RHS2$ the leading truncation error is encountered in row 9 (8th derivative terms). For multi-dimensional Taylor series expansions rank checking is essential. An example is the sixth order accurate CCV6 scheme. The ordered derivative terms are given in Table 2.3. Full rank is not exceeded until row 22, which is the leading truncation

error row for $RHS1$ (zeroth order edge derivatives). For $RHS2$ (first order edge derivatives) the row-number of the leading truncation error is 29.

For uniform schemes the above outlined procedure for the symbolic derivation of finite difference and finite volume schemes in one and two dimensions is very reliable. The same holds of course for all explicit schemes. For non-uniform implicit (i.e. compact) schemes the increased complexity of the symbolic arithmetic operations during matrix inversion might hamper the derivation of large-stencil finite difference schemes and almost certainly will in case of the intrinsically multi-dimensional implicit finite volume schemes.

Table 2.3: Example of 2D Taylor series expansions for the CCV6 schemes

Deriv.	LHS						RHS1	RHS2
coeffs.	$A_{-1}^{(0,0)}$	$A_{1}^{(0,0)}$	$A_{-1}^{(1,0)}$	$A_{1}^{(1,0)}$	$A_{-1\to 0}^{(0,0)}$	$A_{0\to 1}^{(0,0)}$	$A_{0}^{(0,0)}$	$A_{0}^{(1,0)}$
$f(x_0,y_0)^{(0,0)}$	1	1	0	0	1	1	1	0
$f(x_0,y_0)^{(1,0)}$	$-\Delta x$	Δx	1	1	$-\frac{\Delta x}{2}$	$\frac{\Delta x}{2}$	0	1
$f(x_0,y_0)^{(0,1)}$	0	0	0	0	0	0	0	0
$f(x_0,y_0)^{(2,0)}$	$\frac{\Delta x^2}{2}$	$\frac{\Delta x^2}{2}$	$-\Delta x$	Δx	$\frac{\Delta x^2}{6}$	$\frac{\Delta x^2}{6}$	0	0
$f(x_0,y_0)^{(1,1)}$	0	0	0	0	0	0	0	0
$f(x_0,y_0)^{(0,2)}$	$\frac{\Delta y^2}{24}$	$\frac{\Delta y^2}{24}$	0	0	$\frac{\Delta y^2}{24}$	$\frac{\Delta y^2}{24}$	$\frac{\Delta y^2}{24}$	0
$f(x_0,y_0)^{(3,0)}$	$-\frac{\Delta x^3}{6}$	$\frac{\Delta x^3}{6}$	$\frac{\Delta x^2}{2}$	$\frac{\Delta x^2}{2}$	$-\frac{\Delta x^3}{24}$	$\frac{\Delta x^3}{24}$	0	0
$f(x_0,y_0)^{(2,1)}$	0	0	0	0	0	0	0	0
$f(x_0,y_0)^{(1,2)}$	$-\frac{\Delta x\Delta y^2}{24}$	$\frac{\Delta x\Delta y^2}{24}$	$\frac{\Delta y^2}{24}$	$\frac{\Delta y^2}{24}$	$-\frac{\Delta x\Delta y^2}{48}$	$\frac{\Delta x\Delta y^2}{48}$	0	$\frac{\Delta y^2}{24}$
$f(x_0,y_0)^{(0,3)}$	0	0	0	0	0	0	0	0
$f(x_0,y_0)^{(4,0)}$	$\frac{\Delta x^4}{24}$	$\frac{\Delta x^4}{24}$	$-\frac{\Delta x^3}{6}$	$\frac{\Delta x^3}{6}$	$\frac{\Delta x^4}{120}$	$\frac{\Delta x^4}{120}$	0	0
$f(x_0,y_0)^{(3,1)}$	0	0	0	0	0	0	0	0
$f(x_0,y_0)^{(2,2)}$	$\frac{\Delta x^2\Delta y^2}{48}$	$\frac{\Delta x^2\Delta y^2}{48}$	$-\frac{\Delta x\Delta y^2}{24}$	$\frac{\Delta x\Delta y^2}{24}$	$\frac{\Delta x^2\Delta y^2}{144}$	$\frac{\Delta x^2\Delta y^2}{144}$	0	0
$f(x_0,y_0)^{(1,3)}$	0	0	0	0	0	0	0	0
$f(x_0,y_0)^{(0,4)}$	$\frac{\Delta y^4}{1920}$	$\frac{\Delta y^4}{1920}$	0	0	$\frac{\Delta y^4}{1920}$	$\frac{\Delta y^4}{1920}$	$\frac{\Delta y^4}{1920}$	0
$f(x_0,y_0)^{(5,0)}$	$-\frac{\Delta x^5}{120}$	$\frac{\Delta x^5}{120}$	$\frac{\Delta x^4}{24}$	$\frac{\Delta x^4}{24}$	$-\frac{\Delta x^5}{720}$	$\frac{\Delta x^5}{720}$	0	0
$f(x_0,y_0)^{(4,1)}$	0	0	0	0	0	0	0	0
$f(x_0,y_0)^{(3,2)}$	$-\frac{\Delta x^3\Delta y^2}{144}$	$\frac{\Delta x^3\Delta y^2}{144}$	$\frac{\Delta x^2\Delta y^2}{48}$	$\frac{\Delta x^2\Delta y^2}{48}$	$-\frac{\Delta x^3\Delta y^2}{576}$	$\frac{\Delta x^3\Delta y^2}{576}$	0	0
$f(x_0,y_0)^{(2,3)}$	0	0	0	0	0	0	0	0
$f(x_0,y_0)^{(1,4)}$	$-\frac{\Delta x\Delta y^4}{1920}$	$\frac{\Delta x\Delta y^4}{1920}$	$\frac{\Delta y^4}{1920}$	$\frac{\Delta y^4}{1920}$	$-\frac{\Delta x\Delta y^4}{3840}$	$\frac{\Delta x\Delta y^4}{3840}$	0	$\frac{\Delta y^4}{1920}$
$f(x_0,y_0)^{(0,5)}$	0	0	0	0	0	0	0	0
$f(x_0,y_0)^{(6,0)}$	$\frac{\Delta x^6}{720}$	$\frac{\Delta x^6}{720}$	$-\frac{\Delta x^5}{120}$	$\frac{\Delta x^5}{120}$	$\frac{\Delta x^6}{5040}$	$\frac{\Delta x^6}{5040}$	0	0
$f(x_0,y_0)^{(5,1)}$	0	0	0	0	0	0	0	0
$f(x_0,y_0)^{(4,2)}$	$\frac{\Delta x^4\Delta y^2}{576}$	$\frac{\Delta x^4\Delta y^2}{576}$	$-\frac{\Delta x^3\Delta y^2}{144}$	$\frac{\Delta x^3\Delta y^2}{144}$	$\frac{\Delta x^4\Delta y^2}{2880}$	$\frac{\Delta x^4\Delta y^2}{2880}$	0	0
$f(x_0,y_0)^{(3,3)}$	0	0	0	0	0	0	0	0
$f(x_0,y_0)^{(2,4)}$	$\frac{\Delta x^2\Delta y^4}{3840}$	$\frac{\Delta x^2\Delta y^4}{3840}$	$-\frac{\Delta x\Delta y^4}{1920}$	$\frac{\Delta x\Delta y^4}{1920}$	$\frac{\Delta x^2\Delta y^4}{11520}$	$\frac{\Delta x^2\Delta y^4}{11520}$	0	0
$f(x_0,y_0)^{(1,5)}$	0	0	0	0	0	0	0	0
$f(x_0,y_0)^{(0,6)}$	$\frac{\Delta y^6}{322560}$	$\frac{\Delta y^6}{322560}$	0	0	$\frac{\Delta y^6}{322560}$	$\frac{\Delta y^6}{322560}$	$\frac{\Delta y^6}{322560}$	0
$f(x_0,y_0)^{(7,0)}$	$-\frac{\Delta x^7}{5040}$	$\frac{\Delta x^7}{5040}$	$\frac{\Delta x^6}{720}$	$\frac{\Delta x^6}{720}$	$-\frac{\Delta x^7}{40320}$	$\frac{\Delta x^7}{40320}$	0	0

Chapter 3

Baseflow Solvers

Stability analysis has its roots in perturbation methods. We are faced with a problem, the full Navier-Stokes equations, that cannot be solved readily. Regarded as an initial value problem, there exists an infinity of solutions. Fortunately there is one particular solution, the steady solution which from this point on will be termed baseflow, that might be easier to calculate. A solution to the original problem can be decomposed into the baseflow plus a perturbation. The latter will be linear in a vicinity around the steady baseflow, and consequently can be decomposed into a basis of linearly independent parts, e.g. in Fourier space. This enables a successive solution strategy. Three baseflow solution methods of increasing complexity are presented in this chapter. The remaining chapters will deal with solution methods for the disturbances.

3.1 Selfsimilarity Solutions

For convectively dominated flows ($Re \gg 1$) viscous stresses are important only in thin layers around solid bodies: The boundary layers. An order of magnitude analysis reveals that the displacement thickness δ of the viscous layer relates to a characteristic length of the body L as

$$\frac{\delta}{L} = O\left(Re_L^{-\frac{1}{2}}\right) \tag{3.1}$$

This allows to simplify considerably the governing flow equations, the steady incompressible Navier-Stokes equations, which become the incompressible boundary layer equations. Assuming uniformity in the spanwise direction these are:

$$\begin{aligned} U_x + V_y &= 0 && \text{continuity} \\ UU_x + VU_y - \frac{1}{Re}U_{yy} &= -P_x && \text{x-momentum} \\ P_y &= 0 && \text{y-momentum} \\ UW_x + VW_y - \frac{1}{Re}W_{yy} &= 0 && \text{z-momentum} \end{aligned} \tag{3.2}$$

Note that pressure is constant throughout the boundary layer, thus imposed by the pressure distribution of the outer inviscid flow, obtainable either numerically from potential theory e.g. a panel method, or experimentally from a carefully conducted laminar flow. Given the external

pressure distribution, the inviscid flowfield at the outer edge of the boundary layer is calculated from the Bernoulli equation.

$$\begin{aligned} U_e(x) &= Q_\infty \cos\varphi_\infty \sqrt{1 - c_p(x)} \\ W_e &= Q_\infty \sin\varphi_\infty \end{aligned} \tag{3.3}$$

The boundary equations of (3.2) are known.

$$y = 0: \quad U = V = W = 0 \qquad y = \infty: \quad U = U_e, \quad W = W_e \tag{3.4}$$

Introducing a stream function that inherently satisfies continuity

$$U = \frac{\partial \psi}{\partial y} \qquad V = -\frac{\partial \psi}{\partial x}\,, \tag{3.5}$$

and assuming the existence of a local similarity variable

$$\chi = \sqrt{\frac{U_e(x) Re}{x}}\, y\,, \tag{3.6}$$

we arrive after some manipulation at a partially uncoupled set of nonlinear ordinary differential equations

$$F''' + \frac{1+m}{2} F F'' + m(1 - F'^2) = 0 \tag{3.7}$$

$$G'' + \frac{1+m}{2} F G' = 0\,, \tag{3.8}$$

where

$$F(x,\chi)\sqrt{\frac{xU_e}{Re}} = \Psi(x,\chi) \tag{3.9}$$

$$G(x,\chi) W_e = W(x,\chi) \tag{3.10}$$

$$m = \frac{x}{U_e}\frac{\partial U_e}{\partial x} \tag{3.11}$$

For the chosen similarity variable, χ, the assumption of self-similarity is valid if and only if m is constant. Otherwise F and G will also depend on the streamwise position x. For two-dimensional boundary layers (3.8) will vanish. If $m = 0$ and $W_e = 0$ (3.7) leads to the flat plate Blasius solution. Same case with $m = 1$ leads to a two-dimensional stagnation line flow, and if $W_e \neq 0$ the solution of (3.7-3.8) is the three-dimensional swept Hiemenz stagnation line flow. The set of ODEs (3.7-3.8) are to be solved sequentially due to the partial coupling. One can either apply an implicit line-solver with Newton iteration to cope with the nonlinearities, or use an explicit shooting method with Newton iteration on start values for F and G at the wall. The latter approach was adopted by the author using standard 4'th order Runge-Kutta integration in the wall normal direction of the local similarity variable.

3.2 Parabolic Boundary Layer Solver

In the more common case of non-similarity (3.7-3.8) take on some terms on the right-hand-side, and become a transformed replicate of the set of boundary equations (3.2).

$$F''' + \frac{1+m}{2} F F'' + m(1 - F'^2) = x \left(F' \frac{\partial F'}{\partial x} - F'' \frac{\partial F}{\partial x} \right) \tag{3.12}$$

$$G'' + \frac{1+m}{2} F G' = x \left(F' \frac{\partial G}{\partial x} - G' \frac{\partial F}{\partial x} \right) \tag{3.13}$$

The boundary value problem has now become an initial value problem amenable to parabolic marching in the streamwise direction. The newly added non-similarity terms will in most cases have a rather slow streamwise variation and the x-derivatives can be implemented adequately using a first-order implicit Euler discretization. The modification of the shooting method to account for the upwind history of the boundary layer flow is straightforward. As initial condition for the marching procedure in the vicinity of the leading edge, one must resort to the similarity equations (3.7-3.8), in most cases either the Blasius, Hiemenz or swept hiemenz solution.

3.3 A Sixth-Order-Accurate Combined Compact Finite Volume Multigrid Solver

Relying on two recent developments in the field of higher order numerics, combined (a.k.a. coupled) compact differencing and compact finite volume, a unifying discretization scheme for the solution of the incompressible Navier-Stokes equations is presented and its resolution power quantified and compared. For the solver we use multigrid with a time preconditioned explicit smoother. The stability issue is addressed using Fourier analysis. Usability is extended by allowing anisotropic grids. A small series of testcases serves to illustrate the overall performance of the method.
In the quest for ever more efficient Navier-Stokes solvers there has been for the last decades a continuing interest towards higher order differencing, where by ‘higher’ we mean a formal order of accuracy in terms of Taylor series expansions of more than two. The implications of increasing the order of accuracy, measured in computer memory (storage) and processing time (cpu), are:

- Increased cpu and in many cases storage per Degree of Freedom (DoF).
- Decreased number of DoFs necessary to obtain a given error threshold for a given test case.

If we by ‘efficient’ mean low-resource our criterion for a more efficient Navier-Stokes solver as compared to lower order solvers can be formulated in plain words: Decrease the necessary number of DoFs relatively more than you increase the computer resources (storage,cpu) per DoF. Whether this criterion is fulfilled for a particular higher-order scheme is highly application and error threshold dependent. Higher-order schemes have been particularly useful in areas of fluid dynamics where the flow features to be resolved are of wavy nature such as linear- and non-linear instability, transition and turbulence, which are all characterized by spatial waves.

Most efforts concerning higher-order schemes have been applied in a finite difference framework. The first compact finite volume schemes were recently formulated by Kobayashi (1999), and an implicit Newton-Krylow fourth-order method for incompressible Navier-Stokes equations was then constructed by Pereira et. al. (2001) based on these schemes. Strong conservation was enforced due to strict edge-based flux evaluation.
Multigrid strategies are still the most reliable, if not the only, means of ensuring linear scale-up for fluid problems of increasing size. The achievable O(N) scaling between size (DoFs) and computational work is optimal, and thus desirable, if large fluid problems are to be addressed. Different aspects of robustness concern grid anisotropy and Reynolds number insensitivity. For this purpose we propose a smoother with time preconditioning to eliminate stiffness associated with multiple scale eigenvalues motivated by Vierendeels et al (1999), and defect correction using lower/higher order discretization for prediction/correction respectively.
Briefly outlining, the new sixth-order schemes are analyzed and compared with existing higher-order compact schemes, as they have emerged over the last two decades. Next, the governing equations are presented, proceeded by the details of the multigrid approach. In particular the smoother is given special attention, the robustness of which is to be demonstrated using 2D Fourier analysis, followed by testcases and a summary.

Scheme Analysis

Most known among higher order finite difference schemes are the compact difference schemes as presented by Lele (1992) in his influential paper. Here the virtues of compact differencing are laid out clear: Low truncation and dispersion error of the schemes compared to their non-compact analogous schemes. Low dispersion is equivalent to a high resolution of waves. Except for the different approach taken by Spotz (1995), most compact schemes express the n'th derivative as a combination of 0'th derivatives as in standard finite differencing plus n'th derivatives in neighboring points included by the chosen stencil. Hence the name 'compact', since a smaller stencil is needed than for standard differencing to achieve a certain order of accuracy. The Hermite formula for a 3-point stencil using standard finite difference (FD), compact finite difference (CD) and combined compact finite difference (CCD) respectively for a first derivative are given by

$$u_0^{(1)} = h^{-1}a_0^{(0)}u_0^{(0)} + \sum_{k=-1,2}^{1} h^{-1}a_k^{(0)}u_k^{(0)} \tag{3.14}$$

$$u_0^{(1)} = h^{-1}a_0^{(0)}u_0^{(0)} + \sum_{k=-1,2}^{1} (h^{-1}a_k^{(0)}u_k^{(0)} + a_k^{(1)}u_k^{(1)}) \tag{3.15}$$

$$u_0^{(1)} = h^{-1}a_0^{(0)}u_0^{(0)} + \sum_{k=-1,2}^{1} (h^{-1}a_k^{(0)}u_k^{(0)} + a_k^{(1)}u_k^{(1)} + ha_k^{(2)}u_k^{(2)}) \tag{3.16}$$

h denotes the grid spacing, bracketed superscripts denote derivative order and subscripts the discretization mesh index. a is the coefficient set, u is the dependent variable. The summation operator sums over the indices -1,1 in accordance with the 3-point stencil. We note the conceptual ease of extending CD into CCD. Mahesh (1998) gives an extensive introduction to combined compact finite differencing. The maximum obtainable order of accuracy for first

Table 3.1: Difference scheme coefficients

Scheme	Eq.	Derivative	n_0	$a_{-1}^{(0)}$	$a_{-1}^{(1)}$	$a_{-1}^{(2)}$	$a_0^{(0)}$	$a_1^{(0)}$	$a_1^{(1)}$	$a_1^{(2)}$	$a_{-1\to 0}^{(0)}$	$a_{0\to 1}^{(0)}$
FD1	(3.18)	First	1	-1	0	0	1	0	0	0	-	-
FD2	(3.18)	First	1	$\frac{-1}{2}$	0	0	0	$\frac{1}{2}$	0	0	-	-
	(3.18)	Second	2	1	0	0	-2	1	0	0	-	-
CD4	(3.18)	First	1	$\frac{-3}{4}$	$\frac{-1}{4}$	0	0	$\frac{3}{4}$	$\frac{-1}{4}$	0	-	-
	(3.18)	Second	2	$\frac{6}{5}$	0	$\frac{-1}{10}$	$\frac{-12}{5}$	$\frac{6}{5}$	0	$\frac{-1}{10}$	-	-
CV4	(3.20)	Zeroth	0	$\frac{-1}{4}$	0	0	-	$\frac{-1}{4}$	0	0	$\frac{3}{4}$	$\frac{3}{4}$
	(3.20)	First	1	0	$\frac{-1}{10}$	0	-	0	$\frac{-1}{10}$	0	$\frac{-6}{5}$	$\frac{6}{5}$
CCD6	(3.18)	First	1	$\frac{-15}{16}$	$\frac{-7}{16}$	$\frac{-1}{16}$	0	$\frac{15}{16}$	$\frac{-7}{16}$	$\frac{1}{16}$	-	-
	(3.18)	Second	2	3	$\frac{9}{8}$	$\frac{1}{8}$	-6	3	$\frac{-9}{8}$	$\frac{1}{8}$	-	-
CCV6	(3.20)	Zeroth	0	$\frac{-7}{16}$	$\frac{-1}{16}$	0	-	$\frac{-7}{16}$	$\frac{1}{16}$	0	$\frac{15}{16}$	$\frac{15}{16}$
	(3.20)	First	1	$\frac{9}{8}$	$\frac{1}{8}$	0	-	$\frac{-9}{8}$	$\frac{1}{8}$	0	-3	3
				$a_{-1}^{(0)}$	$a_{-\frac{1}{2}}^{(1)}$	$a_{\frac{1}{2}}^{(1)}$	$a_1^{(0)}$				$a_{-\frac{1}{2}\to\frac{1}{2}}^{(0)}$	
CCV6s	(3.35)	Zeroth	0	$\frac{7}{254}$	$\frac{17}{254}$	$\frac{-17}{254}$	$\frac{7}{254}$				$\frac{120}{127}$	
				$a_{-1}^{(1)}$	$a_{-\frac{1}{2}}^{(0)}$	$a_{\frac{1}{2}}^{(0)}$	$a_1^{(1)}$				$a_{-1\to 0}^{(0)}$	$a_{0\to 1}^{(0)}$
	(3.36)	First	1	$\frac{5}{94}$	$\frac{-144}{47}$	$\frac{144}{47}$	$\frac{5}{94}$				$\frac{102}{47}$	$\frac{-102}{47}$

derivatives using (3.14),(3.15) and (3.16) is 2, 4 and 6. If the 0'th derivatives are available at the time of derivative evaluation, these are found either directly (3.14), solving a tridiagonal system (3.15), or solving a 2x2 block-tridiagonal system (3.16).
In Table 3.1 scheme coefficients for 3-point central schemes of increasing accuracy are given. 'FD', 'CD' and 'CV' stand for 'Finite Difference', 'Compact Difference' and 'Compact Volume'. A preceding 'C' refers to the 'Coupled' discretization method, and the proceeding number indicates the accuracy order of the method. The two sixth order coupled compact volume schemes have, as to the extent of our knowledge, not been treated in literature. The latter CCV6s scheme is a staggered variant of the CCV6 scheme, where the 0'th order derivative fluxes of the dependent variables are evaluated at mid-cell instead of at the cell edges. 3-point Families of CD and CCD schemes respectively can be constructed generically:

$$u_0^{(n)} = \sum_{k=-1,2}^{1} (h^{-n} a_k^{(0)} u_k^{(0)} + a_k^{(n)} u_k^{(n)}) + h^{-n} a_0^{(0)} u_0^{(0)} \tag{3.17}$$

$$u_0^{(n)} = \sum_{k=-1,2}^{1} \sum_{N=0}^{N_{max}} (h^{N-n} a_k^{(N)} u_k^{(N)}) + h^{-n} a_0^{(0)} u_0^{(0)}, \tag{3.18}$$

where $n \geq 0$ is the derivative order to be evaluated in point indexed 0. N_{max} is the largest derivative order. The case $n = 0$ leads to an interpolation scheme.
We now introduce the compact finite volume (CV) and combined compact finite volume (CCV)

Table 3.2: Dispersion- and truncation-error

Scheme	Equation	$PPW(\epsilon = 10^{-2})$	$PPW(\epsilon = 10^{-3})$	$PPW(\epsilon = 10^{-4})$	Truncation error
FD1	Advection	25.6	81.1	256	$\frac{-1}{2}u^{(2)}h$
FD2	Advection	25.6	81.1	256	$\frac{1}{6}u^{(3)}h^2$
	Diffusion	12.8	40.5	128	$\frac{1}{12}u^{(4)}h^2$
CD4/CV4	Advection	5.63	9.77	17.2	$\frac{-1}{120}u^{(5)}h^4$
	Diffusion	4.32	7.58	13.5	$\frac{-1}{200}u^{(6)}h^4$
CCD6/CCV6	Advection	3.50	4.76	6.67	$\frac{1}{5040}u^{(7)}h^6$
	Diffusion	3.13	4.54	6.59	$\frac{1}{20160}u^{(8)}h^6$
CCD6s	Advection	4.88	7.19	10.6	$\frac{31}{20160}u^{(7)}h^6$
	Diffusion	3.13	4.48	6.46	$\frac{1}{20160}u^{(8)}h^6$

schemes generically:

$$\begin{aligned}\left[\bar{u}^{y,(n)}\right]_0 &= \sum_{k=-1,2}^{1}\left(h^{-n}a_k^{(0)}\left[\bar{u}^{y,(0)}\right]_k + a_k^{(n)}\left[\bar{u}^{y,(n)}\right]_k\right)\\ &+ \sum_{k=-\frac{1}{2}}^{\frac{1}{2}} h^{-n}a^{(0)}_{k-\frac{1}{2}\to k+\frac{1}{2}}\left[\bar{u}^{xy,(0)}\right]_{k-\frac{1}{2}\to k+\frac{1}{2}} \qquad (3.19)\\ \left[\bar{u}^{y,(n)}\right]_0 &= \sum_{k=-1,2}^{1}\sum_{N=0}^{N_{max}} h^{N-n}a_k^{(n)}\left[\bar{u}^{y,(n)}\right]_k\\ &+ \sum_{k=-1/2}^{1/2} h^{-n}a^{0}_{k-\frac{1}{2}\to k+\frac{1}{2}}\left[\bar{u}^{xy,(0)}\right]_{k-\frac{1}{2}\to k+\frac{1}{2}}, \qquad (3.20)\end{aligned}$$

where $n \geq 0$ is the derivative order to be evaluated in point indexed 0. The hermite polynomia (3.19), (3.20) for finite volume discretization are functions of compound variables indicated by bars to distinguish from the point variables used for the finite difference equivalents (3.17), (3.18). These compound variables are the averages over either cell faces or cell volumes. In 2D we have

$$\bar{u}^{y,(n)} = \frac{\int_{-\Delta y/2}^{\Delta y/2} u^{(n)}(x, y+\eta)d\eta}{\Delta y} \qquad (3.21)$$

$$\bar{u}^{xy,(n)} = \frac{\int_{-\Delta x/2}^{\Delta x/2}\int_{-\Delta y/2}^{\Delta y/2} u^{(n)}(x+\xi, y+\eta)d\xi d\eta}{\Delta x \Delta y} \qquad (3.22)$$

$n \geq 0$ denotes the derivative order perpendicular to the cell face. Expansion of (3.21), (3.22) into Taylor series and calculation of scheme coefficients, truncation error and formal order of accuracy is a lengthy algebraic exercise even for small three-point CV or CCV schemes. Hence, the use of symbolic arithmetic software becomes helpful, even crucial in the design of upwinded schemes for domain boundaries and correction terms for nonlinearities to be presented.

In Table 3.2 different schemes from Table 3.1 are evaluated for their dispersion- and truncation-error. The resolution power of a scheme can be quantified as the least Points Per Wavelength

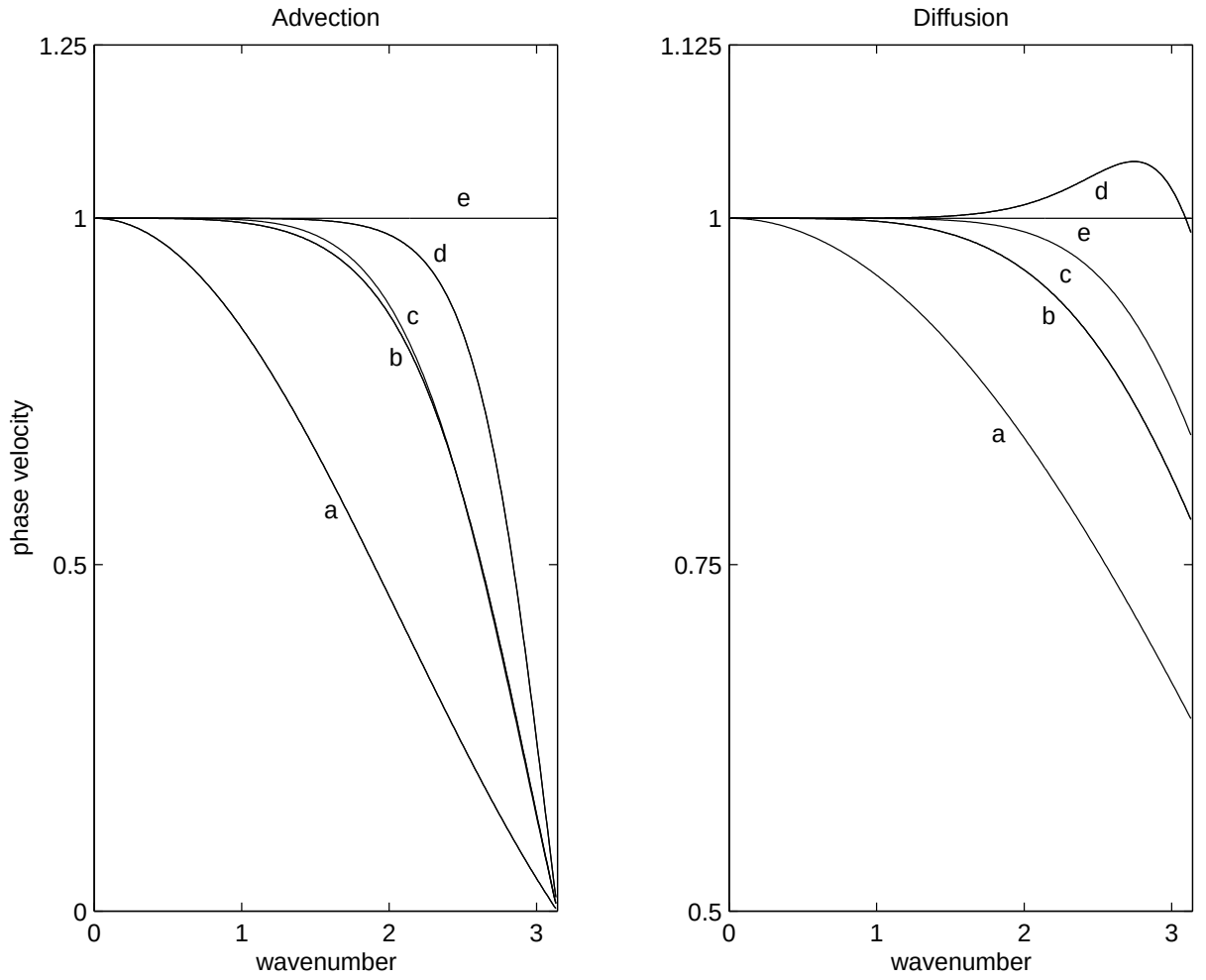

Figure 3.1: Plot of phase speed versus grid wave number for advection/diffusion using different schemes: (a) FD1/FD2 (not FD1 for diffusion), (b) CD4/CV4, (c) CCV6s, (d) CCD6/CCV6, (e) exact.

(PPW) necessary to reduce the relative phase-velocity error, i.e. the dispersion error, below a given threshold, ε , when a pure 1D wave in a periodic domain is introduced into a model equation in fourier space. The chosen model equations are the advection and diffusion scalar equations with unity phase-speed.

$$u_t + u_x = 0 \tag{3.23}$$

$$u_t + u_{xx} = 0 \tag{3.24}$$

The dispersion errors displayed in Fig.3.1 can then be viewed as the phase-speed discrepancy from unity for the discretized model equation. See Lele (1992) for further details. Overall the dispersive error analysis shows that the higher order schemes have superior resolution power, and that the relative benefit of the compact schemes in terms of $PPW(\varepsilon)$ increases significantly as the threshold error, ε, decreases. The advective dispersion error of the CCV6s scheme is somewhat larger than for the CCV6 scheme, but still clearly superior to the CV4 scheme for low error thresholds, see Table 3.2. The mid-cell evaluation of the averaged 0'th derivative flux

is insufficient in a finite volume context if strong conservation is to be enforced. Cell-edge flux evaluations are therefore performed a posteriori as will be shown, which inevitably introduces additional error into the discretization, the formal order of accuracy remaining unchanged. If the CCV6s mid-cell evaluation had been used directly in the dispersion analysis, this scheme would have superseded the non-staggered CCV6 equivalent in resolution power. The benefit of staggering the coupled derivatives will become clear in the stability analysis of the coupled compact volume multigrid smoother.

Discretization of Governing Equations

The steady incompressible Navier-Stokes equations in 2D are

$$div(\mathbf{v}) = 0 \tag{3.25}$$

$$\frac{\partial \mathbf{v}}{\partial t} + div(\mathbf{v} \otimes \mathbf{v} - \nu(grad\,\mathbf{v} + (grad\,\mathbf{v})^T)) + grad\,p = 0, \tag{3.26}$$

where $\mathbf{v}$ denotes the velocity vector field, p the specific pressure and ν the kinematic viscosity assumed to be constant. Integrating over a control volume for an infinitesimal volume applying the Gauss divergence theorem, eqs. (3.25) and (3.26) become

$$\int_{\partial\theta} \mathbf{v} \cdot \mathbf{n} = 0 \tag{3.27}$$

$$\int_{\partial\theta} (\frac{\partial \mathbf{v}}{\partial t} + (\mathbf{v} \cdot \mathbf{n})\mathbf{v} - \nu(grad\,\mathbf{v} + (grad\,\mathbf{v})^T) \cdot \mathbf{n} + p\mathbf{n}) = 0 \tag{3.28}$$

which conserve the physical quantities of mass and momentum inside the boundary $\partial\theta$ of an infinitesimal control volume θ. (3.27), (3.28) can be represented as a system of acoustic, convective and diffusive fluxes. In the steady limit the temporal term will vanish.

$$\mathbf{C}_{acu}(\mathbf{v}, p) + \mathbf{C}_{conv}(\mathbf{v}) + \mathbf{C}_{visc}(\mathbf{v}) = 0 \tag{3.29}$$

Introducing finite sized control volumes, the discretized system listed in the order of equations, continuity, x-momentum, y-momentum takes the form

$$[\mathbf{C}_{acu}(\mathbf{v}, p)]_{i+\frac{1}{2},j+\frac{1}{2}} = \begin{bmatrix} \mathrm{diff}(\bar{u}, x) + \mathrm{diff}(\bar{v}, y) \\ \mathrm{diff}(\bar{p}, x) \\ \mathrm{diff}(\bar{p}, y) \end{bmatrix} \tag{3.30}$$

$$[\mathbf{C}_{conv}(\mathbf{v})]_{i+\frac{1}{2},j+\frac{1}{2}} = \begin{bmatrix} 0 \\ \mathrm{diff}(\overline{uu}, x) + \mathrm{diff}(\overline{vu}, y) \\ \mathrm{diff}(\overline{uv}, x) + \mathrm{diff}(\overline{vv}, y) \end{bmatrix} \tag{3.31}$$

$$[\mathbf{C}_{visc}(\mathbf{v})]_{i+\frac{1}{2},j+\frac{1}{2}} = \begin{bmatrix} 0 \\ \mathrm{diff}(\bar{u}_x, x) + \mathrm{diff}(\bar{u}_y, y) \\ \mathrm{diff}(\bar{v}_x, x) + \mathrm{diff}(\bar{v}_y, y) \end{bmatrix} \tag{3.32}$$

The flux-difference of a quantity, say $\bar{u}$, over a finite volume in either direction is

$$\mathrm{diff}(\bar{u}, x) = \left([\bar{u}^y]_{i+1} - [\bar{u}^y]_i\right) \Delta y \tag{3.33}$$

$$\mathrm{diff}(\bar{u}, y) = \left([\bar{u}^x]_{j+1} - [\bar{u}^x]_j\right) \Delta x \tag{3.34}$$

Edge-averaged scalars, $\bar{p}$, $\bar{u}$ and $\bar{v}$, and their first-order derivatives are calculated using a difference scheme. The zeroth and first derivative line-averages, e.g. $[\bar{u}^x]_j$ and $[\bar{u}^x_x]_j$ are unknowns to be evaluated implicitly. Omitting truncation error the CCV6s schemes from Table 3.1 for zeroth and first derivative edge averages are

$$\begin{aligned}
[\bar{u}^y]_{i+\frac{1}{2}} &= \frac{17}{254}\Delta x\left([\bar{u}^y_x]_i - [\bar{u}^y_x]_{i+1}\right) + \frac{7}{254}\left([\bar{u}^y]_{i-\frac{1}{2}} + [\bar{u}^y]_{i+\frac{3}{2}}\right) \\
&+ \frac{120}{127}[\bar{u}^{xy}]_{i+\frac{1}{2}} \qquad (3.35)\\
[\bar{u}^y_x]_i &= \frac{5}{94}\left([\bar{u}^y_x]_{i-1} + [\bar{u}^y_x]_{i+1}\right) + \frac{144}{47\Delta x}\left(-[\bar{u}^y]_{i-\frac{1}{2}} + [\bar{u}^y]_{i+\frac{1}{2}}\right) \\
&+ \frac{102}{47\Delta x}\left([\bar{u}^{xy}]_{i-\frac{1}{2}} - [\bar{u}^{xy}]_{i+\frac{1}{2}}\right) \qquad (3.36)
\end{aligned}$$

Note that the zeroth derivative line is located at mid-cell, indexed $i+\frac{1}{2}$. The zeroth derivative average on the edge, indexed $i+1$, can a posteriori be computed explicitly as

$$\begin{aligned}
[\bar{u}^y]_i &= \frac{1}{4}\Delta x\left(-[\bar{u}^y_x]_{i-1} + [\bar{u}^y_x]_{i+1}\right) + 8\left([\bar{u}^y]_{i-\frac{1}{2}} + [\bar{u}^y]_{i+\frac{1}{2}}\right) \\
&- \frac{15}{2}\left([\bar{u}^{xy}]_{i-\frac{1}{2}} + [\bar{u}^{xy}]_{i+\frac{1}{2}}\right) \qquad (3.37)
\end{aligned}$$

The CCV6 schemes contain all line averages on the edge:

$$\begin{aligned}
[\bar{u}^y]_i &= \frac{1}{16}\Delta x\left(-[\bar{u}^y_x]_{i-1} + [\bar{u}^y_x]_{i+1}\right) - \frac{7}{16}\left([\bar{u}^y]_{i-1} + [\bar{u}^y]_{i+1}\right) \\
&+ \frac{15}{16}\left([\bar{u}^{xy}]_{i-\frac{1}{2}} + [\bar{u}^{xy}]_{i+\frac{1}{2}}\right) \qquad (3.38)\\
[\bar{u}^y_x]_i &= \frac{1}{8}\left([\bar{u}^y_x]_{i-1} + [\bar{u}^y_x]_{i+1}\right) + \frac{9}{8\Delta x}\left([\bar{u}^y]_{i-1} - [\bar{u}^y]_{i+1}\right) \\
&+ \frac{3}{\Delta x}\left(-[\bar{u}^{xy}]_{i-\frac{1}{2}} + [\bar{u}^{xy}]_{i+\frac{1}{2}}\right) \qquad (3.39)
\end{aligned}$$

At this point the necessary equations for the linear part of the system are given. The convective terms, however, require some care. The edge-averaged products, $\overline{uu}$, $\overline{vu}$, $\overline{uv}$ and $\overline{vv}$, are calculated using the product of edge-averaged scalars, $\bar{u}$ and $\bar{v}$. This results in the second order accuracy known from the vast majority of existing finite volume solvers. Examination of the truncation error for $\overline{uv}$:

$$[\overline{uv}^y]_{i,j+\frac{1}{2}} - [\bar{u}^y]_{i,j+\frac{1}{2}}[\bar{v}^y]_{i,j+\frac{1}{2}} = E(h^2), \qquad (3.40)$$

where

$$\begin{aligned}
E(h^2) &= \frac{1}{12}\Delta y^2 u^{(0,1)}_{i,j+\frac{1}{2}} v^{(0,1)}_{i,j+\frac{1}{2}} \\
&+ \Delta y^4\left(\frac{1}{480}u^{(0,1)}_{i,j+\frac{1}{2}} v^{(0,3)}_{i,j+\frac{1}{2}} + \frac{1}{720}u^{(0,2)}_{i,j+\frac{1}{2}} v^{(0,2)}_{i,j+\frac{1}{2}} + \frac{1}{480}u^{(0,3)}_{i,j+\frac{1}{2}} v^{(0,1)}_{i,j+\frac{1}{2}}\right) \qquad (3.41)
\end{aligned}$$

The punctual derivatives that constitute the second order truncation error up to sixth order are given below. Note that sixth order accuracy is not needed for these terms since they already

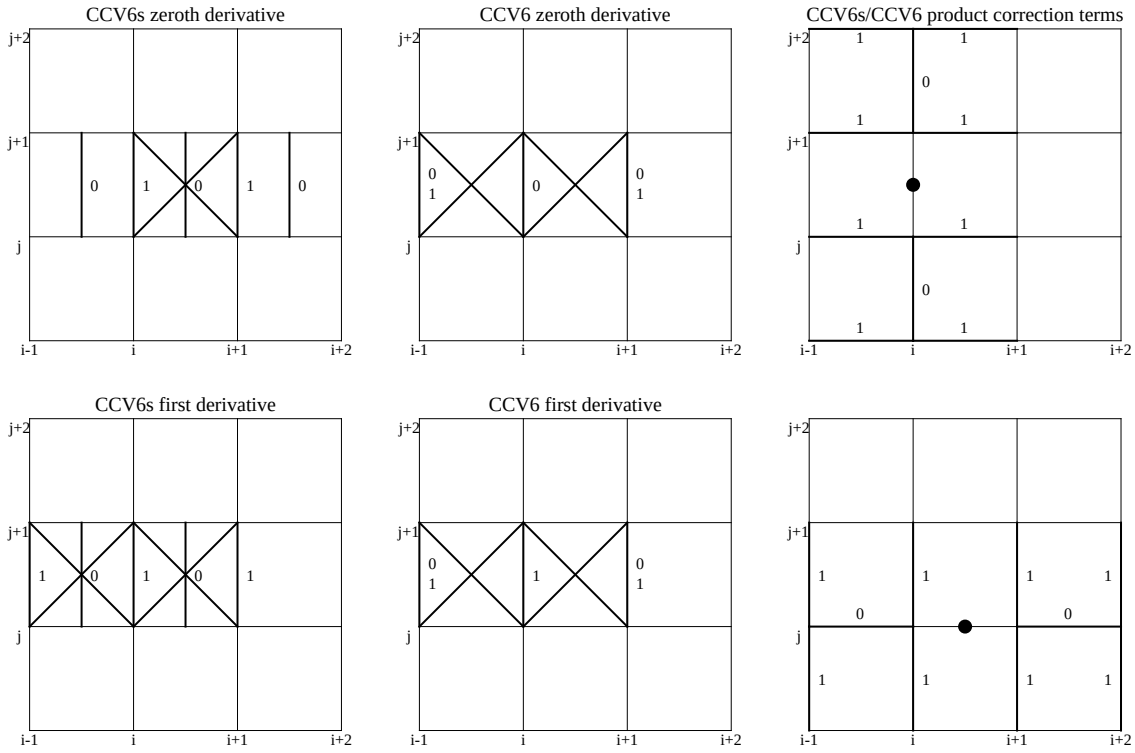

Figure 3.2: compact stencils. Crossed volumes are included in the stencil as well as edges numerated for the derivative, 0 and/or 1.

appear in (3.41) with a multiplicity of Δy^4.

$$
\begin{aligned}
u^{(0,1)}_{i,j+\frac{1}{2}} = \frac{1}{2\Delta y} \quad & \left([\bar{u}^y]_{i,j+\frac{3}{2}} \quad -[\bar{u}^y]_{i,j-\frac{1}{2}}\right) \\
+ \frac{5}{96} \quad & \left(\left[\bar{u}^x_y\right]_{i-\frac{1}{2},j+1} + \left[\bar{u}^x_y\right]_{i+\frac{1}{2},j+1} + \left[\bar{u}^x_y\right]_{i-\frac{1}{2},j} + \left[\bar{u}^x_y\right]_{i+\frac{1}{2},j}\right. \\
& \left. - \left[\bar{u}^x_y\right]_{i-\frac{1}{2},j+2} - \left[\bar{u}^x_y\right]_{i+\frac{1}{2},j+2} - \left[\bar{u}^x_y\right]_{i-\frac{1}{2},j-1} - \left[\bar{u}^x_y\right]_{i+\frac{1}{2},j-1}\right) \qquad (3.42)
\end{aligned}
$$

$$
\begin{aligned}
u^{(0,2)}_{i,j+\frac{1}{2}} = \frac{9}{16\Delta y} \quad & \left(\left[\bar{u}^x_y\right]_{i-\frac{1}{2},j+1} + \left[\bar{u}^x_y\right]_{i+\frac{1}{2},j+1} - \left[\bar{u}^x_y\right]_{i-\frac{1}{2},j} - \left[\bar{u}^x_y\right]_{i+\frac{1}{2},j}\right) \\
+ \frac{1}{48\Delta y} \quad & \left(-\left[\bar{u}^x_y\right]_{i-\frac{1}{2},j+2} + \left[\bar{u}^x_y\right]_{i+\frac{1}{2},j+2} - \left[\bar{u}^x_y\right]_{i-\frac{1}{2},j-1} - \left[\bar{u}^x_y\right]_{i+\frac{1}{2},j-1}\right) \qquad (3.43)
\end{aligned}
$$

$$
\begin{aligned}
u^{(0,3)}_{i,j+\frac{1}{2}} = \frac{1}{4\Delta y^2} \quad & \left(-\left[\bar{u}^x_y\right]_{i-\frac{1}{2},j+1} - \left[\bar{u}^x_y\right]_{i+\frac{1}{2},j+1} - \left[\bar{u}^x_y\right]_{i-\frac{1}{2},j} - \left[\bar{u}^x_y\right]_{i+\frac{1}{2},j}\right. \\
& \left. + \left[\bar{u}^x_y\right]_{i-\frac{1}{2},j+2} + \left[\bar{u}^x_y\right]_{i+\frac{1}{2},j+2} + \left[\bar{u}^x_y\right]_{i-\frac{1}{2},j-1} + \left[\bar{u}^x_y\right]_{i+\frac{1}{2},j-1}\right) \qquad (3.44)
\end{aligned}
$$

figure 3.2 illustrates the combined compact stencils for the above expresions.

Solution Strategy

The overall solution process includes three steps.

Preprocessing

In order to solve (3.29) the initial flowfield and boundary conditions are needed. For non-homogenous boundary conditions care must be taken to specify the edge-averaged value of e.g. a Dirichlet value.

Iterative solver

The governing equations (3.25), (3.26) constitute a spatially elliptic system with parabolicity along the temporal dimension. As demonstrated in a following section, time-preconditioning will alter the nature of the system to become purely hyperbolic, thus amenable to explicit single/multi-stage pseudotime-marching. The effect of multi-staging is to expand the domain of stability to include all eigenvalues of the iterative operator. Note that the order of accuracy in time is of no interest. Only the steady solution matters, since the transient behavior becomes non-physical due to artificial compressibility (time-preconditioning). We use a first-order six-stage scheme.

$$\begin{aligned} \mathbf{Q}_0 &= \mathbf{Q}^n \\ \mathbf{Q}_i &= \mathbf{Q}_0 + \alpha_i cfl \Delta \mathbf{Q}_{i-1} \qquad i = 1:6 \\ \mathbf{Q}^{n+1} &= \mathbf{Q}_6, \end{aligned} \tag{3.45}$$

where $\alpha = [0.15\ 0.28\ 0.39\ 0.63\ 1.04\ 1]^T$. This scheme works on the system

$$\overline{\mathbf{P}} \Delta \mathbf{Q} + \overline{\mathbf{C}} \mathbf{Q} = 0 \tag{3.46}$$

The first matrix defines the iterative strategy, the smoother. This term vanishes upon convergence. The second matrix is the system to be solved, see (3.29). Solution of one stage involves

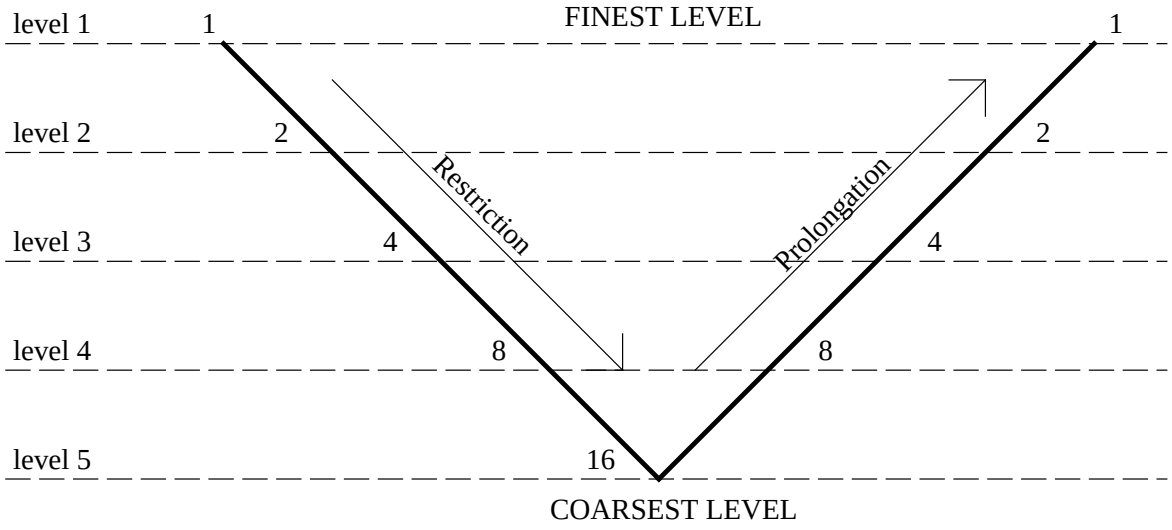

Figure 3.3: One V-cycle for 5 mesh levels. The number of pre- and post-smoothings for each level during restriction/prolongation respectively is indicated.

two steps. First: The iteration matrix, $\overline{\mathbf{P}}$, must be inverted to find the update of the volume-averaged primitive variables. if $N = m \cdot n$ is the number of nodes in the structured mesh, this means N inversions of a 3x3 subsystem (point-implicit). For anisotropic meshes line-implicity across high-aspect-ratio cells perpendicular to the boundary layer leads to n inversions of a 3x3 block-tridiagonal system of length m blocks. Second: Once the volume-averaged updates are available, the edge-averaged variables must be updated. The combined compact volume schemes are solved along each spatial direction. In total m pentadiagonal banded matrices of length $3n$ for edge-averages over vertical edges (y), and vice versa for the horizontal edges (x). Using the CCV6 scheme instead of CCV6s would have led to 2x2 block-tridiagonal systems instead of the banded ones. A full approximation scheme using V-cycles with as many levels as the problem size allows is employed. For better estimating the initial solution full multigrid (FMG) is implemented where the converged coarse grid solution serves to offer a qualified initial solution on the next finer mesh in a repeated fashion until V-cycles are initiated on the finest mesh. Minimum 2x2 finite volumes are needed on the coarse mesh. All prolongation uses simple bilinear interpolation. Half weighting is used for the restriction operator. The number of pre- and post-smoothings increases exponentially with the number of levels in the V-cycles as depicted on Fig.3.3. This rapid increase of smoothings on the coarser meshes lead to a computational cost increase. Making the simplified, but almost correct, assumption that all cpu work originates from the smoothings during the iterative solution process, the cost increase per V-cycle as compared to a single grid computation is unbounded for 1D problems as the number of levels increases, 100% for 2D problems and 33.3% for 3D problems.

Postprocessing

The primitive parameters p, u and v at the nodal points of the mesh must be calculated from the resolved flowfield, given by the edge- or volume-averaged parameters $\overline{p}^y$, $\overline{p}^x$, $\overline{p}^y_x$, $\overline{p}^x_y$ and $\overline{p}^{xy}$ and likewise for u and v. One can adopt the implicit recovery of punctual values used by Pereira et. al. [57] with the coupled derivative extension additionally. However, for sixth order accuracy the following explicit interpolation scheme is a simpler choice.

$$\begin{aligned}
u^{(0,0)}_{i,j} &= \frac{1}{144}([\overline{u}^{xy}]_{i-\frac{3}{2},j-\frac{3}{2}} + [\overline{u}^{xy}]_{i-\frac{3}{2},j+\frac{3}{2}} + [\overline{u}^{xy}]_{i+\frac{3}{2},j-\frac{3}{2}} + [\overline{u}^{xy}]_{i+\frac{3}{2},j+\frac{3}{2}}) \\
&+ \frac{37}{720}([\overline{u}^{xy}]_{i-\frac{3}{2},j-\frac{1}{2}} + [\overline{u}^{xy}]_{i-\frac{3}{2},j+\frac{1}{2}} + [\overline{u}^{xy}]_{i+\frac{3}{2},j-\frac{1}{2}} + [\overline{u}^{xy}]_{i+\frac{3}{2},j+\frac{1}{2}} + \\
&\qquad [\overline{u}^{xy}]_{i-\frac{1}{2},j-\frac{3}{2}} + [\overline{u}^{xy}]_{i+\frac{1}{2},j-\frac{3}{2}} + [\overline{u}^{xy}]_{i-\frac{1}{2},j+\frac{3}{2}} + [\overline{u}^{xy}]_{i+\frac{1}{2},j+\frac{3}{2}}) \\
&+ \frac{101}{720}([\overline{u}^{xy}]_{i-\frac{1}{2},j-\frac{1}{2}} + [\overline{u}^{xy}]_{i-\frac{1}{2},j+\frac{1}{2}} + [\overline{u}^{xy}]_{i+\frac{1}{2},j-\frac{1}{2}} + [\overline{u}^{xy}]_{i+\frac{1}{2},j+\frac{1}{2}}) \\
&+ \frac{1}{10}\Delta x([\overline{u}^{y}]_{i-1,j-\frac{1}{2}} + [\overline{u}^{y}]_{i-1,j+\frac{1}{2}} - [\overline{u}^{y}]_{i+1,j-\frac{1}{2}} - [\overline{u}^{y}]_{i+1,j+\frac{1}{2}}) \\
&+ \frac{1}{10}\Delta y([\overline{u}^{x}]_{i-\frac{1}{2},j-1} + [\overline{u}^{x}]_{i+\frac{1}{2},j-1} - [\overline{u}^{x}]_{i-\frac{1}{2},j+1} - [\overline{u}^{x}]_{i+\frac{1}{2},j+1}) \qquad (3.47)
\end{aligned}$$

Boundary proximity causes the stencil to become non-centered, but the size remains the same.

Multigrid Smoother

The smoother is of the generic type given by (3.46). The iteration matrix, $\overline{\mathbf{P}}$, is in the simple case just a diagonal of temporal coefficients. In the present approach stiffness associated with

infinite acoustic speeds is alleviated by scaling the acoustic speed to match the convective speed. Next we introduce defect correction to further enhance the eigenvalue spectrum of the iterative operator.

Time-preconditioning

Also labelled 'artificial compressibility' this method is of ancient origin, Chorin (1967). Consider the inviscid subsystem of the incompressible Navier-Stokes equations (3.25), (3.26) with a time derivative of pressure added to the otherwise static continuity equation.

$$\begin{pmatrix} p \\ u \\ v \end{pmatrix}_t + \underbrace{\begin{bmatrix} 0 & \beta^2 & 0 \\ 1 & 2u & 0 \\ 0 & v & 0 \end{bmatrix}}_{\overline{\mathbf{A}}} \begin{pmatrix} p \\ u \\ v \end{pmatrix}_x + \underbrace{\begin{bmatrix} 0 & 0 & \beta^2 \\ 0 & v & u \\ 1 & 0 & 2v \end{bmatrix}}_{\overline{\mathbf{B}}} \begin{pmatrix} p \\ u \\ v \end{pmatrix}_y = 0 \tag{3.48}$$

The eigenvalues of the spatial part, $\overline{\mathbf{A}}n_x + \overline{\mathbf{B}}n_y$, are real, and according to theory of characteristics we have a hyperbolic system with propagation speeds (eigenvalues)

$$\lambda = \begin{cases} \mathbf{v}\cdot\mathbf{n} \\ \mathbf{v}\cdot\mathbf{n} + \sqrt{\mathbf{v}^2+\beta^2} \\ \mathbf{v}\cdot\mathbf{n} - \sqrt{\mathbf{v}^2+\beta^2} \end{cases} \tag{3.49}$$

n is the unit vector of arbitrary direction. Increasing β towards infinity makes (3.48) become less and less compressible until the incompressible limit, characterized by infinite acoustic speeds, and thus: Infinite numerical stiffness. The choice of β is therefore based on reducing the stiffness. Setting $\beta = max(|\mathbf{v}|)$ makes the acoustic speeds equal or faster than the convective speeds in any direction, and ensures acoustic propagation in any direction, which must be satisfied for incompressible flows. The local timestep can be defined conveniently as

$$\Delta t = \frac{1}{\frac{u+\sqrt{u^2+\beta^2}}{\Delta x} + \frac{v+\sqrt{v^2+\beta^2}}{\Delta y}} \tag{3.50}$$

$$\Delta t = \frac{1}{\frac{u+\sqrt{u^2+\beta^2}}{\Delta x}}, \tag{3.51}$$

for the point- and line-implicit method respectively. The dependence of Δy on the allowable timestep disappears when this direction is treated implicitly. In the case of a very low cell Reynolds number, either caused by high viscosity or very small edge lengths (including high anisotropy), the viscous terms dominate. Neumann stability analysis on the diffusion equation with explicit time-integration reveals a timestep maximum limit of $\Delta y^2/2\nu$. Taking this into account, the local artificial compressibility parameter, β, for a mesh point becomes, for the point- and line-implicit method

$$\beta = max(|\mathbf{v}|) + \frac{\Delta x^2}{2\nu} + \frac{\Delta y^2}{2\nu} \tag{3.52}$$

$$\beta = max(|\mathbf{v}|) + \frac{\Delta x^2}{2\nu} \tag{3.53}$$

Defect correction

The iteration matrix, see (3.46), from pure time integration of the volume-averaged variables $\bar{p}^{xy}$, $\bar{u}^{xy}$ and $\bar{v}^{xy}$ would be a 3x3 block-diagonal matrix of size 3N, each block being in fact diagonal

$$\overline{\mathbf{P}}_{3x3} = \Delta x \Delta y \begin{bmatrix} \frac{1}{\beta^2 \Delta t} & 0 & 0 \\ 0 & \frac{1}{\Delta t} & 0 \\ 0 & 0 & \frac{1}{\Delta t} \end{bmatrix} \tag{3.54}$$

A less scattered eigenvalue spectrum, significantly in the line-implicit case, allowing a larger cfl-number, results from using an iteration matrix that resembles the higher order system better, such as the lower order equivalent. Using the volume-averaged set of primitive variables we include a part of the time-preconditioned lower order discretized version of (3.46) in the iteration matrix, namely the subsystem that is contained in the volume-averaged variables that we treat implicitly: An array of all single cells for the point method, or vectors of aligned cells for the line method. This subsystem is based on standard second order central differences for acoustic and diffusive terms, and first order upwinding on convective terms. For the point-implicit method the diagonal blocks have more entries

$$\frac{\overline{\mathbf{P}}_{3x3}}{\Delta x \Delta y} = \frac{\overline{\mathbf{P}}_{temp,3x3} + \overline{\mathbf{P}}_{conv,3x3} + \overline{\mathbf{P}}_{visc,3x3}}{\Delta x \Delta y} = \\ \begin{bmatrix} \frac{1}{\beta^2 \Delta t} & 0 & 0 \\ 0 & \frac{1}{\Delta t} & 0 \\ 0 & 0 & \frac{1}{\Delta t} \end{bmatrix} + \begin{bmatrix} 0 & 0 & 0 \\ 0 & \frac{u}{\Delta x} + \frac{v}{\Delta y} & 0 \\ 0 & 0 & \frac{u}{\Delta x} + \frac{v}{\Delta y} \end{bmatrix} + \begin{bmatrix} 0 & 0 & 0 \\ 0 & \frac{2\nu}{\Delta x^2} + \frac{2\nu}{\Delta y^2} & 0 \\ 0 & 0 & \frac{2\nu}{\Delta x^2} + \frac{2\nu}{\Delta y^2} \end{bmatrix} \tag{3.55}$$

The line-implicit method leads to the 3x3 block-tridiagonal iteration matrix. The sub-off-diagonal block is

$$\frac{\overline{\mathbf{P}}_{3x3}}{\Delta x \Delta y} = \frac{\overline{\mathbf{P}}_{temp,3x3} + \overline{\mathbf{P}}_{acu,3x3} + \overline{\mathbf{P}}_{conv,3x3} + \overline{\mathbf{P}}_{visc,3x3,0}}{\Delta x \Delta y} = \\ \begin{bmatrix} \frac{1}{\beta^2 \Delta t} & 0 & 0 \\ 0 & \frac{1}{\Delta t} & 0 \\ 0 & 0 & \frac{1}{\Delta t} \end{bmatrix} + \begin{bmatrix} 0 & 0 & \frac{-1}{2\Delta y} \\ 0 & 0 & 0 \\ \frac{-1}{2\Delta y} & 0 & 0 \end{bmatrix} + \begin{bmatrix} 0 & 0 & 0 \\ 0 & \frac{-v}{\Delta y} & \frac{-u}{2\Delta y} \\ 0 & 0 & \frac{-v}{\Delta y} + \frac{-v}{2\Delta y} \end{bmatrix} + \begin{bmatrix} 0 & 0 & 0 \\ 0 & \frac{-\nu}{\Delta y^2} & 0 \\ 0 & 0 & \frac{-\nu}{\Delta y^2} \end{bmatrix} \tag{3.56}$$

The convective upwinding terms are included in (3.56) for clarity purposes, but could of course have been oppositely upwinded as well, depending on the direction of u, v. The defect correction presented here can be successfully applied for any of the higher order schemes, CV4, CCV6 or CCV6s.

Stability Analysis

In this section the linearized version of the governing equations (3.25,3.26) with constant convective speeds, is decomposed into Fourier modes in 2D. The steady part of the decomposition with zero wavenumbers, $\omega_x, \omega_y = (0, 0)$ in both spatial directions, is the solution, which we

assume constant and periodic in space to facilitate the analysis. Nonzero wavenumbers are associated with disturbances (Fourier modes), which fluctuate in time and space, that must reduce in temporal fluctuation magnitude for each multistage timestep in order to converge. Due to the superposition principle it suffices to consider each disturbance separately:

$$\hat{\mathbf{Q}}'(x,y,t) = \hat{\mathbf{Q}}_{0,0} + \hat{\mathbf{Q}}_{\omega_x,\omega_y}(t)e^{i(\omega_x x+\omega_y y)} \tag{3.57}$$

The hat superscript denotes Fourier space. Insertion of (3.57) into the iterative solver (3.46) leads to a Fourier space equivalent system for a given mode ω_x, ω_y. After subtraction of the steady part, the fluctuating error amplitude can be expressed.

$$\widehat{\overline{\mathbf{P}}}\Delta\hat{\mathbf{Q}} + \widehat{\overline{\mathbf{C}}}\hat{\mathbf{Q}} = 0 \tag{3.58}$$

Applying the multistage timescheme (3.45) to (3.58) the amplitude ratio between the solution at two subsequent timesteps can be quantified from

$$\hat{\mathbf{Q}}^{n+1} = \overline{\mathbf{A}}_{\mathcal{F}}\hat{\mathbf{Q}}^{n}\,, \tag{3.59}$$

where

$$\begin{aligned} \overline{\mathbf{A}}_{\mathcal{F}} &= I - \alpha_6\overline{\mathcal{F}} + \alpha_6\alpha_5\overline{\mathcal{F}}^2 - \alpha_6\alpha_5\alpha_4\overline{\mathcal{F}}^3 + ... \quad , \\ \overline{\mathcal{F}} &= cfl\widehat{\overline{\mathbf{P}}}^{-1}\widehat{\overline{\mathbf{C}}} \end{aligned} \tag{3.60}$$

I being the identity matrix and $\overline{\mathcal{F}}$ the Fourier symbol for the solver. Now, if follows that the iteration scheme is convergent if and only if $|\lambda_i| < 1$ for all eigenvalues of $\overline{\mathbf{A}}_{\mathcal{F}}$. In the complex plane the stability domain is found as a function of proposed eigenvalues of $\overline{\mathcal{F}}$ for which the modulus of all eigenvalues of the resulting scheme matrix, $\overline{\mathbf{A}}_{\mathcal{F}}$, are less than unity. If a posteriori all eigenvalues of $\overline{\mathcal{F}}$ turn out to be inside the domain bounded by the contour of unity eigenvalues for $\overline{\mathbf{A}}_{\mathcal{F}}$, then the solver is stable. This domain is optimized by tuning $\alpha_i\,,\ i = 1:6$, such that the eigenvalues of the Fourier symbol are well contained within the stable domain for as large a cfl-number as possible. The α-vector optimized for the CCV schemes is given in (3.45). The associated region of stability, e.g. on Fig.3.4, is characterized by extending more into the right half-plane than normally seen for explicit time-schemes. The eigenvalues of the CCV solvers for a series of 9 generic cases is presented on Figs.3.4-3.8 These cases are:

1. Inviscid flow aligned to the x-axis, AR=1.
2. Viscous flow aligned to the x-axis, AR=1, Re=1.
3. Viscous stagnation (vanishing convection), AR=1.
4. Inviscid flow aligned to the y-axis, AR=1.
5. Inviscid flow aligned to the y-axis, AR=1000.
6. Inviscid flow aligned to the x-axis, AR=1000.
7. Viscous flow aligned to the x-axis, AR=1000, Re=1.
8. Viscous flow aligned to the y-axis, AR=1000, Re=1.

9. Viscous stagnation (vanishing convection), AR=1000.

where AR is the cell aspect ratio. For cases with uniform meshes the point-implicit solver is used to calculate $\overline{\mathcal{F}}$. For the anisotropic cases with $AR = 1000$ stretched in x-wise direction the line-implicit solver is used. Fig.3.4 shows the CCV6s eigenvalue spectra and error amplification rate for cases 1-3. The mesh is uniform, $AR = 1$, and $cfl = 1$. For the viscous cases the error is well damped. For the inviscid case 1, the lack of upwinding and/or artificial dissipation refrains the eigenvalue spectrum to curve into the left half-plane. It mainly coincides with the imaginary axis, and it is to this end that the multistage time-scheme has been optimized. This is further emphasized in Fig.3.5, same scheme and cfl-number, where the eigenvalue spectrum of case 4 even extends into the right half-plane. The anisotropic mesh used for case 5-6 leads to reasonable error damping when implicitness is applied in the direction of high cell-density. The pseudo-time-step limit for the point-implicit solver would otherwise render a virtually undamped solver. Fig.3.6 for cases 7-9 ends the fourier results for the CCV6s scheme. The beneficial effect of staggering the zeroth and first-order edge-derivatives is quantified in Fig.3.7, where eigenvalue spectra for the non-staggered CCV6 scheme are presented. Note the much lower maximum allowable $cfl = 0,5$ leading to less damping of the error. Fourier analysis for the CV4 scheme are depicted in Fig.3.8. The spectra and allowable cfl-number are quite similar to those of the CCV6s solver.

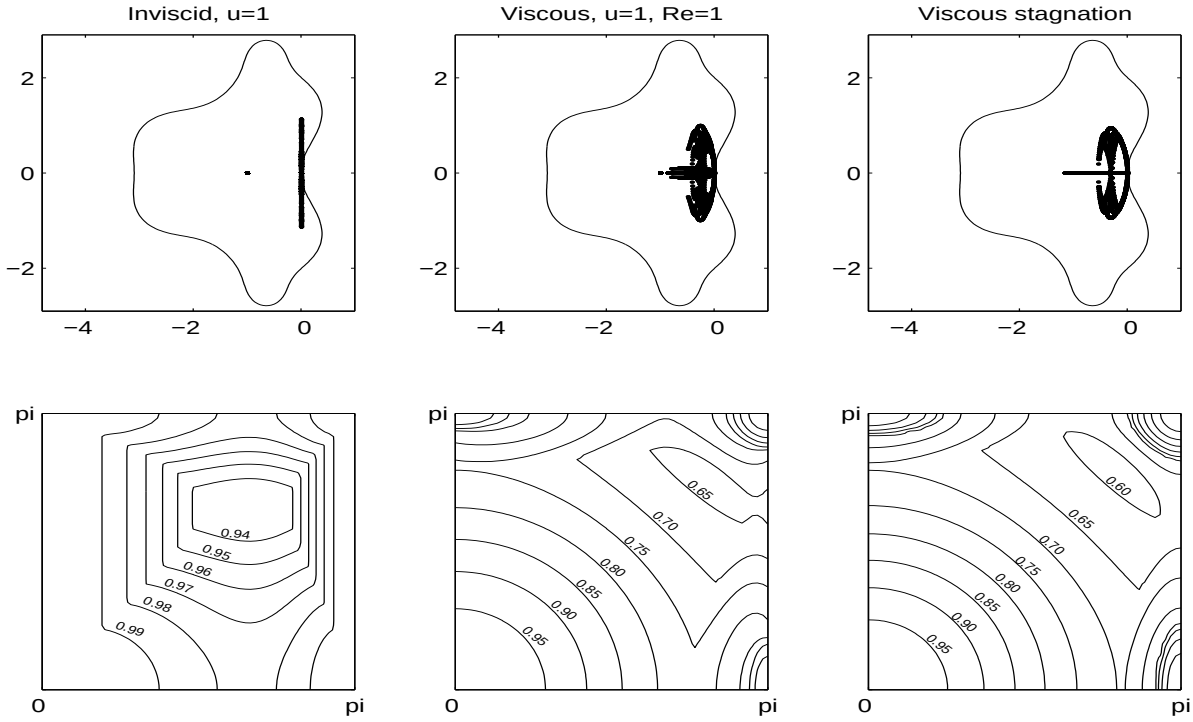

Figure 3.4: Stability results for CCV6s. $cfl = 1.0$. From left to right are the cases 1-3.

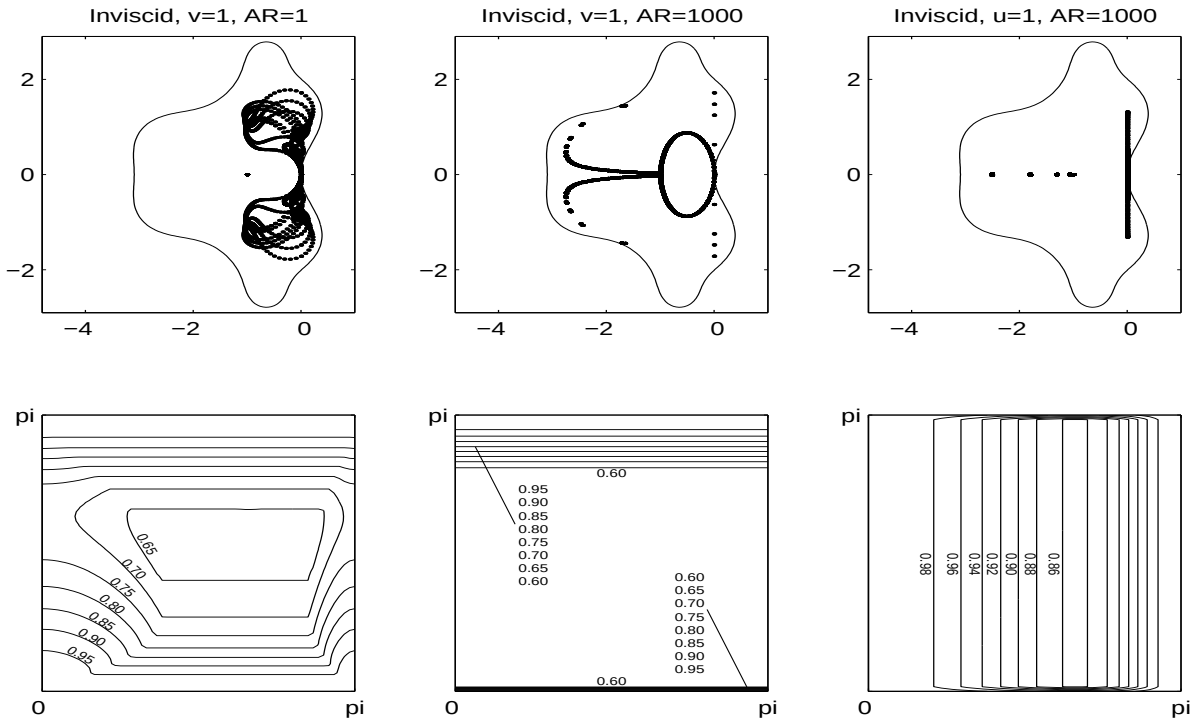

Figure 3.5: Stability results for CCV6s. $cfl = 1.0$. From left to right are the cases 4-6.

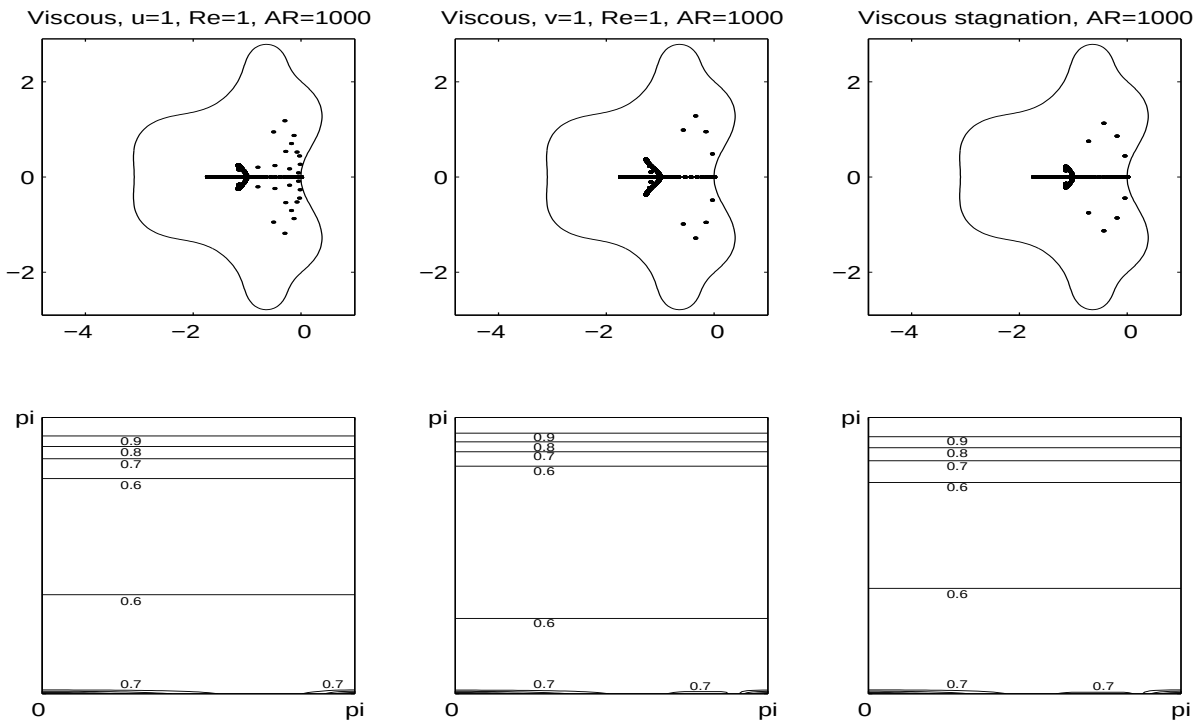

Figure 3.6: Stability results for CCV6s. $cfl = 1.0$. From left to right are the cases 7-9.

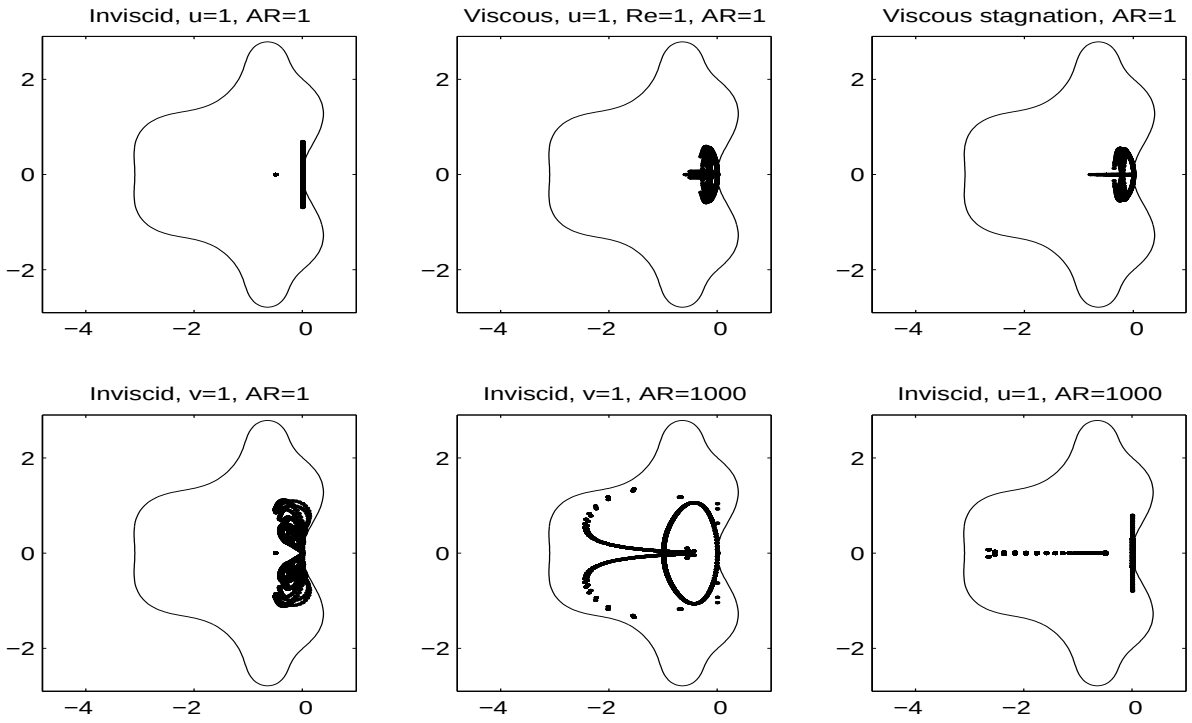

Figure 3.7: Stability results for CCV6. $cfl = 0.5$. From left to right are the cases 1-3 upper row, and 4-6 lower row.

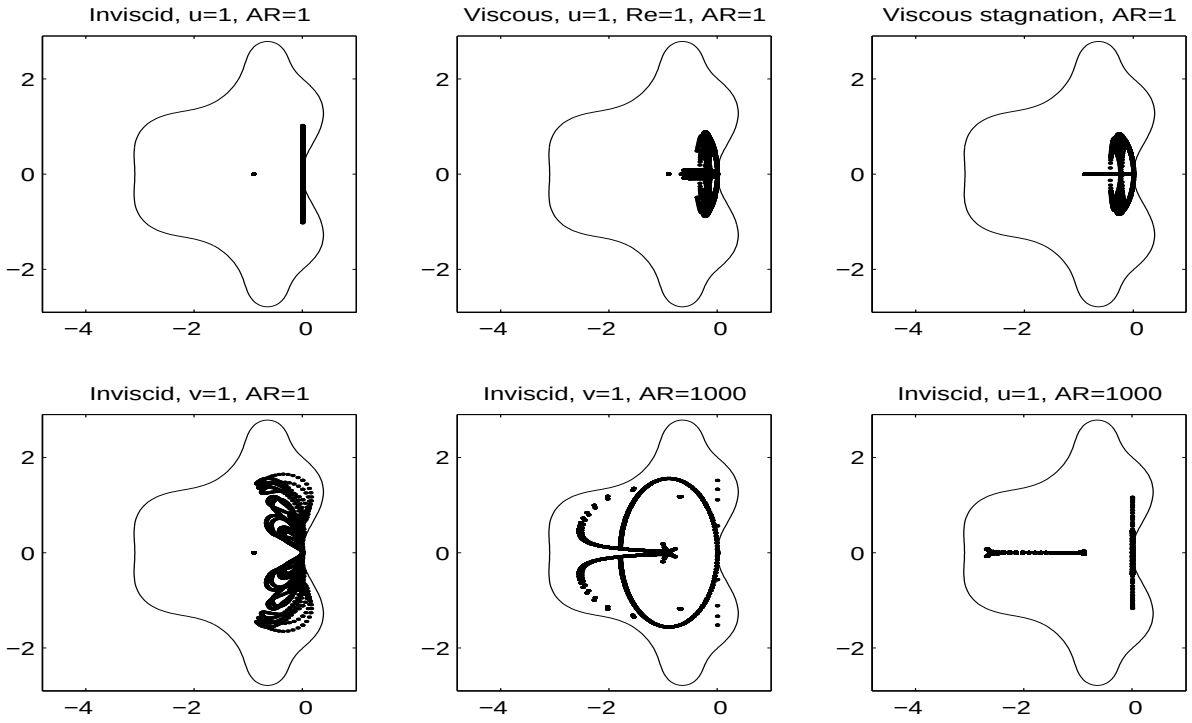

Figure 3.8: Stability results for CV4. $cfl = 0.9$. From left to right are the cases 1-3 upper row, and 4-6 lower row.

Testcases

The accuracy of the CCV6s schemes and the efficiency of the multigrid method is demonstrated through a few testcases.

Analytical Cavity

An analytical variant of the better known driven cavity flow is obtained by imposing a vertical body force on the governing Navier-Stokes equation. This case was originally presented by Shih et al. [66]. In contrast to the driven cavity flow it has a bounded solution for the pressure, and the analytical solution is Reynolds number independent. The body force to go on the RHS of the y-aligned momentum equation is given by

$$\begin{aligned} B(x,y,Re) &= \frac{8}{Re}\left[24\int\left(\zeta_1(x)+2\zeta_1^{'}(x)\zeta_2^{''}(y)+\zeta_1^{'''}(x)\zeta_2(y)\right)\right] \\ &- 64\left[Y_2(x)Y_3(y)+\zeta_2(y)\zeta_2^{'}(y)Y_1(x)\right] \end{aligned}$$

where

$$\begin{aligned} \zeta_1(x) &= x^4-2x^3+x^2 \\ \zeta_2(y) &= y^4-y^2 \\ Y_1(x) &= \zeta_1(x)\zeta_1^{''}(x)-\left[\zeta_1^{'}(x)\right]^2 \\ Y_2(x) &= \int\zeta_1(x)\zeta_1^{'}(x) \\ Y_3(y) &= \zeta_2(y)\zeta_2^{'''}(y)-\zeta_2^{'}(y)\zeta_2^{''}(y) \end{aligned}$$

The domain is the square cavity, $(x,y)\in\Omega\equiv[0,1]^2$. Homogenous Dirichlet boundary conditions are imposed for the velocities, except on the upper boundary where

$$u(x,1)=16\zeta_1(x), \qquad x\in[0,1]$$

Table 3.3: Residual error reduction for converged solutions on different meshes. $Re=1$.

	Grid	8x8	16x16	32x32	64x64
p	Max. residual error	1.52e-3	1.83e-4	5.10e-6	1.43e-6
	Order of accuracy		3.05	5.16	
	Mean residual error	2.26e-4	1.47e-5	3.11e-7	7.87e-7
	Order of accuracy		3.94	5.56	
u	Max. residual error	7.53e-6	5.90e-7	7.74e-9	3.47e-9
	Order of accuracy		3.67	6.25	
	Mean residual error	9.33e-7	7.80e-8	3.30e-9	1.10e-9
	Order of accuracy		3.58	4.56	
v	Max. residual error	5.54e-6	1.95e-7	4.21e-9	3.20e-9
	Order of accuracy		4.83	5.53	
	Mean residual error	1.70e-6	4.56e-8	1.12e-9	1.03e-9
	Order of accuracy		5.22	5.35	

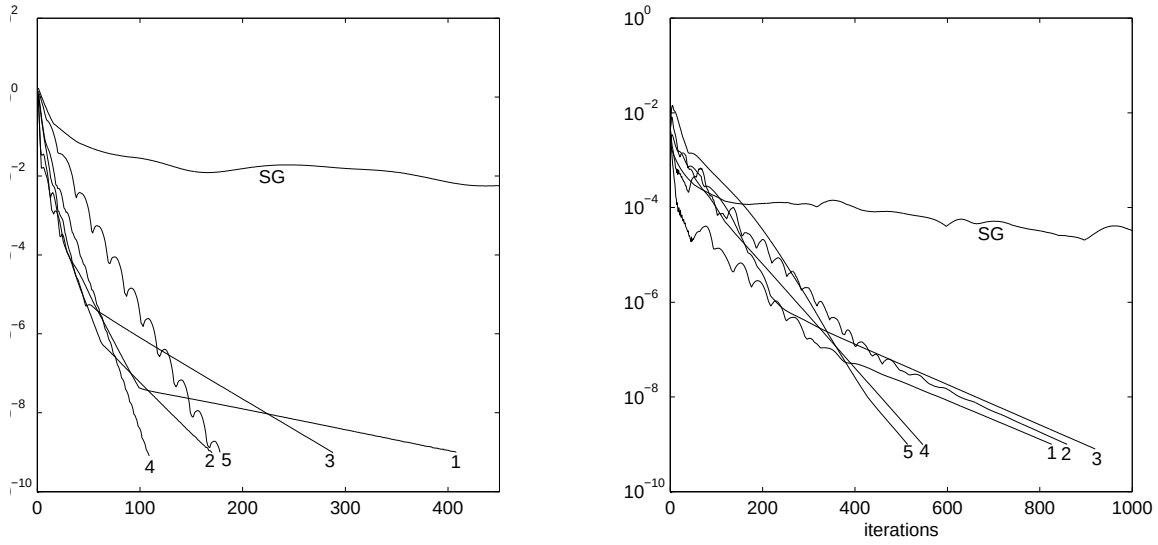

Figure 3.9: Multigrid convergence for analytical cavity testcase. Left: $Re = 1$, right: $Re = 1000$. Mesh level 1: 64x64, mesh level 5: 4x4.

An analytical solution for the problem is known to exist

$$\begin{aligned} u(x,y) &= 8\zeta_1(x)\zeta_2^{'}(y) \\ v(x,y) &= -8\zeta_1^{'}(x)\zeta_2(y) \\ p(x,y,Re) &= \frac{8}{Re}\left[\left(\int \zeta_1(x)\right)\zeta_2^{'''}(y) + \zeta_1^{'}(x)\zeta_2^{'}(y)\right] \\ &+ 64Y_2(x)\left(\zeta_2(y)\zeta_2^{''}(y) - \left[\zeta_2^{'}(y)\right]^2\right) \end{aligned}$$

The testcase has been solved on four uniform meshes as can be seen from table 3. The error between the analytical reference and the converged solution is composed of the discretization error and the machine precision error for 8 byte doubles, $2.22e^{-16}$. How early the accumulated effect of the latter comes into play, when successively refining the mesh, depends on the orthogonality of the linear system. The upwinded CCV6s boundary schemes have limited orthogonality, which is the reason why the machine precision limit halts the error reduction from the 32x32 to the 64x64 mesh. The high order accuracy is confirmed, although sixth order error reduction is not fully achieved. We attribute this to the early onset of the machine precision limit.

Fig.3.9 shows the multigrid acceleration for two Reynolds numbers, $Re = 1$ and $Re = 1000$. The viscous dominated problem for unity Reynolds number exhibits the highest convergence rates, but also a pronounced decline in convergence rate when exceeding four mesh levels. Hardly any penalty for using more levels is encountered in the convectively dominated case for $Re = 1000$. Increasing Re by another three orders of magnitude will lead to a roughly unchanged convergence rate. Numerically stability in the inviscid limit was expected from the fourier analysis, but physical instability will refrain the pseudo-time integration to reach a steady state. It should be noted that all multigrid convergence tests consist of five levels, the three coarsest being computed without the higher order correction, and the two finest levels

with the higher order correction. Using the first-order upwind prediction for the convective terms without correction leads to a computational speed-up, but will not have a positive effect on the convergence rate. Thus, the observed penalty for using five or more meshes for viscous dominated problems is an artefact of the low order predictor method rather than the higher order correction. Both for low and high Re-numbers, the convergence speed-up from a single grid (SG) computation is very significant, and for the high Re computation the number of iterations is nearly independent of the mesh size. Although full multigrid (FMG) is implemented, the coarse mesh solution is not used to find a qualified initial solution on the next finer mesh in the convergence tests shown. This is in order to better show the capability of the V-cycles alone.

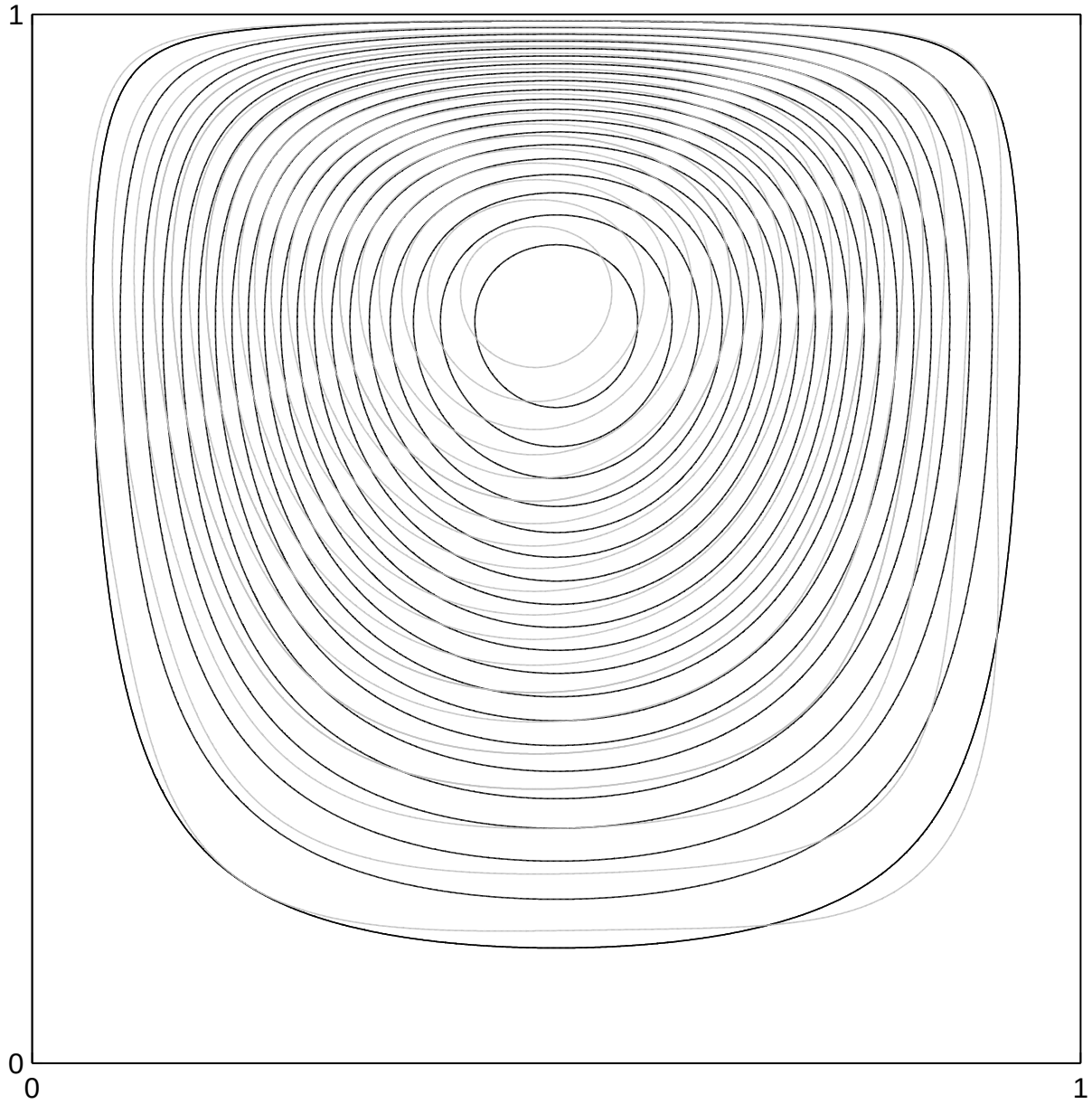

Figure 3.10: Streamlines for analytical cavity testcase.

With the FMG option disabled the convergence problem for each mesh level is independent of that of the preceding level. Inclusion of each convergence history merely shows how the multigrid method scales with increasing size.
Fig.3.10 shows the converged solution on the 64x64 mesh. The superposed grey contour streamlines are from the similar solution without higher order correction. The discrepancy is notable.

Driven Cavity

The classical driven cavity flow is our next testcase. The domain is unchanged from the preceeding testcase. The only non-homogenous Dirichlet boundary condition is for the x-aligned velocity of the upper domain boundary which is unity. The physics is governed by the incompressible 2D Navier-Stokes equations. No analytical solution is known to exist. Particular features of the flow are the counter-rotating recirculation zones at the lower corners and the viscosity-related unboundedness of the pressure in the vicinity of the upper corners where the driving lid interacts with the stationary walls. The multigrid convergence on Fig.3.11 is quite similar to that of the analytical testcase, and seemingly not adversely affected by the singularity points for the pressure at the upper corners. Again, the high Re-number computation shows the most consistent convergence behavior as the mesh is refined and the number of levels in the V-cycle increased. Here, optimal O(N) scaling is obtained for all but the next-finest mesh. The stream-function contour lines of Fig.3.12 shows the flow pattern. After deconvolution of the converged solution on the 64x64 mesh the punctual values of a 256x256 mesh is obtained through coupled compact interpolation, and finally the streamfunction is found from standard integration over the domain. Overall these post-processing steps add complexity to the method from an application viewpoint, but the computational cost is negligible.

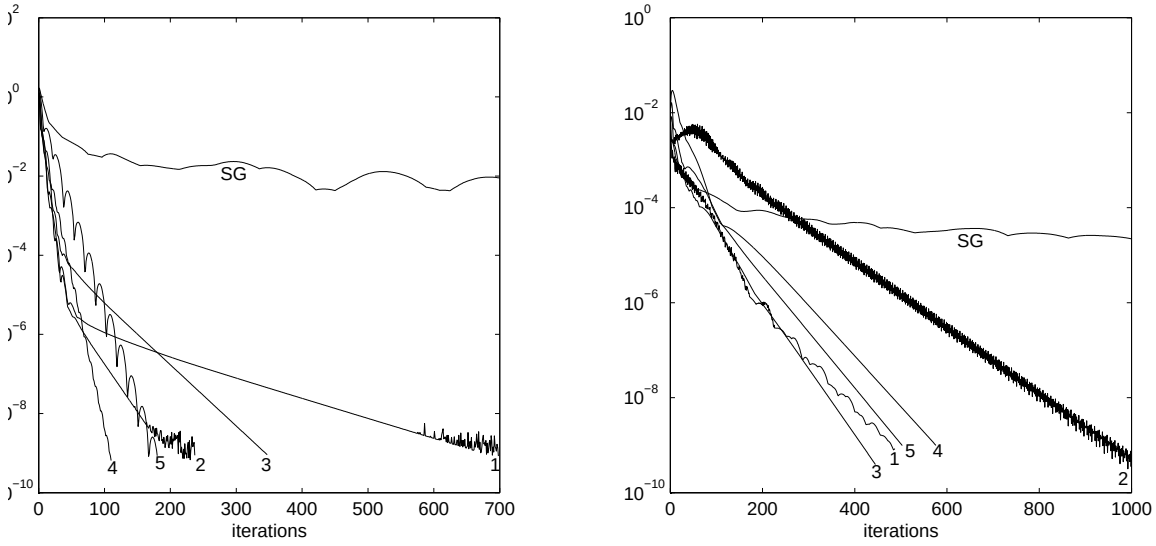

Figure 3.11: Multigrid convergence for driven cavity testcase. Left: $Re = 1$, right: $Re = 1000$. Mesh level 1: 64x64, mesh level 5: 4x4.

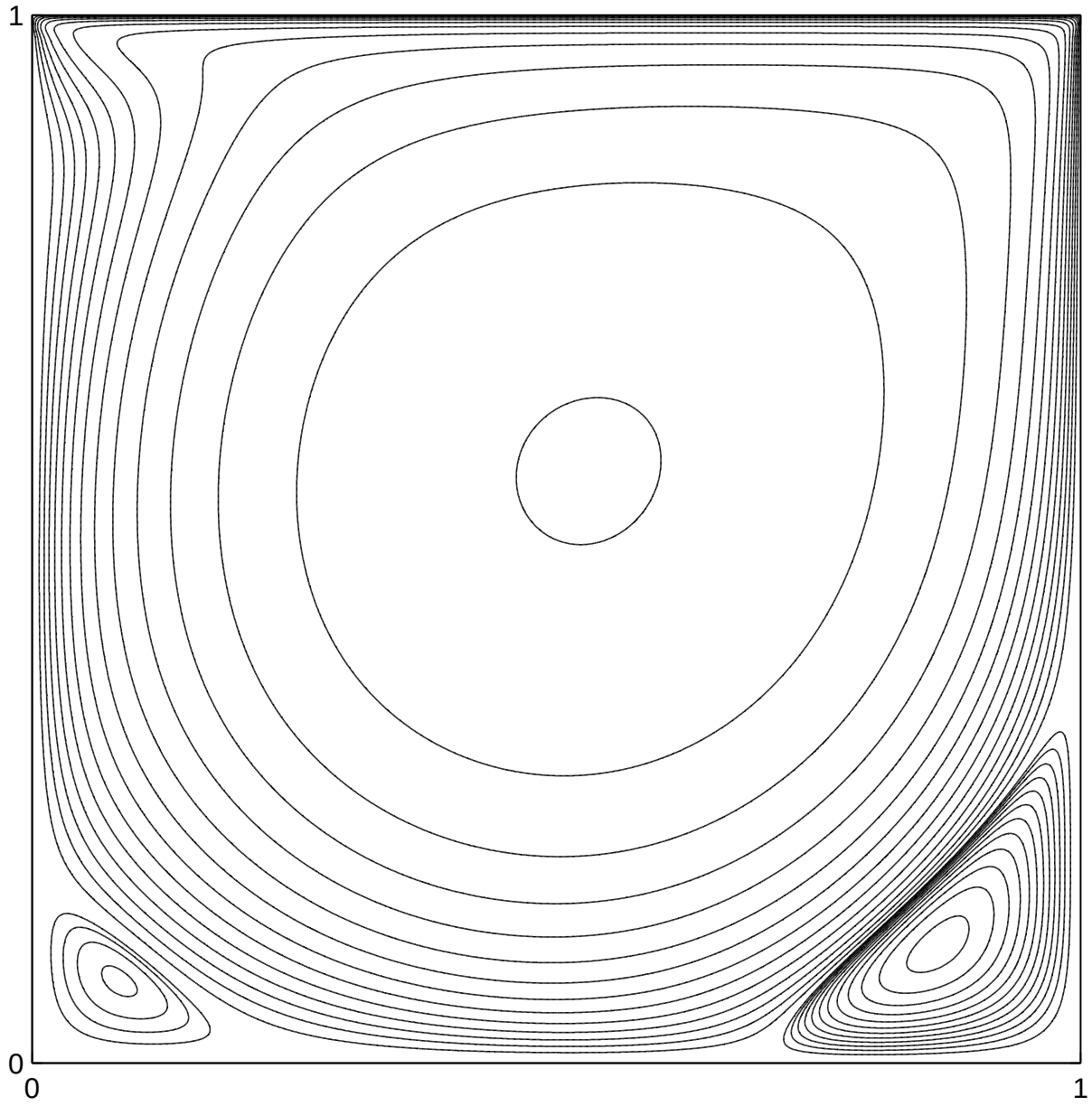

Figure 3.12: Streamlines for driven cavity testcase.

Summary

An edge-based strongly conservative coupled compact volume sixth order accurate scheme with multigrid acceleration has been developed for the incompressible Navier-Stokes equations in 2D. The contribution compared to earlier investigations on compact volume applications consists in the coupled derivative evaluation leading to an even higher order of accuracy, and the artificial compressibility modification of continuity enabling explicit multistage pseudo-time marching. The absence of artificial dissipation and upwinding is made possible by enlarging the stability region of the time marching scheme, which suppresses oscillatory behavior often encountered for central and/or higher order schemes, if the region of stability only marginally

includes the eigenvalues of convective origin clustered around the imaginary axis. Through fourier analysis a defect-correction approach with the staggered coupled compact scheme being contained exclusively in the explicit correction terms is found to yield convergence for all Re-numbers. Scheme accuracy and satisfactory multigrid convergence is assessed through test-cases. Future research for the method will aim at improving the residual error reduction of the smoother leading to faster convergence, and to pinpoint the mechanism that hampers further multigrid acceleration for viscous dominated problems when the number of grid levels in the V-cycle increases.

Chapter 4

Linear Stability Theory (LST)

Assuming that a baseflow solution is available, it remains to solve the perturbed remainder of the governing equations. This chapter brifly introduces the concept of LST, the underlying assumtions and the possibilities for transitional modelling based on LST. We limit our attention to spatial analysis, where instability amplitudes evolve along the streamwise dimension. In temporal analysis disturbance amplitudes are allowed to evolve along the temporal dimension only, thus assuming uniform disturbance amplitudes in both streamwise and spanwise direction. For this reason spatial analysis is by far the most interesting from an engineering point of view.

4.1 Disturbance Equations

The non-dimensionalized incompressible Navier-Stokes equations for mass and momentum in a cartesian reference have the form

$$U_x^{'} + V_y^{'} + W_z^{'} = 0 \tag{4.1}$$

$$\begin{aligned}
U_t^{'} + U_x^{'}U^{'} + U_y^{'}V^{'} + U_z^{'}W^{'} - \frac{1}{Re}(U_{xx}^{'} + U_{yy}^{'} + U_{zz}^{'}) + P_x^{'} = 0 \\
V_t^{'} + V_x^{'}U^{'} + V_y^{'}V^{'} + V_z^{'}W^{'} - \frac{1}{Re}(V_{xx}^{'} + V_{yy}^{'} + V_{zz}^{'}) + P_y^{'} = 0 \\
W_t^{'} + W_x^{'}U^{'} + W_y^{'}V^{'} + W_z^{'}W^{'} - \frac{1}{Re}(W_{xx}^{'} + W_{yy}^{'} + W_{zz}^{'}) + P_z^{'} = 0
\end{aligned} \tag{4.2}$$

As anticipated in the introduction we now decompose the primitive variables into a steady baseflow and a fluctuating part

$$\begin{aligned}
P^{'} &= P + p^{'} \\
U^{'} &= U + u^{'} \\
V^{'} &= V + v^{'} \\
W^{'} &= W + w^{'}
\end{aligned} \tag{4.3}$$

Insertion of decomposed variables (4.3) into the Navier-Stokes equations (4.1-4.2) and subsequent subtraction of the baseflow solution yields a set of perturbation equations

$$u_x^{'} + v_y^{'} + w_z^{'} = 0 \tag{4.4}$$

$$
\begin{aligned}
u_t^{'} + U_x u^{'} + U u_x^{'} + U_y v^{'} + V u_y^{'} + W u_z^{'} - \frac{1}{Re}(u_{xx}^{'} + u_{yy}^{'} + u_{zz}^{'}) + p_x^{'} &= -u^{'} u_x^{'} - v^{'} u_y^{'} - w^{'} u_z^{'} \\
v_t^{'} + V_x u^{'} + U v_x^{'} + V_y v^{'} + V v_y^{'} + W v_z^{'} - \frac{1}{Re}(v_{xx}^{'} + v_{yy}^{'} + v_{zz}^{'}) + p_y^{'} &= -u^{'} v_x^{'} - v^{'} v_y^{'} - w^{'} v_z^{'} \\
w_t^{'} + W_x u^{'} + U w_x^{'} + W_y v^{'} + V w_y^{'} + W w_z^{'} - \frac{1}{Re}(w_{xx}^{'} + w_{yy}^{'} + w_{zz}^{'}) + p_z^{'} &= -u^{'} w_x^{'} - v^{'} w_y^{'} - w^{'} w_z^{'}
\end{aligned}
\tag{4.5}
$$

Baseflow z-derivatives vanish due to spanwise uniformity. For a given baseflow the system (4.4-4.5) is equivalent to the 2.5D Navier-Stokes equations. The LHSs of the fluctuating momentum equations (4.5) are linear with respect to the fluctuating variables. The nonlinearities are the quadratic convective terms collected on the RHSs.

Next step in the analysis concerns the choice of a proper "wave ansatz" to describe the disturbances. The form of the wave ansatz is the main feature to differentiate LST, PSE and ESE. Traditional LST assumes an ansatz based on a fixed amplitude distribution in the wall-normal direction and periodicity along the streamwise, spanwise and temporal dimension.

$$
q^{'}(x,y,z,t) = \sum_{l=-\infty}^{\infty} \sum_{n=-\infty}^{\infty} \sum_{m=-\infty}^{\infty} q_{lmn}(y) e^{i(l\alpha_1 x + n\beta_1 z - m\omega_1 t)}\,, \tag{4.6}
$$

where the amplitude vector $q_{lmn} = [p_{lmn}, u_{lmn}, v_{lmn}, w_{lmn}]^T$ is complex and the triple Fourier sum $q^{'} = [p^{'}, u^{'}, v^{'}, w^{'}]^T$ must be real as the physical perturbation flowfield. This is ensured by the symmetric inclusion of temporal frequencies in the Fourier sum, since the mode for a negative frequency is the complex conjugate of its positive frequency counter-mode. α_1, β_1 and ω_1 are the primary wavenumbers and simply represent a discretization size in Fourier space. Due to spanwise and temporal periodicity this type of decomposition is a natural choice along these dimensions. In streamwise direction the wavenumber, α, is normally solved for such that it will not necessarily coincide with any integer multiple of α_1, $l\alpha_1$. In this case the perturbation $q^{'}$ from (4.6) takes the form

$$
q^{'}(x,y,z,t) = \sum_{l=-\infty}^{\infty} \sum_{n=-\infty}^{\infty} \sum_{m=-\infty}^{\infty} q_{lmn}(y) e^{i(\alpha_l x + n\beta_1 z - m\omega_1 t)}\,, \tag{4.7}
$$

where in general $\alpha_l \neq l\alpha_1$. For a given temporal and spanwise wavenumber, m, n, α_1 corresponds to the fundamental viscous mode and α_2, α_3 etc. correspond to the higher harmonics. For linear analysis this does not pose any problem, since the modes are independent. For non-linear analysis, however, the mode interaction between the discrete wavenumbers will cause nonlinear forcing on integer multiples of these wavenumbers. The non-periodicity of the streamwise direction will cause some degree of α's not coinciding with the Fourier discretization. To remedy this Fourier space interpolation is one work-around, another is simply to allow $\alpha_l \neq l\alpha_1$, and still distribute the nonlinear forcing between the modes as if $\alpha_l = l\alpha_1$, thus abandoning the strict integer multiplicity between the streamwise wavenumbers and hope that the committed error is small. This will generally be the case when there is one dominant unstable mode that initiates the cascading of excited modes, which is the physical scenario normally observed. The issue will be pursued later. To enable solutions of (4.4-4.5) we further assume:

- No streamwise changes of baseflow solution (the parallel baseflow assumption).

- Nonlinearities are small and hence negligible.
- Homogenous boundary conditions for the fluctuating velocities at wall and outer boundary layer edge.

The perturbed momentum equations (4.5) then simplify to

$$\begin{aligned}
u_t^{'} + Uu_x^{'} + U_y^{'}v + Vu_y^{'} + Wu_z^{'} - \frac{1}{Re}(u_{xx}^{'} + u_{yy}^{'} + u_{zz}^{'}) + p_x^{'} = 0 \\
v_t^{'} + Uv_x^{'} + V_y^{'}v + Vv_y^{'} + Wv_z^{'} - \frac{1}{Re}(v_{xx}^{'} + v_{yy}^{'} + v_{zz}^{'}) + p_y^{'} = 0 \\
w_t^{'} + Uw_x^{'} + W_y^{'}v + Vw_y^{'} + Ww_z^{'} - \frac{1}{Re}(w_{xx}^{'} + w_{yy}^{'} + w_{zz}^{'}) + p_z^{'} = 0
\end{aligned} \tag{4.8}$$

The linearity assumption allows us to treat individual Fourier modes independently, since mode interaction only can occur through the neglected nonlinear terms. Insertion of a single Fourier mode from (4.6) in (4.4) and (4.8) leads to the normal-mode equations for mass and momentum. For an arbitrary mode (l, m, n) we have

$$i\alpha u + i\beta w + Dv = 0 \tag{4.9}$$

$$\begin{aligned}
i(\alpha U + \beta W - \omega)u + (DU)v + i\alpha p - \frac{1}{Re}(D^2 - \alpha^2 - \beta^2)u = 0 \\
i(\alpha U + \beta W - \omega)v + Dp - \frac{1}{Re}(D^2 - \alpha^2 - \beta^2)v = 0 \\
i(\alpha U + \beta W - \omega)w + (DW)v + i\beta p - \frac{1}{Re}(D^2 - \alpha^2 - \beta^2)w = 0
\end{aligned} \tag{4.10}$$

where $D = d/dy$ and the homogenous boundary conditions are

$$y = 0: \quad u = v = w = 0 \qquad y = \infty: \quad u = v = w = 0 \tag{4.11}$$

4.2 The Local Eigenvalue Problem

From the LST normal-mode equations some algebraic manipulation leads to the Orr-Sommerfeld equation

$$\left\{ \left(\frac{D^2 - \alpha^2 - \beta^2}{Re} - i\left(\alpha U + \beta W - \omega\right) \right) \left(D^2 - \alpha^2 - \beta^2\right) + i\left(\alpha D^2 U + \beta D^2 W\right) \right\} v = 0 \tag{4.12}$$

with the clamped boundary conditions for v

$$y = 0: \quad v = Dv = 0 \qquad y = \infty: \quad v = Dv = 0 \tag{4.13}$$

to be solved solved locally as an eigenvalue problem for the streamwise wavenumver α since streamwise baseflow changes have been neglected. The real part of the eigenvalue is the spatial frequency of the Fourier wave, whereas the imaginary part is the exponential rate of amplification. Note that due to the the LST wave ansatz, streamwise amplitude changes can

only occur through this mechanism, since the amplitude vector q has no dependency of the chord position x.

Numerically (4.12) can be solved using either a local or a global eigenvalue solver. The local solver will need a suitable initial guess, often found by a global approach for a similar problem, and then Newton-iterate on the eigensolution until convergence. Each iteration scales $O(N)$ and will for a good initial guess converge quadratically requiring only a few iterations. In contrast the global eigen-spectrum is obtained by solving the entire linear system as a general eigenvalue-problem

$$\mathbf{A}\,\mathbf{V} = \mathbf{B}\,\mathbf{V}\,\lambda \tag{4.14}$$

where $\mathbf{V}$ is the matrix of eigensolutions and λ is the diagonal matrix of eigenvalues for ω (temporal analysis) or α (spatial analysis). For temporal analysis $\mathbf{A}$ and $\mathbf{B}$ are

$$\begin{aligned}\mathbf{A} &= \left(\frac{D^2-\alpha^2-\beta^2}{Re} - i\left(\alpha U+\beta W\right)\right)\left(D^2-\alpha^2-\beta^2\right) + i\left(\alpha D^2U+\beta D^2W\right)\\ \mathbf{B} &= -i\left(D^2-\alpha^2-\beta^2\right)\end{aligned} \tag{4.15}$$

For spatial analysis the occurrence in (4.12) of α in powers up to four complicates matters a little. Auxiliary equations are therefore introduced $\alpha_4 = \alpha^3\alpha$, $\alpha_3 = \alpha^2\alpha$ and $\alpha_2 = \alpha\alpha$. With the new unknowns α_4, α_3 and α_2 the expanded system for spatial analysis becomes

$$\mathbf{A} = \begin{bmatrix} \mathbf{A_{11}} & \mathbf{A_{12}} & \mathbf{A_{13}} & \mathbf{A_{14}} \\ \mathbf{I} & & & \\ & \mathbf{I} & & \\ & & \mathbf{I} & \end{bmatrix}, \quad \mathbf{B} = \begin{bmatrix} & & & -i\mathbf{I} \\ \mathbf{I} & & & \\ & \mathbf{I} & & \\ & & \mathbf{I} & \end{bmatrix}, \tag{4.16}$$

where $\mathbf{I}$ is an identity NxN submatrix and

$$\begin{aligned}\mathbf{A_{11}} &= iD^4 - 2i\beta^2D^2 + Re\beta WD^2 - Re\omega D^2 + i\beta^4 - Re\beta^3W - Re\beta W + Re\omega\beta^2\\ \mathbf{A_{12}} &= ReUD^2 - ReU_{yy} + Re\beta^2U\\ \mathbf{A_{13}} &= -2iD^2 + 2i\beta^2 + Re\omega - Re\beta W\\ \mathbf{A_{14}} &= -ReU\end{aligned} \tag{4.17}$$

Due to the one-dimensionality of the OS-equation, opting for the global method is easily affordable in terms of cpu. Using the pseudo-spectral ODE-discretization described earlier, a moderate N of 60-70 will suffice. Solving the eigen-spectrum for (4.15) scales $O(N^3)$ and $O((4N)^3)$ for (4.16), where the multiplicity of α makes it necessary to treat α^2, α^3 and α^4 as auxiliary eigenvalues. It takes a fraction of a second and a few seconds respectively using e.g. Matlab on a 500MHz Pentium III processor. Once the eigensolution of interest has been identified - the fundamental mode, one of the higher harmonics, or simply the least stable mode, which in most cases is the fundamental eigenmode - the remaining amplitude vectors u, w and p are calculated from the normal-mode equations (4.9-4.10).

4.3 Transition Modelling using LST

Despite the total inability of LST, based on the OS-equation (4.12), to cope with all but one of the five stages comprising the non-by-passed route to transition, fact remains that the semi-empirical e^N-method, Smith (1956) and independently Van Ingen (1956), is the most employed

transition prediction method in use today for boundary layer flows. The idea is to integrate the growth of the unstable modes in the streamwise direction by solving the local OS-equation at a number of chord positions sufficient to resolve the gradient in baseflow and eigenvalues. The modelled transition point, x_t where the most amplified Fourier-mode reaches a streamwise accumulated modulus amplification of e^N is then used as criterion for transition onset.

$$N = \max_{\omega} n\left(x_t;\omega\right) \ , \qquad n\left(x;\omega\right) = -\int_{x_0}^{x} \alpha_i\left(x;\omega\right) dx \tag{4.18}$$

The empirically based value of N is dependent on receptivity impacts like roughness, vibration and free-stream turbulence. The less noise, the higher the value of N, typically in the range 7-11. Most successful is the method for transition scenarios where modal linear instability plays a dominant role, e.g. 2D boundary layers. 3D boundary layers, e.g for swept wings, are prone to trigger 3D instability: a) Stationary crossflow vortices, a roughness induced steady disturbance that impede the development of unsteady modes in the nonlinear stage, and makes the e^N-method very case dependent. b) Travelling crossflow vortices which in many cases are more unstable than the most unstable 2D disturbance giving motivation for the introduction of two N values: N_{TS} (or just N) for two-dimensional Tollmien-Schlichting modes and N_{CF} for crossflow modes. Furthermore the path for integration of the N-factor introduces another ambiguity: Is one to integrate along the inviscid streamline, along the chord or in the direction of the group velocity (the velocity at which energy propagates in conservative systems) for the particular Fourier mode. Arnal (1994) provides an extensive review on the LST e^N-method. In case of by-pass transition the use of the method becomes highly questionable.

Chapter 5

Parabolized Stability Equations (PSE)

By allowing for streamwise changes of the baseflow, non-homogenous boundary conditions and enabling an effective methodology for nonlinear mode interaction, the PSE considerably extend the usefulness of stability analysis based on a wave ansatz. This chapter adds to the LST concepts introduced earlier by formulating the PSE and explains the prospects for a less empirical, and thus wider applicable, transition model.

5.1 Disturbance Equations

The perturbed momentum equations that we set out to solve are given by (4.5). Let us restate

$$u_x^{'} + v_y^{'} + w_z^{'} = 0$$

$$\begin{aligned}
u_t^{'} + U_x u^{'} + U u_x^{'} + U_y v^{'} + V u_y^{'} + W u_z^{'} - \frac{1}{Re}(u_{xx}^{'} + u_{yy}^{'} + u_{zz}^{'}) + p_x^{'} &= -u^{'} u_x^{'} - v^{'} u_y^{'} - w^{'} u_z^{'} \\
v_t^{'} + V_x u^{'} + U v_x^{'} + V_y v^{'} + V v_y^{'} + W v_z^{'} - \frac{1}{Re}(v_{xx}^{'} + v_{yy}^{'} + v_{zz}^{'}) + p_y^{'} &= -u^{'} v_x^{'} - v^{'} v_y^{'} - w^{'} v_z^{'} \\
w_t^{'} + W_x u^{'} + U w_x^{'} + W_y v^{'} + V w_y^{'} + W w_z^{'} - \frac{1}{Re}(w_{xx}^{'} + w_{yy}^{'} + w_{zz}^{'}) + p_z^{'} &= -u^{'} w_x^{'} - v^{'} w_y^{'} - w^{'} w_z^{'}
\end{aligned}$$

This is a vast improvement from (4.8) used in the LST analysis, since no terms are neglected. The PSE "wave ansatz" is

$$\begin{aligned}
q^{'}(x,y,z,t) &= \sum_{l=-\infty}^{\infty} \sum_{n=-\infty}^{\infty} \sum_{m=-\infty}^{\infty} q_{lmn}(x,y) e^{i(\theta_{lmn}(x) + n\beta_1 z - m\omega_1 t)} \\
\theta_{lmn}(x) &= \int_{x_0}^{x} \alpha_{lmn}(\xi)\, d\xi
\end{aligned} \tag{5.1}$$

We note that our solution procedure can no longer be local: The streamwise dependency on α and q_{lmn} implies that a nonlocal method must be devised, that can account for the upstream history. We also note an ambiguity: amplitude growth can now be assimilated into the exponential growth through the imaginary part of the streamwise phase θ_{lmn} as in LST, or directly into the amplitude vector q_{lmn}. A closure equation is required. First, however, we obtain the set

of elliptic stability equations for mass and momentum by insertion of a single wave ansatz (5.1) mode into the linear LHS of (4.4-4.5)

$$i\alpha u + Dv + i\beta w + u_x = 0 \tag{5.2}$$

$$\begin{aligned}
&\left(-\frac{1}{Re}\left(D^2-\alpha^2-\beta^2-i\alpha_x\right)+i\left(\alpha U+\beta W-\omega\right)+U_x+VD\right)u \\
&\qquad\qquad +\left(U-\frac{2i\alpha}{Re}\right)u_x+DUv+i\alpha p+p_x \qquad =\frac{1}{Re}u_{xx} \\
&\left(-\frac{1}{Re}\left(D^2-\alpha^2-\beta^2-i\alpha_x\right)+i\left(\alpha U+\beta W-\omega\right)+DV+VD\right)v \\
&\qquad\qquad +\left(U-\frac{2i\alpha}{Re}\right)v_x+V_xu+Dp \qquad =\frac{1}{Re}v_{xx} \\
&\left(-\frac{1}{Re}\left(D^2-\alpha^2-\beta^2-i\alpha_x\right)+i\left(\alpha U+\beta W-\omega\right)+VD\right)w \\
&\qquad\qquad +\left(U-\frac{2i\alpha}{Re}\right)w_x+W_xu+DWv+i\beta p \quad =\frac{1}{Re}w_{xx}
\end{aligned} \tag{5.3}$$

5.2 Linear PSE

The key to obtain a parabolized set of stability equations consists in selecting α such that the elliptic terms of (5.2-5.3) become negligibly small. We identify the primary source of ellipticity to be the RHS of (5.3) and proceed by defining a closure equation for α such that the streamwise change $\partial q/\partial x$ of the amplitude distribution is minimized. Various possibilities exist. A first attempt could be the imposition of α such that the vector sum of q_x at some normal position, $y = y_p$, equals zero. To avoid the dependence on a rather arbitrarily chosen normal position, y_p, we imply no streamwise amplitude change in an averaged sense across the domain by integration: $\int_\Omega q_x dy = 0$. Further improvement can be obtained by multiplying a weight on the integrant that renders satisfactory convergence and minimizes the effect of the PSE approximation. By far the most used weight is the complex conjugate amplitude, $q^\dagger$, proposed by Herbert (1994) leading to

$$\int_\Omega q^\dagger q_x dy = 0 \tag{5.4}$$

Under the constraint (5.4) the streamwise derivatives of the amplitude functions, u_x, v_x, w_x, p_x, will scale with Re in accordance with Prandtl's boundary layer assumptions for the baseflow, i.e. $\frac{\partial}{\partial x} \sim V \sim O(Re^{-1})$. Hence, the RHS of (5.3) scales $O(Re^{-3})$ while the LHS scales $O(Re^{-2})$ or larger, indicating that the PSE assumption is well justified for flows governed by the boundary layer equations or other nearly parallel flows e.g. jets. These scaling assumptions also explain why the low order backward Euler marching scheme performs very well despite the high truncation error, since the streamwise amplitude derivatives scale $O(Re^{-1})$, which is orders of magnitudes less than the dominating $O(1)$ terms. The linear PSE for incompressible flow is then given by the equations (5.2-5.4) where the elliptic terms of viscous origin on the RHSs of (5.3) are minimized upon completion of the constraint (5.4) and neglected. Are the

PSE parabolic? The answer is no. There exists a residual ellipticity mainly of acoustic nature, which will cause numerical instability for very small streamwise steps in the parabolic marching procedure. The critical stepsize is normally small, only a fraction of the streamwise wavelength, and will not be encountered in the computation, but in some occasions it might be necessary to further reduce ellipticity. This can be done in at least two ways:

- Ignore the streamwise change of the pressure amplitude p_x from the x-momentum. This will reduce the minimum stepsize by orders of magnitude, which will be sufficient for all practical purposes. Still, the PSE are not parabolic, and are in theory ill posed.
- Introduce a stabilization term, Andersson et al. (1998), that totally removes the ellipticity and leads to a well posed parabolic set of stability equations.

Both approaches are good with minimal impact on the result. The former is chosen in this work due to its particular ease of implementation.

As implied in (5.1) by the linear independency of modes, the closure equation, and thus α, must be satisfied independently for each Fourier mode contained in the calculation. Each mode is solved by marching an initial solution in the streamwise direction. The initial solution is an LST eigensolution that will adapt to the PSE after a slightly transient response during the first marching steps. The solution strategy for a mode is the following

1. Advance x-position one step.
2. Update the solution for $q(x)$ (5.2-5.3) by solving a linear system.
3. Update $\alpha(x)$ by satisfying (5.4) using e.g. a secant method.
4. Check for convergence on $\alpha(x)$. If not converged go to 2). Otherwise go to 1)

The secant method exhibits nearly quadratic convergence, and will converge after 4-6 iterations. As opposed to the global eigensolver used for LST, the PSE linear solve can benefit greatly from a local discretization method yielding $O(N)$-efficiency due the resulting matrix sparsity. As demonstrated coupled compact differencing has nearly spectral resolution capabilities and can be applied directly to a non-uniform y-discretization. The schemes (2.12-2.13) are used for all PSE computations. The (12x12) block tri-diagonal linear system can be solved fast using a customized block-solver, that takes into account the sparsity of the lower block-diagonal. Partial pivoting on a block level only, must be used to invert the dense diagonal blocks during the forward sweep.
Boundary conditions for u, v and w are of Dirichlet type as for LST but can be non-homogenous and therefore incorporate receptivity mechanisms like vibrations, roughness and free-stream turbulence.

5.3 Nonlinear PSE

The nonlinear terms of (4.5) can be maintained in the PSE method, but they must be decomposed into Fourier modes prior to inclusion as RHS forcing on the array of linear modes contained in the calculation. The mechanism is often self-inductive: The dominant primary Fourier

mode will interact with itself and generate two new mode frequencies given as the sum and the difference of the interacting mode wavenumbers. In the self-inductive case the result will be a new mode with double frequency, and another new mode with no frequency: A mean flow distortion. This qualitatively explains the cascading effect of high-amplitude disturbances, and gives a hint of why highly disturbed flows exhibit fundamental changes. The only mode that affects e.g. drag and lift coefficients is the zero-frequency mean flow distortion mode q_{000}, which is generated by nonlinearity. All other modes average out due to their periodic nature. Fourier decomposition of the nonlinear forcing is applied in the directions of full periodicity, the spanwise and temporal dimension

$$\sum_{n=-2n_{max}-1}^{2n_{max}} \sum_{m=-2m_{max}-1}^{2m_{max}} F_{mn} e^{i(n\beta_1 z - m\omega_1 t)} = \text{FFT}\,(RHS)$$

$$RHS = \begin{bmatrix} 0 \\ -u^{'}u^{'}_{x} - v^{'}u^{'}_{y} - w^{'}u^{'}_{z} \\ -u^{'}v^{'}_{x} - v^{'}v^{'}_{y} - w^{'}v^{'}_{z} \\ -u^{'}w^{'}_{x} - v^{'}w^{'}_{y} - w^{'}w^{'}_{z} \end{bmatrix}, \tag{5.5}$$

where FFT is the Fast Fourier Transformation operator and RHS is the total nonlinear forcing in physical space, whose individual terms are evaluated by summation of modes. To exemplify, the streamwise disturbance velocity, $u^{'}$, and its streamwise gradient, $u^{'}_{x}$, are found at each normal discretization point as

$$u^{'} = \sum_{n=-n_{max}}^{n_{max}} \sum_{m=-m_{max}}^{m_{max}} u_{mn} e^{i(\theta_{mn} x + n\beta_1 z - m\omega_1 t)}$$

$$u^{'}_{x} = \sum_{n=-n_{max}}^{n_{max}} \sum_{m=-m_{max}}^{m_{max}} \left(\frac{\partial u_{mn}}{\partial x} + i\alpha_{mn} u_{mn} \right) e^{i(\theta_{mn} + n\beta_1 z - m\omega_1 t)} \tag{5.6}$$

The expansion along the periodic dimensions must span the largest period

$$t = [\ 0; \frac{2\pi}{\omega_1}\ [\qquad z = [\ 0; \frac{2\pi}{\beta_1}\ [\tag{5.7}$$

To prevent aliasing, the number of points in t and z must be at least twice the number of modes in temporal and spanwise direction respectively, as indicated by (5.5).The FFT coefficients from (5.5) are then distributed to the respective modes as RHS force terms. The nonlinear PSE for a random mode assume the form

$$lin(PSE)_{mn} = F_{mn} e^{-i(\theta_{mn})}, \tag{5.8}$$

for continuity, x-, y-, and z-momentum, where $lin(PSE)_{mn}$ is the LHS linear PSE from (5.2-5.3). Again, all modes are subject to the parabolizing closure equation for the local streamwise wavenumber

$$\int_{\Omega} q^{\dagger}_{mn} \frac{\partial q_{mn}}{\partial x} dy = 0 \tag{5.9}$$

Note that for the nonlinear analysis the subscript l has been excluded from the expansion (5.6). This implies that for a temporal and spanwise wavenumber index m, n we only consider the

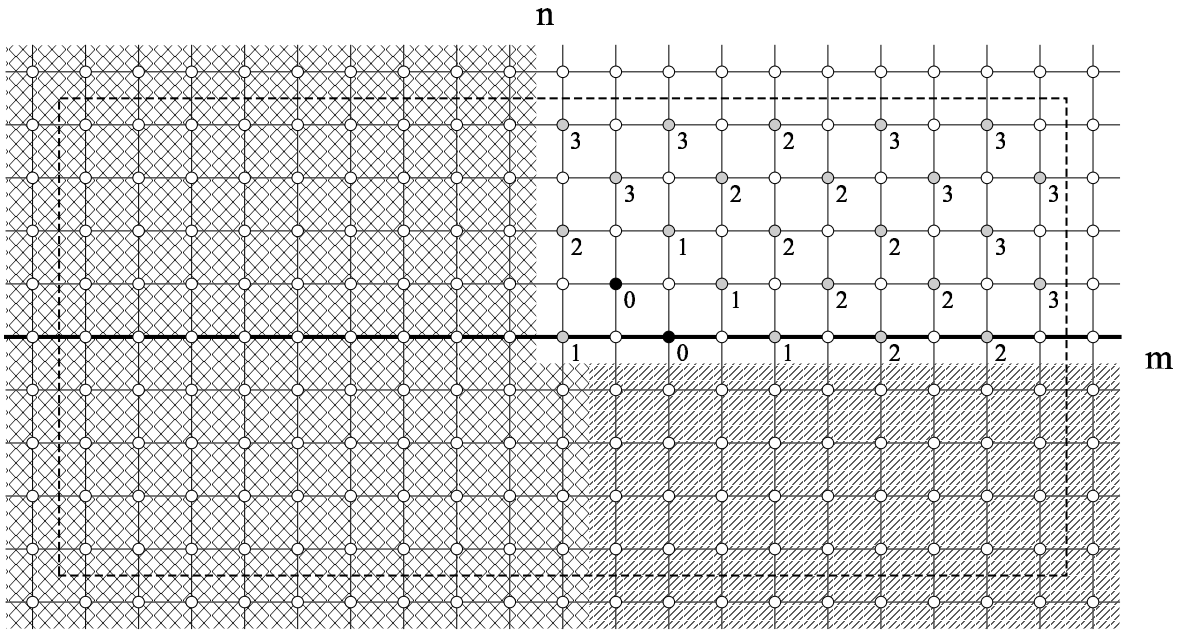

Figure 5.1: Schematic of modes.

dominating fundamental mode α_{mn} with fixed streamwise wavenumber index, l. Otherwise the Fourier decomposition of the nonlinear terms would not be straightforward, since neither the mode amplitudes nor the wavenumbers are uniform in the chordwise direction, but the effect on the physical solution is assumed to be very small. The selection of ω_1, β_1, m and n is largely based on trial and error. LST and linear PSE can provide a good overview of the instability region, and ω_1, β_1 are then chosen accordingly. m and n must be chosen large enough to contain all relevant mode interaction.

Symmetric inclusion of positive and negative temporal modes in the nonlinear PSE computation ensures that the FFT operand is real and physical. Only the temporal modes for non-negative m need to be explicitly calculated in the marching procedure. Symmetry properties can be derived from the PSE equations (5.2-5.3), (5.5) and are summerized below for two- and three-dimesional baseflows.

$$\begin{array}{lll} \text{2D:} & \omega \curvearrowright -\omega & \Rightarrow \quad real(\alpha) \curvearrowright -real(\alpha)\,, \quad \beta \curvearrowright -\beta\,, \quad q \curvearrowright q^{\dagger} \\ & \beta \curvearrowright -\beta & \Rightarrow \quad \omega \curvearrowright -\omega\,, \quad \text{if spanwise symmetric modes only} \\ \text{3D:} & \omega \curvearrowright -\omega & \Rightarrow \quad real(\alpha) \curvearrowright -real(\alpha)\,, \quad \beta \curvearrowright -\beta\,, \quad q \curvearrowright q^{\dagger} \end{array}$$

The modes in the dashed frame of Fig. 5.1 constitute the physical disturbance flowfield. The crosshatched modes are always excluded from the computation, while the linehatched modes can be excluded only if the baseflow and the initial disturbances are physically 2D, thus assuming symmetric inclusion of oblique modes.

The nonlinearities can be calulated either explicitly or implicitly in the solution procedure, the latter being more stable, which allows for larger marching steps. An outline of the strategy for

nonlinear PSE is

1. Advance x-position one step.
2. Outer loop: Calculate the FFT nonlinear forcing coefficients (5.5).
3. For each mode, perform inner loop:
   - **a** Update the solution for $q(x)$ (5.8) by solving a linear system.
   - **b** Update $\alpha(x)$ by satisfying (5.9) using e.g. a secant method.
   - **c** Check for convergence on $\alpha(x)$ from previous linear solve. If not converged go to a).
4. If explicit nonlinearity, proceed to 1). Else if implicit nonlinearity, check for convergence on $\alpha(x)$ from previous FFT: If not converged go to 2), otherwise go to 1)

For implicit nonlinearity, the issue of having a nested iteration for each marching step is not serious. One outer loop will give a clear improvement to the maximum allowable stepsize, so that more than two FFT evaluations per marching step will have limited effect only.

The remaining issue concerning nonlinear PSE is how far it can be marched into the last stages of transition. Successful PSE runs have been extended far into the strongly nonlinear stage with significant Mean-Flow-Distortion (MFD). Extension into turbulence has not been reported and is not very likely to happen either. In turbulence the predominant unidirectional flow of discrete frequencies from the transition stages is superseded by a sudden broadening of the Fourier spectrum, random directions of wave propagation and increased streamwise variation of the amplitude distribution vector q. This affects the validity of the PSE approximation. Furthermore regions of absolute instability are probably inherent turbulent features, certainly not suitable for a parabolized approach.

Some remarks on the Meanflow Distortion and Meanflow Correction

The central role of the MFD mode from a physical point of view has been mentioned. Numerically, the mode is essentially governed by the boundary layer equations. All oscillatory behavior is filtered out due to the fourier decomposition, and the closure equation becomes needless since $\alpha_{00} \equiv 0$. The streamwise pressure amplitude derivative, p_x, accounts for upstream acoustic propagation, which can not be parabolized by multiple scaling, because the MFD mode by nature is non-oscillatory. Hence, p_x must be neglected.
The MFD mode will not vanish far from the wall as the oscillatory modes, but maintain the wall-normal velocity offset from the baseflow value accumulated by non-linear mode interaction inside the boundary layer. This is easiest accomplished by replacing the farfield homogenous Dirichlet condition for v with a homogenous Neumann condition in the special MFD case. Furthermore the MFD is unique in that it has the same zero wavenumber as the baseflow. This enables an alternative treatment of the mode with enhanced coupling between the modes as will be demonstrated. The original approach mostly used in PSE-codes perform the decomposition of linear and nonlinear terms respectively as

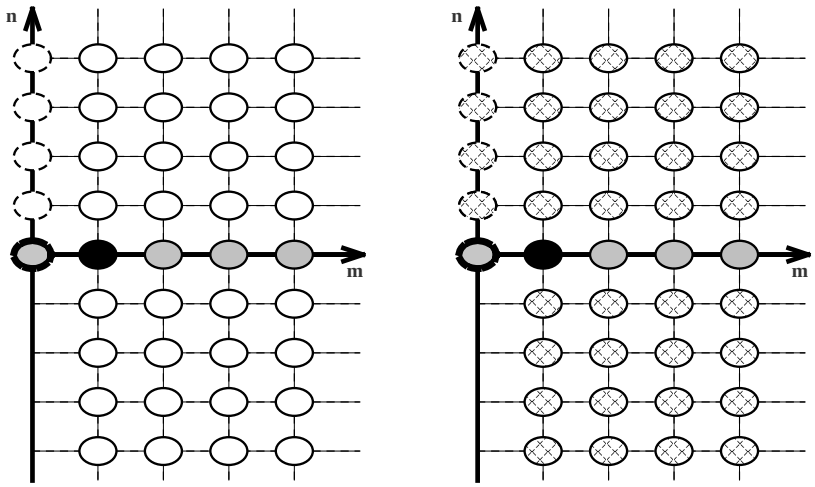

Figure 5.2: Two types of mode-coupling. Left: Without MFC. Right: With MFC. The black mode is an example of a primary mode, which will generate and interact with modes along the Fourier line at $n = 0$ in both cases. The right figure cross-hatching indicates modes only interacting with the Mean Flow Distortion (MFD). The left figure blank modes do not feel the disturbance modes and will hence not initiate a modal interaction.

$$U' = U + \sum_{n=-\infty}^{\infty} u_n e^{-in\omega t} \tag{5.10}$$

$$U'V' = UV + U \sum_{n=-\infty}^{\infty} v_n e^{-in\omega t} + V \sum_{n=-\infty}^{\infty} u_n e^{-in\omega t} + \sum_{n=-\infty}^{\infty} v_n e^{-in\omega t} \sum_{n=-\infty}^{\infty} u_n e^{-in\omega t} \tag{5.11}$$

where $u_n = u_n(x, y, z)$. For simplicity only the temporal fluctuation has been assimilated into the exponential fast-varying scale. Attempting to unify the baseflow component with the MFD mode in the decomposition we arrive at

$$U' = (U + u_0) + \sum_{n=-\infty}^{\infty, n\neq 0} u_n e^{-in\omega t} \tag{5.12}$$

$$\begin{aligned} U'V' = {} & UV - u_0 v_0 \\ & + (U + u_0) \sum_{n=-\infty}^{\infty} u_n e^{-in\omega t} \\ & + (V + v_0) \sum_{n=-\infty}^{\infty} v_n e^{-in\omega t} \\ & + \sum_{n=-\infty}^{\infty, n\neq 0} u_n e^{-in\omega t} \sum_{n=-\infty}^{\infty, n\neq 0} v_n e^{-in\omega t} \end{aligned} \tag{5.13}$$

This decomposition is the one implemented in our PSE-code. We note the difference: The MFD component forms part of the steady coefficients, formerly the baseflow coefficients alone, now

with the MFD mode added on. Day et al. (1999) use the term 'Mean Flow Correction', MFC. In (5.11) all modes contributed to the nonlinear terms to be evaluated in physical space, FFT'ed and distributed to the corresponding RHSs. In (5.13) the MFD part has been extracted from the nonlinear summation. The advantage of (5.12), (5.13), over (5.10), (5.11) is the stronger coupling of the steady mode with the oscillatory ones. This is clearly felt as a changed receptivity for modes not directly affected by the nonlinear interaction of the oscillatory mode. Thus, any mode nonlinearity will instantly be felt in the entire fourier space included in the computation. The improved coupling is illustrated in Fig.5.2.
A variation of (5.12), (5.13) is

$$U' = U_0 + \sum_{n=-\infty}^{\infty, n\neq 0} u_n e^{-in\omega t}, \qquad U_0 = U + u_0 \tag{5.14}$$

$$\begin{aligned} U'V' = {} & U_0 V_0 \\ & + U_0 \sum_{n=-\infty}^{\infty, n\neq 0} u_n e^{-in\omega t} \\ & + V_0 \sum_{n=-\infty}^{\infty, n\neq 0} v_n e^{-in\omega t} \\ & + \sum_{n=-\infty}^{\infty, n\neq 0} u_n e^{-in\omega t} \sum_{n=-\infty}^{\infty, n\neq 0} v_n e^{-in\omega t}, \end{aligned} \tag{5.15}$$

for linear and nonlinear decomposition respectively. The sole difference from (5.12), (5.13) lies in the treatment of the 0'th mode as the sum of baseflow and MFD. This leads to a solution procedure for the Navier-Stokes equations, not just the perturbation equations. (5.14), (5.15) is beneficial when a steady baseflow solution is not easily obtainable. For general flows around airfoils this is often the case, since time marching methods at some Re will mimic the unstable nature of the flow of interest, and flow solvers that do not employ time marching (e.g. Newton solvers or parabolic boundary layer solvers) are only applicable either to very small problems or to flows with attached boundary layers with no or very limited recirculation. Usage of this decomposition method is not employed in the present work, but seems to be the only alternative when/if PSE or related methods are to be used for general engineering applications.

5.4 Transition Modelling using PSE

The e^N-method can be based on linear PSE as well as LST. The PSE-based version will due to its nature incorporate non-parallel and eventually receptivity effects, both of which were absent using LST. Whether this improvement is substantial or rather insignificant in comparison with the neglected nonlinearity and the empiricism of the determination of the N factor will be investigated.

The potential of nonlinear PSE can be used to simulate directly some of the last flow mechanisms prior to the final breakdown into turbulence. This would eliminate the empirical input and promise a new era of transition prediction. Some of these very-close-to-turbulence indicators are:

- Increased average wall shear.
  This turbulence indicator has ample experimental evidence, and is a consequence of the nonlinear MFD mode. Chang & Malik (1994) used compressible PSE with this transition point indicator for a supersonic flat-plate boundary layer. Stolte et al. (1995) used compressible PSE on the subsonic real case boundary layer data from the VFW 614/ATTAS flight test, and could successfully predict transition based on increased wall shear. This in turn would emphasize the not fulfilled need for reliable receptivity data and computation of nonmodal transient growth.

- High frequency secondary instability.
  Although this mechanism has not been used as a stand-alone indicator of break-down to turbulence, experimental evidence suggests that these higher order modes, possibly in conjunction with other mechanisms, lead to transition shortly downstream of their appearance. For low-amplitude receptivity this has been confirmed for the channel Poiseulle flow by Nishioka et al. (1975) and for the Blasius flow by Corke & Mangano (1989). The suggestion that secondary instability leads to final breakdown once the mean flow profile becomes inflectional, seems to be case dependent and does not motivate general conclusions

- Detection of absolute instability regions.
  Due to the ellipticity of such regions, PSE is arguably not a very strong tool for this. Nevertheless nonlinear PSE solutions may reveal boundary layer regions where computed instantaneous velocity profiles have negative streamwise velocity-components, either away from the wall, or in its vicinity leading to negative wall shear, indicating an unsteady flow separation, Chang & Malik (1994).

An all-encompassing nonlinear PSE based transition model does not exist, but further development is likely to offset from the above outlined mechanisms.

Chapter 6

Elliptic Stability Equations (ESE)

If we abandon the streamwise parabolic assumption of the baseflow and its perturbation, upstream propagation of both becomes admissible. The PSE wave ansatz will be extended rather than modified, such that PSE forms a subset of ESE in the same way as LST forms a subset of PSE. The equations to solve are the perturbed Navier-Stokes equations (4.4-4.5) where the nonlinear terms are neglected for the linear analysis. The ESE solution strategy will still be a marching procedure, but along another dimension. Two alternatives exist, which will both be presented.

6.1 Temporal ESE

"Temporal" refers to the marching direction. The temporal wavenumber of each mode is fixed as for PSE, whereas a temporal amplitude derivative is introduced to direct the evolution in time. The temporal ESE wave ansatz used to decompose the physical disturbance is

$$
\begin{aligned}
q^{'}(x,y,z,t) &= \sum_{l=-\infty}^{\infty} \sum_{n=-\infty}^{\infty} \sum_{m=-\infty}^{\infty} q_{lmn}(x,y,t) e^{i(\theta_{lmn}(x,t)+n\beta_1 z - m\omega_1 t)} \\
\theta_{lmn}(x,t) &= \int_{x_0}^{x} \alpha_{lmn}(\xi)\, d\xi
\end{aligned}
\tag{6.1}
$$

, applicable for 2D and 2.5D flows. The extension from the PSE wave ansatz (5.1) consists of the temporal dependence of the ESE amplitude function $q(x,y,t)$ and the phase θ. For the linear analysis the modes decouple. Insertion of a single mode of (6.1) into (4.4-4.5) leads to the temporal ESE

$$
i\alpha u + Dv + i\beta w + u_x = 0 \tag{6.2}
$$

$$
\begin{aligned}
&\left(-\frac{1}{Re}\left(D^2-\alpha^2-\beta^2-i\alpha_x\right)+i\left(\alpha U+\beta W+\alpha_t-\omega\right)+U_x+VD\right)u \\
&\qquad+\left(U-\frac{2i\alpha}{Re}\right)u_x+DUv+i\alpha p+p_x+u_t-\frac{1}{Re}u_{xx} &&=0 \\
&\left(-\frac{1}{Re}\left(D^2-\alpha^2-\beta^2-i\alpha_x\right)+i\left(\alpha U+\beta W+\alpha_t-\omega\right)+DV+VD\right)v \\
&\qquad+\left(U-\frac{2i\alpha}{Re}\right)v_x+V_xu+Dp+v_t-\frac{1}{Re}v_{xx} &&=0 \\
&\left(-\frac{1}{Re}\left(D^2-\alpha^2-\beta^2-i\alpha_x\right)+i\left(\alpha U+\beta W+\alpha_t-\omega\right)+VD\right)w \\
&\qquad+\left(U-\frac{2i\alpha}{Re}\right)w_x+W_xu+DWv+i\beta p+w_t-\frac{1}{Re}w_{xx} &&=0 \qquad (6.3)
\end{aligned}
$$

The same closure equation for the streamwise wavenumber, α, is used for ESE as for PSE (5.4). However, in the case of ESE, the purpose is not to parabolize along the x-direction by neglecting the second derivatives of the amplitude functions. In ESE all terms are included, and the purpose off minimizing the streamwise variation of the amplitudes is only to enable a low-order difference method on a coarse x-discretization. This has proven adequate and effective for PSE and the same holds for ESE. The solution strategy is

- Part 1: Initial solution for the (x, y)-domain at $t = t_0$. Use the PSE algorithm. If the baseflow is partly upstream propagating by the presence of a reversed flow region, the PSE method might become ill posed. In this case replace the baseflow with another non-reversed baseflow. It can then be gradually converted back to its original during the first temporal ESE marching steps in Part 2. This correction procedure will not affect the converged solution.

- Part 2: Temporal marching.

  1. Advance one timestep.
  2. March the new solution downstream using the PSE algorithm for the ESE equations (5.4,6.2-6.3) at each x-position. For each (x, t)-position indexed (i, j) in space and time respectively, the solution is updated using $\alpha_{i-1,j}$, $\mathbf{v_{i-1,j-1}}$, $\mathbf{v_{i,j-1}}$ and $\mathbf{v_{i+1,j-1}}$.
  3. if convergence problem steady amplitude analysis, check for temporal convergence on $\alpha(x, t)$ and $\mathbf{v}$ against a given threshold. If not converged go to 1). If transient problem check if $t >= t_{max}$. If not go to 1).

A few implementation issues are worth noting. As to the normal discretization a higher order method is preferable. The 6'th order coupled compact difference scheme for non-uniform 1D meshes is used. In streamwise direction the ordinary 2nd order central difference scheme is a good choice. The time-integration can be performed in two ways: Either as a convergence problem, where only the final solution is of interest, or as a transient problem, where also the time history must be captured. For the former, 1st order implicit Euler should be applied in time. In addition the terms $i\alpha_t\mathbf{v}$ can be neglected. This eliminates the need to update the phase at each x-position at each timestep, and significantly speeds up convergence, since only the slowly varying amplitude remains time-dependent. For the latter, a three-point 2nd order implicit scheme

could be applied. Transient problems of interest are e.g. those of slightly frequency modulated waves reported by Shaikh & Gaster (1994) to have a large impact on instability growth and the onset of non-linear mode interaction. In this work only the convergence problem will be exemplified.
Strictly speaking the introduced streamwise ellipticity is for the slow scales, the amplitudes, only, since the fast scale, the streamwise wavenumber, is updated prarabolically as for PSE. This agrees well with the nature of both scales. The ESE solution process will break down when the flow ceases to be convectively unstable. The motivation of our temporal ESE testcase to be presented is to investigate the onset of absolute instability as the reverse flow magnitude increases in a laminar separation bubble.

6.2 Spanwise ESE

is conceptually analog to the temporal ESE and yet different. Again we march the solution along a "new" direction, this time the spanwise. In contrast to time marching, parabolicity is not granted from physics, and the closure equation serves to parabolize the equations along the marching direction just as for PSE. As for temporal ESE, the ellipticity is introduced for the slow scale perturbation amplitude. Spanwise parabolicity implies that only baseflows that are uniformly convected in one spanwise direction are applicable for spanwise ESE. To this class of flows belong 3D boundary layers over swept wings due to a sweep angle, e.g. the DLR swept plate flow, and boundary layers over rotating airfoils, where the spanwise motion is induced primarily by centrifugal forces. Spanwise ESE is fully 3D in space and exhibits similarities to true 3D PSE (not 2.5D PSE often erroneously referred to as 3D PSE) of which only one reference exists, Herbert (1997). Herbert prescribes two directions, streamwise and spanwise, along which initial solutions are to be applied. The solution of the flowfield spanned by the lines of initial data is found by parabolic marching in two dimensions. In addition to the PSE closure equation, a uniqueness condition for the wave phase closes the 3D PSE formulation. Spanwise ESE can be viewed as Herbert's 3D PSE method with ellipticity instead of parabolicity in streamwise direction. The physical disturbance is composed of modes with a wave ansatz extended from PSE:

$$
\begin{aligned}
q^{'}(x,y,z,t) &= \sum_{l=-\infty}^{\infty}\sum_{n=-\infty}^{\infty}\sum_{m=-\infty}^{\infty} q_{lmn}(x,y,z)e^{i(\theta_{lmn}(x,z)-m\omega_1 t)} \\
\theta_{lmn}(x,z) &= \int_{x_0}^{x} \alpha\left(\xi\right) d\xi
\end{aligned}
\tag{6.4}
$$

The perturbed momentum equations are now fully 3D maintaining spanwise baseflow derivatives, which have been neglected for LST, PSE and temporal ESE. Nonlinear terms are neglected below, but can be included with similar additional effort as for 2D or 2.5D nonlinear PSE.

$$
\begin{aligned}
&u_t^{'} + U_x u^{'} + U u_x^{'} + U_y v^{'} + V u_y^{'} + U_z w^{'} + W u_z^{'} - \frac{1}{Re}(u_{xx}^{'} + u_{yy}^{'} + u_{zz}^{'}) + p_x^{'} = 0 \\
&v_t^{'} + V_x u^{'} + U v_x^{'} + V_y v^{'} + V v_y^{'} + V_z w^{'} + W v_z^{'} - \frac{1}{Re}(v_{xx}^{'} + v_{yy}^{'} + v_{zz}^{'}) + p_y^{'} = 0 \\
&w_t^{'} + W_x u^{'} + U w_x^{'} + W_y v^{'} + V w_y^{'} + W_z w^{'} + W w_z^{'} - \frac{1}{Re}(w_{xx}^{'} + w_{yy}^{'} + w_{zz}^{'}) + p_z^{'} = 0
\end{aligned}
\tag{6.5}
$$

After insertion of a single mode of (6.4) into (4.4,6.5) we arrive at

$$i\alpha u + Dv + i\beta w + u_x + w_z = 0 \tag{6.6}$$

$$\begin{aligned}
&\left(-\frac{1}{Re}\left(D^2-\alpha^2-\beta^2-i\alpha_x-i\beta_z\right)+i\left(\alpha U+\beta W-\omega\right)+U_x+U_z+VD\right)u \\
&\quad+\left(W-\frac{2i\beta}{Re}\right)u_z+\left(U-\frac{2i\alpha}{Re}\right)u_x+DUv+i\alpha p+p_x+\frac{1}{Re}u_{xx} &&=-\frac{1}{Re}u_{zz} \\
&\left(-\frac{1}{Re}\left(D^2-\alpha^2-\beta^2-i\alpha_x-i\beta_z\right)+i\left(\alpha U+\beta W-\omega\right)+U_z+DV+VD\right)v \\
&\quad+\left(W-\frac{2i\beta}{Re}\right)v_z+\left(U-\frac{2i\alpha}{Re}\right)v_x+V_xu+Dp+\frac{1}{Re}v_{xx} &&=-\frac{1}{Re}v_{zz} \\
&\left(-\frac{1}{Re}\left(D^2-\alpha^2-\beta^2-i\alpha_x-i\beta_z\right)+i\left(\alpha U+\beta W-\omega\right)+U_z+VD\right)w \\
&\quad+\left(W-\frac{2i\beta}{Re}\right)w_z+\left(U-\frac{2i\alpha}{Re}\right)w_x+W_xu+DWv+i\beta p+p_z+\frac{1}{Re}w_{xx} &&=-\frac{1}{Re}w_{zz}
\end{aligned} \tag{6.7}$$

The uniqueness condition of the phase, θ, simply states

$$\frac{\partial^2\theta}{\partial x\partial z}=\frac{\partial^2\theta}{\partial z\partial x} \tag{6.8}$$

meaning that the integration of the phase from the phase derivatives, $\alpha=\frac{\partial\theta}{\partial x}$ and $\beta=\frac{\partial\theta}{\partial z}$, is independent of the path of integration. The spanwise amplitude variations are minimized by a PSE closure equation

$$\int_\Omega q^\dagger q_z dy = 0 \tag{6.9}$$

which closes the formulation. (6.9, 6.6-6.8) constitute the spanwise ESE. As for PSE, the second derivatives of the amplitude functions (RHS of (6.7)) are neglected in the direction of parabolization. These terms scale $O(Re^{-3})$ compared to $O(Re^{-2})$ or larger for the remaining terms on the LHS. The solution strategy and implementation issues are very similar to temporal ESE. The spanwise wavenumber, $\beta(x,z)$, is found from (6.9) and subsequently the streamwise wavenumber, $\alpha(x,z)$, from the condition (6.8). As to which wavenumber to compute from the PSE closure equation and which to compute from the imposition of uniqueness, there is no choice since the spanwise amplitude variation must be minimized for the parabolization to be fully valid, and hence, the spanwise wavenumber must be computed accordingly. The streamwise wavenumber does not impact the validity of any approximation, since the x-ellipticity allows all x-derivative terms to be included.

6.3 Towards a Bigger Challenge

For the complete nonlocal stability analysis of the rotating airfoil the combination of LST,PSE and ESE forms a viable suite of tools adequate for the task. For the linear analysis one might

rightly argue if local LST based on Orr-Sommerfeld is not sufficient - despite its shortcomings - to obtain useful results. However, both PSE and ESE lend itself readily for inclusion of nonlinearity. Examples of PSE nonlinearity will be given in a proceeding chapter. The solution strategy of the complete nonlocal stability analysis shall be briefly outlined, to put the ESE results, that will be presented, into a larger context:
Rotating airfoils on large wind turbines often experience laminar separation close to the leading edge and a uniform chordwise direction for the convection cannot be assumed. On the other hand, the centrifugal effects will force the flow over the airfoils outwards along the span and no spanwise reverse flow will occur. The effective sweep angle is low compared to the swept boundary layer flow on a delta wing combat aircraft, so stagnation line contamination from upspan/upstream instabilities will be low and not impede the assumption of an initial solution line in the vicinity of stagnation. These solutions can be calculated using LST, eventually supplied with frozen coefficient PSE in 2.5D . In chordwise direction another initial solution line must be defined. In the case of chordwise reverse flow 2.5D temporal ESE could be used to obtain a converged initial solution along the chord. The (x, z) domain is marched using spanwise ESE. The analysis can be either linear or nonlinear.

Chapter 7

Linear Stability Results

The four examples of linear stability to be presented in this chapter range from well known testcases, of which the first is included only for reasons of validation and gentle introduction, to a testcase for the newly proposed ESE. The e^N transition prediciton method will be used based on LST, PSE, ESE and a local PSE, the latter being a hybrid LST-PSE version, the motivation for which will be given.

7.1 Poiseuille Flow

The class of analytical parallel incompressible boundary layer flows in 2D is limited. It consists of the Couette flow and the plane Poiseuille flow. The parallel feature leads to cancellation of the nonlinear convective baseflow terms, so any combination of Couette and Poiseuille flow will be a valid parallel solution also. If we imply uniform convective propagation also, only the Poiseuille flow meets the criteria, which makes it the unique testcase, where LST for downstream propagating small-amplitude linear modes will provide exact eigensolutions to within mashine- and/or discretization-accuracy.
The flow is restricted between two parallel plates, as depicted in Fig.7.1, and driven by a constant pressure gradient in streamwise direction.

$$U(y) = 1 - y^2, \qquad P_x = const., \tag{7.1}$$

with no-slip boundary conditions at the walls. The flow is nondimensionalized by half the channel width, centerline velocity and kinematic viscosity.

$$Re = \frac{U_{cl}^* h^*}{2\nu^*}\,, \tag{7.2}$$

where superscripts $*$ denote dimensional quantities. Orszag (1971) launched the use of spectral methods in hydrodynamic stability, and calculated a critical Reynolds number for instability of 5772.22, below which all eigenmodes will decay. Fig.7.3 shows the fundamental viscous eigensolution of temporal LST (4.14),(4.15) for $Re = 10^4$ and $\alpha = 1.0$. Orszag obtained the eigenvalue $\omega = 0.2375265 + 0.00373967i$ for this slightly unstable mode. The convergence behavior of this eigenvalue for increasing the number of points N along the 1D domain, using the numerical techniques presented in Chapter 2, is presented in Fig.7.2. For comparison reasons the same discretization has been used, although the nonuniform 8'th order coupled compact

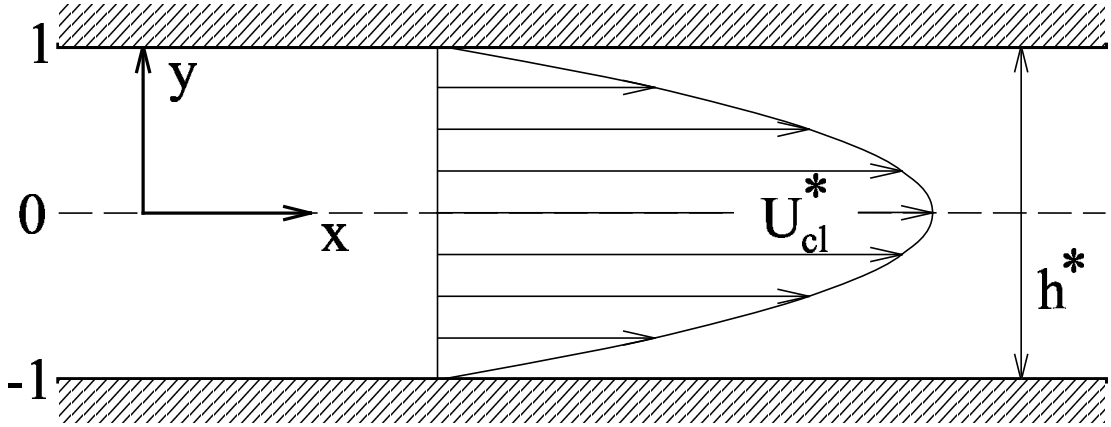

Figure 7.1: Laminar baseflow: Plane Poiseuille flow.

scheme might benefit slightly from a less dense point-distribution in the vicinity of the walls. It is clearly demonstrated that both methods can effectively solve the Orr-Sommerfeld equation, and that the pseudo-spectral method is superior. The converged eigenvalue for large N using the pseudo-spectral method agrees perfectly with reference and is chosen as reference. The straight line in Fig.7.2 for the spectral method marks exponential convergence. For the CCD8 scheme it marks convergence of a constant order of accuracy. The slope of this line corresponds to the order 8.06, well in agreement with theory. The initially steeper slope of the points for $20 < N < 30$ could be due to the formal 10'th order accuracy of the 1st and 2nd derivative evaluations in the CCD8 scheme. The other less steep line in the upper right corner is for a 2nd order discretization. Its insufficiency for global eigenvalue problems is obvious.
The converged eigenvalue spectrum is displayed in Fig.7.3 for $Re = 10000$, $\alpha = 1$ and $\beta = 0$.

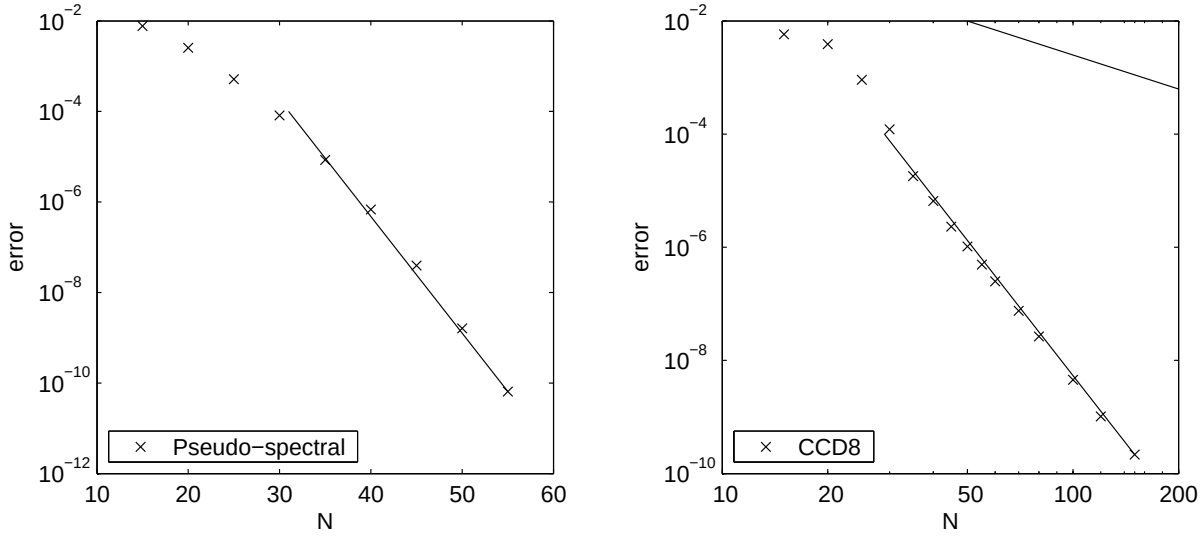

Figure 7.2: Poiseuille laminar baseflow unstable eigenvalue error: Higher order convergence.

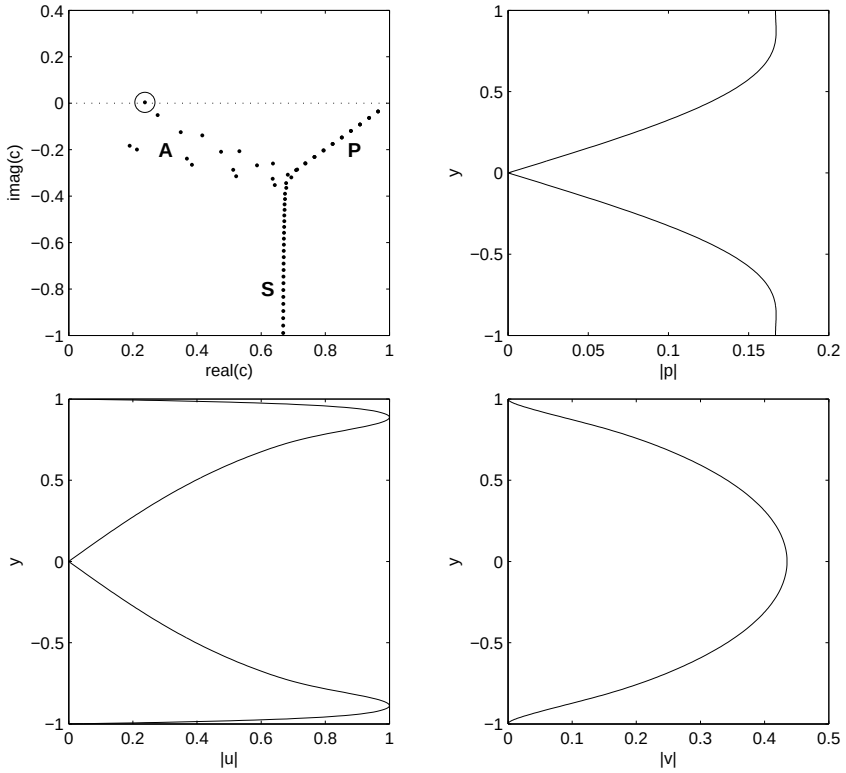

Figure 7.3: Upper left: Poiseuille eigenvalue spectrum, $Re = 10000$. The unsteady mode eigenvalue is circled. Upper right, lower: Modulus of pressure, streamwise and normal amplitude functions for the unstable mode.

$c = \frac{\omega}{\alpha}$ is the streamwise phase-speed of the corresponding eigenmodes. This Orr-Sommerfeld solution was also computed by Schmid & Henningson (2001) p.64, with identical result. The existence of an unsteady mode (encircled), despite the absence of an inflection point for the streamwise velocity profile, leads one to conclude that the mode is of viscous origin. In fact, these viscous instabilities are the first to appear in most boundary layers, due to the Rayleigh inflection point criterion stating that inviscid instability will only occur if the baseflow profile has an inflection point. In a boundary layer this will normally happen further downstream of the onset of viscous instability, either in the presence of an adverse pressure gradient causing inflection of the laminar profile, or as a consequence of the mean flow distortion (MFD) from high-amplitude nonlinearly interacting modes. The linear instabilities of interest for the baseflows treated in the present work will all be of viscous type.

The eigenvalue spectrum constituted by the three branches, named A, P and S by Mack (1976), is common for viscous boundary layers. Branch A contains two sub-branches, one for even modes (e.g. the unstable one) and one for uneven modes. If the baseflow profile is symmetric, say for the plane Poiseuille flow, even/uneven modes will be symmetric/antisymmetric respectively. Type A modes have low phase-speeds and peak amplitude magnitudes in areas of large shear close to the wall, hence the notion 'viscous modes'. In contrast the P branch modes, of which even and uneven mode eigenvalues are practically indistinguishable, have their highest amplitude magnitudes away from the wall in areas of low shear. The phase-speeds, c_r, of these

'inviscid modes' approach the unity centerline stream velocity. Only a discrete number of A- and P-modes exists, whereas the heavily damped S-mode branch extends towards $-\infty$ for infinitely damped modes. Increasing the number of DOFs in the discretization thus leads to an increasing number of ever more damped modes. S-modes all have the same phase-speed, c_r, coinciding with the mean velocity of the flow, which is $\frac{2}{3}$ in the plane Poiseuille case.

7.2 Blasius Flow

The 2D flat-plate Blasius boundary layer flow is the self-similar solution to (3.7) for $m = 0$ corresponding to a vanishing streamwise pressure gradient. This provides the baseflow. The starting point of the analysis is chosen at $\hat{Re} = 400$ just upstream of the critical local Reynolds number, $\hat{Re}_{crit}$, at 519.4, Schmid & Henningson (2001), where the first eigenmode becomes linearly unstable. Throughout this thesis all calculations are carried out with non-dimensionalized variables. The non-local methods are scaled according to the displacement thickness at the starting point, where the inflow conditions for the perturbation(s) are specified.

$$Re = \frac{U_\infty \delta_0^*}{\nu^*} \tag{7.3}$$

For self-similarity baseflows the conversion relations between local and non-local (global) scales are

$$\hat{Re} = \sqrt{xRe}, \quad \hat{\alpha} = \alpha \frac{\hat{Re}}{Re}, \quad \hat{\beta} = \beta \frac{\hat{Re}}{Re}, \quad \hat{\omega} = \omega \frac{\hat{Re}}{Re}, \tag{7.4}$$

where the caret indicates local scaling.
Fig.7.4 illustrates the Blasius solution for the constant global scaling and the linearly distorted

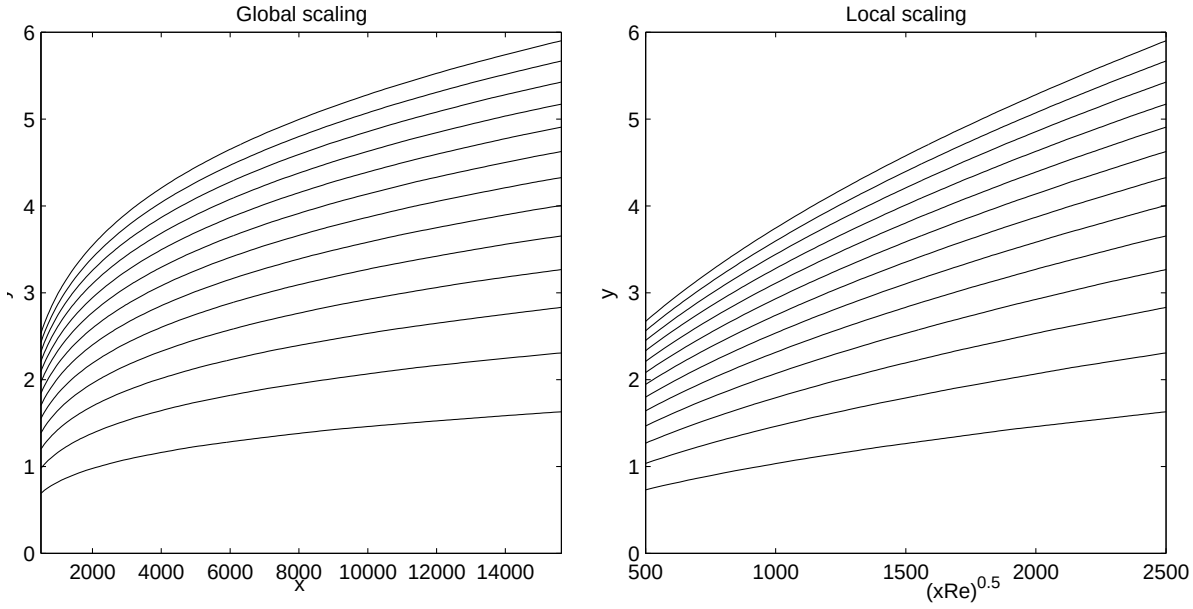

Figure 7.4: Blasius streamlines for global and local scaling of the x-axis. The two domains are identical.

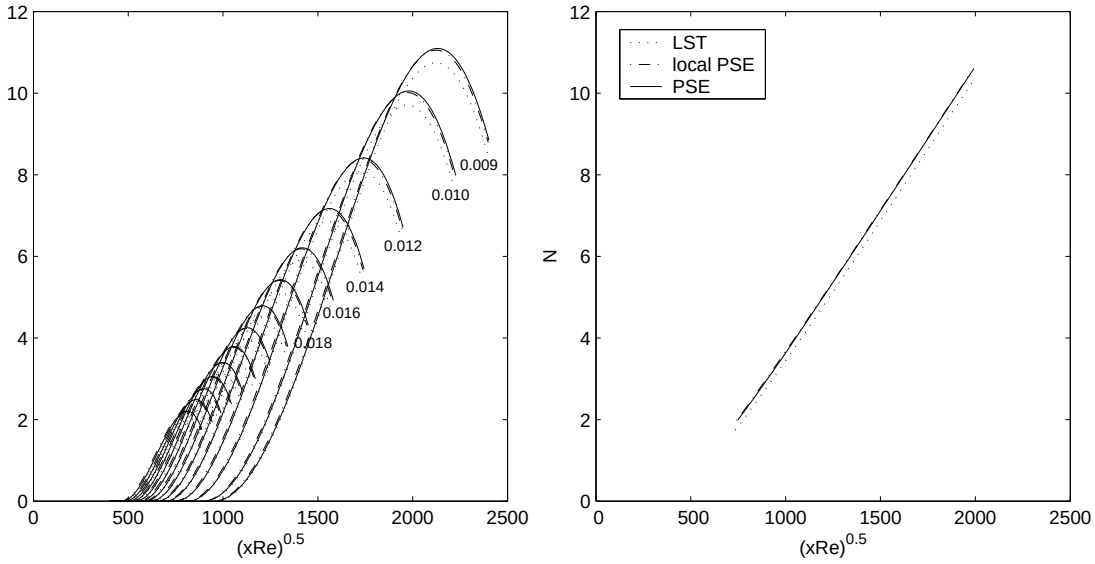

Figure 7.5: e^N-method for Blasius boundary layer. Left: N-factors for distinct frequencies. Right: Containing envelope lines.

local scaling respectively. The accumulated N-factors for distinct frequencies, ω, are presented in Fig.7.5. As $\hat{Re}$ increases, so do the spatial scales of the disturbances, causing the most unstable frequency to decrease in streamwise direction. The annotated frequencies refer to the global scale. Three methods have been employed to calculate the amplifications: LST, PSE and a hybrid method termed local PSE. It is similar to the PSE, except that the streamwise amplitude gradient terms, p_x, u_x and v_x, are decimated by several orders of magnitude, such that the upstream history of each mode is eliminated, rendering a local method, which still accounts fully for the non-parallelism of the baseflow. The local PSE is relevant in situations where the upstream dependence adds unwanted complexity to the task to be undertaken. An example is a growth rate database for classes of boundary layer profiles, where upstream dependence would introduce an ambiguity in the determination of α. The containing envelope curves for the three methods show that the upstream dependence only has a negligible impact on the growth rates, since the PSE and local PSE curves virtually coincide. The physical eigenmodes are thus almost exclusively governed by the local baseflow. Note that this is only the case for spatially oscillating modes. Nonlinear PSE results will reveal the mean flow distortion (MFD) with zero streamwise wavenumber to be profoundly influenced by the upstream history. The PSE methods also calculate the Blasius flow to be slightly more unstable than under the LST parallel baseflow assumption. The offset between the PSE and LST containing envelope lines is mainly created upstream closer to the leading edge at $\hat{Re} < 500$, where the LST parallel assumption becomes less valid. The linear nature of the envelope curves when plotted against $\hat{Re}$ is an artifact of the baseflow self-similarity. The envelopes agree well with literature, Schmid & Henningson (2001). The finding that LST-based growth rates are underestimated for the Blasius flow has been confirmed experimentally by Klingmann et al. (1993) and numerically by Berlin et al. (1998).

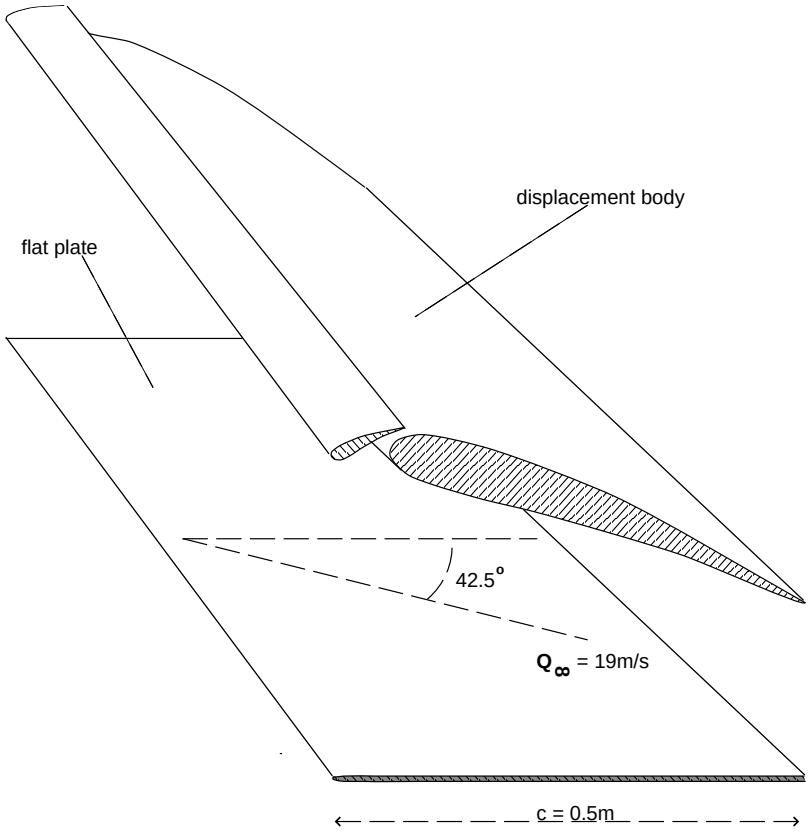

Figure 7.6: Test section of DLR swept plate experiment.

7.3 The DLR Experiment

This laminar baseflow has been used in many numerical studies of perturbations around the steady state of the flow. The setup is sketched in Fig.7.6 and a schematic of domain and coordinate system in Fig.7.7. The experimentally measured input to the parabolic boundary layer solver, (3.12-3.13), is the pressure distribution, which can be accurately approximated by the piecewise analytical expressions, continuous across the pieces up to the 2nd derivative

$$\begin{aligned}
\text{Region I} \quad & (x^* \leq 0.02): && c_p(x^*) = a(x^* - 0.01)^2 + 1 \\
\text{Region II} \quad & (0.02 \leq x^* \leq 0.05): && c_p(x^*) = bx^{*4} + cx^{*3} + dx^{*2} + ex^* + f \\
\text{Region III} \quad & (x^* \geq 0.05): && c_p(x^*) = 0.941 - 1.690x^*,
\end{aligned} \tag{7.5}$$

where

$$a = -214.818, \quad b = -167610, \quad c = 25852, \quad d = -1363.7, \quad e = 24.592, \quad f = 0.852153 \tag{7.6}$$

Other measured quantities are: $\rho^*_\infty = 1.21\frac{kg}{m^3}$, $\nu^*_\infty = 1.51 \cdot 10^{-5}\frac{m^2}{s}$, $c^* = 0.5m$, $Q^*_\infty = 19.0\frac{m}{s}$ and $\varphi_\infty = 42.5^o$. As viewed in Fig.7.8 the stagnation line at $x^* = 0.01m$ is slightly offset from origin of the chord-aligned x-axis at the leading edge. The initial position for parabolic

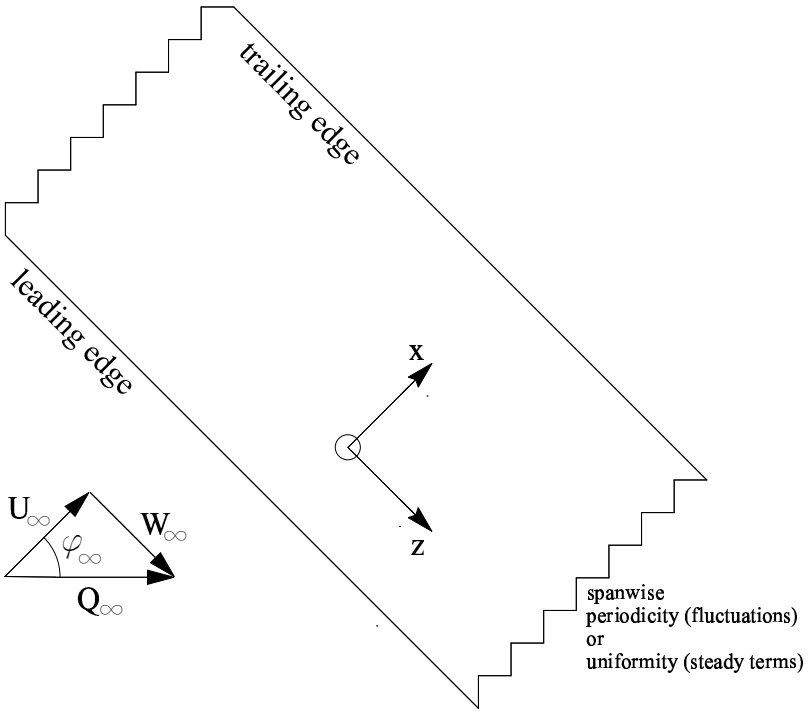

Figure 7.7: Coordinate system for boundary layer flow over DLR swept plate.

marching of the boundary layer solver is in the vicinity of the stagnation line at $x_0^* = 0.02m$, where the swept Hiemenz self-similarity solution to (3.7-3.8) for $m = 1$ and W_e given by (3.3)

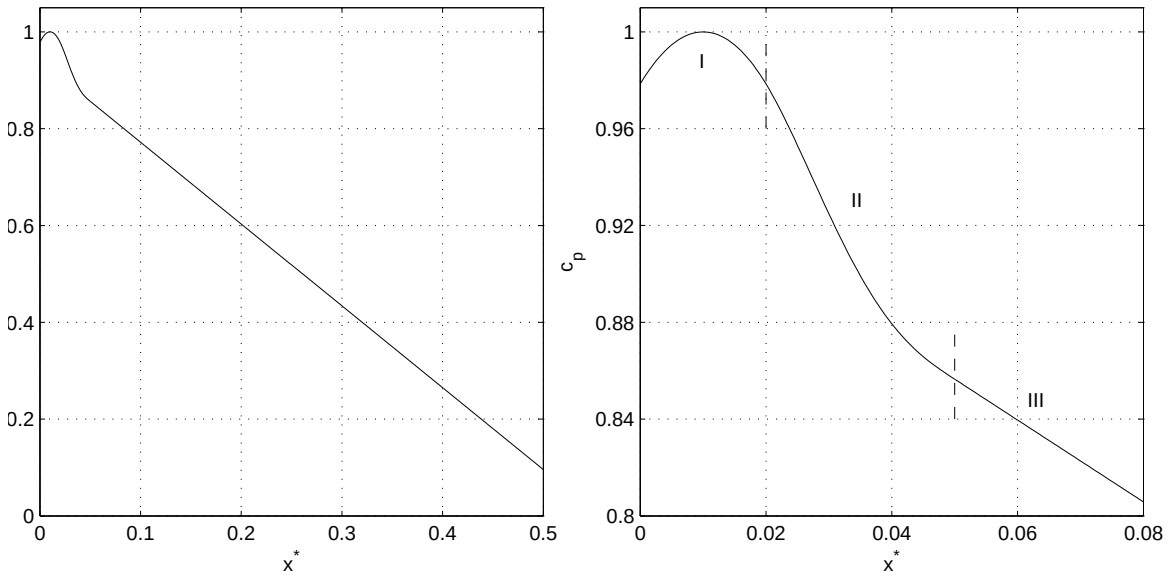

Figure 7.8: Left: Pressure distribution along DLR swept plate. Right: Close-up near the stagnation line at $x^* = 0.01m$

provides the initial steady solution. Global non-dimensionalization of the variables for the PSE is based on the boundary displacement thickness, $\delta_0^* = 1.5441 \cdot 10^{-4} m$, at the initial point. This leads to

$$Re = \frac{Q_\infty^* \delta_0^*}{\nu_\infty^*}, \quad \omega = \frac{\omega^* \delta_0^*}{Q_\infty^*}, \quad \beta = \beta^* \delta_0^* \tag{7.7}$$

The computed baseflow is shown in Fig.7.9 for different chord positions. The negative value of the normal velocity at the boundary layer edge and beyond indicates that the boundary layer is accelerated throughout the chord-length, as also seen from the negative slope of the pressure distribution on Fig.7.8.

The initial perturbation at x_0 is found from an iterative procedure termed 'the frozen coefficient method'. It simply consists of a fundamental viscous mode found by LST, which is then pseudo-marched with the PSE-method using the constant 'frozen' baseflow coefficients given at x_0 until convergence. When the actual PSE marching is started the initial transients often seen, e.g. when an LST initial solution is suddenly marched with a different set of equations, will no longer be present. For wider applicability reasons, the frozen coefficient method has been extended, such that the baseflow coefficients, Reynolds number, Re, and the wavenumbers ω and β can be varied smoothly during the pseudo-marching iterations. Experience has shown that perturbations belonging to the same family of modes, such as the branch A family of viscous modes from Fig.7.3, can be easily tracked across wavenumbers and Re from one baseflow to another through smooth iterative variation. Throughout the present thesis this procedure has been favored over the more direct computation of LST eigenmodes as initial solutions. The main advantage, apart from avoiding initial numerical transients, is its robustness, which enables trouble-free calculation of all initial solutions including the heavily damped viscous fundamentals for high wavenumbers and the steady MFD disturbance (both used in nonlinear PSE). In fact all initial solutions have been generated by the extended 'frozen coefficient method' from just one spatial viscous LST mode: The fundamental Blasius disturbance at $\hat{Re} = 400$, $\hat{\omega} = 0.0344$. Due to the three-dimensionality of the DLR swept plate boundary layer flow, the assumption

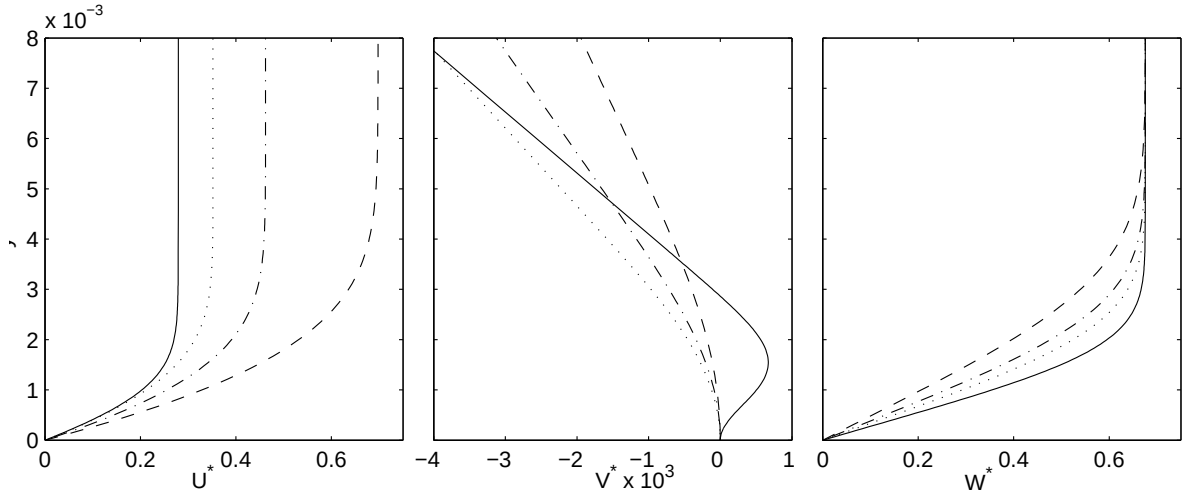

Figure 7.9: DLR swept plate baseflow velocity profiles. Solid lines: $x^* = 0.05$, dotted lines: $x^* = 0.1$, dash-dot lines: $x^* = 0.2$, dashed lines: $x^* = 0.5$.

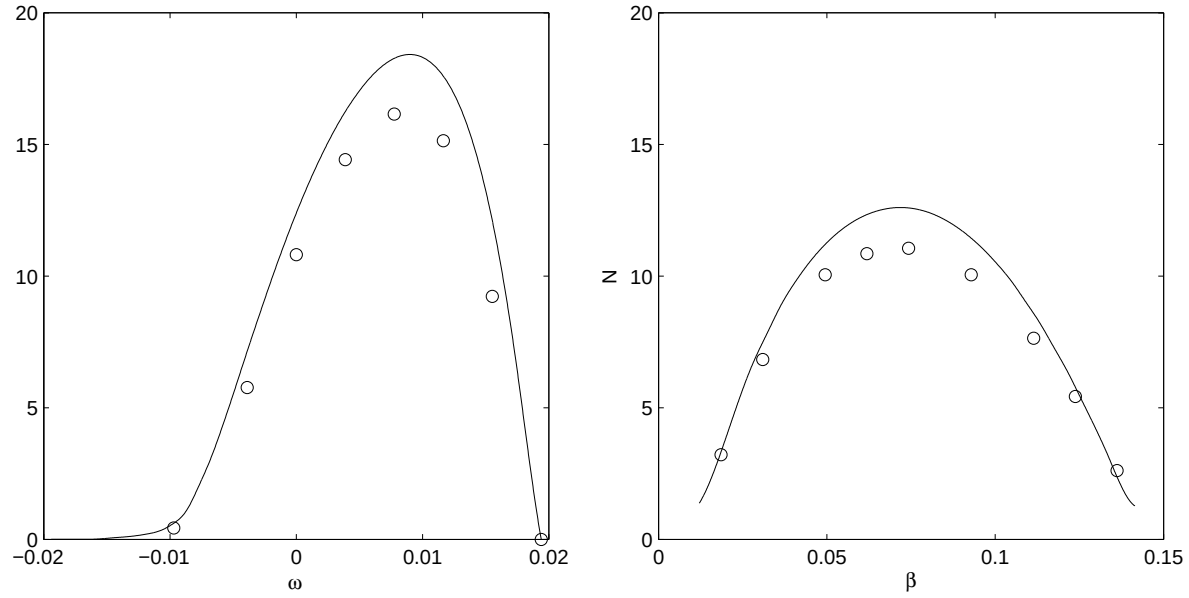

Figure 7.10: N-factors at end of the plate. Right: Stationary crossflow vortices. Left: Travelling vortices for $\beta = 0.081$. Lines: Present results, circles: Stolte (1999)

from the 2D Blasius flow of maximum instability for plane TS waves propagating in the chordwise direction with zero spanwise wavenumber is no longer valid. Numerous experiments have illustrated another route to transition for 3D (swept) boundary layers, caused by another type of mode being the most linearly unstable. These modes are referred to as cross-flow (CF) instabilities due to non-zero β. Such oblique perturbations with wavefronts propagating in a skew angle, $\arctan(\frac{\beta}{\alpha_{real}})$, to the chord-aligned x-axis, can be either steady or unsteady termed 'stationary' and 'travelling' crossflow vortices respectively. Similarly to TS waves, crossflow instabilities are of viscous type and will coincide with the TS waves upon gradual reduction of the spanwise baseflow velocity component.

In pursuit of the most unstable mode over the swept plate, the N-factor has been integrated along the chord for a range of β at zero frequency, ω. Fig.7.10 (right) shows that the most unstable steady crossflow mode in an average sense over the chord occurs at $\beta = 0.0721$ ($\beta^* = 74.3\frac{periods}{m}$) with $N = 12.60$. For $\beta = 0.081$ ($\beta^* = 83.3\frac{periods}{m}$) the temporal wavenumber, ω, has been varied and the N-factors integrated in Fig.7.10 (left), where the most unstable frequency is encountered for $\omega = 0.0088$ ($f^* = 172.3Hz$) with $N = 18.39$. These finding match well those of Stolte (1998) for the same baseflow. Discrepancies are attributed to different methods for calculating the initial upstream modes, where our 'frozen coefficients method' is opposed to a semi-non-parallel method employed by Stolte (1999). For the nonlinear analysis to be presented in the proceeding chapter, the most unstable mode should be used as initial seed. This so-called primary instability is chosen for $\beta = 0.081$, $\omega = 0.0069$ ($f^* = 135Hz$) in accordance with Stolte. This will enable strict comparison and validation of the nonlinear PSE code.

7.4 The Laminar Separation Bubble

The formation of separation bubbles in boundary layers has almost inevitably a decremental effect on the airfoil performance. Its presence on the suction side leads to a reduced pressure peak magnitude, and thus a reduced lift. The boundary layer can separate under the influence of an adverse pressure gradient, undergo transition, and eventually reattach forming the recirculation bubble. A multitude of unsteady bubble scenarios exists. Common for all is the receptivity to Tollmien-Schlichting (TS) wave instability, the wave-length of which is small compared to the bubble length. In some instances either separation or reattachment is not firmly defined, and the whole bubble might engage in oscillatory motion of long wave-length. This phenomenon is clearly undesirable from an engineering viewpoint, since slow large-scale oscillations are more prone to interact with the structural eigenmodes of the airfoil, at worst endangering the entire structure. These kind of instabilities are probably global in nature. Or more precisely: A global bubble instability will affect the bubble as a whole due to upstream propagating wave amplification, and violent large-scale boundary layer motion of some sort is certain to follow.

This motivates our bubble analysis, in particular under which circumstances global instability will occur. To the present much research has been undertaken: Michalke (1990), Gaster (1991), Allen & Riley (1995), Hammond & Redekopp (1998), Alam & Sandham (2000), Rist & Maucher (2002) all use local Linear Stability Theory (LST) applied to different reverse flow velocity pro-

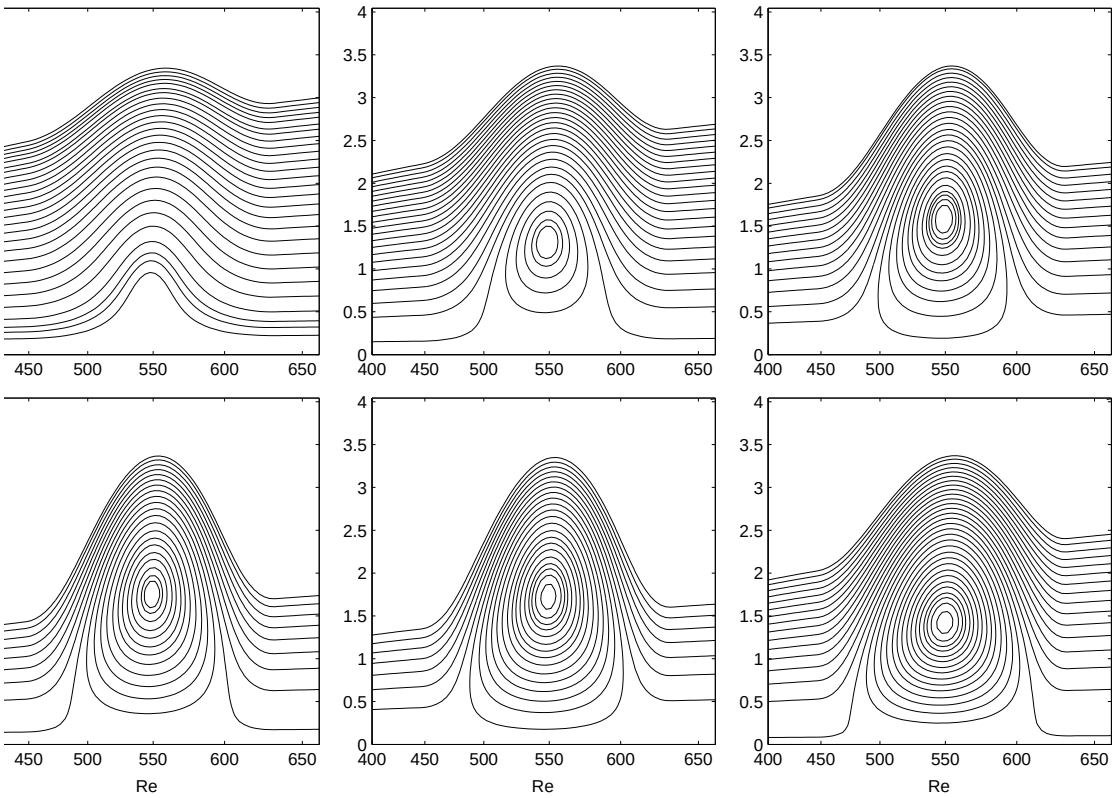

Figure 7.11: Streamlines for different maximum magnitudes of reverse flow. Upper row from left: $U_R = 0.0$, $U_R = -0.1$, $U_R = -0.2$. Lower row from left: $U_R = -0.3$, $U_R = -0.4$, $U_R = -0.5$.

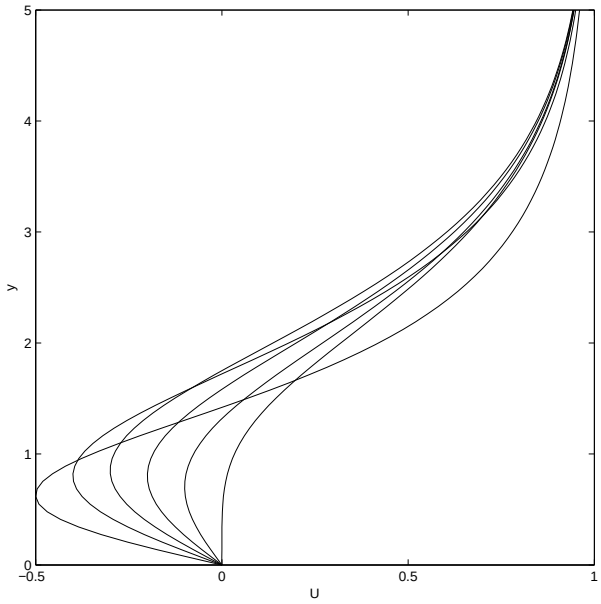

Figure 7.12: Reversed flow velocity profiles for $U_R = 0.0$, $U_R = 0.1$, ... , $U_R = 0.5$.

files. The key parameter is the maximum magnitude of the reverse flow, U_R, found to be in the interval between 15% free stream velocity in the inviscid limit up to beyond 30% at lower Re, for absolute unstable modes to exist.
The analytical velocity profiles proposed by Alam & Sandham are used.

$$U(y) = \tanh(y) - 2\frac{\tanh(y/C)}{\cosh(y/C)^2} \tag{7.8}$$

, where the tuning parameter, C, is adjusted iteratively using a secant method to comply with the required U_R. $C = 2$ for $U_R = 0$ and $C = 0.466$ for $U_R = 0.5$. A sample of profiles is shown in Fig.7.12.
For reference purpose these profiles are analyzed locally using LST based on the O-S equation (4.12). For the nonlocal temporal ESE approach, the reverse flow profiles (7.8) are smoothly blended into the Blasius boundary layer as depicted on Fig.7.11. Prior to this, the reverse flow profiles are stretched in y as to equal the 99% free stream velocity position for the Blasius curve. The initial point of the ESE-computations is at $x_0 = 400$ and the scaled reverse flow profile is mixed into the boundary layer for $500 < x < 1000$. The blending function is an offset cosine valued 0 at the ends of the mixing interval $x \in [500 : 1000]$, and 1 in the symmetric middle $x = 750$.

The Navier-Stokes system is violated by merging the reverse flow profiles into the Blasius solution. U is given by the profiles and V is computed by reinforcing continuity. For momentum the concept of an externally applied body force to balance the equations can offer a physical justification, and most importantly then: The temporal ESE still govern the linear perturbed remainder after subtraction of the steady solution.
The propagation direction of the disturbance energy is given by the group velocity.

$$c_g = \frac{\partial \omega}{\partial \alpha} \tag{7.9}$$

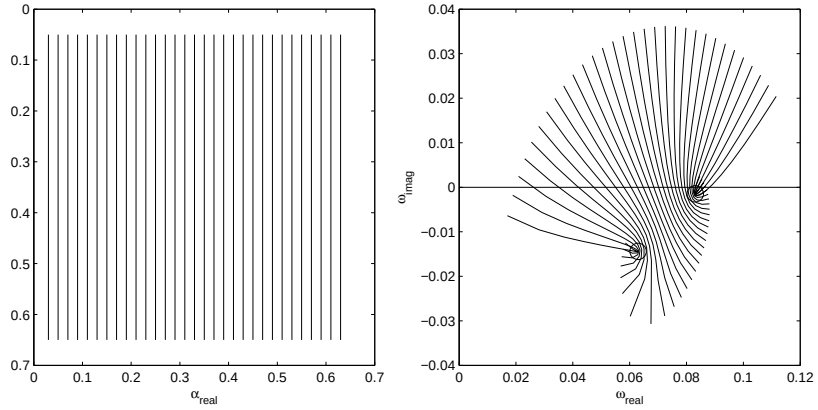

Figure 7.13: Mapping of the complex α-plane into the complex ω-plane for $U_R = 0.25$. The two 'cusps' are encircled.

A disturbance mode will be absolutely unstable if $c_g = 0$ and $\omega_i > 0$, such that the unconvected mode is temporally unstable. The cusp map procedure, e.g. Schmid & Henningson pp 280-281 (2001), is applied to detect global instability. The Figs.7.13-7.14 show the mapping of the complex α-plane into the complex ω-plane at $x = 750$, where the most unstable eigen-frequency, ω, identifies $\omega(\alpha)$. Note that $\hat{Re}_{x=750} = \sqrt{xRe_0} = 548$ for the local analysis. The singularity from vanishing group velocity will be manifested by a slope discontinuity, a "cusp", of the mapped line trajectories. The value of ω_i at the cusp determines if the unconvected energy from that mode (α, ω) increases or decreases in time. The figures reveal the critical reverse flow magnitude where absolute instability can exist at U_R less than 26% and larger than 25% free stream velocity. In order to enable proper comparison with temporal ESE where only real frequencies, ω, are considered, the cases $U_R = 0.25U_\infty$, $U_R = 0.26U_\infty$ are displayed as frequency isolines for ω_r and ω_i on the α-domain, Fig.7.15.
This is the Briggs' method where vanishing mode propagation is identified as saddle points. The spatial branches of neutral temporal stability are marked with bold dashes. The upper branch for

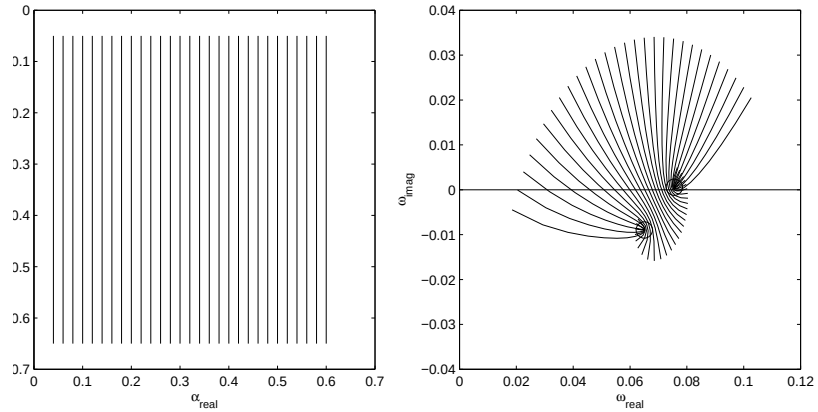

Figure 7.14: Mapping of the complex α-plane into the complex ω-plane for $U_R = 0.26$. The two 'cusps' are encircled.

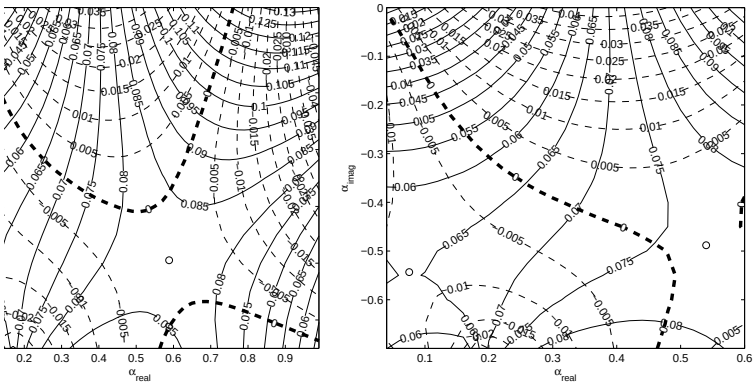

Figure 7.15: Saddle points $U_R = 0.25$ (left) and $U_R = 0.26$ (right).

$U_R = 0.25U_\infty$ is the one encountered in spatial analysis for convected instabilities or physical experiments. These are to be compared with the ESE analysis. As the absolute instability is encountered the spatial branches reconnect. Beyond the onset of absolute instability the

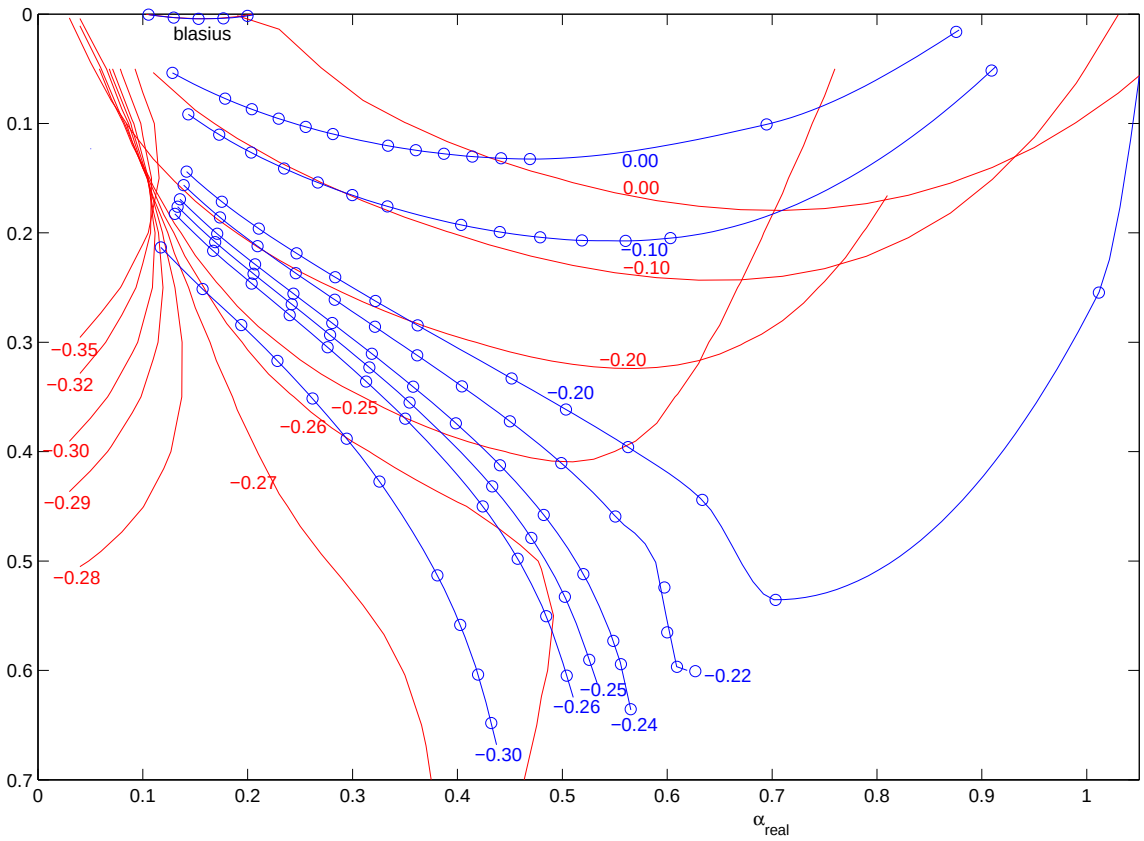

Figure 7.16: Curves off neutral temporal stability (red line: LST, blue line: ESE) for a range of reverse flow magnitudes, U_R, at the bubble center position, $x = 750$, ($\hat{Re}_{x=750} = 548$). U_R is annotated each curve.

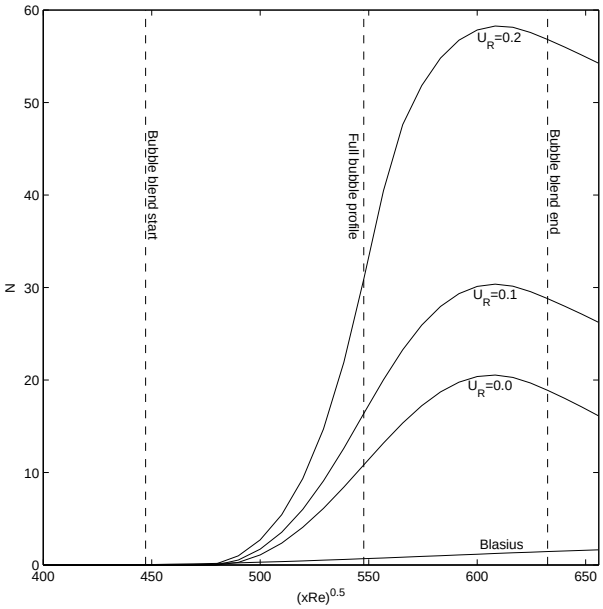

Figure 7.17: N-factors most unstable frequency at $x = 750$ ($\hat{Re} = 548$) for different baseflows (see annotation). The temporal frequencies, ω, are 0.0402, 0.1205, 0.1132 and 0.1132 in order of incresed N-factors

spatial branches for neutral spatial stability where $\omega_i = 0$ are not encountered physically, since they violate the temporal instability encompassed in the absolute instability. On Fig.7.16 the spatial branches for a larger range of reverse flow magnitudes are presented for LST and ESE.

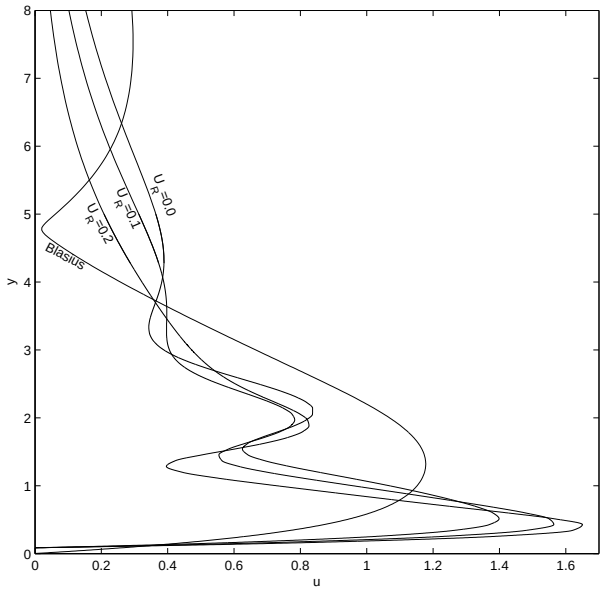

Figure 7.18: Amplitude distributions. Most unstable frequency for different baseflow profiles at $x = 750$.

Each blue point represents a converged ESE computation, where the temporal and streamwise wavenumbers have been scaled a posteriori to the local LST domain and modified according to (7.4) because of the streamwise amplitude variation . Several observations are to be made:

- Increasing levels of baseflow non-parallelism leads to increasing discrepancy between the non-approximated ESE and the LST for which the parallel baseflow assumption apply. Thus, the nearly parallel Blasius flow shows excellent agreement with coinciding neutral stability lines on Fig.7.16, while the reversed flow calculations differ significantly.

- It seems that ESE encounters absolute instability for $U_R > 0.20U_\infty$, but the saddle point and spatial branch reconnection are not clearly detectable. Upstream wave amplification will have to "compete" with downstream propagating convected instability and vanishing absolute instability away from the reverse flow peak at $x = 750$. This might smear the distinct saddle observed for the local LST analysis.

- The convective wave amplification of both LST- and ESE-modes reveals growth rates for the reversed flow approximately two orders of magnitude larger than for the Blasius flow as seen on Fig.7.17. The N-factor will integrate up to the critical N_{crit} over a fraction of the bubble length and transition to turbulence inside the bubble seems inevitable. Whether reverse flow magnitude of more than 20% are obtainable for common flows of medium to high Re is questionable. Alam & Sandham conducted direct numerical simulations of 'short' laminar separation bubbles and found the transition to turbulence to refrain the reverse flow magnitude to obtain levels of more than 8%, and concluded that the basic instability mechanism for these bubbles is convective in nature. Fig.7.17 further suggests that even for the tiniest bubble with $U_R \approx 0^+$, the integrated N-factor peak at approx. 20 will lead the flow into turbulent transition. This observation only holds for the applied baseflow, but it seems plausible to assume that most boundary layer flows are substantially destabilized already at the separation point and regardless of the bubble length. Several baseflow parameters, primarily Re and the adverse pressure gradient chordwise distribution, must be varied systematically to allow firm conclusions.

- The very high U_R-threshold for absolute instability, renders temporal ESE an effective tool to deal with elliptic convectively unstable eigenmodes.

The mode shapes of the streamwise disturbance velocities for different U_R are presented on Fig.7.18. The stronger the bubble and the wall shear, the more 'viscous' the mode shape, in the sense that the amplitude peak location moves closer to the wall and decays faster in the wall-normal direction.

Chapter 8

Nonlinear Stability Results

Prior to a nonlinear PSE calculation choices have to be made for the vector of discrete frequencies to include along the chordwise, spanwise and temporal directions. For the latter two, $-n_{max}\beta_1$:β_1:$n_{max}\beta_1$, and 0:ω_1:$m_{max}\omega_1$ the considerations for the 2D fourier space to be spanned are:

- The most unstable mode(s) should be included.
- The most unstable mode(s) should be located in the 2D fourier space as to allow sub- and/or superharmonic modal interactions to be included in the computation.
- m_{max},n_{max} determine the number of modes. The more modes the better the chance of capturing the real physics of the flow.

The chordwise frequency vector, will normally contain only 1 element to be calculated for each mode at each marching step. The inherent assumption that modal interaction will be confined to the fourier plane spanned by the wavenumber vectors $(l(m = m_{max}, n = 0), m_{max}, 0)$ and $(l(m = 0, n = n_{max}), 0, n_{max})$ is good in most cases, and the associated error can be quantified a posteriori as will be demonstrated.

8.1 Blasius Flow

2D Waves

A logical extension of the linear Blasius testcase from the preceding chapter is the self-induction of the primary wave into superharmonics and a Mean Flow Deflection (MFD). The testcase has been amply computed in literature and serves for validation purpose. The point/line of initial solution is at $x_0 = Re_{x_0} = 400$. The r.m.s of the initial u-amplitude is 0.0025, $\omega_1 = 0.0344$, $\beta_1 = 0$, marching stepsize $\Delta x = 10$. Infinity boundary conditions are imposed at $y_\infty = 20\delta(x)$. 400 non-uniformly distributed mesh points are used for the 6'th order coupled compact difference scheme. This number is well in excess of what is necessary for grid convergence, but the above configuration is kept constant through all the subsequent Blasius sessions, unless otherwise stated, and higher resolution will ensure proper capturing of the physics in areas of strong nonlinear interaction. The 6 modes considered are (l,m,n) = (0,0,0), (1,1,0) ... (5,5,0). On Fig.8.1 we recognize the linear result. For r.m.s values of the of the maximum streamwise

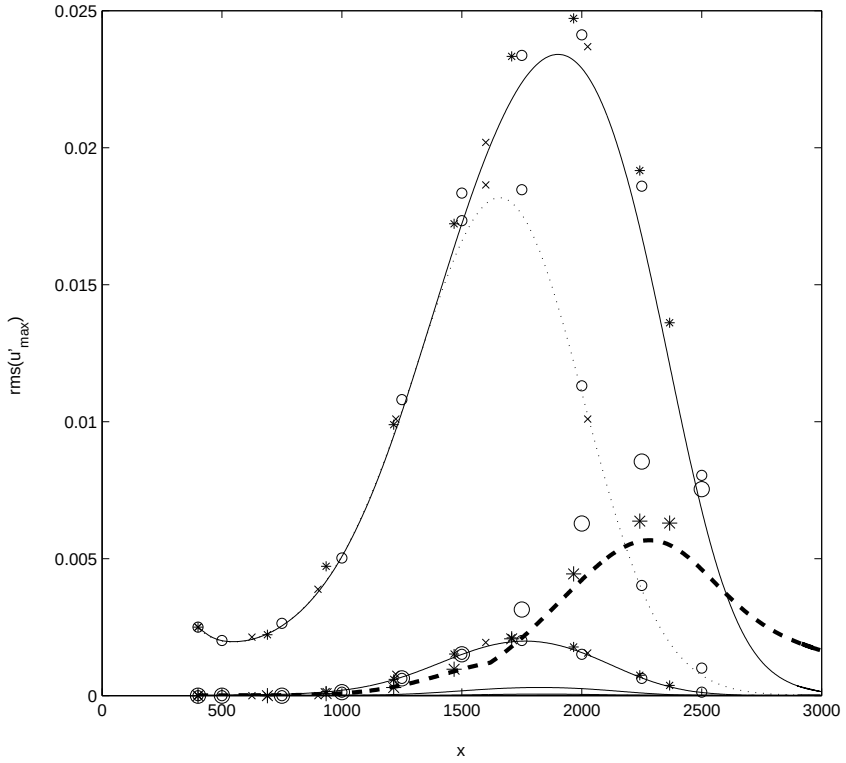

Figure 8.1: Linear (thin dotted line) and nonlinear (full lines) evolution of 2D TS-wave. MFD mode is the thick dotted line. Reference comparisons are: Crosses : Bertolotti et al. (1992), asterices : Joslin et al. (1993) and circles : Herbert (1994)

velocity for the primary wave, mode (1,1,0), above 0.5% nonlinear effects come into play: The higher harmonic (2,2,0) emerges as well as the (0,0,0) Mean Flow Deviation (MFD) mode. For r.m.s. values above 1.5% the nonlinear prediction of the primary wave clearly exceeds that of the linear one. It peaks at 2.34% for $x = 1900$ ($Re_x = 872$). Mode (2,2,0) peaks at 0.20% for $x = 1765$ ($Re_x = 840$) slightly upstream of the primary wave peak, which indicates that the mode is only sustained through nonlinear forcing, and stable to the MFD-corrected baseflow. In contrast the MFD mode continues to grow and peaks at 0.57% for $x = 2280$ ($Re_x = 955$) proceeded by a rather slow decline, even when all other modes have practically vanished at the end of the computation. This illustrates the pronounced upstream dependence of the MFD mode in contrast to unsteady modes which are largely governed by the local conditions, i.e. baseflow and nonlinear forcing. A peculiarity of the MFD mode evolution is the slope discontinuity for $x = 1618$ ($Re_x = 820$), which is on artifact of plotting only the maximum u-value of the physical mode. Different local maxima of the mode are associated with different y-positions. If a local maximum suddenly becomes the global maximum for that mode, then a slope discontinuity in the plot for u'_{max} will be the evidence. This testcase is in agreement with identical testcases by Bertolotti et al. (1992), Joslin et al. (1993) and Herbert (1994). Small discrepancies are attributed to the location of the infinity boundary condition, the numerical stabilization strategy for enabling small stepsizes and the PSE formulation (primitive variable or vorticity based).

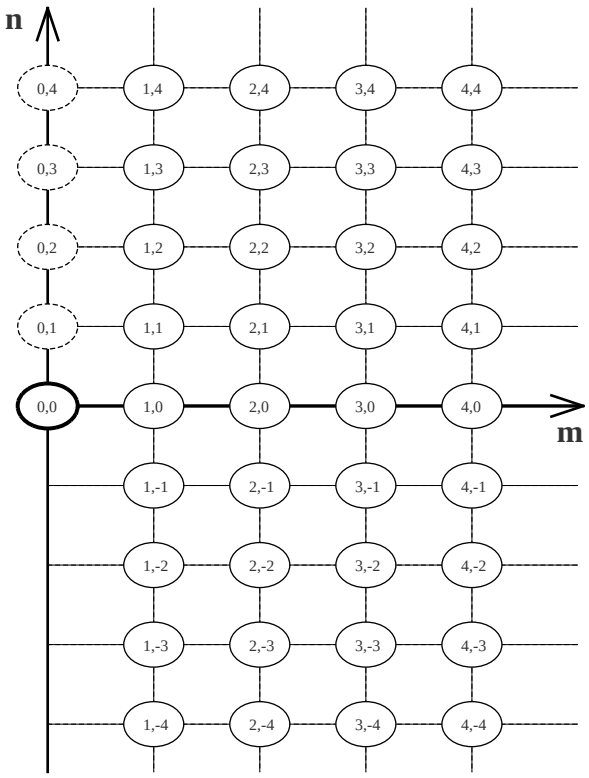

Figure 8.2: Projection of the 2D-plane of (l,m,n) modes onto the 2D-plane spanned by the m-, and n-axis.

3D Waves, Fourier Space

The exclusion of oblique waves in the fourier subspace for instabilities in blasius flow is mostly of academic interest. All experimental evidence demonstrate profound 3D effects of the nonlinearly distorted boundary layer flow that precede the final breakdown to turbulence. That there is no such thing as 2D turbulence is common wisdom. Hence, we expand our fourier subspace to a 2D plane, the projection of which is shown in Fig.8.2. $\omega_1 = 0.011$, $\beta_1 = 1.43$, $m_{max} = n_{max} = 4$ leading to a total of 41 modes. The primary temporal frequency is chosen as to enable tracing the envelope of TS-waves all the way to transition even for small initial amplitudes. The choice of primary spanwise frequency is based on theoretical predictions, Craik (1971), and experimental observations, Corke & Mangano (1989) , of resonant growth between plane 2D waves with spatial wavenumbers $(\alpha, 0)$ and subharmonic oblique waves with wavenumbers $(\frac{1}{2}\alpha, \pm\beta)$. While the Craik model favors this so-called resonant triad of modes, experiments suggest that many modal interactions between the most amplified plane wave and a subharmonic oblique wave or pair of waves exhibit resonance, including the steady modes $(0, \pm\beta)$. Determination of the $\frac{\beta}{\alpha}$ ratio is based on trial and error. Our value of 1.43 agrees well with findings in literature, i.e. Herbert & Bertolotti (1985), and is not a unique value. Deviations of the spanwise wavenumber vector of up to 40% will lead to qualitatively similar results.

We aim the present investigation on the influence of the initial upstream conditions on the downstream evolution of modes, with special attention to the onset of three-dimensionality,

the structural properties of the flow and the final stage of transition until the x-location where the PSE-method will no longer converge and the marching procedure halts. The 9 Blasius computations are organized as follows.

- Session 1-4:
  Dependence of initial amplitude magnitude on all modes. For session 2,3 and 4 the initial amplitude magnitudes from the previous session, i.e. session 1, 2 and 3 respectively, are increased by one order of magnitude. The primary disturbances are unsteady and an order of magnitude larger than the remaining modes

- Session 5-8:
  Dependence of initial amplitude magnitude on steady modes only. For session 6,7 and 8 the initial steady mode amplitude magnitudes from the previous session are increased by one order of magnitude.

- Session 9:
  Dependence of 3D single oblique unsteady modes versus 2D pairs of unsteady modes.

Initial data is given as Fourier modes using the frozen coefficients technique on a harmonic viscous mode obtained by the Orr-Sommerfeld equation. Thus, the receptivity stage is not modelled. However, The choice of initial data reflects some aspects of the nature of the physical receptivity. Steady disturbances such as roughness lead to steady modes. In a contrary manner, unsteady disturbances such as especially free stream turbulence but also localized wall vibrations or sound, will lead to unsteady modes. The ratio of unsteady modal energy to steady modal energy at the initial line determines if the initial receptivity was governed by roughness or by free stream turbulence, vibration and/or sound. The application of boundary inhomogeneties has not been employed, so that downstream of the point of initiation the Blasius boundary layer flow propagates in an ideal smooth environment.
On Fig.8.3 the primary nine modes are for $m = 4$ with initial u'_{max} $4.0 \cdot 10^{-5}$. All other modes are initiated with initial u'_{max} $1.0 \cdot 10^{-5}$. The background noise is set to $1.0 \cdot 10^{-6}$ and no mode can decay to a u'_{max} below this value. Infinity is extended from $y_\infty = 20\delta(x)$ to $y_\infty = 40\delta(x)$. One observes the fans of mode evolutions for $m = 4$, $m = 3$ and $m = 2$. The most amplified in each fan is always the plane 2D wave for a 2D baseflow, the less amplified are the eight oblique waves (of which four coincide due to symmetry). The linear evolution of the plane waves are seen to coincide with the nonlinear analysis for $m = 4$, $m = 3$ and $m = 2$. For $m = 1$ the first discrepancy with nonlinear predictions occurs at u'_{max} 0.4% for $x = 8100$ ($Re_x = 1800$). In this case nonlinearity stabilizes the growth of the 2D wave. Overall the situation is not so: For $x > 6000$ the steady modes with spanwise fourier index $n = 1$–4 experience a rapid growth that exceeds that of any modal linear prediction. This growth continues and also affects the less amplified oblique waves for $m = 1$. We cannot depict a distinct modal resonnace, but rather a self-induced growth between the linearly unstable waves and the steady oblique disturbances. For $x > 10000$ the baseflow has become highly disturbed by the steady oblique modes with streamwise velocity magnitudes peaking at 17% for mode $(0, 3)$. This changes the receptivity of the baseflow to higher frequency waves (the waves that were linearly unstable at the start of the plate) and together with nonlinear forcing these waves amplify rapidly, then couple and finally cause a breakdown of the marching procedure at $x = 10900$ ($Re_x = 2088$).

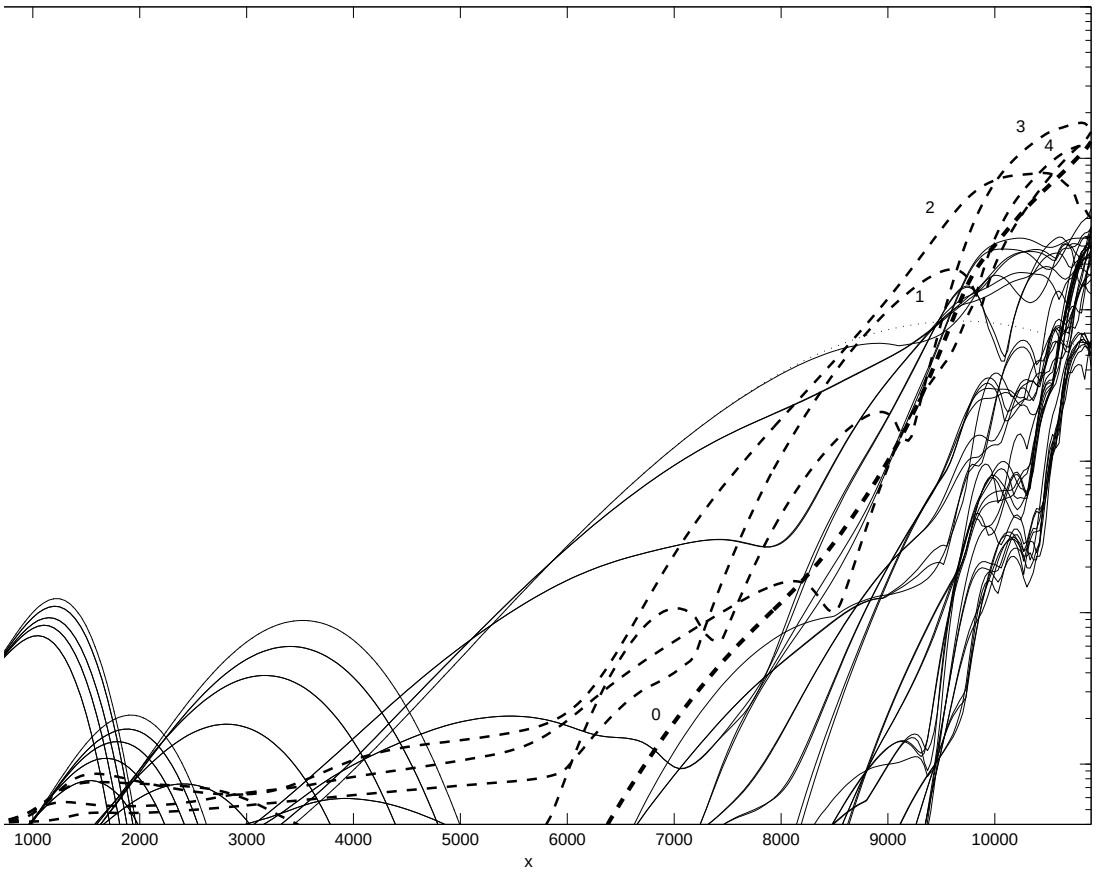

Figure 8.3: Session 1. Linear and nonlinear evolution of disturbances of initial amplitude of primary modes $4 \cdot 10^{-5}$. The thick dotted line denotes the MFD mode $(m, n) = (0, 0)$, normal dotted lines are the other steady modes $(m, n) = (0, 1), (0, 2)...(0, 4)$. Annotations 0-4 refer to the value of n in fourier space for these steady disturbances. Full lines are the non-steady modes. The first fan of unsteady modes that become dominant are the 9 modes $(m, n) = (4, -4), (4, -3), ...(4, 4)$. The second fan of 9 modes are $(m, n) = (3, -4), (3, -3), ...(3, 4)$ and so on. The last fan of modes is $(m, n) = (1, -4), (1, -3), ...(1, 4)$. For each fan of modes the most amplified is the plane wave, the least amplified are the most oblique waves, at least until the onset of nonlinear effects. The thin dotted lines are the linear calculations of modes $(m, n) = (1, 0), (2, 0), ...(4, 0)$. They serve to illustrate the nonlinear impact.

One more thing to note is the slight amplification of the steady oblique waves right after initiation at $x_0 = 400$. Although the inhomogenities that cause the amplification is of nonlinear origin, the underlying mechanism must be linear. The magnitude of the first fan of waves ($m = 4$) peaks around $u'_{max} = 1.0 * 10^{-4}$ which creates nonlinear forcing in the order of $1.0 * 10^{-8}$. At these magnitudes linear PSE is fully adequate and govern the disturbance flow. What we have encountered is an example of nonmodal growth. The steady modes are slightly damped according to Orr-Sommerfeld based LST, but will respond to nonmodal forcing by transient growth, which can be considerable, before the amplitude settles and decays in accordance with the modal behavior. Reddy & Henningson (1993) accredited the phenomenon to the non-

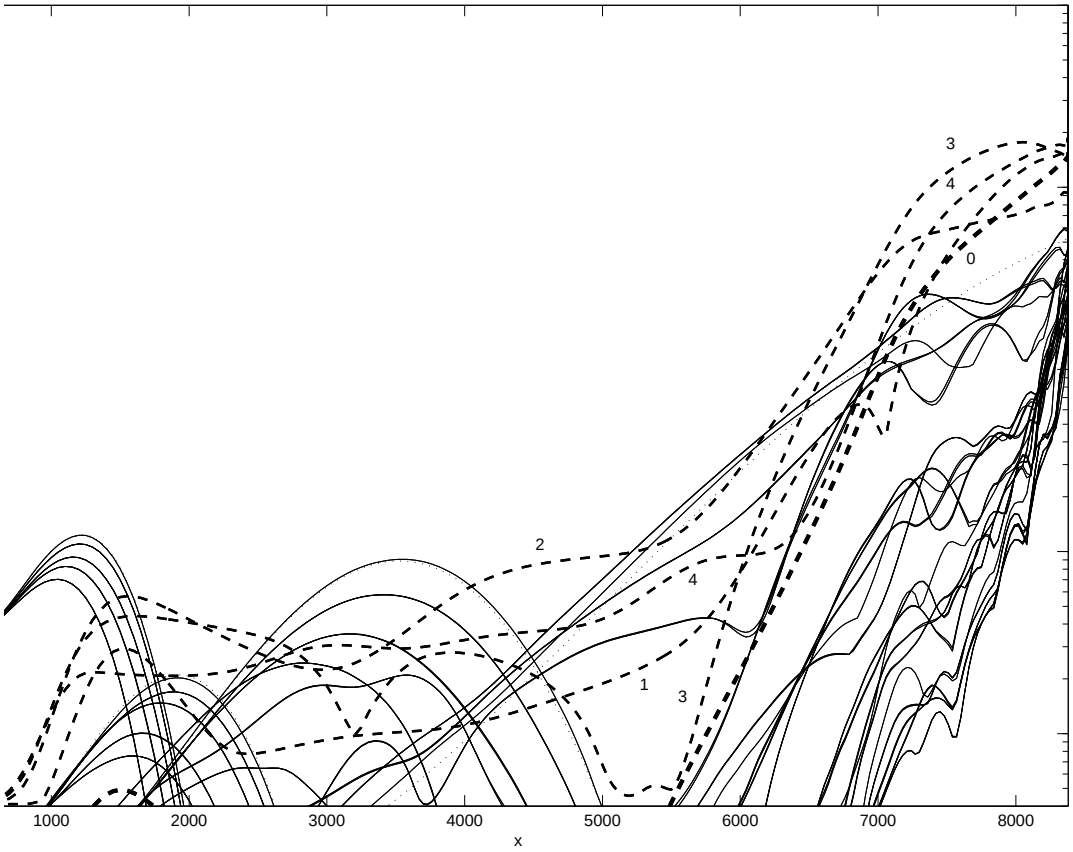

Figure 8.4: Session 2. Linear and nonlinear evolution of disturbances of initial amplitude of primary modes $4 \cdot 10^{-4}$. For lines and annotations, see Fig.8.3.

orthogonality of the Orr-Sommerfeld operator in cases where the non-orthogonal eigenmodes that comprise a given physical disturbance experience different exponential decay. Also Herbert (1994) identified these u-dominated streamwise counter-rotating steady modes to hold the largest potential for transient growth, and noted their close resemblance with Görtler vortices known from centrifugal instability on concave surfaces. Experimentally these modes were first discovered by Klebanoff (1971) whose name they bear. As we shall see longitudinal vorticity, either as steady or unsteady modes, have a key role to play in most transition scenarios. Sometimes the term 'streaks' is used to distinguish these free-stream aligned rotating structures from Tollmien-Schlichting plane or oblique waves.

The initial three-dimensionality of session 1–8 is provided by the steady spanwise modes only: (m, n)=$(0, 1)$,$(0, 2)$,$(0, 3)$ and $(0, 4)$ on Fig.8.2. The unsteady three-dimensional modes for $n \neq 0$ are all mirrored across the m-axis, so that the spanwise velocity fluctuations for these modes cancel out in pairs $(1, 1)$ with $(1, -1)$ etc. The growth of Klebanoff modes marks the onset of steady spanwise velocity fluctuation. The onset of unsteady spanwise fluctuations is indicated in fourier space by the amplitude splitting of the modes (m, n), $(m, -n)$ and by gradual counter-phasing of the paired oblique modes. On Fig.8.3 these modes coincide in amplitude until $x = 9000$ ($Re_x = 1897$) from where they depart from each other, but still following simi-

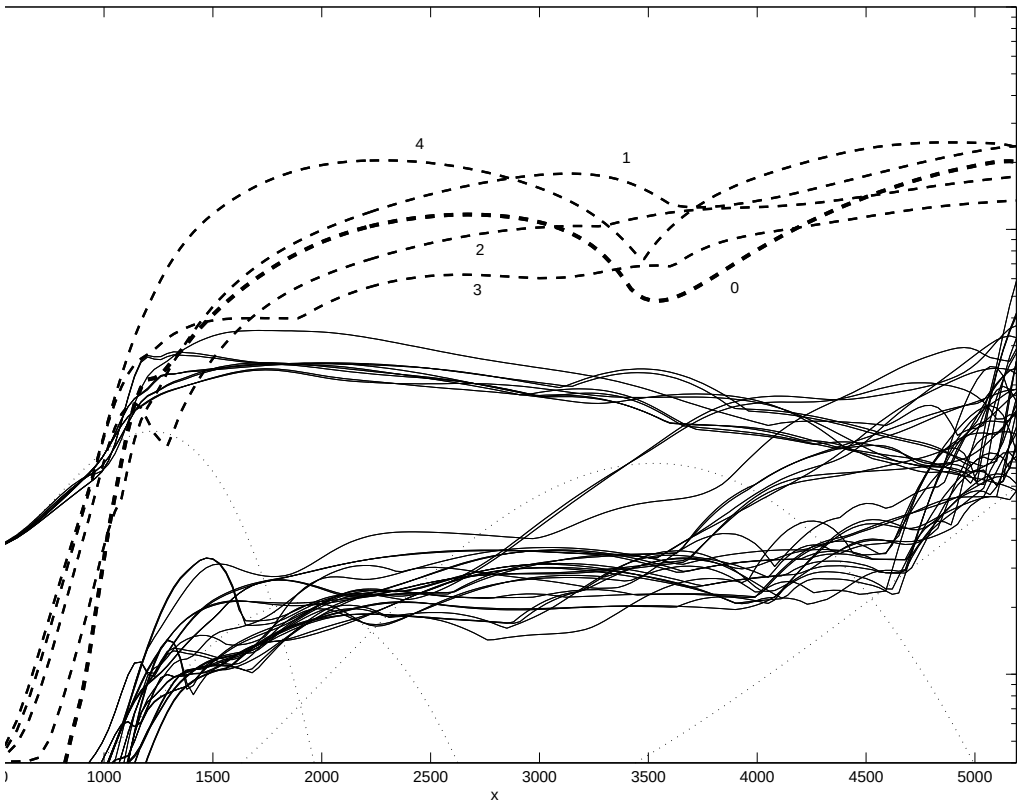

Figure 8.5: Session 3. Linear and nonlinear evolution of disturbances of initial amplitude of primary modes $4 \cdot 10^{-3}$. For lines and annotations, see Fig.8.3.

lar trends in the streamwise evolution.

On Fig.8.4 all the initial amplitudes of primary modes, other modes and background noise level are increased ten-fold. Only minor changes from session 1 are noted. The initial transient growth of the Klebanoff modes exceeds that of the TS plane and oblique waves and peaks locally at $x = 1550$ ($Re_x = 787$). Following a near-modal decay the Klebanoff modes once again start to accumulate momentum as they interact with TS-waves of higher amplitude and lead the flow into transition as they couple with the dominant TS-waves and cause strong coupled amplification of higher frequency modes. At $x = 8050$ maximum u-velocity of the steady oblique mode $(0, 3)$ peaks at 18% of the free-stream. As for session 1, the linear prediction (dotted lines) of the plane waves is seen to be valid up to the nonlinear stage when u'_{max} of the dominant modes approach 1%.

Increasing once again all initial amplitudes by one order of magnitude, similar to lowering the critical N-factor N_{crit} by 2.3, Fig.8.5 shows how the linear instability stage from session 1–2 is almost entirely bypassed: Only for $x < 959$ ($Re_x = 619$), is the growth by the dominant mode given by that of TS-amplfication. Downstream of this position Orr-Sommerfeld LST or linear PSE does not even remotely approximate the physics of the flow, and any use of a linear transition prediction model such as the e^N-method ought to be abandoned. In contrast to the very much independent development of linearly governed TS-waves, we note a clear

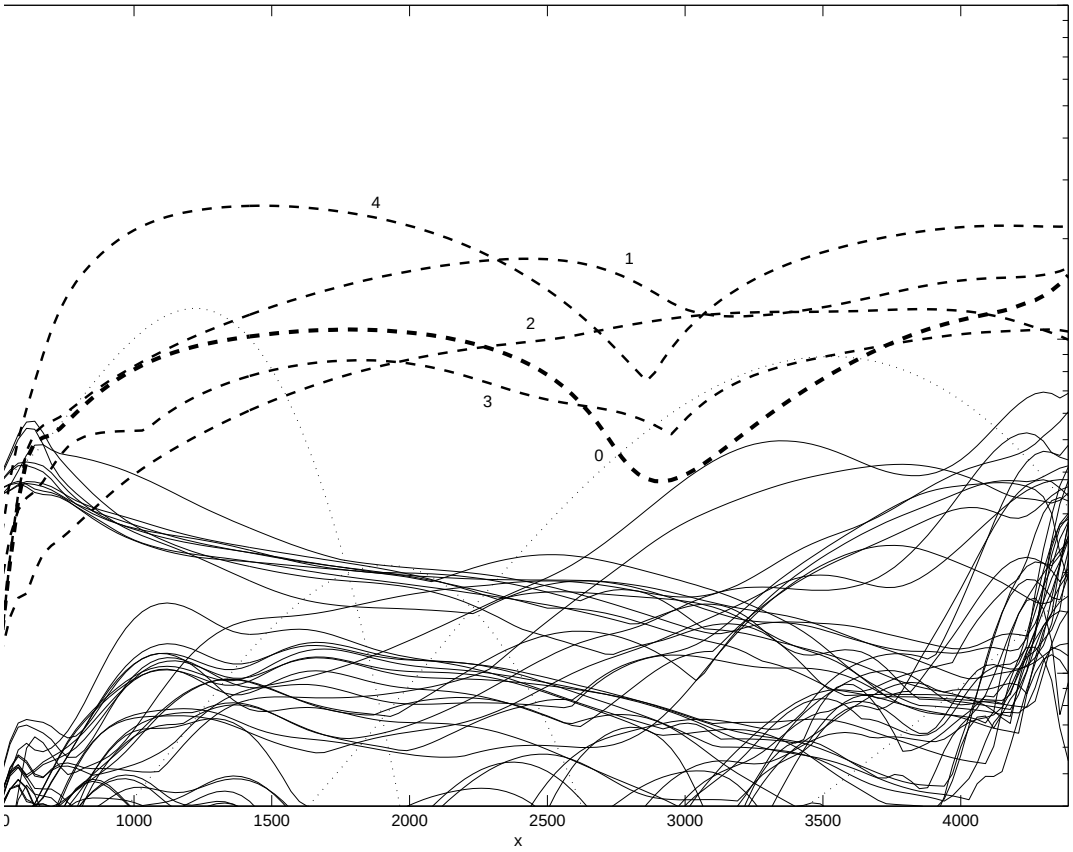

Figure 8.6: Session 4. Linear and nonlinear evolution of disturbances of initial amplitude of primary modes $4 \cdot 10^{-2}$. For lines and annotations, see Fig.8.3.

indication of coupling between certain modes. Three groups of coupling modes are present: The steady oblique modes (Klebanoff modes), the higher frequency primary modes along the line $m = 4$ in the fourier plane and finally all the other unsteady modes. To ease subsequent formulations we adopt the term 'mode clusters' for the nonlinearly interacting clearly visible group of modes in fourier space. The dominating Klebanoff mode cluster interacts internally along the line $m = 0$ in a self-contained way due to the zero frequency. In anticipation of the trend to be demonstrated, one should note the alignment in fourier space of the non-dominating mode clusters with the dominating mode cluster. The higher frequency mode cluster cannot interact internally. On the other hand its main modal forcing will occur under the influence of the dominating mode cluster. Examples are $(0,0) + (4,0) \Rightarrow (4,0)$, $(0,1) + (4,1) \Rightarrow (4,1)$, $(0,2) + (4,2) \Rightarrow (4,2)$ etc. The mode cluster of the remaining part of unsteady frequencies is the least energetic, and shows a similar tendency of mode cluster alignment with the dominating mode cluster. This session seemingly ends when the unsteady mode clusters synchronize their streamwise phase-speed (see Fig.8.8) and evolves into strong amplification. The largest disturbance is once again a Klebanoff mode. It peaks twice, at $x = 2280$ ($Re_x = 955$) and $x = 4890$ ($Re_x = 1399$) with maximum streamwise velocity magnitudes of u-velocities of 20% and 24% respectively. The long-wave streamwise coupled spatial oscillation of the Klebanoff modes is a

noteworthy feature, characteristic of dominant steady mode clusters as we shall see.
Further increase of the initial level, Fig.8.6, leads to very high initial disturbances where full by-pass transition occurs. The scenario is very similar to the former, but more pronounced. The initial growth of Klebanoff modes is an order of magnitude higher than any TS-wave. The dotted line of linear prediction is in error right from the initial point at $x_0 = 400$. The oblique pairs of primary waves $(4, n \neq 0)$ outgrow the plane primary wave $(4, 0)$ for $x < 640$ and split before decaying into a high frequency mode cluster. The long wave steady oscillation is qualitatively unchanged from session 3, but has moved upstream due to stronger initial growth of the Klebanoff modes and increased the period by 22%. The peaks are at $x = 1450$ ($Re_x = 761$) and $x = 4150$ ($Re_x = 1288$) with maximum streamwise velocity magnitudes of u-velocities of 24% and 22% respectively. It should be noted that the sessions 3-4 are somewhat under-resolved due to the violent initial growth of the high wavenumber Fourier modes $(0, 3)$, $(0, 4)$. Their nonlinear interaction into higher order modes is outside the truncated Fourier space, and hence not accounted for in the PSE computations. Qualitatively this should not affect the overall scenario, but to obtain quantitative agreement with DNS more spanwise modes ought to be included.

Session 5–8 deal with initial uniformly distributed unsteady amplitudes and varying steady amplitudes. Session 5 resembles session 2 concerning the initial data. Only change is that all unsteady modes are now primary modes with initial u'_{max} $4.0 \cdot 10^{-4}$ and background noise rather high at $2.0 \cdot 10^{-4}$ Steady modes are unchanged at u'_{max} $4.0 \cdot 10^{-5}$ at x_0. Subsequent sessions 6–8 increase the steady mode initial amplitudes by one order of magnitude successively. In session 9 the symmetric distribution of oblique unsteady modes leading to a pairwise cancellation of unsteady spanwise oscillation is abandoned. Instead, the 16 unsteady oblique modes ($m > 0, n < 0$) from session 6 are marginalized at initial amplitudes two orders of magnitudes lower, while the 16 opposite modes ($m > 0, n > 0$) are doubled in initial amplitude in order to maintain approximately the same initial disturbance energy. Thus session 9 of single oblique modes is to be compared with session 6 of oblique pairs.
The results in fourier space are presented in Fig.8.7. The scenarios are those of natural (non-bypassed) transition as for session 1–2. Note that in the calculation of u'_{max} a physical mode is the sum of mode (m, n) and the complex conjugate mode $(-m, -n)$. the MFD mode (0,0) is real and the only mode not to have a complex conjugate mode in fourier space. This is why the initial level of the MFD is only half that of the other steady modes. The initial level of steady disturbances leading to fastest flow distortion and transition is for session 6 where all initial mode amplitudes are equal. Lower and higher initial steady amplitudes slightly delay the process, despite higher initial disturbance energy in session 7. Session 8 is the only of all sessions where the nonlinear forcing on the steady oblique modes is too small to influence the low modal damping of these modes. From a physical point of view, the high initial level of the steady modes in session 8 is probably not obtainable due to their potential for transient growth. Session 9 reveals that imposing 3D single oblique waves at the initial line instead of 2D symmetric oblique pairs delays transition rather than promoting a 3D-effect that could precipitate transition.

The streamwise phase-speeds depicted in Fig.8.8 for natural and by-pass transition reflect the different nature of the two scenarios. The former is characterized by the linear amplification stage where modes propagate the phases independently, followed by the nonlinear stage with phase coupling of all the modes, and finally the transition stage where the phase-lock gradually loosens up and allow the modes to convey the phases at different speeds. The streamwise phase-speeds for by-pass transition are much higher, which could indicate that the disturbances

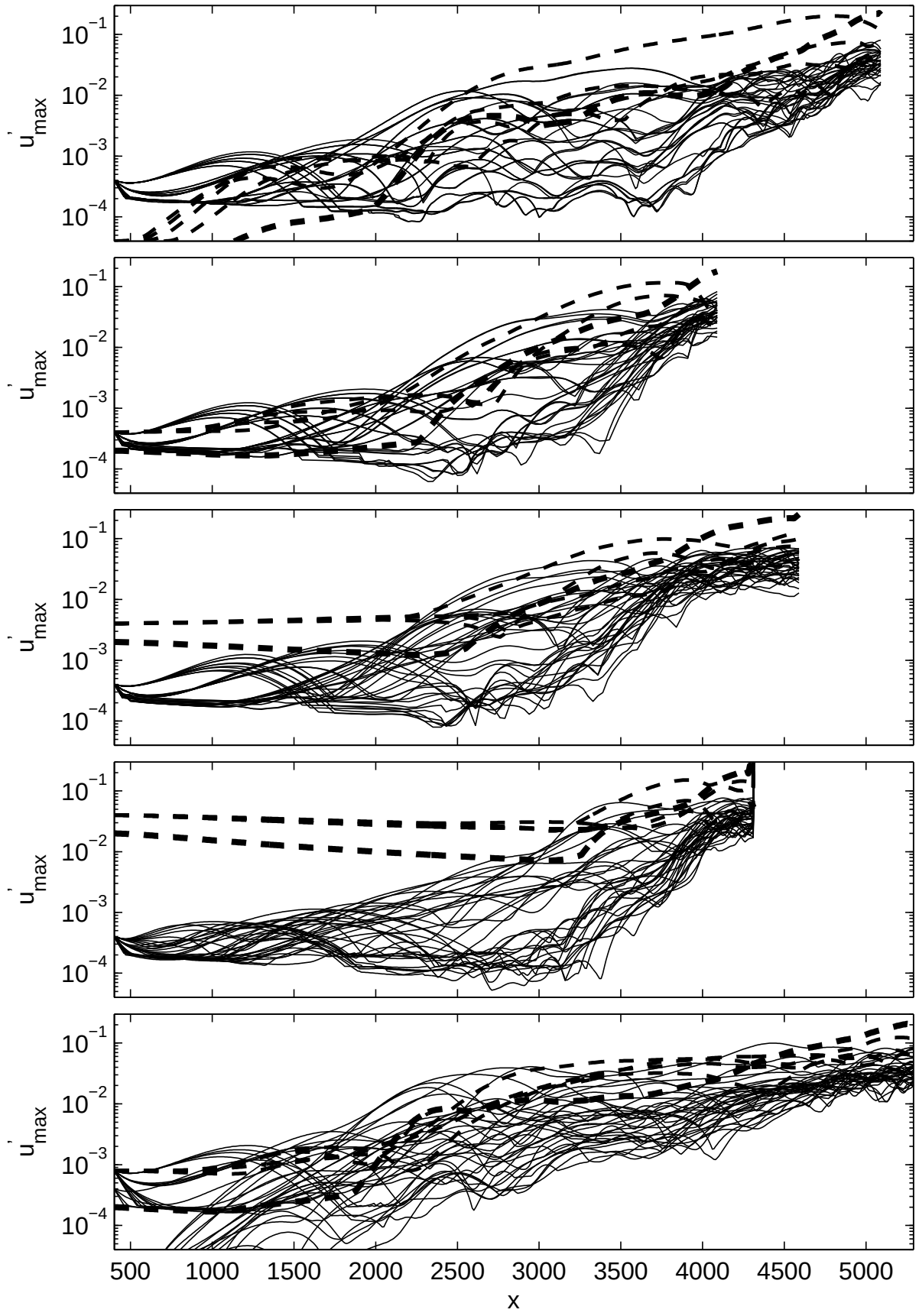

Figure 8.7: From above: Session 5–9. nonlinear evolution of disturbances.

are located in the upper boundary layer, and maybe because of the nearly instant onset of nonlinearity all modes never phase-lock. Four mode clusters of which only one exhibits strong internal phase-lock can be observed. The phase coupling of two mode clusters seems to mark the start of the transition phase.

The single most important mode is the MFD $(0, 0)$ mode. Unlike any other mode, it has a direct influence on all modes, and the change of physical quantities like skin friction, pressure coefficient, displacement- and momentum-thickness in the distorted flow field is solely governed by the MFD. Contributions from the steady oblique modes $(0, n \neq 0)$ cancel out along the spanwise dimension, while contributions from the unsteady modes $(m \neq 0, n)$ cancel out in time also. An indication of transition to turbulence in a boundary layer is the sudden rise of skin friction on the wall as one moves downstream. Fig.8.9 shows the MFD velocity distribution for u_{MFD} and v_{MFD} across the boundary layer for session 1–4 in the transition stage. The very high normal gradient of the streamwise velocity in the vicinity of the wall, indicates the sharpening of the laminar profile towards a 'more turbulent' one. The effect on the skin friction can be seen on Fig.8.10. for session 1–4. In session 1 the skin friction starts to rise at $x = 9000$, when the dominating mode streamwise velocity amplitudes exceed approximately 1.0% (see Fig.8.3). Increasing the initial amplitudes in session 2–4 causes the position of skin friction rise to move upstream succesively. In the natural transition cases (session 1–2) the rise is smooth, while

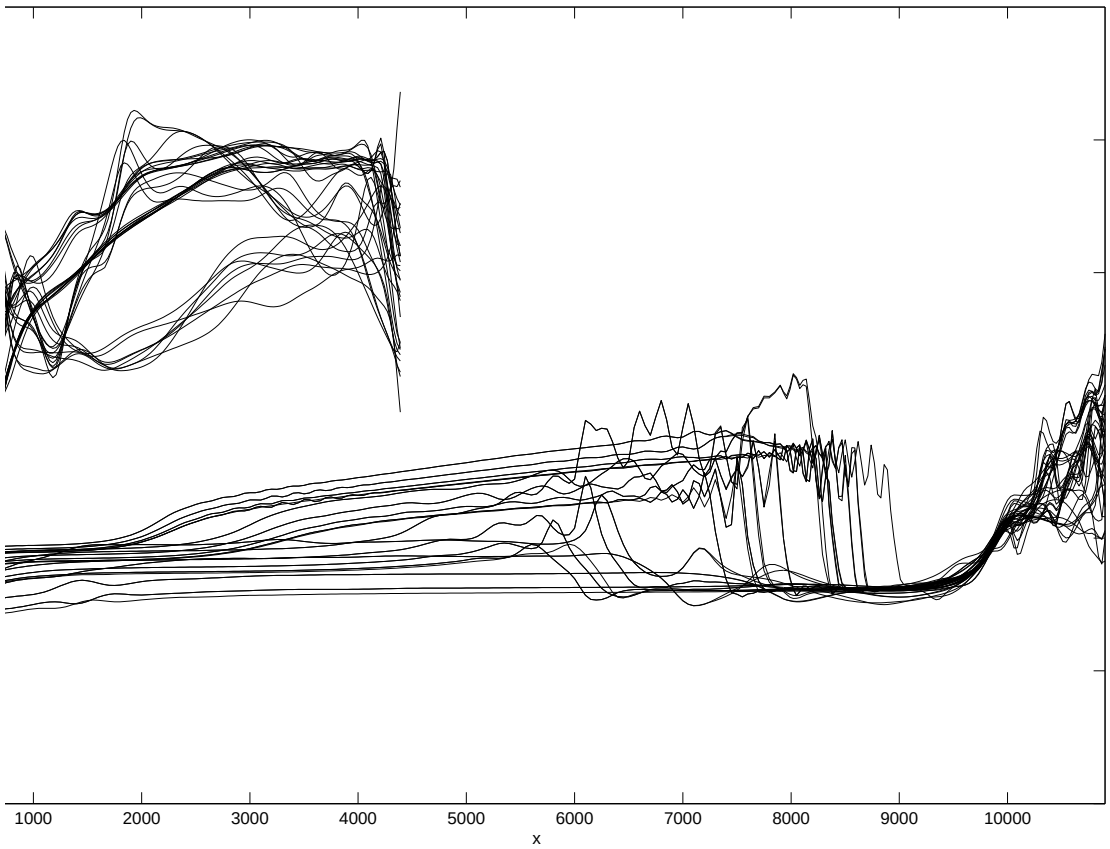

Figure 8.8: Streamwise phase-speed, u_θ, for unsteady modes in session 1 (natural transition, below) and session 4 (by-pass transition, above).

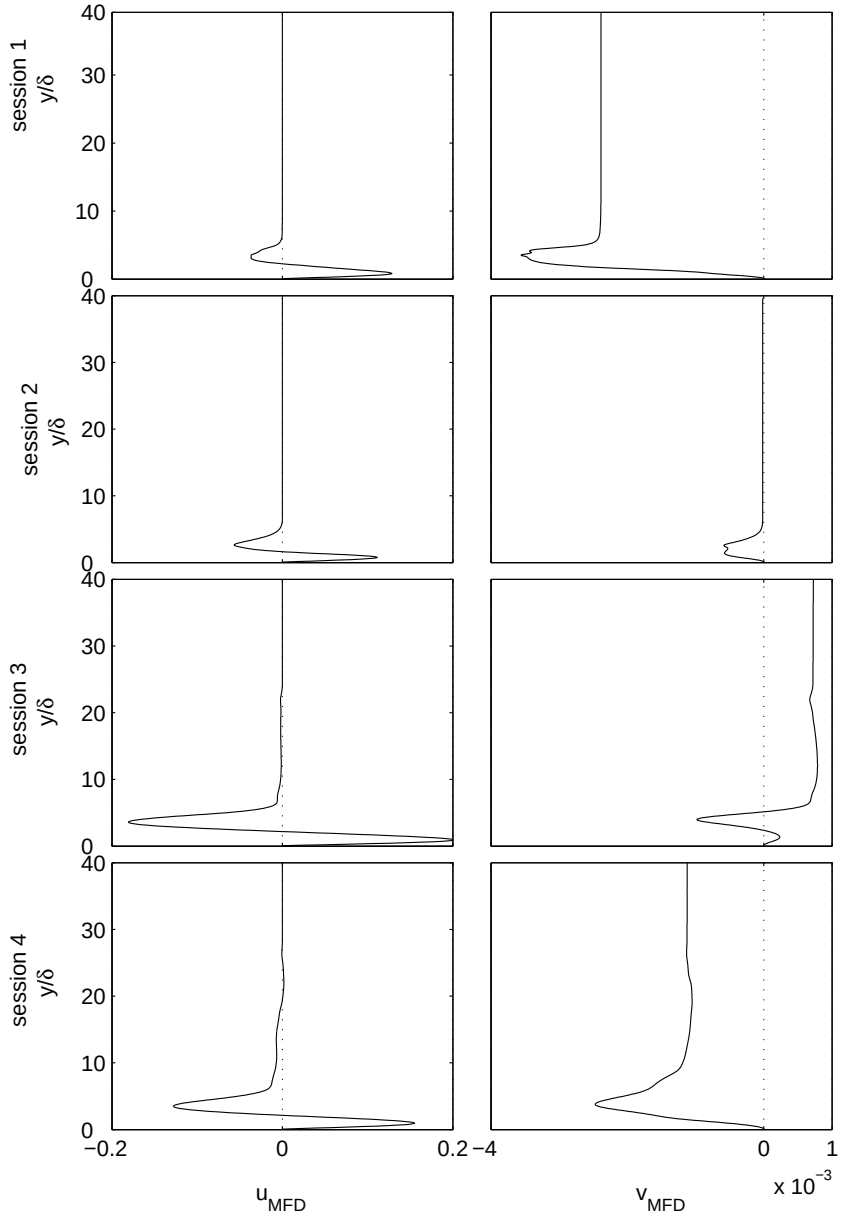

Figure 8.9: MFD-modes at transition stage for session 1–4.

the by-pass transition scenarios (session 3-4) experience an early elevation of the skin friction which is maintained at a level well beyond the laminar level during the nonlinear stage until it rises sharply and continue to rise until the end of the computation. These observations compare qualitatively well with reference, e.g. Chang & Malik (1994), despite that they investigate compressible flat plate boundary layers. The other end of the normal domain is very little affected by the MFD for obvious reasons. The streamwise velocity MFD component vanishes completely for y/δ exceeding 6 in the natural transition sessions 1–2, whereas the streak-dominated bypass scenarios, especially session 4, has an MFD-mode extending far up in the boundary layer. For y/δ larger than 10 the baseflow profile of the streamwise velocity has settled at the free-stream value of unity. Therefore, the appearance of a positive u_{MFD}-component for $19 < y/\delta < 26$

implies a localized super-free-stream mean velocity in this region. The wall normal MFD velocity component is two orders of magnitude lower. The sign of v_{MFD} at the upper end of the normal domain indicates whether the displacement thickness streamwise evolution is larger or smaller than predicted by the Blasius laminar baseflow solution. Fig.8.9 does not enable a conclusive answer. In fact, plot of x versus v_{MFD} for sessions 1–4 would reveal subtle oscillations during the nonlinear stage, but no general pattern appear, although the displacement thickness evolution for the by-pass sessions shows increase during the nonlinear stage in comparison with the laminar evolution.

3D Waves, Physical Space

Evaluation of the results in physical space does not offer the possibility of detecting wave phenomena as mode interaction, phase-coupling, clustering and resonance. In exchange for that it enables the visualization of coherent structures and a general contextualization by the human mind of the physical procession of events contained in the flow. Besides, flow representations in physical space relate better to experimental flow visualizations, thus serving an important purpose of validation. Of the two kinds of displaying the flow none is the better one, rather they complement each other.
On figures 8.11–8.17 are shown the isosurfaces in x-y-z space where the streamwise velocity $u(t = 0) = 0.5U$, i.e. where the u-component of the physical flow equals 50% of the free stream velocity at t=0. The 'virtual snapshot' is taken from above in direction perpendicular to the wall with the light source placed directly over the flow. It's a little like looking at a disturbed water surface at high daylight right from above, except that this is an iso-surface, not a physical surface. Figs.8.11–15 present isosurfaces for the natural transition sesssions 5-9. Dif-

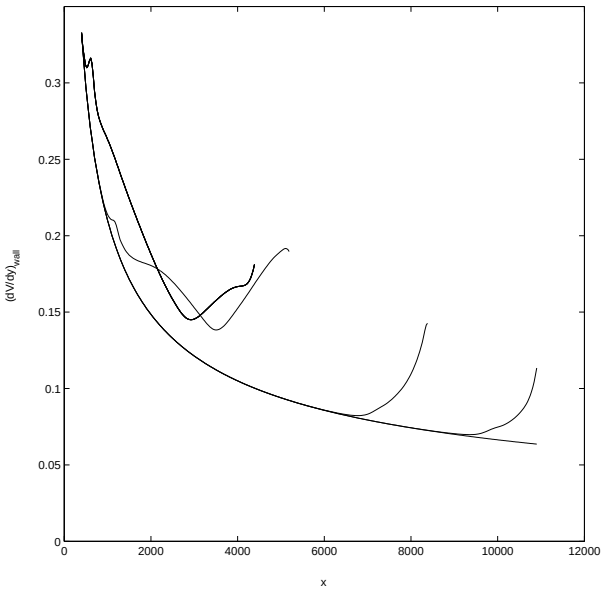

Figure 8.10: Normal gradient of wall-parallel mean-velocity magnitude for sessions 1–4 and undisturbed Blasius baseflow.

fuse light reflections indicate a plane surface due to small perturbation amplitudes. On the other hand, large perturbation amplitudes creates a distinct 3D effect to be observed. In the x-z plane only one spanwise period is shown for better resolution. The largest spanwise wavelength is $\beta_1/2\pi = 399.4$. The x-domain is shown on each figure. All snapshots are for $t = 0$. The general observation is the staggered pattern of low speed momentum which appears as small tilted mountains on the surface. This is the classical H-type instability theoretically found by Herbert & Morkovin (1980). H-type transition a.k.a. sub-fundamental transition is the natural transition that will occur in a low disturbance (modally dominated) environment, as evidenced experimentally by Corke & Mangano (1989). Its characteristic feature is the peak-valley distribution of streamwise velocity in the x-z plane. smoke-visualizations show alternating lines of peaks in a staggered order which creates the peak-valley pattern. The streamwise wavenumber of the streamwise aligned peaks is half that of the dominating TS-wave, hence the name sub-fundamental. According to experimental observations, the final breakdown to turbulence is not violent, preceded by streamwise velocity spikes (impulses of low speed) and then the gradual increase in concentration of high frequency turbulent spot formations. Visual measurements at a peak location, x_{peak}, of the streamwise peak-period, λ_{peak}, in the peak-valley regions of sessions 5-9 (Figs.8.11–15) are presented below and compared with the period of the dominant TS-wave, λ_{TS}. Which TS-mode dominates at $3000 < x < 3400$ for each of the sessions 5-9 is determined from Fig.8.7 to be $(m, n) = (3, 0)$. The experimental and theoretical value of the ratio $\frac{\lambda_{TS}}{\lambda_{peak}}$ is 0.5. This prediction is accurately met by our numerical experiments, even though the initial seed of unsteady modes at the inflow was kept uniform. This confirms suggestions in recent literature that sub-fundamental H-type transition is the natural transition for the Blasius layer in low disturbance environments.

Session	x_{peak}	λ_{TS}	λ_{peak}	Ratio
5	3391	119.2	222.0	0.540
6	3010	107.0	212.4	0.504
7	3014	106.9	209.0	0.512
8	3273	110.8	212.2	0.522
9	3059	136.9	296.3	0.462

The early onset of unsteady three-dimensionality at streamwise positions where the pairwise oblique mode amplitudes still coincide, is explained by counter-phasing of the pairing oblique modes $(\alpha, \pm\beta)$.

The Klebanoff disturbances, though crucial for the peak-valley instability to develop, are not very notable, and heavily superposed by unsteady disturbances. In Fig.8.13 another feature from experimental observations of natural transition has been captured by the nonlinear PSE-method: The small dark objects on the surface for $x \approx 4000$ are very elongated peninsulas of low-speed streamwise momentum protruding up in the boundary layer some 5–10 times higher than the peak-valley normal height difference. Neither their spatial convective, nor their temporal behavior can be depicted from a virtual snapshot: In the transition stage the phase-speeds vary between the modes, so in contrast to the phase-coupled nonlinear stage, the flow features do not simply propagate downstream, but exhibit very irregular oscillations in time and space. Nevertheless, these formations will probably appear as the experimentally reported velocity spikes for a virtual hot-wire placed correctly in the flow. Due to the phase-decoupling of the modes in the transition stage, Figs.8.11–15 only allow us to conclude that for $t = 0$ only session 7 has these very localized far-protruding peninsulas of low-speed momentum lifted into

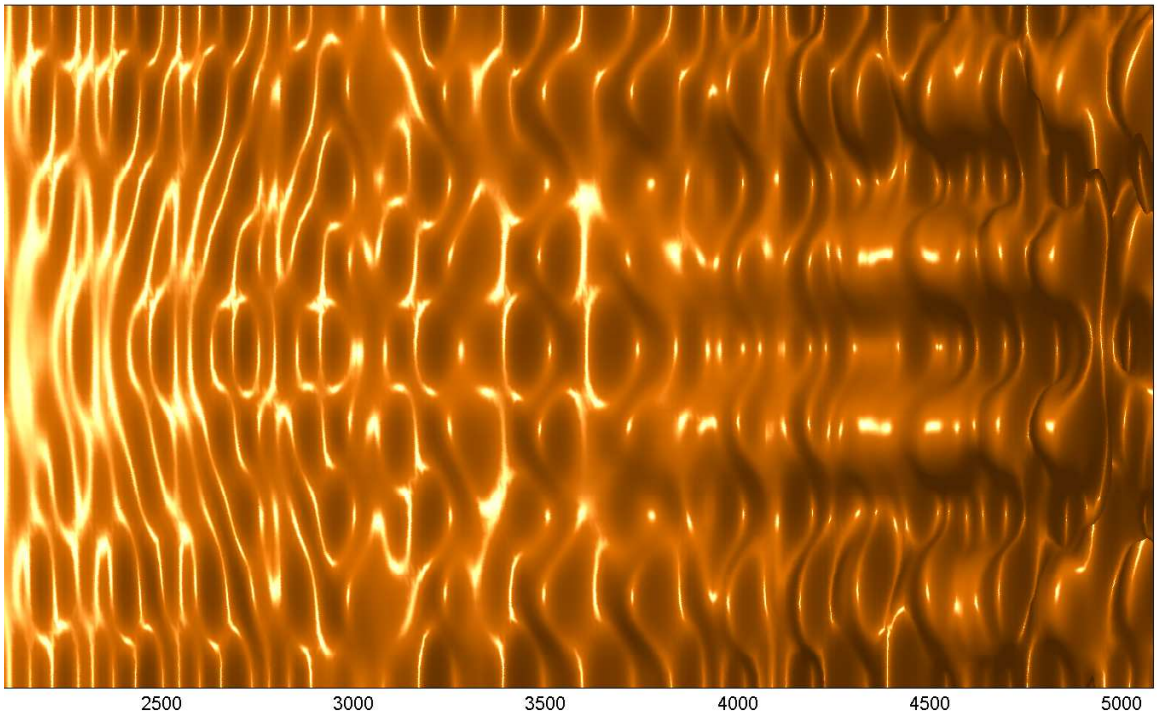

Figure 8.11: Session 5: Natural transition scenario.

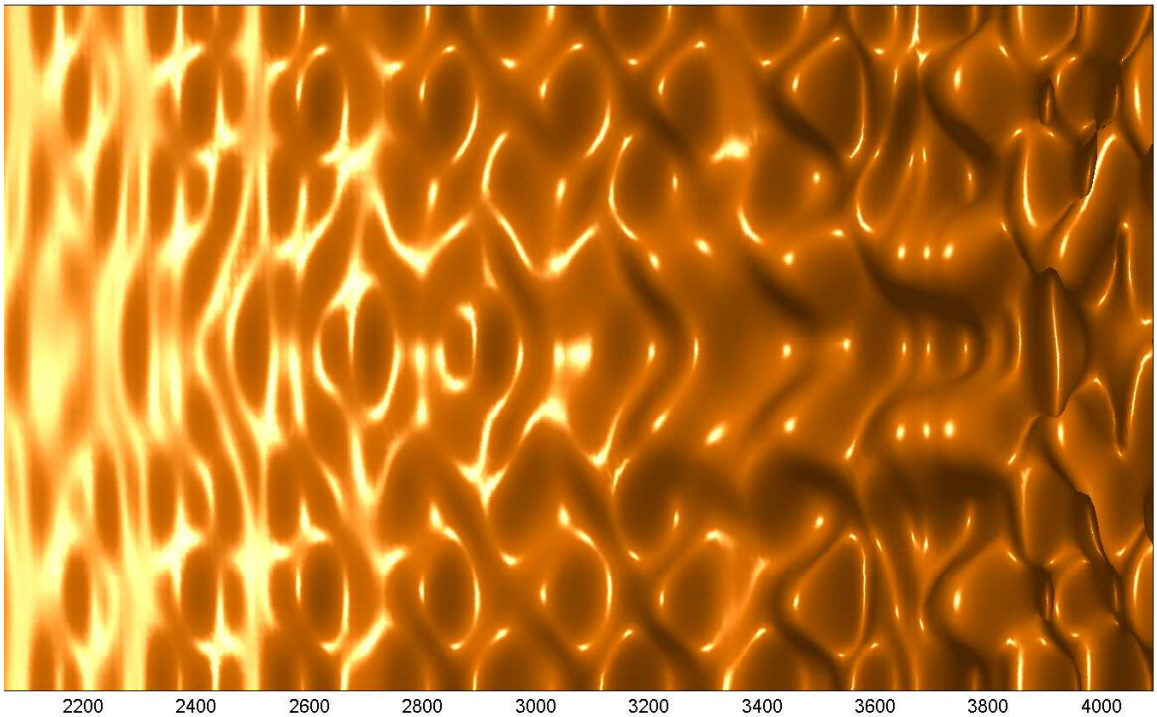

Figure 8.12: Session 6: Natural transition scenario.

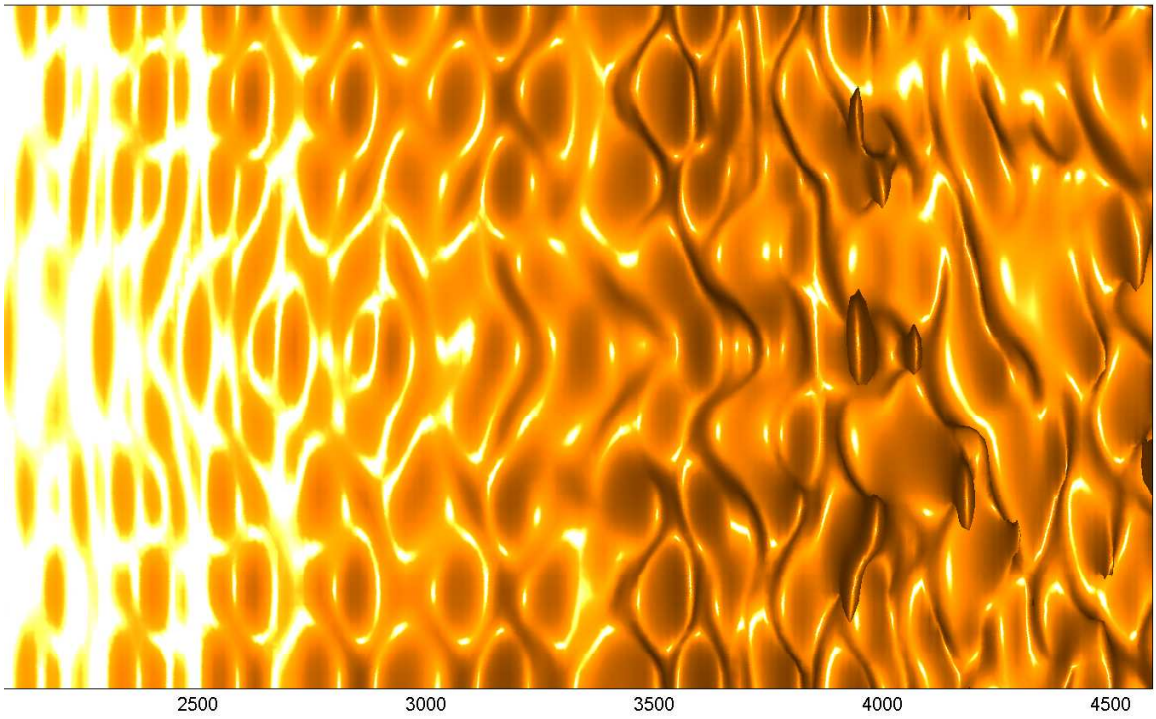

Figure 8.13: Session 7: Natural transition scenario.

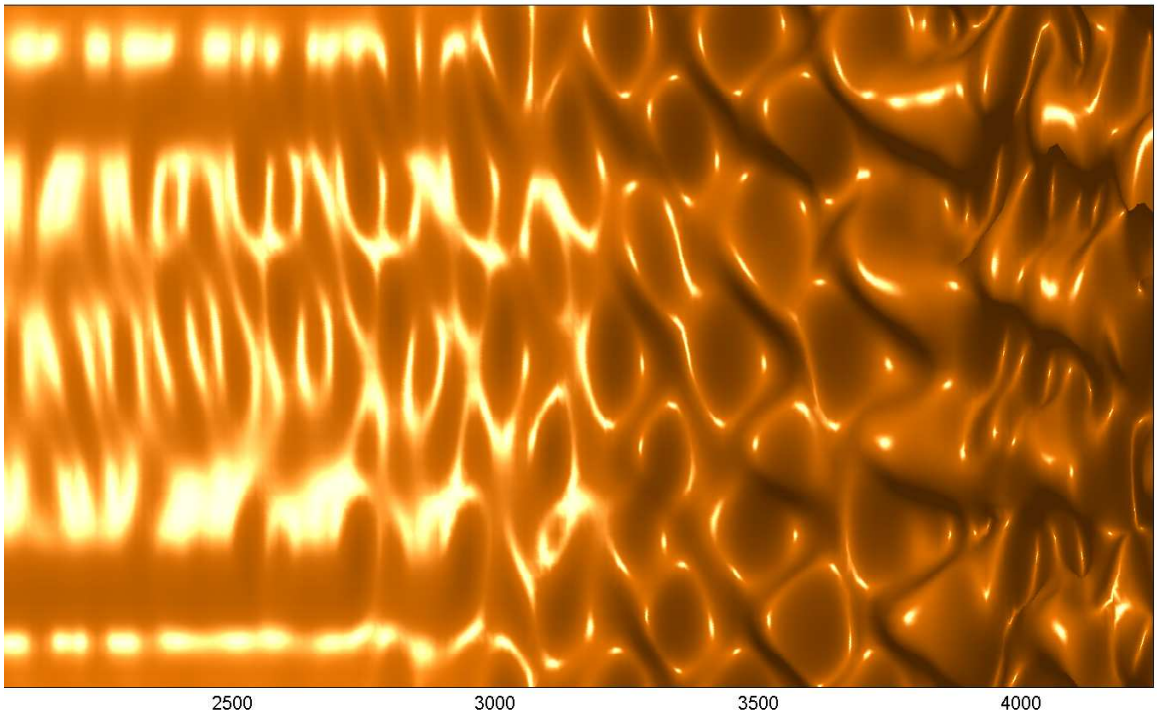

Figure 8.14: Session 8: Natural transition scenario.

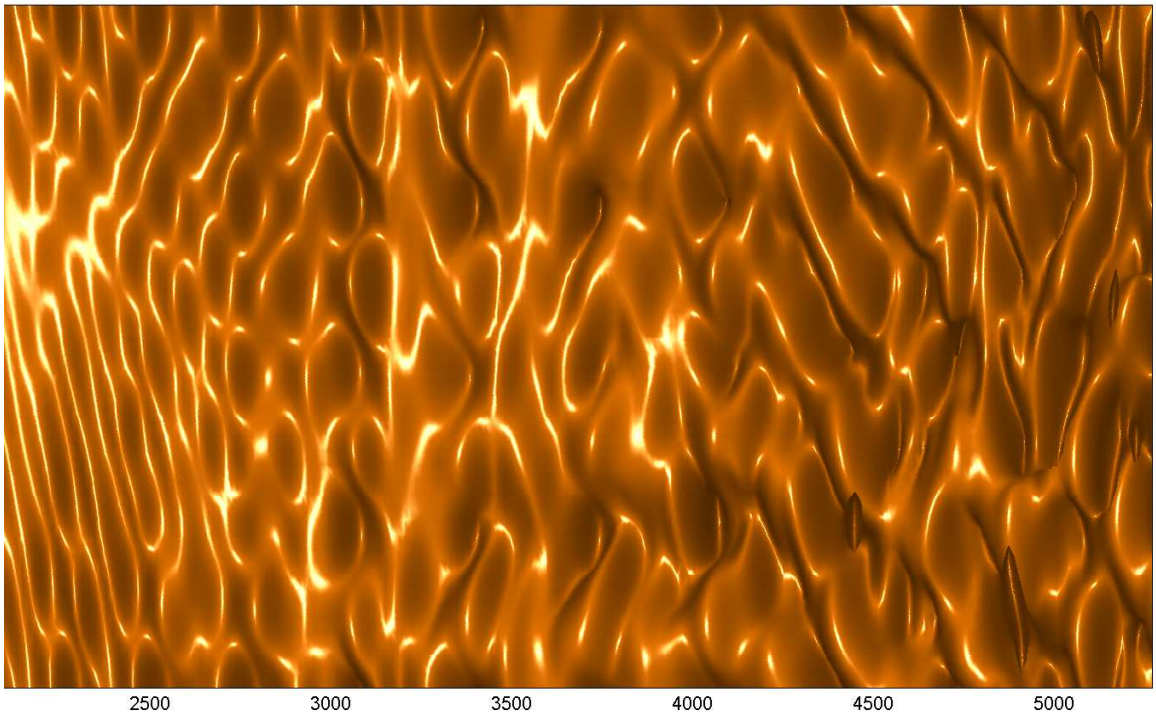

Figure 8.15: Session 9: Natural transition scenario.

the boundary layer at transition. At other positions in the temporal period, this might very well change.

Figs.8.16–17 are the by-pass scenarios, session 3–4. One spanwise period of length 399.4 is shown as it develops in space from the initial point $x_0 = 400$ to the breakdown at transition for $t = 0$. In Fig.8.17 the spanwise phase of the period has been offset by π to position the main feature along the centerline of the domain. The two sessions are very similar, session 4 being the most spectacular due to its higher initial amplitude, and it will receive the attention in the following.

In Fig.8.17 the only reminiscence of influential TS-instability is immediate downstream of the initial line. As it decays prominent Klebanoff modes take over, mode $(0, 4)$ dominating as also displayed by Fig.8.6. between $x = 2500$ and $x = 3000$ a peculiar restructuring of the streaks seems to take place. This is the long-wave oscillation of the streaks noted in fourier space. Towards the end, the 50% isosurface for the u-velocity becomes wiggly under the influence of unsteady perturbations and the computation breaks down. The MFD-mode for this by-pass transition (session 4) extends very far into the flow, see Fig.8.9, which motivates us to search for coherent fluid motion in the upper part of the boundary layer. Figs.8.18–19 show from different angles the same 50% u-isosurface from Fig.8.17 plus a 102% super-free-stream speed u-isosurface. The latter consists of two streamwise columns of accelerated fluid at equal heights symmetrically positioned above the centerline. These high-speed columns gain size in downstream direction and are periodically connected or nearly connected by inter-column bridges of high velocity. Vertical tongues of high speed fluid are lifted up from the columns periodically and alternating between them. These tongues grow farther and farther into the boundary layer as one advances downstream, some loosing connection with the column from

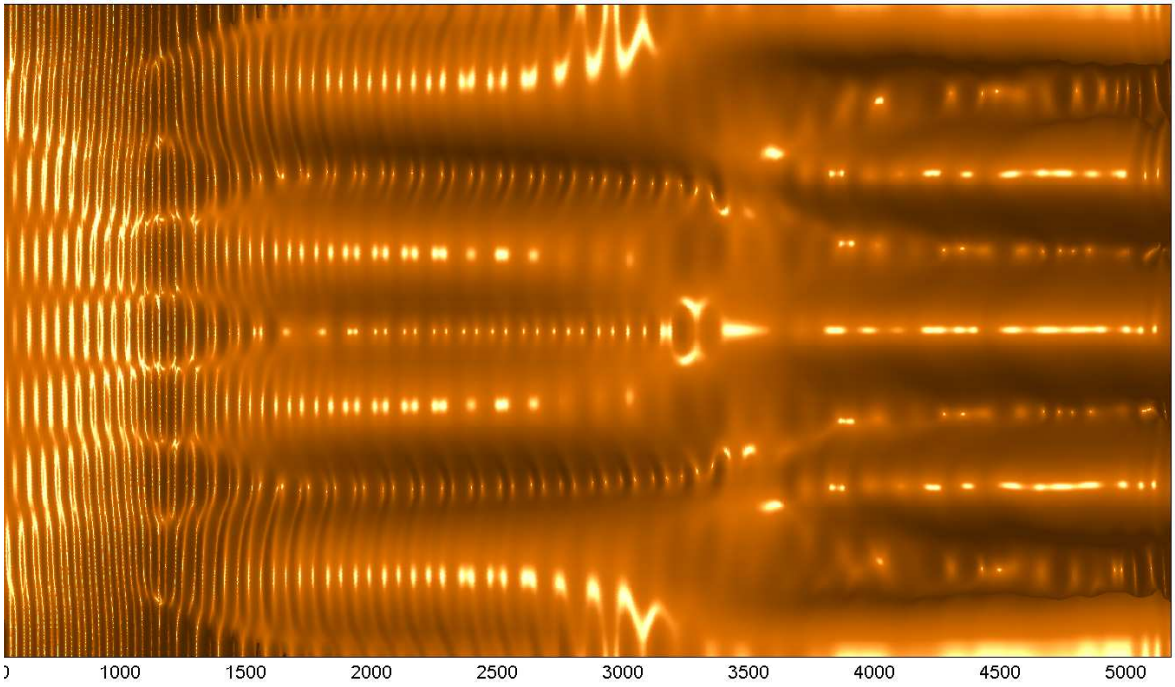

Figure 8.16: Session 3: By-pass transition scenario.

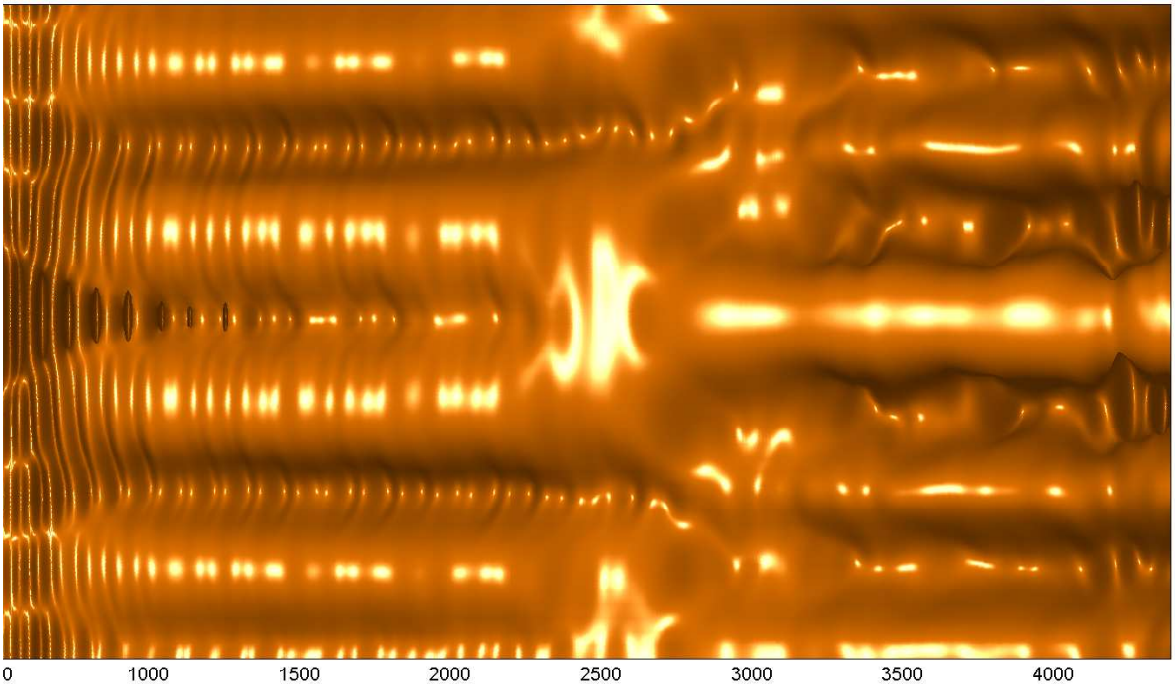

Figure 8.17: Session 4: By-pass transition scenario.

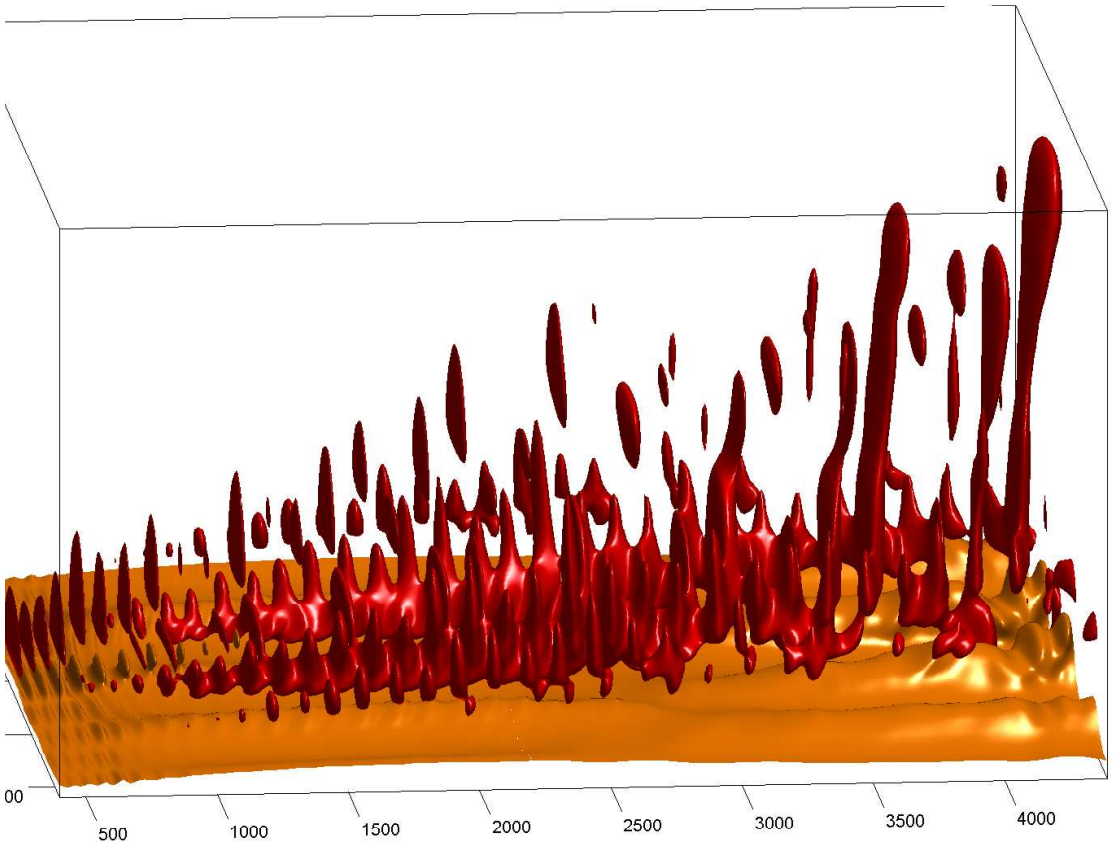

Figure 8.18: Session 4: By-pass transition scenario. Orange and red iso-surfaces are for $U(x, y, z, t = 0) = 0.50 \cdot U$ and $U(x, y, z, t = 0) = 1.02 \cdot U$ respectively.

where they emanated, others maintaining a connected volume of high speed fluid with their respective column of origin. The connected tongues are the most accelerated also. At 110%, the overall structure of the high speed surfaced volume is still apparent (not shown) and volumes of u-velocities in excess of 125% free-stream velocity is present in most downstream part of the columns as well as in the very upper part of the last and most protruding tongue at $x \approx 4200$. Before attempting to explain the observed series of events in the by-pass transition, Fig.8.21 of iso-surfaces for positive and negative normal vorticity of magnitude 0.001 reveals the tongues to be hairpin vortices with accelerated fluid in the middle due to counter-rotation. On Fig.8.20 the colored shades indicate streamwise velocity in the z-y plane at $x = 2000$. The dark red regions mark the columns of accelerated fluid clearly visible at $z \approx 330$ and $z \approx 420$. The streamlines reveal 8 more or less distorted streamwise counter-rotating vortices, where the pair centered about $z \approx 380$ dominates and actually contains the high-speed columns in their upper part. A strong sink in the dividing line between these vortices feeds on the above flow and forces a massive downward motion of fluid between $z \approx 310$ and $z \approx 460$ up to $y \approx 23$ where the natural evolution of the undisturbed Blasius layer gradually takes over. Fluid sources are located on the outer sides of the super-free-stream columns. Sinks and sources mark the streamwise acceleration and deceleration of fluid passing the plane. This correlates well to phase-change of the long-wave spatial oscillation of the Klebanoff modes physically visible on

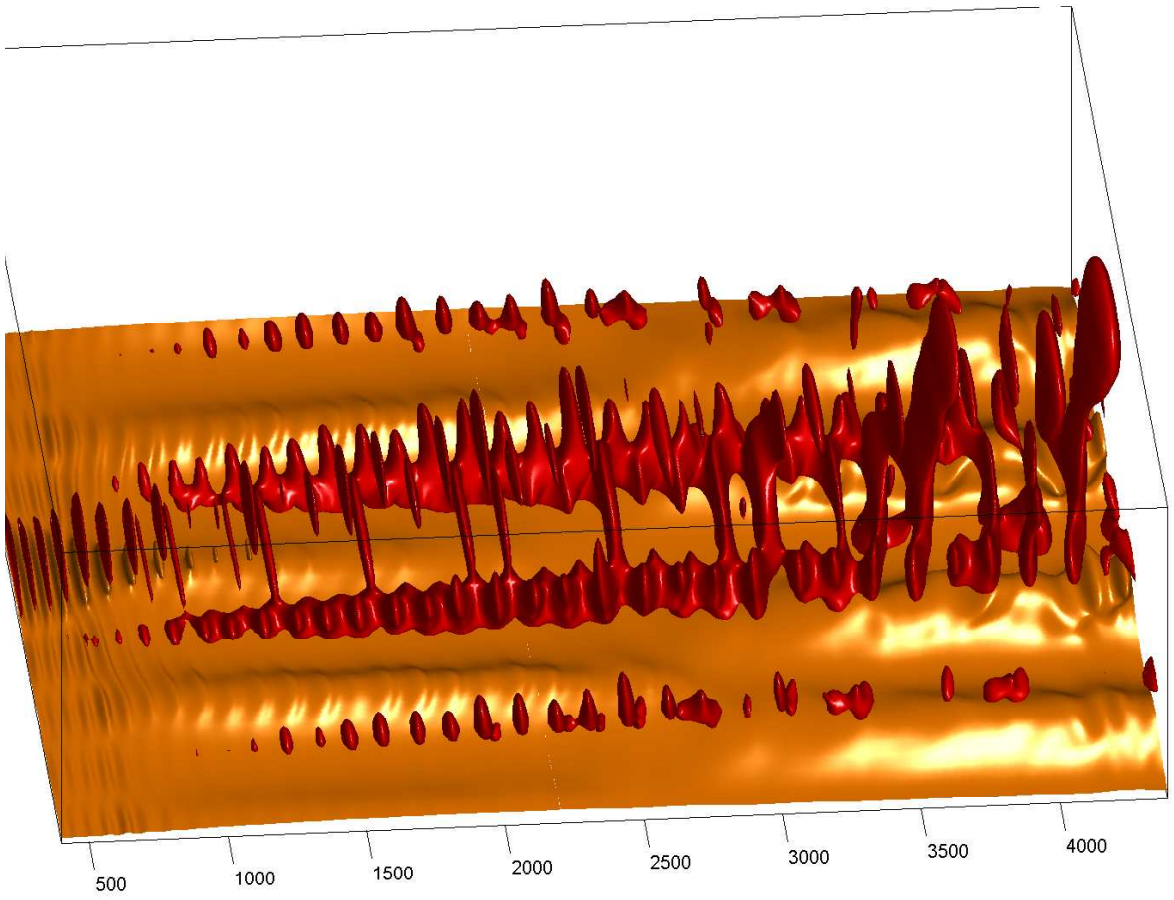

Figure 8.19: Session 4: By-pass transition scenario. Orange and red iso-surfaces are for $U(x, y, z, t = 0) = 0.50 \cdot U$ and $U(x, y, z, t = 0) = 1.02 \cdot U$ respectively.

Fig.8.17 and in fourier space on Fig.8.6. The high-speed columns are clearly nurtured by the outer layer fluid sucked in by the streamwise counter-rotating vortex pair and the streamwise acceleration. At the initial line the four vortex pairs create four high-speed columns of which only a pair of two amplifies downstream. After the Klebanoff phase-change at $x \approx 2500$ this column pair continues to exist, although ejections of high-speed tongues in the upper layer tend to evolve more from the middle space between the columns and less from the columns. This is because most upper layer high-speed fluid is sucked down in the middle part of the spanwise domain (see Fig.8.18), and not as upstream of the Klebanoff phase change, where fluid was sucked down on each side of the center iso-surface ridge of uplifted low-speed momentum.
The unsteady motion is initially dwarfed by the dominating Klebanoff modes. Nevertheless the regular ejections of these tongues of accelerated fluid, that further downstream can be identified as hairpin vortices, seems to be the main role of the TS-waves. The fact that they release modal energy into the upper boundary layer, where it is passively convected downstream, might be the reason why these modes are so effectively damped: They break apart. The key elements for these vorticity ejections to occur are strong streamwise counter-rotating streaks (Klebanoff modes) and minor TS-instabilities, which must deviate the paired vorticity contained in the streaks enough to release portions of it in the upward normal direction.

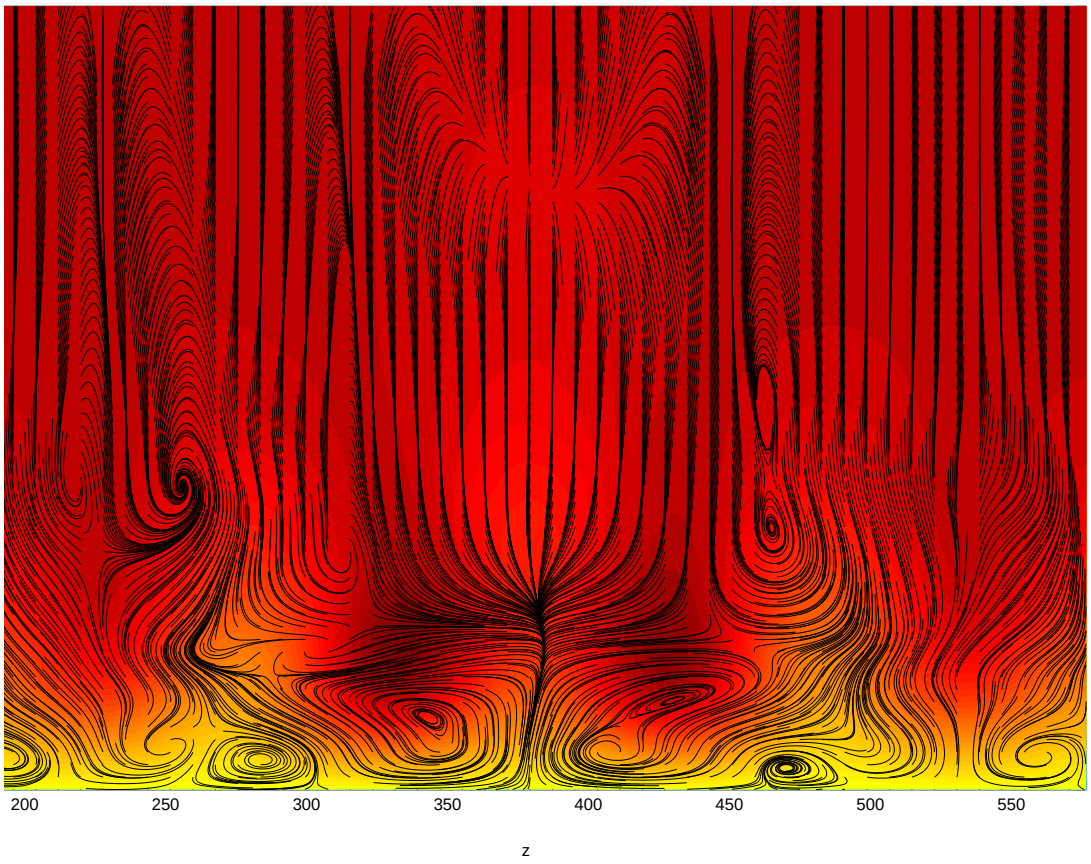

Figure 8.20: Session 4: Stream trajectories in yz-plane at x=2000 and t=0.

The computation halts before the end of the transition stage. The hairpin scenario is well known from literature, see e.g Haidari & Smith (1994), Asai & Nishioka (1995). The top of the hairpin vortex, its 'head', will start to bend forward as it grows. Finally the head will induce high frequency disturbances, and the whole vortex will break down. At supercritical Reynolds number for the flat plate, the break down is most likely to initiate turbulence. A vague sign of imminent head tilting can be observed on Fig.8.21. The purely numerical departure mode observed the final marching steps of the PSE procedure, could indicate that the outer boundary conditions imposed at 40δ is not sufficient to reach an undisturbed state. Increasing this number might extend the computation even further.

3D Waves, Error Assessment

The error introduced by distributing the FFT'ed nonlinear terms on the corresponding spanwise-temporal modes, is negligible when the streamwise wavenumbers vary linearly with the spanwise-temporal wavenumbers. When this is not the case, RHS nonlinear forcing will be applied to modes with streamwise wavenumbers that deviate from the streamwise wavenumbers of the forcing terms. This deviation is easy to quantify as the relative error between the computed streamwise wavenumbers in 3D fourier space for all modes, and the best planar fit to

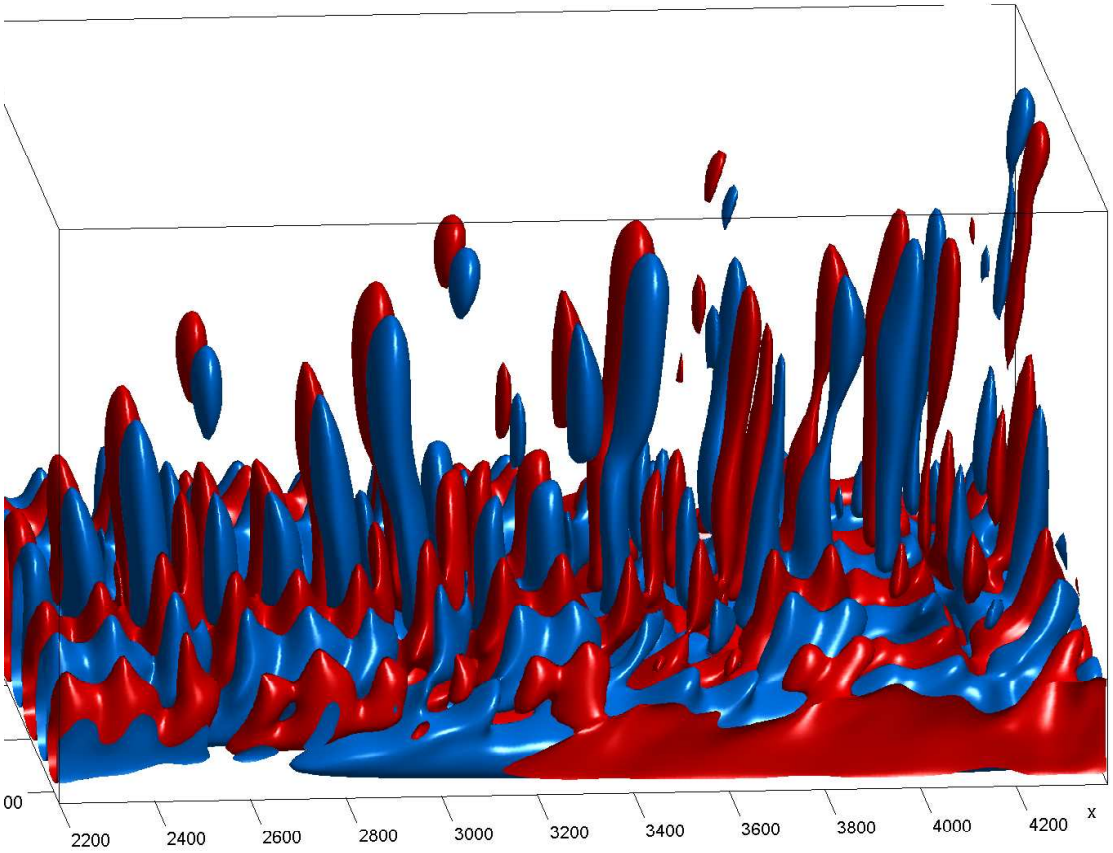

Figure 8.21: Session 4: By-pass transition scenario. Wall-normal vorticity iso-surface, $\omega_y = \pm 0.001$.

these streamwise wavenumbers. The table below present the results for sessions 1–9.

Session	Transition type	$x = 1000$ $max(abs(\epsilon_{rel}))$	$mean(abs(\epsilon_{rel}))$	$x = x_{end} - 100$ $max(abs(\epsilon_{rel}))$	$mean(abs(\epsilon_{rel}))$
1	Natural	13.3	2.1	19.7	7.0
2	Natural	16.7	1.9	21.3	6.6
3	By-pass	18.6	4.6	24.1	6.2
4	By-pass	13.8	2.9	21.0	5.1
5	Natural	25.2	3.7	37.9	5.8
6	Natural	17.4	2.0	33.0	6.0
7	Natural	17.9	2.0	32.4	4.7
8	Natural	21.5	3.3	32.9	5.3
9	Natural	13.7	3.1	31.5	5.5

The percentage error is computed at $x = 1000$ and at $x = x_{end} - 100$. The overall assumption of modal interaction of modes in a 3D fourier plane is good in all sessions, also in the highly distorted areas preceding the failure to march the solution further at x_{end}. The maximum deviations are somewhat high, but still acceptable.

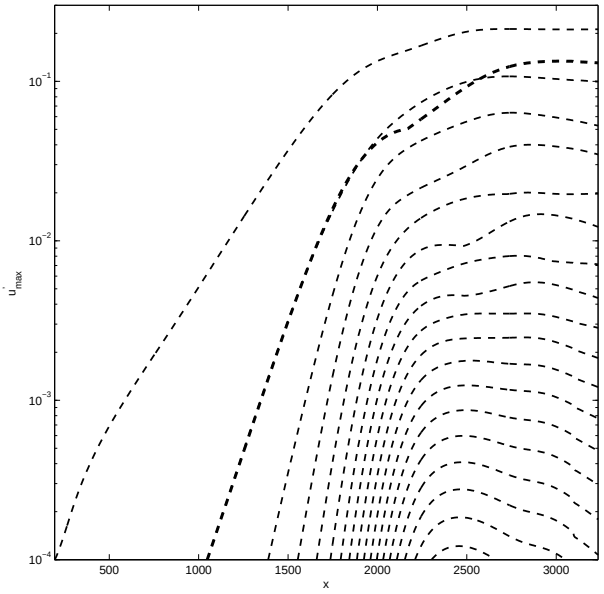

Figure 8.22: Nonlinear evolution of disturbances of initial primary mode amplitude $1.0 \cdot 10^{-4}$, the higher harmonics and the MFD (bold dotted line).

8.2 The DLR Experiment

The nonlinear effects of the DLR swept plate flow will be illustrated through a series of examples differing through the choice of inflow conditions at x_0. Focus will be on the development of mode clusters and their implications on the physical flow. The nondimensionalized domain corresponds to the $0.5m$ chord from $x_0^* = 0.01m$ to the trailing edge at $0.5m$. $Re_{x0} = 194.3$

Steady Vortices

The swept plate at baseflow conditions unchanged from the treatment in the chapter of linear PSE, is susceptible to steady three-dimensional co-rotating crossflow vortices. The isolated nonlinear interaction between these steady modes without the influence of unsteady waves is investigated by considering the modes along the n-axis for $m = 0$ in Fig.8.2. The Fourier space included is (m, n)=$(0, 0)$, $(0, 1)$ ... $(0, 32)$ with $\beta_1 = 0.0808$, as found from the parameter study in the linear results chapter. The negative part of the n-axis is implicitly contained as complex conjugate counterparts for the included modes on the positive part of the n-axis, since the physical flow is real. The primary disturbance is the unstable $(0, 1)$ stationary crossflow mode, initiated at streamwise velocity amplitude $1.0 \cdot 10^{-4}$. The background noise level at which all other modes are initiated is $1.0 \cdot 10^{-6}$. $\Delta x = 5$. Infinity boundary conditions are imposed at $y_\infty = 40\delta(x)$ and the normal domain consists of 400 non-uniformly distributed mesh points. These settings, except for the inflow amplitudes, are kept constant through all swept plate sessions. As one observes on Fig.8.22 the linear prediction of the maximum streamwise velocity amplitude, u'_{max}, is followed by the primary mode until it gradually saturates at 21%. The higher modes $(0, 2)$, $(0, 3)$ etc, are induced succesively from nonlinear interaction, but do not

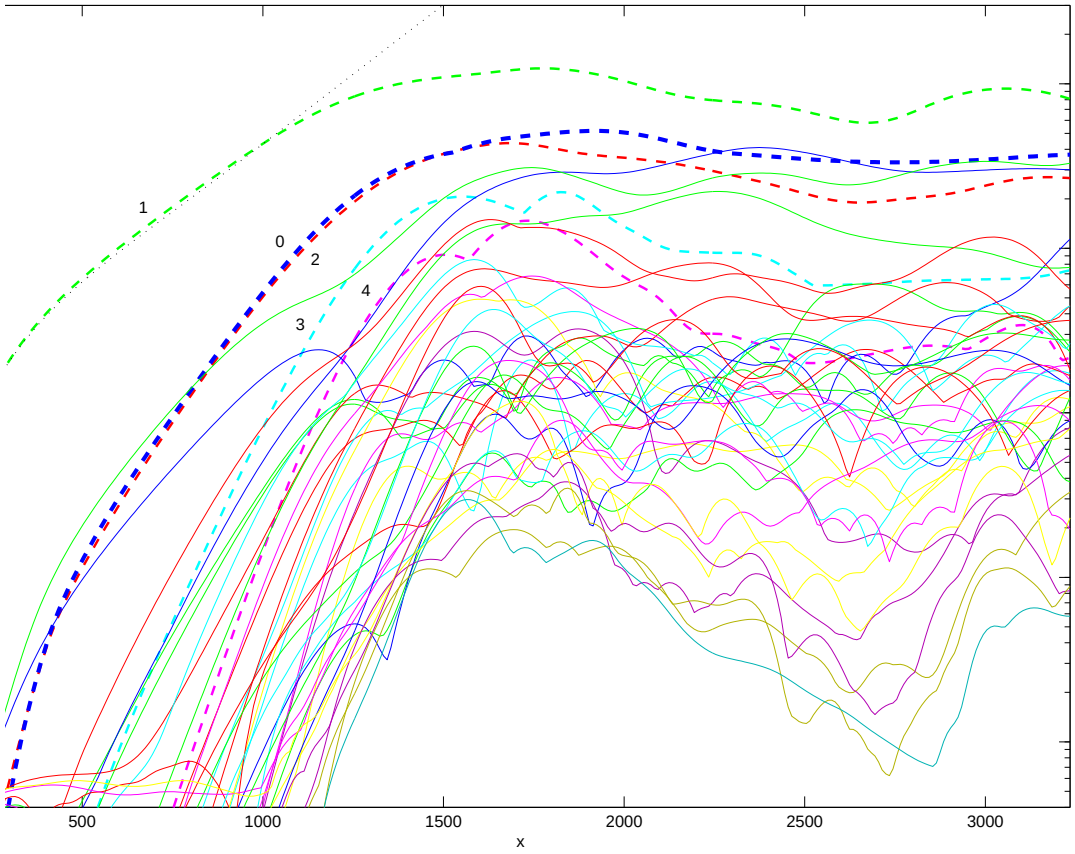

Figure 8.23: Session 1: Dominant crossflow vortices at low primary mode initial amplitude $1.0 \cdot 10^{-3}$. Dotted lines denote the steady vortices, the thick dotted line is the MFD mode. Annotations 0-4 refer to the value of n in fourier space for the steady disturbances.

encounter any instability mechanism of their own. The predominant cascading of modal energy from low to higher wavenumbers is a characteristic of most instability mechanisms. The lack of stronger instability mechanisms is a consequence of neglecting all temporal instabilities. This testcase is in perfect agreement with the similar one considered by Stolte (1999) including the modes $(0, 0)$, $(0, 1)$ ... $(0, 16)$, which is still sufficient, although the introduction of initial modes is different. His use of a local non-parallel method leads to a transient response immediately downstream of x_0, whereas our use of the frozen coefficient pseudo-marching technique seems to give a smoother introduction of modes. Notice also how the highest modes on Fig.8.22 are damped towards the end. This precipitates a long-wave spatial oscillation, somewhat like the one encountered for the Klebanoff modes in the Blasius testcase. Stolte pursued the phenomenon by pseudo-marching the solution at fixed streamwise points, and attributed the behavior to the existence of a spatial Hopf-bifurcation beyond a certain streamwise position. The nonlinearly perturbed high-amplitude steady saturated state with regions of pronounced shear has motivated the hydrodynamic instability community to investigate its receptivity properties to high-frequency modes. This task is so far performed only by use of Floquet

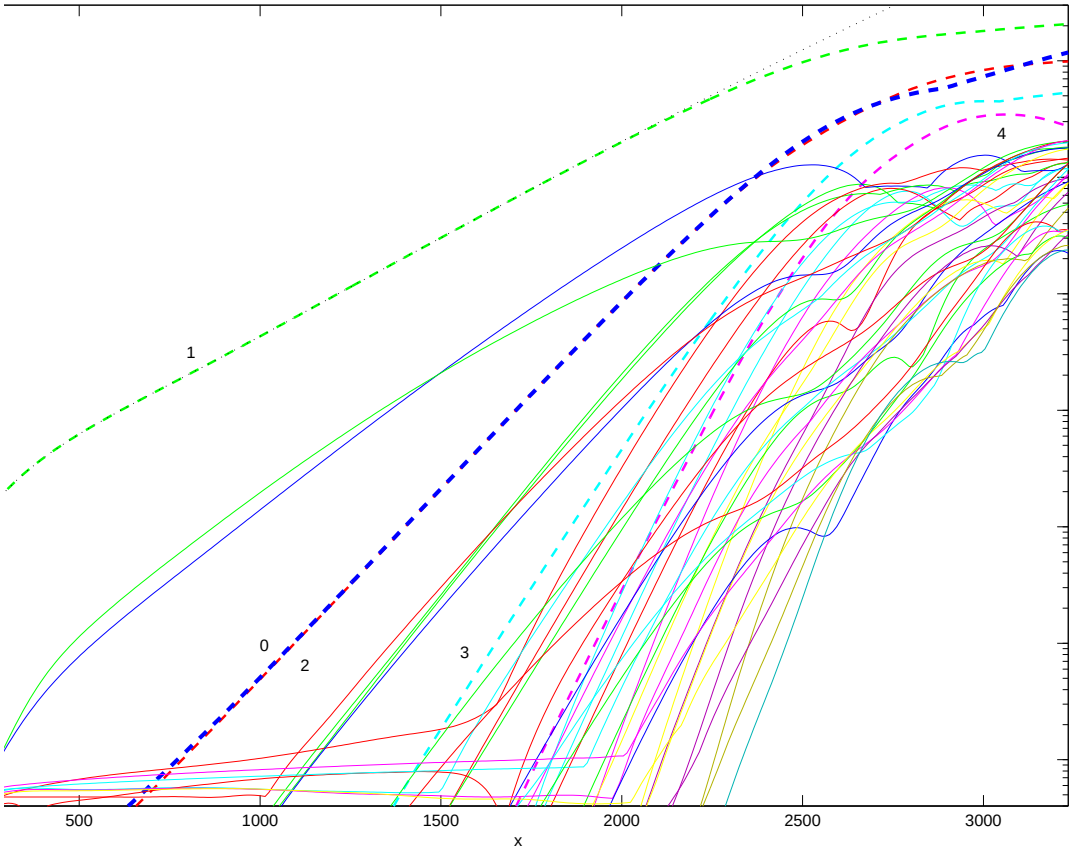

Figure 8.24: Session 2: Dominant crossflow vortices at very low primary mode initial amplitude $1.0 \cdot 10^{-5}$. For lines and annotations, see Fig.8.23.

theory, see e.g. Herbert (1988), Stolte (1999). The possibility of using PSE for the task appears attractive, but would lead to a huge number of modes. The implications are briefly discussed later in this chapter.

Fourier Space

As discovered in the preceding chapter, the DLR swept plate boundary layer flow is unstable to stationary crossflow vortices as well as traveling waves. Thus, inclusion of both makes for realistic initial conditions. Six sessions will be demonstrated, all of which have rather low initial amplitudes, thereby excluding by-pass transition scenarios. Experimental evidence, Müller (1990), leads us to anticipate the downstream dominant perturbations to depend on the initial ratio between free-stream turbulence/perturbation and surface roughness, as well as the magnitudes of both. This has been confirmed numerically by DNS, Wagner (1992), Müller (1995), by Large-eddy simulation, Huai et al. (1999), and by earlier PSE studies, Malik et al. (1994), Bertolotti (1996), Stolte (1999). Our sessions are:

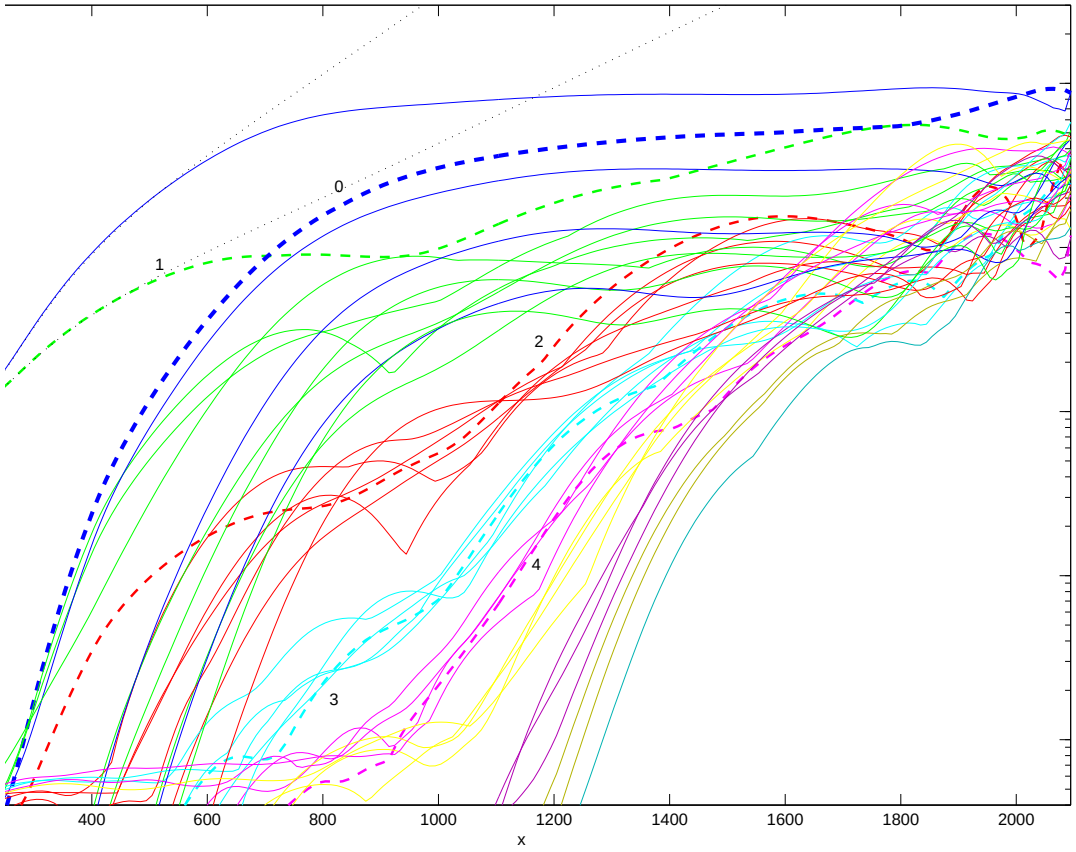

Figure 8.25: Session 3: Co-dominant crossflow vortices and unsteady waves at low primary mode initial amplitude $1.0 \cdot 10^{-3}$. For lines and annotations, see Fig.8.23.

- Session 1-2:
  Stationary vortex dominance at inflow for low and very low initial amplitudes.

- Session 3-4:
  Stationary vortex and travelling wave co-dominance at inflow for low and very low initial amplitudes.

- Session 5-6:
  Travelling wave dominance at inflow for low and very low initial amplitudes.

The reason for the engineering interest in crossflow instabilities is its occurrence on swept wings at sonic, transonic and supersonic conditions. At free flight the natural noise level is low, which explains our choice of low initial amplitudes for the nonlinear PSE-method. For all sessions 1-6 the primary modes are $(0, 1)$ and $(1, 1)$. In accordance with our previous findings from linear PSE, we set $\omega_1 = 0.00689$.
Before commenting session 1 on Fig.8.23 the employed colors call for a few words. The modes are colored in clusters, for reasons that will become apparent. The location of these clusters in the (m, n) fourier space is presented on the right drawing of Fig.8.29. For clarity the upper

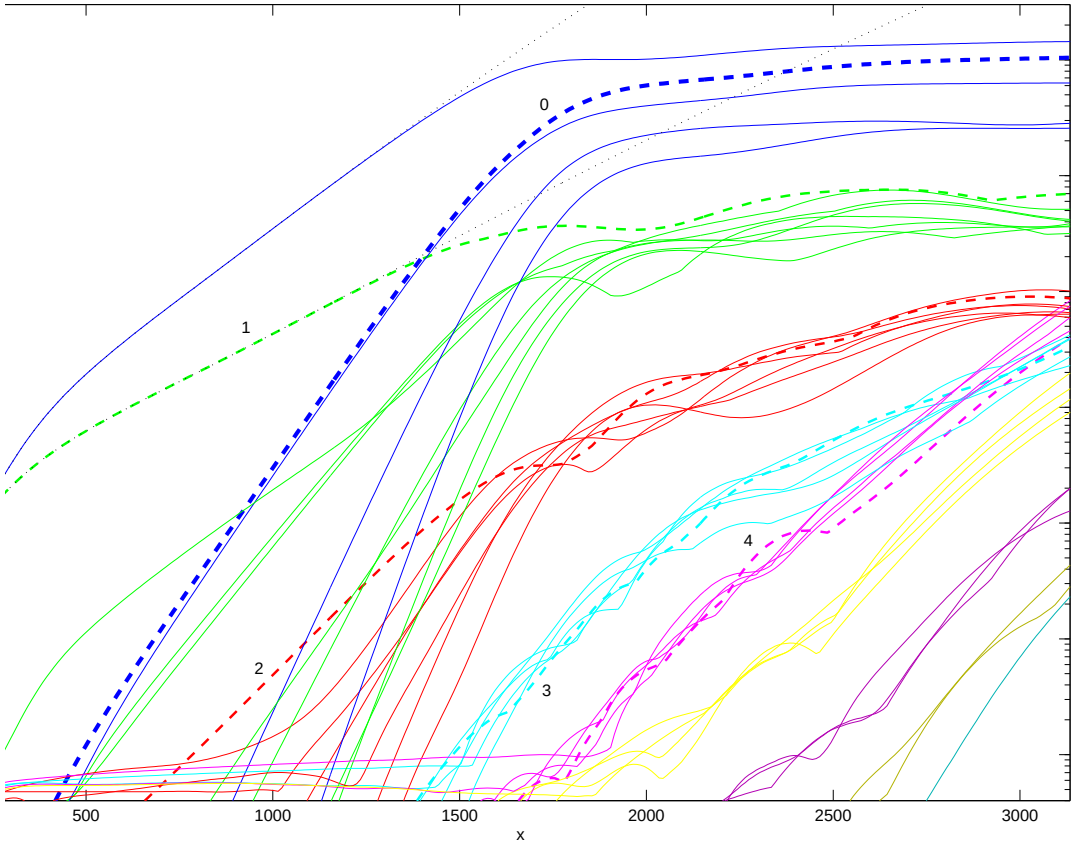

Figure 8.26: Session 4: Co-dominant crossflow vortices and unsteady waves at very low primary mode initial amplitude $1.0 \cdot 10^{-5}$. For lines and annotations, see Fig.8.23.

left triangular part of the domain has been relocated to their physically identical but complex conjugate position in the mirrored lower left part, in order to highlight the alignment of these clusters. Fig.8.23 shows the initial linear growth of the primary vortex, its saturation at 12% for $x = 1774$, and slightly oscillatory evolution towards the end of the plate. We recall our linear PSE result that the unstable wave $(1, 1)$ exhibits larger linear growth rates than the vortex. Nevertheless its growth is suppressed by nonlinear forcing and it peaks substantially lower than the vortex. The tendency for the higher harmonics are similar. The waves are suppressed for the benefit of the vortices. Clearly the modes do not cluster according to colors or in any other way. Due to high amplitudes the dominant line of interaction in fourier space is $m = 0$, i.e the stationary crossflow vortices.

A reduction of the initial amplitudes by two orders of magnitude leads to another scenario. Session 2 on Fig.8.24 once again shows unsteady suppression by the steady vortices, and even clearer. Note how the delayed saturation, caused by lower initial disturbance, leads to higher amplitudes of the vortex that grows monotonically to 20% of the free-stream magnitude at the end of the plate. Anticipating the physical space visualizations, the reason for this seems to be the better alignment of the crossflow vortices with the undisturbed free-stream before saturation, which causes stronger suppression of competing modes or mode clusters. The steady

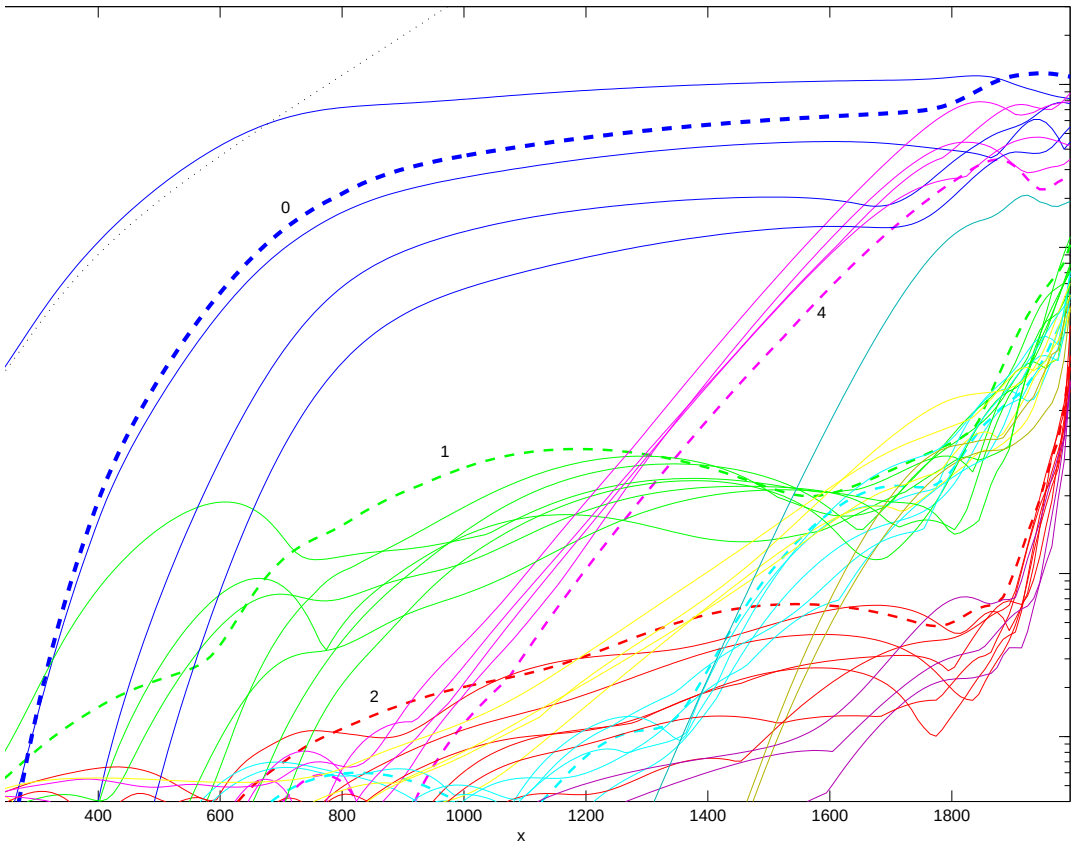

Figure 8.27: Session 5: Dominant unsteady waves at low primary mode initial amplitude $1.0 \cdot 10^{-3}$. For lines and annotations, see Fig.8.23.

modes do not cluster, but form the dominant line of nonlinear interaction. The unsteady modes don't either, but narrow their amplitude magnitudes at the outflow of the domain, displaying increased modal attraction.
Session 3 on Fig.8.25 of co-dominating wave/vortex interaction offers a different picture. The wave gains dominance due to its higher linear growth, saturates and peaks at 9.4% for $x = 1854$. A few observations: First, the clustering of modes according to colors. The dominant cluster, although scattered, is the blue one consisting of the MFD $(0, 0)$ mode, the primary $(1, 1)$ mode and the higher harmonics $(2, 2)$, $(3, 3)$ etc. As for the by-pass transitions in the Blasius testcase, the non-dominant clusters align in fourier space with the dominant one. Second, the repeated co-alignment of clusters leads to a capturing of the steady modes, the semibold dotted lines, in different clusters with one crossflow vortex mode in each. In other words, the steady modes are disrupted from one another with no or very little modal attraction between them. This excludes them from gaining the dominant line of interaction. The computation ends prematurely before the end of the plate at $x = 2194$ due to fast spectral broadening in the saturated nonlinear stage.

A two-decade lowering of initial amplitudes has similar effects as for the crossflow dominated sessions: The dominating mode peaks higher (14%), the dominating cluster is tighter bundled and the suppression of non-dominant clusters is stronger. Fig.8.26 is the natural scenario for

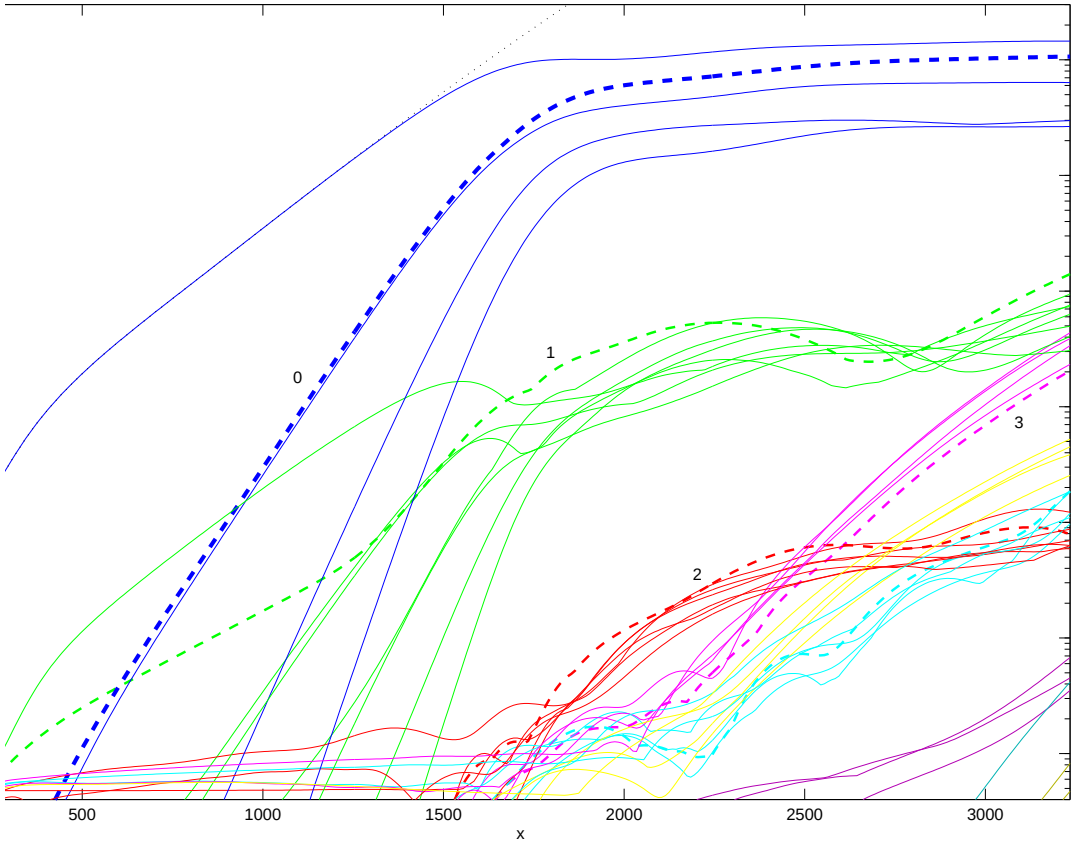

Figure 8.28: Session 6: Dominant unsteady waves at very low primary mode initial amplitude $1.0 \cdot 10^{-5}$. For lines and annotations, see Fig.8.23.

swept plate boundary layers in very quiet environments. The natural selection of modes favors the most linearly unstable travelling wave mode $(1, 1)$, and the pattern of clusters arrange accordingly. The transition stage, as seen on Fig.8.25 follows that of spectral broadening as all modes grow beyond approximately $u'_{max} > 1\%$ where nonlinearity starts to govern the modes. The last two sessions 5-6 are heavily dominated by travelling waves. The effect of later saturation is repeated: 11% for the the low initial amplitude session 5 versus 14% for the very low initial amplitude session 6. Surprisingly the very regular pattern of mode clusters from sessions 3-4 is not encountered. The clusters will form, but not according to the cascading recipe, where the dominant cluster feeds the next dominant cluster and so on. Rather than that a distinct growth of the cluster containing the steady vortex $(0, 4)$ especially in session 5 indicates a more complex mechanism. This session also ends prematurely when that cluster grows beyond the nonlinear threshold, $u'_{max} \approx 1\%$, interacts mutually with the dominant cluster for $x > 1700$, and brings lower energy clusters into strongly amplified resonance.

The observations of wave suppression, the effect of early saturation on the peak maximum streamwise velocity amplitude and the general modal histories of session 1-6 agree very well with the findings of Stolte (1999). As for the steady vortex example the only notable discrepancy is at the inflow, where our use of the frozen coefficients method, leads to a non-transient

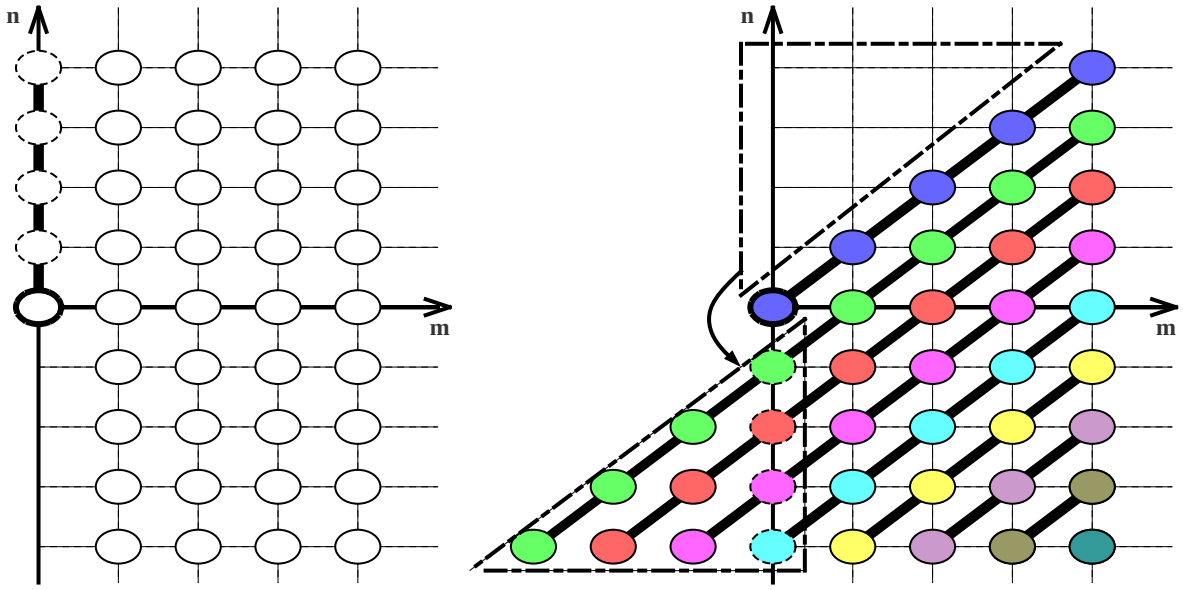

Figure 8.29: The thick straight lines connecting some modes in the discrete Fourier domain mark possible directions of dominating modal interaction in the DLR swept flow. Left: Dominating line of interaction for stationary vortex dominated transition. Right: Dominating lines of interaction for travelling vortex dominated transition. Note the color code used for the interacting lines (clusters) used for Fig.8.23-28

introduction of modes.

Physical Space

The virtual snapshots, Fig.8.30–32, for $t = 0$ of sessions 1, 3 and 5 are aligned with the free stream and thus rotated $\varphi_\infty = 42.5^o$ with respect to the cartesian reference. To ease comparison with fourier space results, the original cartesian x-axis is maintained on the figures. In the rotated spanwise direction slightly more than one period, $(2\pi/\beta_1)\sqrt{1+\sin^2\varphi_\infty} = 93.8$, is included. Common for all snapshots is the initial constant phase alignment of wave/vortices perpendicular to the free stream, and its downstream gradual alignment with the free stream. This is caused by the non-zero spanwise velocity profile of the baseflow in the rotated cartesian reference aligned with the free stream. For the stationary crossflow dominated session 1, the dominating mode $(0, 1)$ will not move in time. The higher wavenumber modes that superpose the flow downstream of $x = 2000$ are the unsteady modes $(1, 2)$ and $(2, 2)$ with phases propagating upstream at a skew angle in time. The dominating mode of Figs.8.31–32 is the primary unsteady mode $(1, 1)$, also with upstream propagating phases. In the hybrid session 3 the steady crossflow vortex $(0, 1)$ becomes visible downstream of $x = 600$. The onset of co-dominant higher wavenumber modes leading the flow into the transition stage and early computational break down are of different origin. For session 3 practically all modes come into play in the end with phases propagating in random directions. For session 5 the high wavenumber modes emerging downstream of $x = 1400$ are all from the cluster of modes $(0, 3)$, $(1, 4)$, $(1, -2)$, $(2, -1)$, $(3, 0)$ and $(4, 1)$ most of them propagating the constant phase lines in downstream di-

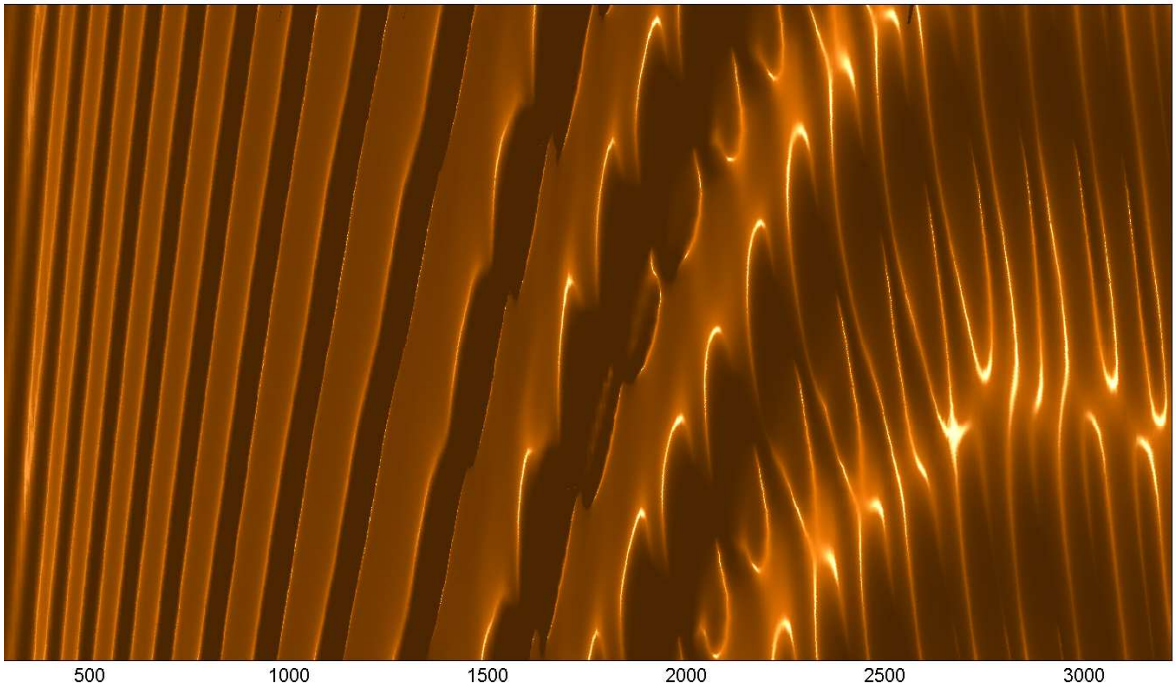

Figure 8.30: Session 1: Stationary vortex dominated transition. Snapshot aligned with free stream.

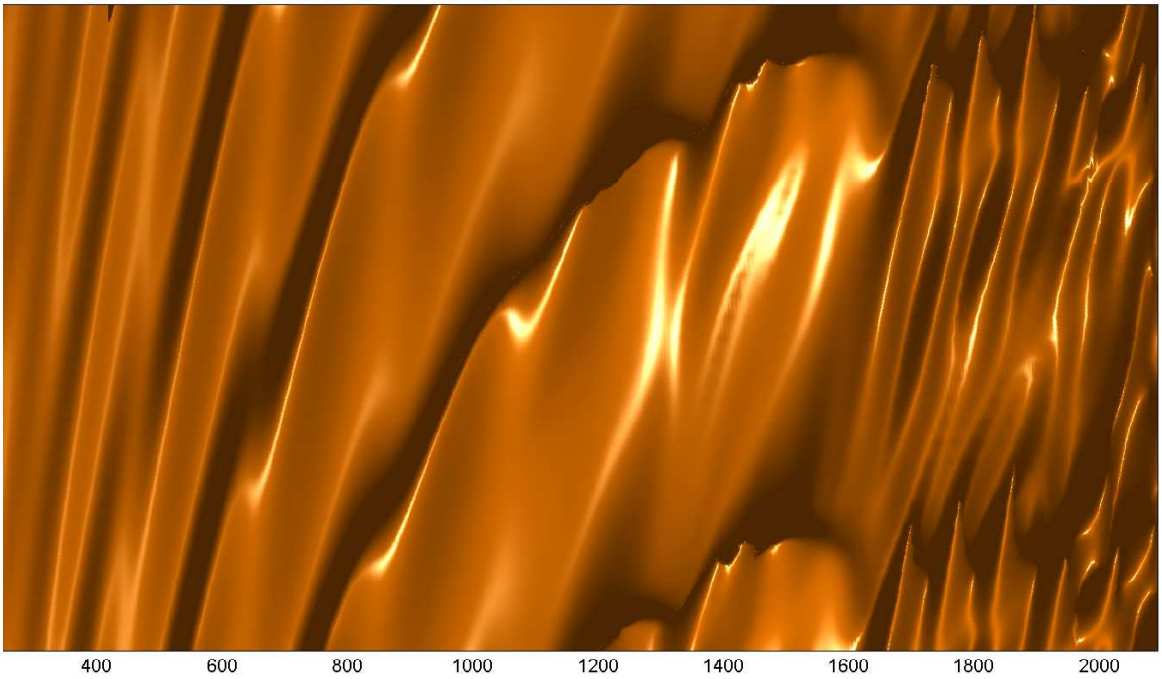

Figure 8.31: Session 3: Vortex/wave co-dominated transition. Snapshot aligned with free stream.

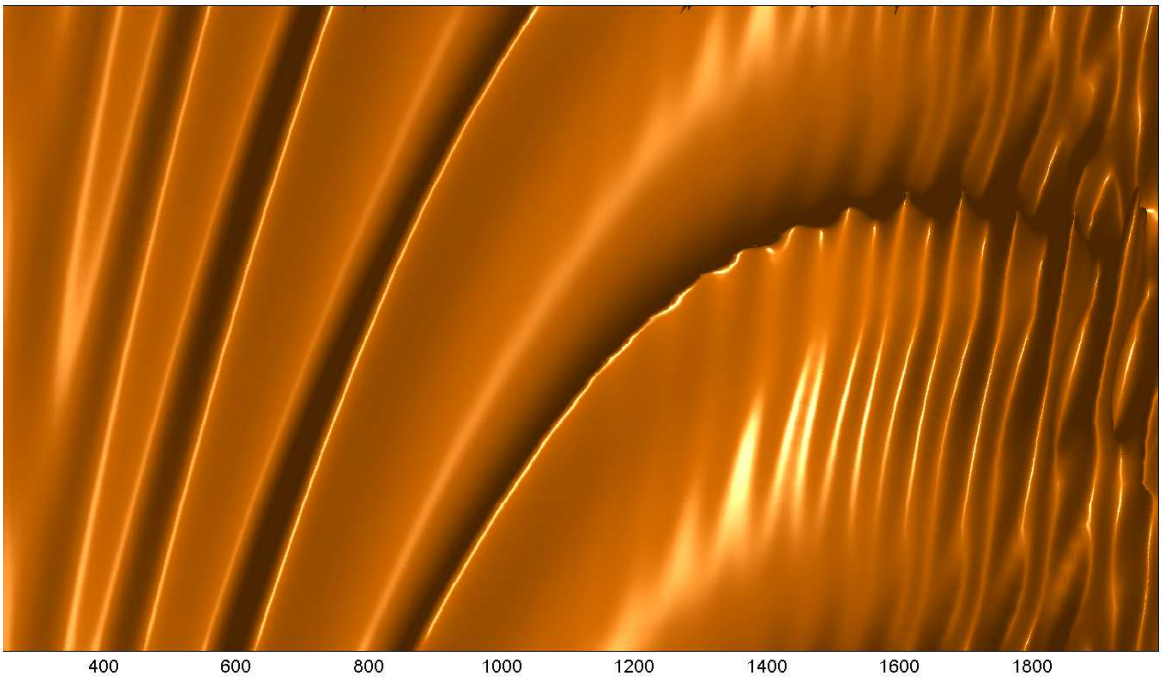

Figure 8.32: Session 5: Travelling wave dominated transition. Snapshot aligned with free stream.

rection.

High Frequency Secondary Instabilities

As to the exact nature of the breakdown to turbulence, the marching procedure is not extended far enough. However, plots of the MFD mode close to the numerical breakdown of session 3 and 5 indicate a calm upper layer, as for natural transition in a Blasius flow. Experimental observations, Kohama et al. (1991), report explosive growth of high-frequency secondary instabilities of inviscid type. This correlates well with the inflectional meanflow profile in the distorted area. The possibility for inclusion of the high-frequency secondary instabilities in the non-linear PSE procedure has been investigated. The idea of an all-encompassing method, which it would then be, is obviously appealing. Nevertheless it faces a series hurdles to be circumvented. The investigation performed on high-frequency modes is only briefly outlined below, as the findings do not motivate further analysis.
A testcase is designed with 2113 modes(!). The vector of spanwise wavenumbers is that of the steady vortex example, Fig.8.22. The vector of temporal wavenumbers is $(0\omega_1, 0)$, $(1\omega_1, 0)$, $(2\omega_1, 0)$, ... $(32\omega_1, 0)$. This should enable us to find a large part of the unstable secondary instabilities although not the most high-frequent for the most distorted areas of the baseflow, Stolte (1999). We define the initial 2080 unsteady amplitudes to be vanishing small. The initial steady amplitudes are exactly as the steady vortex example of Fig.8.22. Initial data is succesfully found by the frozen coefficients technique for all modes, which here prove to be very robust for localizing the heavily damped high-frequency viscous modes. Due to the high initial steady amplitudes compared to the very very small initial amplitudes of the unsteady modes, the non-

linear interaction between steady oblique and unsteady modes vanish. The internal nonlinear interaction between the unsteady modes is negligible also. The nonlinear interaction between the steady modes become that of the already calculated steady vortex example. The remaining nonlinear interaction between the MFD mode and the unsteady modes decouples and becomes uni-directional: The MFD-mode affects the receptivity of all the unsteady modes, but the unsteady modes have very low amplitudes incapable of contributing to the MFD mode. Now the task becomes clear. It consists of investigating the linear PSE evolution of the unsteady modes to the MFD-corrected baseflow, where the MFD mode is available from the steady vortex example. We would expect the unstable mode $(1, 1)$ to be accompanied by a whole array of more unstable modes as the pre-calculated MFD mode grows and affects the effective baseflow upon marching downstream. However, The PSE method fails completely to gradually convey some of the considered modes into high-frequency secondary instability, as the MFD correction becomes more prominent in the downstream marching direction. The considered modes located in a fourier plane only change minimally and new instabilities do not appear. The lessons learned are:

- Although the MFD correction to the baseflow ensures an impact on the receptivity for all other modes, high-frequency secondary instability modes are not likely to be encountered. A plot of the corrected baseflow profiles reveals an inflection point in the outer part of the boundary layer. Hence, the sought-after new instabilities are probably not of the inner layer viscous type, but rather belongs to one or more different inviscid family/families of modes.

- A succesful PSE computation of high-frequency secondary modes should therefore be able to include more than one (viscous) family of modes. This requirement would force us to abandon the Fourier plane domain in favour of a complete 3D Fourier volume domain spanned by the temporal, spanwise and streamwise wavenumber-vectors. Even so, the identification of the high-frequency instabilities is far from granted by the standard PSE-method alone. It must be doubted if such a complex PSE computation would be worth the effort, since the cpu cost increase by adding one dimension to the considered Fourier space is considerable.

Chapter 9

Concluding Remarks

9.1 Summary

High-order numerical schemes have been derived and implemented in a suite of tools for analyzing hydrodynamic instability in the incompressible regime. It consists of baseflow solvers in physical space and perturbation solvers in Fourier space. All solvers deal with convergence problems, either in pursuit of a steady flow or an array of oscillatory convectively dominated modes with steady amplitudes. These modes can be uncoupled or coupled for linear and nonlinear analysis respectively.
The baseflow solvers for 2D or 2.5D are: A local self-similarity boundary profile solver, a nonlocal parabolic boundary layer solver and a novel 6'th order accurate coupled compact volume Navier-Stokes solver with multigrid acceleration. Stability analysis revealed that among several compact volume solvers, the staggered CCV6s scheme had the best behavior in terms of numerical stability. Optimal complexity, i.e. O(N)-scaling with size, was obtained for some testcases, which all demonstrated good multigrid acceleration.
The perturbation solvers are:

- A local LST eigenvalue solver based on the Orr-Sommerfeld equation for temporal or spatial analysis. The matrix system is obtained using differentiation matrices that are constructed either from the well-known pseudo-spectral method using Chebyshev polynomials, or from a novel non-uniform 8'th order accurate coupled compact difference scheme (CCD8). Both schemes performed well, the CCD8 scheme not quite as efficient in error reduction as the spectral discretization, but with full flexibility in the choice of 1D point distribution.

- A non-local linear/nonlinear 2.5D PSE implementation employing the non-uniform CCD6 scheme in the wall-normal direction. The linear PSE results mainly served to validate against literature references, and to enable comparison between the LST- and the PSE-based e^N-method, which exhibited only minor differences. Improved nonlinear mode-interaction was obtained through Mean Flow Correction (MFC) and examples of natural and bypass transition scenarios were presented. The appearance of hairpin-vortices in the late stages of by-pass transition on a flat plate is, to the extent of our knowledge, a result not previously obtained with PSE. Another observation for the swept plate flow is the ordering of nonlinear interaction along lines in Fourier space along the direction of the primary instability for travelling wave dominated transition scenarios,

or only along the steady spanwise mode axis in the case of stationary vortex dominated scenarios.

- A non-local linear 2.5D ESE solver using the same compact discretization as the PSE solver. It was applied to a semi-analytically derived bubble baseflow, and compared to LST for the same testcase. In contrast to the PSE-LST comparison, much larger discrepancies were encountered for the spatial amplification, which were attributed to the large non-parallelism of the reversed boundary layer flow. Overall, the very high spatial growth rates agreed well with LST, as did the reverse flow magnitude at which absolute or global instability would occur. The high N-factors even at low reverse-flow magnitudes make us conclude that the transition onset from convected instabilities will precede global instability of the laminar bubble.

9.2 Outlook

For the linear analysis it would be appealing to use spatial spanwise ESE to track modes over a rotating turbine blade. The baseflow solution should be obtained from a 3D boundary layer code with strong viscous-inviscid interaction capable of marching through zones of recirculation, and the transition criterion based on the e^N-method.
For the non-linear analysis the PSE method has reached a state of maturity from where further advances seem cumbersome. The unavoidable failure of nonlinear PSE to converge at the late stages of transition causing the marching procedure to halt could be avoided by abandoning the Fourier decomposition in the streamwise direction altogether, and use a higher-order scheme to resolve this dimension. This leaves us with a Fourier space consisting of the ω-β plane. Each mode in the plane should then be marched in pseudo-time and the nonlinear interaction between the modes updated at each timestep until convergence, using artificial compressibility and multigrid acceleration in the physical plane spanned by the streamwise and wall-normal directions, e.g. as demonstrated for the CCV6s baseflow solver. This approach would in many ways be a trade-off between non-linear PSE and full DNS, and might prove powerful for 2.5D analysis of airfoil sections.

Bibliography

[1] Airiau C., Casalis G. Linear and nonlinear laminar boundary layer stability using the parabolized stability equations. *Comptes Rendus de l'Academie des Sciences, Serie II*, 1994, **318**, 1295–300.

[2] Alam M., Sandham N.D. Direct numerical simulations of 'short' laminar separation bubbles with turbulent reattachment. *Journal of Fluid Mechanics*, 2000, **410**, 1–28.

[3] Allen T., Riley N. Absolute and convective instabilities in separation bubbles. *Aeron. J. Roy. Aeron. Soc.Wind Energy*, **dec. 1995**, 439–448.

[4] Andersson P., Henningson D.S., Hanifi A. On a stabilization procedure for the parabolic stability equations. *Journal of Engineering Mathematics*, 1998, **33**, 311–332.

[5] Arnal D. Boundary layer transition: Predictions based on linear theory. AGARD report R-793, 1994, paper no. 2.

[6] Asai M., Nishioka M. Boundary layer transition triggered by hairpin eddies at subcritical Reynolds numbers. *Journal of Fluid Mechanics*, 1995, **297**, 101–22.

[7] Berlin S. Oblique waves in boundary layer transition. Ph.D. Thesis, 1998, Royal Institute of Technology, Stockholm, Sweden.

[8] Bertolotti F.P. Linear and nonlinear stability of boundary layers with streamwise varying properties. Ph.D. Thesis, 1991, The Ohio-State University, Columbus, Ohio.

[9] Bertolotti F.P., Herbert Th., Spalart P.R. Linear and nonlinear stability of the Blasius boundary layer. *Journal of Fluid Mechanics*, 1992, **242**, 441–74.

[10] Bertolotti F.P. On the birth and evolution of disturbances in three-dimensional boundary layers. In P.W. Duck and P. Hall, editors, *Proceedings of the IUTAM Symposium on Nonlinear Instability and Transition in Three-Dimensional Boundary Layers*, pp 247–56. Kluwer, 1996.

[11] Bouthier M. Stabilité linéaire des écoulements presque parallèles. *J. Mécanique*, 1972, **11**, 599–621.

[12] Bouthier M. Stabilité linéaire des écoulements presque parallèles. Partie II. La couche limite de Blasius. *J. Mécanique*, 1973, **12**, 75–95.

[13] Brandt L., Henningson D.S. Transition of streamwise streaks in zero-pressure-gradient boundary layers. *Journal of Fluid Mechanics*, 2002, **472**, 229–262.

[14] Chang C-L., Malik M.R., ErleBacher G., Hussaini M.Y. Compressible stability of growing boundary layers using parabolized stability equations. AIAA Paper 91-1636, 1991.

[15] Chang C-L., Malik M.R. Oblique-mode breakdown and secondary instability in supersonic boundary layers. *Journal of Fluid Mechanics*, 1994, **273**, 323–60.

[16] A. J. Chorin, A Numerical Method for Solving Incompressible Viscous Flow Problems, *J. Comput. Phys* **2** (1967) 16–42

[17] Chu P.C., Fan C. A three-point combined compact difference scheme. *Journal of Computational Physics*, 1997, **140**, pp. 370–399.

[18] Chu P.C., Fan C. A three-point sixth-order nonuniform combined compact difference scheme. *Journal of Computational Physics*, 1999, **148**, pp. 663–674.

[19] Corke T.C., Mangano R.A. Resonant growth of three-dimensional modes in transitioning Blasius boundary layers. *Journal of Fluid Mechanics*, 1989, **209**, 93–150.

[20] Craik A.D.D. Nonlinear resonant instability in boundary layers. *Journal of Fluid Mechanics*, 1971, **50**, 393.

[21] Day M.J., Mansour N.N.,Reynolds W.C. Structure and stability of compressible reacting mixing layers. *Report no. TF-75*, 1999, Stanford University, Stanford, California.

[22] Stability of velocity profiles with reverse flow. In *Instability, transition and turbulence*, 1991, pp. 212–215. Springer-Verlag.

[23] Goldstein M.E., Durbin P.A. Nonlinear critical layers eliminate the upper branch of spatially growing Tollmien-Schlichting waves. *Physics of Fluids*, 1986, **29**, 2344–2345.

[24] Haidari A.H., Smith C.R. The generation and regeneration of single hairpin vortices. *Journal of Fluid Mechanics*, 1994, **277**, 135–62.

[25] Hall P. The linear development of Görtler vortices in growing boundary layers. *Journal of Fluid Mechanics*, 1983, **130**, 41–58.

[26] Hammond J.A., Redekopp L.G. Local and global instability properties of separation bubbles. *Eur. J. Mech. B Fluids*, 1998, **17**, 145–164.

[27] Herbert Th. Über endliche amplituden periodischer störungen der grenzschicht an der ebenden platten. *DLR-FB*, 1974, 74–53. (*ESE Tech. Transl.*, 1975, TT-169)

[28] Herbert Th., Morkovin M.V. Dialogue on bridging some gaps in stability and transition research. In *Laminar-Turbulent Transition*, ed. R. Eppler, H. Fasel, pp. 47–72. Berlin: Springer-Verlag 1980.

[29] Herbert Th, Bertolotti, F. The effect of pressure gradients on the growth of subharmonic disturbances in boundary layers. In *Proc. Conf. Low Reynolds number airfoil dyn.* (ed. T. Mueller), 1985, 65–76. Notre Dame University

[30] Herbert Th. Secondary instability of boundary layers. *Annu. Rev. Fluid. Mech.*, 1988, **20**, 487–526.

[31] Herbert Th. Parabolized stability equations. AGARD Report R-793, 1994, paper no. 4.

[32] Herbert Th. Stability and transition of 3D boundary layers. Personal comunication, unpublished.

[33] Herbert Th. Parabolized stability equations. *Annu. Rev. Fluid. Mech.*, 1997, **29**, 245–83.

[34] Huai X., Joslin R.D., Piomelli U. Large-eddy simulation of boundary-layer transition on a swept wedge. *Journal of Fluid Mechanics*, 1999, **381**, 357–80.

[35] Itoh N. Spatial growth of finite wave disturbances in parallel and nearly parallel flows. Part II. *Trans. Japan Soc. Aero. Space Sci.*, 1974, **17**, 175–86.

[36] Joslin R.D., Streett C.L., Chang C.-L. Spatial direct numerical simulation of boundary-layer transition mechanisms: Validation of PSE theory *Theoretical and Computational Fluid Dynamics.*, 1993, **4**, 271–88.

[37] Kachanov Yu.S., Kozlov V.V., Levchenko V.Ya. Nonlinear development of a wave in a boundary layer. *Fluid Dyn.*, 1977, **3**, 383–390.

[38] Klebanoff P.S. Effect of free-stream turbulence on a laminar boundary layer. *Bull. Am. Phys. Soc.*, 1971, **16**.

[39] Klingmann B.G.B., Boiko A., Westin K., Kozlov V., Alfredsson P. Experiments on the stability of Tollmien-Schlichting waves. *Europ. J. Mech. B*, 1993, **12**, 493–514.

[40] Kloker M.J. Robust high-resolution split-type compact FD scheme for spatial direct numerical simulation of boundary-layer transition. *Applied Scientific Research (The Hague)*, 1998, **59**, 353–377.

[41] Kobayashi M.H. On a class of Padé finite volume methods. *Journal of Computational Physics*, 1999, **156**, 137–180.

[42] Kohama Y., Saric W.S., Hoos W.S. A high-frequency secondary instability of crossflow vortices, that leads to transition. In *Proceedings of the R.A.S. Conference on Boundary-Layer and Control*, Cambridge, UK, pp. 4.1-4.13, 1991.

[43] Lele S.K. Compact finite-difference schemes with spectral-like resolution. *Journal of Computational Physics*, 1992, **103**, 16–42.

[44] Liepmann H.W. Investigations on laminar boundary-layer stability and transition on curved boundaries. NACA WR W-107 (Formerly NACA ACR 3H30), 1943.

[45] Mack L.M. A numerical study of the temporal eigenvalue spectrum of the Blasius boundary layer. *Journal of Fluid Mechanics*, 1976, **73**, 497–520.

[46] Mack L.M. Boundary-layer linear stability theory. AGARD report R-709, 1984, paper no. 3.

[47] Mahesh K. A family of high order finite difference schemes with good spectral resolution. *Journal of Computational Physics*, 1998, **145**, 332–358.

[48] Malik M.R., Li F., Chang C-L. CrossFlow disturbances in three-dimensional boundary layers: Nonlinear development, wave interaction and secondary instability. *Journal of Fluid Mechanics*, 1994, **268**, 1–36.

[49] Michalke A. On the inviscid instability of wall-bounded velocity profiles close to separation. *ZFW*, 1990, **14**, 24–31.

[50] Mitchell & Griffiths, *The finite difference method in partial differential equations.* (Wiley, 1980).

[51] Müller B. Experimentelle Untersuchung der Querströmungsinstabilität im linearen und nichtlinearen bereich des transitionsgebietes. DLR-FB 90-09, DLR, Köln, 1990. , Li F., Chang C-L. CrossFlow disturbances in three-dimensional boundary layers: Nonlinear development, wave interaction and secondary instability. *Journal of Fluid Mechanics*, 1994, **268**, 1–36.

[52] Müller W. Numerische untersuchung räumlicher umschlagvorgänge in dreidimensionalen grenzschichtströmungen. PhD thesis, Universität Stuttgart, 1995.

[53] Nishioka M., Iida S., Ichikawa Y. An experimental investigation of the stability of plane Poiseuille flow. *Journal of Fluid Mechanics*, 1975, **72**, 731

[54] Nitschke-Kowsky P., Bippes H. Instability and transition of a three-dimensional boundary layer on a swept plate *Phys. Fluids*, 1988, **31**, 786–95

[55] Orr W. The Stability or Instability of the Steady Motions of a Perfect Liquid and of Viscous Liquid. *Proc. Roy. Irish Acad.*, 1907, A **21**, 9–68 and 69–138.

[56] Orszag S.A. Accurate solution of the Orr-Sommerfeld stability equation. *Journal of Fluid Mechanics*, 1971, **50**, 689–703.

[57] J. M. C. Pereira, M. H. Kobayashi and J. C. F. Pereira, A Fourth-Order-Accurate Finite Volume Compact Method for the Incompressible Navier-Stokes Solutions, *J. Comput. Phys* **167** (2001) 217–243

[58] Reddy S., Henningson D.S. Energy growth in viscous channel flows. *Journal of Fluid Mechanics*, 1993, **252**, 209–38.

[59] Rist U., Maucher U. Direct numerical simulation of 2D and 3D instability waves in alaminar separation bubble. In *AGARD CO-551, Application of direct and large eddy simulation to transition and turbulence*, 1994, pp. 34-1–34-7.

[60] Saric W.S., Nayfeh A.H. Nonparallel stability of boundary-layer flows. *Physics of Fluids*, 1975, **18**, 945–50.

[61] Schlichting H. Concerning the origin of turbulence in a rotating cylinder. *Math. Phys. Klasse*, no. 2, 1932, pp. 160–198.

[62] Schmid A.M.O. Transition, pressure gradient and stability theory *Proceedings of the IX International Congress of Applied Mechanics*, 1956, paper no. 4.

[63] schmid P.J., Henningson D.S. *Stability and Transition in Shear Flows*, 2001, Springer-Verlag.

[64] Schrauf G., Herbert Th., Stuckert G. Evaluation of transition in flight tests using nonlinear parabolized stability equation analysis. *Journal of Aircraft*, 1996, **33**, 554–560.

[65] Schubauer G.B., Skramstad H.K. Laminar boundary-layer oscillations and stability of laminar flow. *J. Aeronaut. Sci.*, 1947, **14 no. 2**, pp. 69–78.

[66] T.M. Shih, C.H. Tan and B.C. Hwang, Effects of Grid Staggering on Numerical Schemes, *Int. J. Numer. Methods. Fluids* **9** (1989) 193

[67] Shaikh F.N., Gaster M. The non-linear evolution of modulated waves in a boundary layer. *Journal of Engineering Mathematics*, 1994, **28**, 55–71.

[68] Simen M. Local and nonlocal stability theory of spatially varying flows. In *Instability, transition and turbulence*, 1992, pp. 181–201. Springer-Verlag.

[69] Smith F.T. Nonlinear stability of boundary layers for disturbances of various sizes. *Proc. Roy Soc.*, 1979, A **368**, 573–89.

[70] Sommerfeld A. Ein Beitrag zur Hydrodynamischen Erklaerung der Turbulenten Fluessigkeitsbewegungen. *Proceedings 4th International Congress of Mathematicians*, 1908, Rome, Vol III, pp. 116–24.

[71] Spalart P.R. Strategies for Turbulence Modelling and Simulations. *Int. Journal of Heat and Fluid Flow*, 2000, **21**, 252–263.

[72] Spalart P.R., Strelets M.Kh. Mechanisms of transition and heat transfer in a separation bubble. *Journal of Fluid Mechanics*, 2000, **403**, 329–349.

[73] William Frederick Spotz, High-Order Compact Finite Difference Schemes for Computational Mechanics, dissertation, University of Texas (1995)

[74] Stolte A., Bertolotti F.P., Hein S., Simen M., Dallmann U. Nichtlokale und nichtlinare instabilitätsuntersuchungen an kompressiblen strömungen. Technical Report *DLR-IB 223-95 A54*, 1995, Deutsches Zentrum für Luft- und Raumfahrt (DLR), Göttingen, Germany.

[75] Stolte A. Investigation of transition scenarios in boundary layer flows. Ph.D. Thesis, 1999, Deutsches Zentrum für Luft- und Raumfahrt (DLR), Göttingen, Germany.

[76] Tollmien W. Über die entstehung der turbulenz. *Math. Phys. Kl.*, 1929, pp. 21–44.

[77] Van Ingen J.L.A. A suggested semi-empirical method for the calculation of the boundary-layer region. *Tech. Report no. VTH71, VTH74*, 1956, Delft, The Netherlands.

[78] Jan Vierendeels, Kris Riemslagh and Erik Dick, A Multigrid Semi-Implicit Line-Method for Viscous Incompressible and Low-Mach-Number Flows on High Aspect Ration Grids, *J. Comput. Phys* **154** (1999) 310–341

[79] Wang M. Stability analysis of three-dimensional boundary layers with parabolized stability equations. Ph.D. Thesis, 1994, The Ohio-State University, Columbus, Ohio.

[80] Wagner M. Numerische untersuchungen zum laminar-turbulenten übergang in zwei- und dreidimensionalen grenzschichten. DLR-FB-92-36, DLR, Köln, 1992.

[81] Yen C.C., Messersmith L. Application of parabolized stability equations to the prediction of jet instabilities. *AIAA Journal*, 1998, **36**, 1541–4.

Recent Ph.D.-dissertations in Fluid Mechanics

Sørensen, J.N. Three-Level, Viscous-Inviscid Interaction Technique for the Prediction of Separated Flow Past Rotating Wing, AFM 86-03, 1986

Michelsen, J.A. Modelling of Laminar Incompressible Rotating Fluid Flow, AFM 86-05, and Modelling of Turbulent Incompressible Rotating Fluid Flow, AFM 86-07, 1986

Sørensen, L.S. Three-Dimensional Electro-Fluid-Dynamics in Tuft Corona Wire-Plate Precipitators, AFM 89-03, 1989

Gervang, B. Numerical Simulations of 3-Dimensional Flow in Straight and Curved Ducts of Rectangular Cross Section, AFM 89-09, 1989

Andresen, E. Statistical Approach to Continuum Models for Turbulent Gas Particles Flows, AFM 90-04, 1990

Nielsen, N.F. Low Reynolds Number Fluid Dynamics with Applications to Suspending Feeding Animals, AFM 91-10, 1991

Zamany, J. Modelling of Particle Transport in Commercial Electrostatic Precipitators, Ph.D under ATV, EF316, 1992

Christensen, E.A. Laminar-Turbulent Transition in the Rotating Driven Cavity Problem, AFM 93-12, 1993

Trinh, C.M. Turbulence Modelling of Confined Swirling Flows, Risø-R-647,1993

Mayer, K.E. Experimental and Numerical Modelling of Turbulent Flows and Heat Transfer in Staggered Tube Bundles, AFM 94-03, 1994

Mayer, S. Particle Motion in Unsteady Three-Dimensional Flow at Low Reynolds Numbers , AFM 94-04, 1994

Hansen, M.O.L. Vorticity-Velocity Formulation of Navier-Stokes Equations for Aerodynamic Flows, AFM 94-07, 1994

Hvid, S.L. Curvature Based Smoothing of Plane Cubic B-spline Curves, AFM 93-08, Surface Description using Bicubic B-splines, AFM 93-10, QM3D, 3D Netgenerering, Brugermanual, AFM 94-02 and Three-Dimensional Algebraic Grid Generation, AFM 94-08 1993-94

Walther, J.H. Discrete Vortex Method for Two-Dimensional Flow past Bodies of Arbitrary Shape Undergoing Prescribed Rotary and Translational Motion, AFM 94-11, 1994

Nim, E. Energidissipation og Masseoverførsel af Gas i og Omkring Statiske Miksere med Boblestrømning, Ph.D. under ATV, EF410, 1994

Sørensen, N.N. General Purpose Flow Solver Applied to Flow over Hills, Risø-R-827(EN), 1995

Filippone, A. Interaction of Potential Flow Model with the Navier-Stokes Equations for Rotor Aerodynamics, AFM 95-07, 1995

Jensen, E. Optimization of the Electromagnetic Flowmeter, AFM 95-09, 1995

Schmidt, J.J. Experimental and Numerical Investigation of Separated Flows, ET-PHD 97-01 1997

Nygreen, P. A Vorticity-Streamfunction Formulation of the Navier-Stokes Equations for Predicting Unsteady Flow past Bodies in Arbitrary Movement, ET-PHD 97-02, 1997

Sørensen, D.N. Aerodynamic Modelling and Optimization of Axial Fans, ET-PHD 98-01, 1998

Lennart, A.S. Experimental and Theoretical/Numerical Study of Evaporation from Shallow Pools of Organic Liquids, at Simulated Work Conditions, ET-PHD 98-02, 1998

Johansen, J. Unsteady Airfoil Flows with Application to Aeroelastic Stability, Risø-R-1116(EN), 1999

Ullum, U. Imaging Techniques for Planar Velocity and Concentration Measurements, ET-PHD 99-03,1999

Jørgensen, B.H. Low-Dimensional Modelling and Dynamics of the Flow in a Lid Driven Cavity with a Rotating Rod, ET-PHD 2000-02, 2000

Myllerup, L. Turbulence Models for Complex Flows, ET-PHD 2000-03, 2000

Pedersen, N. Experimental Investigation of Flow Structures in a Centrifugal Pump Impeller using Particle Image Velocimetry, ET-PHD 2000-05, 2000

Voigt, L.P.K. Navier-Stokes Simulations of Airflows in Rooms and Around a Human Body, ET-PHD 2001-00, 2001

Gaunaa, M. Unsteady Aerodynamic Forces on NACA 0015 Airfoil in Harmonic Translatory Motion, MEK-FM-PHD 2002-02, 2002

Pedersen, J.M. Analysis of Planar Measurements of Turbulent Flows, MEK-FM-PHD 2003-01, 2003

Mikkelsen, R. Actuator Disc Methods Applied to Wind Turbines, MEK-FM-PHD 2003-02, 2003

Ullum, T.U. Investigation of Turbulence and Flow Structures in Electrostatic Precipitator, MEK-FM-PHD 2003-03, 2003

Hjort, S. Incompressible Boundary Layer Instability and Transition, MEK-FM-PHD 2004-01, 2004